



HAL
open science

Characterisation of the flow in a water-puddle under a rolling tire with refracted PIV method

Damien Cabut

► **To cite this version:**

Damien Cabut. Characterisation of the flow in a water-puddle under a rolling tire with refracted PIV method. Other. Université de Lyon, 2020. English. NNT : 2020LYSEC025 . tel-03150015

HAL Id: tel-03150015

<https://theses.hal.science/tel-03150015v1>

Submitted on 23 Feb 2021

HAL is a multi-disciplinary open access archive for the deposit and dissemination of scientific research documents, whether they are published or not. The documents may come from teaching and research institutions in France or abroad, or from public or private research centers.

L'archive ouverte pluridisciplinaire **HAL**, est destinée au dépôt et à la diffusion de documents scientifiques de niveau recherche, publiés ou non, émanant des établissements d'enseignement et de recherche français ou étrangers, des laboratoires publics ou privés.



ÉCOLE
CENTRALE LYON

N° d'ordre NNT: 2020LYSEC25

**THÈSE de DOCTORAT DE L'UNIVERSITÉ DE LYON
opérée au sein de l'École Centrale de Lyon**

**École Doctorale N° 162
Mécanique Énergétique Génie Civil Acoustique**

Spécialité de doctorat : Mécanique des Fluides

Soutenue publiquement le 13/10/2020, par

Damien Cabut

**Characterisation of the flow in a water-puddle under a rolling
tire with refracted PIV method.**

Devant le jury composé de:

Bruecker, Christoph	Professeur	City University of London	Rapporteur
Vetrano, Maria-Rosaria	Professeur	Katholieke Universiteit Leuven	Présidente du jury
Gabillet, Céline	Maître de Conférences	Ecole Navale	Examineur
Todoroff, Violaine	Docteur	Michelin	Examineur
Simoens, Serge	Directeur de recherche	École Centrale de Lyon	Directeur de thèse
Michard, Marc	Docteur	École Centrale de Lyon	Co-Directeur de thèse

Abstract :

Résumé :

L'écoulement au sein d'une flaque d'eau lors du passage d'un pneumatique en roulement est étudié dans ce travail. Une méthode de mesure adaptée aux mesures sur piste sous un véhicule en roulement est développée dans un premier temps. Cette méthode basée sur la méthode PIV (Vélocimétrie par Images de Particules), consiste en la réfraction de la nappe laser à l'interface hublot/écoulement afin de pouvoir éclairer les particules par le même accès optique que la collection d'images. Cette technique appelée refracted PIV (R-PIV) est caractérisée dans un premier temps sur un écoulement contrôlé en laboratoire. Cette technique est ensuite adaptée au cas de la piste pour les mesures in-situ. Ces mesures appliquées à la piste ont permis de mettre en évidence différents comportements de l'écoulement dans la flaque d'eau en amont du pneumatique mais également au sein des sillons pneumatiques. En amont du pneumatique les évolutions linéaires de la vitesse du fluide en fonction de la vitesse du véhicule est mise en évidence dans ce travail. Des effets non linéaires sont également observés et mis en lien avec la réduction de l'aire de contact pneu chaussée. Dans un second temps, l'étude de l'écoulement au sein des sculptures du pneumatique dans l'aire de contact nous permet de mettre en évidence deux grands types de sculptures. Le premier est composé de tous les sillons longitudinaux du pneumatique. Dans ces sillons, la vitesse de l'écoulement à travers ces sculptures dépend de la vitesse véhicule mais également de la présence du témoin d'usure du pneumatique. Un écoulement secondaire tourbillonnaire a également été mis en évidence grâce à nos mesures sur piste. Dans le second type des sillons composés de toutes les sculptures orientées transversalement, la vitesse du fluide, en leur sein, dépend de leur position dans l'aire de contact. Cette évolution semble être fonction de la déformation du pneumatique dans l'aire de contact. Pour finir, les interactions entre ces différents types de sculptures sont également discutées dans ces travaux permettant d'expliquer certains comportements spécifiques.

Mots Clés : Vélocimétrie par Images de Particules (PIV), Réfraction, Pneumatique, Hydroplanage, Ecoulements multiphasiques, Surface Libre.

Abstract :

In this work, the fluid flow in a water puddle while a rolling tire crosses the puddle is studied. A measurement method adapted to track measurements under a rolling tire is developed. This method, based on PIV (Particle Image Velocimetry), is based on the refraction of the laser light sheet at the flow/window interface. This allows us to illuminate particles and record their images from a single optical access. This technique called refracted PIV (R-PIV) is characterised with a laboratory controlled experiment. When characterised, this technique is applied to in-situ measurements on the track. Measurements performed allow to highlight specific behaviours in different parts of the flow, in front of the tire and inside tire grooves in the contact patch area between the tire and the road. In front of the tire, the linear evolution of the water velocity in the puddle as a function of the vehicle speed is demonstrated. At high vehicle speed, non-linear effects are highlighted and linked to the shape of the contact patch area which evolves at high vehicle speed. Under the tire contact patch area, two main types of grooves contribute to the draining of water. Firstly, the longitudinal grooves are the straight grooves aligned with the rolling direction. In these grooves, the velocity of the fluid flow depends on the vehicle speed and also on the presence or not of the wear indicator. A secondary vortex like flow structure is also demonstrated in this work. The second type of grooves are the transverse grooves which are the grooves oriented with a certain angle compared to the car rolling direction. In these grooves, this work proved that the velocity is dependent on the groove location in the contact patch area. This seems to be linked to the tire deformation with the load of the car in the contact patch area. Finally, this work discussed the link between the different tire groove types to explain different specific behaviours.

Key words : Particle Image Velocimetry (PIV), Refraction, Tire, Hydroplaning, Multiphase flow, Free-surface.

Remerciements :

Cette thèse a été réalisée dans le cadre d'un projet FUI (Hydrosafe tire) financé par BPI France (n° DOS0051329/00) et la région AURA (n° 16 015011 01). Les partenaires de ce projet étant le Laboratoire de Mécanique des Fluides et d'Acoustique (LMFA) de l'Ecole Centrale de Lyon, le Laboratoire d'Hydrodynamique, d'Energétique et Environnement Atmosphérique (LHEEA) de l'Ecole Centrale de Nantes, Nextflow Software et Michelin.

Je souhaite tout d'abord remercier mes encadrants de thèse pour leur soutien tout au long de ma thèse. Merci à Serge pour la gestion de la thèse et pour m'avoir fait confiance pour ces 3 années. Merci à Marc pour l'aide apportée tout au long de la thèse. Je souhaiterai également remercier les collaborateurs du projet de Centrale Nantes et de Nextflow ainsi que les partenaires de Michelin. Je souhaite tout particulièrement remercier Violaine pour sa disponibilité et les sessions manips à Ladoux avec Jean. Je voulais de plus remercier Loïc pour son aide en optique et Nathalie pour sa disponibilité pour la gestion des ressources.

Je tiens à remercier tous mes collègues doctorants et post-doctorants pour les discussions constructives ou non du midi et les parties de babyfoot endiablées. Je ne me lance pas dans une liste par peur d'oublier quelqu'un mais ils se reconnaîtront. Mention particulière à Yann et Simon pour les petits repas et le tour des restos lyonnais.

Un grand merci également à ma famille et mes amis pour le soutien morale tout le long de ma thèse. Merci à la bande de Puffer pour les instants détentes et la présence pendant la soutenance.

Une petite pensée en la mémoire de Jean-Pierre Hermand qui m'a pris sous son aile pour mes 7-8 mois de stage de recherche à Polytechnique Bruxelles pour ma première expérience en labo de recherche.

Contents

1	Introduction and State of the Art	20
1.1	Context and Motivations.	20
1.2	Analysis of the flow in a puddle with a rolling tire.	22
1.2.1	Experimental studies of the phenomenon.	22
1.2.1.1	Visualisation of the Contact patch area.	23
1.2.1.2	Velocity measurements in presence of water	24
1.2.2	Some Numerical studies of the hydroplaning phenomenon.	24
1.2.3	Purpose of this work.	25
1.3	The flow structure.	26
1.3.1	Different zones of the flow.	26
1.3.2	Flow in front of the tire.	26
1.3.3	Flow in tire groove.	27
1.3.4	Conclusion.	30
1.4	Thesis organisation.	30
2	The refracted PIV (R-PIV) technique.	33
2.1	The Particle Image Velocimetry (PIV).	33
2.1.1	planar PIV technique.	33
2.1.1.1	Description of a planar PIV set-up.	33
2.1.1.2	Description of the cross correlation.	34
2.1.2	Microscopic PIV (μ -PIV) technique.	36
2.1.2.1	Description of a μ -PIV set-up.	36
2.1.2.2	Cross-correlation and integration effect.	36
2.1.3	R-PIV a hybrid technique adapted to confined spaces.	37
2.2	Experiental set-up for R-PIV testing.	38
2.2.1	The bench and operating conditions	38
2.2.2	Emitting Optics	39
2.2.3	Seeding	40
2.2.4	Image acquisition and processing	40
2.3	Optical properties for R-PIV.	41
2.3.1	The laser sheet propagation.	41
2.3.1.1	Measurement of the laser sheet intensity after the refraction.	41
2.3.1.2	Ray tracing model.	43

2.3.1.3	Long range propagation for tire application.	45
2.3.2	Depth of focus.	46
2.3.3	Conclusions.	47
2.4	Cross-correlation statistical model for R-PIV	47
2.4.1	Cross correlation model (CCM).	47
2.4.1.1	The cross-correlation general form.	47
2.4.1.2	Statistical convergence.	50
2.4.2	Analysis of the illumination methods with the CCM	53
2.4.2.1	Model Prediction for P-PIV.	53
2.4.2.2	Model Prediction for R-PIV.	54
2.5	Results and validation of the model	55
2.5.1	Flow Structure.	55
2.5.2	R-PIV results.	56
2.6	Conclusions	59
2.6.1	Optical properties of R-PIV	59
2.6.2	Prediction of the measured velocity using a cross-correlation model	59
3	Application to tire flow measurements.	61
3.1	Experimental set-up for tire measurements.	61
3.1.1	Measurement pit.	61
3.1.1.1	2D2C R-PIV measurement set-up	61
3.1.1.2	2D3C Stereoscopic R-PIV measurement set-up	61
3.1.2	Reception Optic.	63
3.1.3	Seeding particles.	64
3.1.4	Emission Optic.	65
3.1.5	Conclusions.	68
3.2	Measurement protocol for R-PIV measurements.	68
3.3	Tire models studied.	69
3.3.1	Primacy 4 (PCY 4) (commercial summer tire).	69
3.3.2	Wear state.	70
3.4	Coordinate system and contact patch.	70
3.4.1	PCY4 tire.	71
3.4.2	CCP tire.	72
3.5	Flow zones and velocity fields processing.	73
3.5.1	In front of the tire.	74
3.5.2	Inside tire grooves.	74
3.5.3	Repetition strategy and ensemble averaging.	75
4	Sources of Variabilities.	77
4.1	Influence of control parameters.	77
4.1.1	The water height.	77
4.1.2	Vehicle speed.	77
4.1.3	Tire location identification.	78

4.1.4	Contact patch position.	78
4.1.5	Mask positioning.	79
4.2	Metrological sources of variability.	79
4.2.1	In front of the tire.	79
4.2.2	Inside tire grooves.	80
4.3	Hydrodynamic source of variabilities.	81
4.3.1	Transverse grooves position.	81
4.3.2	Wear indicator position.	82
4.3.3	Turbulence.	82
4.4	Conclusions.	83
5	Metrological discussion.	85
5.1	Metrological sources of bias in front of the tire.	85
5.1.1	Geometry of the flow in front of the tire.	85
5.1.2	Fluorescent Particle motion in the fluid.	86
5.1.2.1	Falling time before acquisition.	87
5.1.2.2	Particle behaviour submitted to highly accelerated flows.	90
5.1.3	Boundary Layer presence.	94
5.1.3.1	Mechanisms of boundary layer creation.	94
5.1.3.2	Boundary layer and cross-correlation model.	98
5.2	Metrological sources of bias inside longitudinal grooves.	100
5.2.1	Optical influence of the bubbles in the model.	101
5.2.1.1	Single millimetric bubble.	103
5.2.1.2	Slab of small bubbles.	104
5.2.1.3	Conclusions	106
5.2.2	Cross-correlation model analysis in case of counter-rotating vortices.	106
5.2.3	Discussion on the streamwise velocity.	110
5.2.4	Conclusions.	110
5.3	Illumination in transverse grooves.	110
6	Tire R-PIV measurement results.	114
6.1	PCY4 Tire.	114
6.1.1	Flow in front of the Tire.	114
6.1.1.1	Water-Bank	117
6.1.1.2	Shoulder	118
6.1.1.3	Conclusions	120
6.1.2	Flow inside tire grooves.	120
6.1.2.1	Primary flow inside longitudinal grooves.	121
6.1.2.2	Secondary flow inside longitudinal grooves.	125
6.1.2.3	Flow inside transverse (Type C) grooves.	130
6.2	CCP Tire.	132
6.2.1	Flow in front of the Tire.	132
6.2.1.1	Water-Bank	133

6.2.1.2	Shoulder	134
6.2.2	Flow inside the grooves.	134
6.2.2.1	Flow inside the "zigzag" zone.	134
6.2.2.2	Flow inside Type W grooves.	136
6.3	Conclusions.	138
7	Analysis of the tire flow.	141
7.1	Flow in front of the tire.	141
7.1.1	Evolution of the velocity with the vehicle speed.	142
7.1.2	Evolution of the water-bank length with the vehicle speed.	145
7.1.3	Self-similarity of the flow.	147
7.2	Flow in straight grooves.	150
7.2.1	Flow in the streamwise direction.	150
7.2.1.1	Evolution of the velocity with the Vehicle speed.	150
7.2.1.2	Similarity of the profiles.	151
7.2.2	Vortex structure of the flow.	152
7.2.2.1	Vortices intensity.	152
7.2.2.2	Hypothesis on the vortices creation phenomena.	155
7.3	Flow in transverse grooves.	158
7.4	Interaction of connected grooves.	159
8	Conclusions and Perspectives	162
8.1	Major findings.	162
8.2	Perspectives.	164
A	Demonstration of the cross-correlation model calculation.	166
B	Image Treatment.	176
C	Decreasing interrogation windows size in tire grooves.	179
D	The change of object plane position for the flow in the grooves.	182
E	Boundary layer in tire groove.	184
	Bibliography	187

List of Figures

1	Sketch of the tire specific vocabulary used in the PhD.	18
1.1	Aquaplaning sketch of the 3 different zones.	21
1.2	Images obtained for the contact patch determination from Todoroff et al. 2019 [72].	23
1.3	Scheme of the geometry of the flow in the Hydrodynamic zone (with the three parts highlighted) with the corresponding averaged velocity profile over the water height in z	26
1.4	Sketch of the wall-jet in front of the tire.	27
1.5	Zoom on tire grooves from Todoroff et al. 2019 [72].	28
1.6	Sketch of the vortices inside the tire grooves from Yeager 1974 [81].	29
1.7	Groove images for both new and worn tires. Upper image is the smallest groove and lower image is the largest groove (from Todoroff et al. 2019 [72])	30
2.1	Scheme of a light sheet illuminating particles for P-PIV measurements.	33
2.2	Scheme of the two images recorded with the interrogation windows represented.	34
2.3	Scheme of the decomposition of the cross-correlation function.	35
2.4	Illustration of the 3 components contributions to the total cross-correlation.	35
2.5	Scheme of the set-up configuration for a μ -PIV experiment.	36
2.6	Scheme of the illumination method for velocity measurements inside a liquid film using refraction.	37
2.7	a) Scheme of the hydraulic loop with P for the pump and F for the flow-meter. b) Scheme of a cross-section of the channel. c) Picture of the channel mounted on the PMMA block.	38
2.8	Side view of the experimental setup for a) P-PIV, b) R-PIV. In all the following study, $x^* = \frac{x}{h}$, $y^* = \frac{y}{h}$, $z^* = \frac{z}{h}$	39
2.9	Set-up for the in-situ measurement of the inclined light sheet intensity profile. Left picture is a photo of the emerging light sheet.	41
2.10	Light sheet profile $I_0^*(z^*)$ a) near the beam-waist for P-PIV, b) at $x^* = 8$ for the R-PIV.	42
2.11	Dashed-dotted colored lines are planar horizontal light sheets corresponding to z_{sup}^* , z_{max}^* and z_{inf}^* . Purple dotted line is the position of the camera object plane (Fig.2.17). The normalized intensity profile function of the height (right) is also presented to show the correspondence between limit lines and the intensity distribution, in the case $x^* = 4.984$	42
2.12	Scheme of the propagation of a single ray.	43
2.13	Relative error in the transmission angle (Left) and in the transmission coefficient (Right) as a function of the error in the refractive index ratio.	44
2.14	Normalized light intensity profile versus β_1 (Fig.2.12).	44

2.15	a) Value of the intensity peak depending on the incident angle β_1 (Fig.2.12). b) Percentage of the total transmitted intensity in the fluid function of β_1	45
2.16	Normalized light intensity profile at $x^* = 100$	45
2.17	Normalized gray level profile for an aperture number of 5.6.	46
2.18	Scheme of the optic parameters involved to calculate a particle image diameter.	48
2.19	Scheme of the particle images depending on their relative location inside the light sheet thickness and with respect to the object plane altitude.	48
2.20	Inputs profiles for the CCM intensity, velocity and particle image diameter.	51
2.21	Scheme of the chart of the algorithm.	52
2.22	Simulations performed with both averaging methods and their standard deviations for $N = 15$	52
2.23	Left is the velocity profile $U^*(z^*)$ at $y^* = 0.5$ with the White[78] solution (Eq.2.4) compared to the profile predicted by the model with different laser sheet thickness. Right is the relative error (eq.2.19) between the White[78] and the velocities predicted by the model.	54
2.24	Left is the velocity profile $U^*(z^*)$ at $y^* = 0.5$ with the White[78] solution (Eq.2.4) compared to the profile predicted by the model with different laser sheet thickness. Right is the relative error (eq.2.19) between White[78] and the velocities predicted by the model.	54
2.25	Left is the velocity profile $U_{ref}^*(z_{max}^*(x^*))$ at $y^* = 0.5$ with the White and Corfield 2006 [78] solution (Eq.2.4) compared to the profile predicted by the model with refracted laser beam. Right is the error (eq.2.19) between White and Corfield 2006 [78] at $z_{max}^*(x^*)$ and the velocity predicted by the correlation model for R-PIV.	55
2.27	Left : Zoom on the section $x^*=4.984$ from Fig.2.11. Right : Colored line with cross markers are profiles obtained with P-PIV at fixed z^* , colors corresponding to the color of various z^* horizontal sheets in the left figure. The black line with circle markers represents profile measured with R-PIV.	56
2.26	Measured velocity field in the channel (cubic spline interpolation from 2D slices obtained with P-PIV).	56
2.28	The error Eq.2.19 is represented with U_{ref}^* the velocity measured with R-PIV and $U_{comp}^* = U^*(z_{inf}^*)$ (Red), $U_{comp}^* = U^*(z_{sup}^*)$ (Blue) and $U_{comp}^* = U^*(z_{inf}^*)$ (Green).	57
2.29	Left side is the laser sheet evolution in x^* with the object plane (z_{OP}^*) and the depth of focus shown. Right side is the velocity at $y^* = 0.5$ for the R-PIV measurement (black points) and the velocity obtained with the model for the same position (red line).	58
2.30	Error eq.2.19 is represented with U_{ref}^* the velocity measured with R-PIV and U_{comp}^* the velocity predicted by the model.	58
3.1	Set-up for in-situ measurement of the velocity field in the water puddle.	61
3.2	Scheme of the experimental setup for stereoscopic measurements.	62
3.3	Scheme of the stereoscopic PIV principle with Sheimpflug settlement.	62
3.4	diameter of the image of a particle depending on its height in the puddle.	63
3.5	Images taken of particles.	64
3.6	Sketch of the shape of the diameter distribution of particles.	64
3.7	Scheme of the configuration for intensity profiles determination.	65

3.8	Intensity profiles obtained with the ray tracing model in the inhomogeneous configuration (vertical sticks orange, brown and blue show locations of chosen profiles).	66
3.9	Intensity profiles obtained with the ray tracing model in the homogeneous configuration.	66
3.10	Intensity profiles obtained for two different distances, from the emerging laser point, at $d_0 = 60$ and 200 mm.	67
3.11	Scheme of the tire sculpture pattern for the PCY4.	69
3.12	Scheme of the tire sculpture pattern for the CCP.	70
3.13	Maps of GL with the zone of calculation for GL_{cont}	71
3.14	On left : Gray level map with the averaging border zone in black. On right : mean Gray level profile in y	71
3.15	On left : Gray level map with the averaging zone in black. On right : spatially averaged Gray level over y profile as a function of x	72
3.16	On left : Gray level map with the averaging zone in black. On right : mean Gray level profile in y (y mean profile).	72
3.17	On left : Gray level map with the averaging zone in black. On right : Spatially averaged Gray level profile over y as a function of x	73
3.18	R-PIV images of the contact patch area with the mask superimposed in red thin lines.	73
3.19	Description of the two flow zones (violet and brown lines) in front of the tire.	74
4.1	Contact patch of the tire for two successive measurements at $V_0 = 50$ km/h.	78
4.2	Fig.3.15 with a zoom in the contact patch area front edge (x_c) with an uncertainty δx_c	79
4.3	Evolution of the gray level in front of the central RIB for 8 measurements with a worn tire at $v = 50$ km/h.	80
4.4	Disturbances of the bubble column trajectory with the position of transverse small grooves.	80
4.5	Disturbances of the bubble column trajectory in PIV images.	81
4.6	Scheme of two different configurations of position of Type C grooves near the shoulder.	82
4.7	Scheme of two different configurations of position of wear indicators in the grooves.	82
5.1	Scheme of the tire envelope with the fluid below and the corresponding velocity in the water bank.	85
5.2	Normalized falling velocity of particles of diameter $d_p = 35 \mu\text{m}$ over the time with both formulations.	88
5.3	Falling distance of a $d_p = 35 \mu\text{m}$ particle over the time (Right is a zoom on the early times).	89
5.4	Probability of presence in height of particles in the puddle.	90
5.5	Scheme of the convected forehead of the water-bank. With $x_{FH}(t) = V_0.t$ position of the forehead over the time	90
5.6	Evolution of the velocity of the fluid at $x^*(t^*)$ compared to the velocity of the solid particle.	92
5.7	Evolution of the relative position of a solid particle compared to the water bank forehead position.	93
5.8	Top figure is the fluid velocity and the particle velocity at $x = X_p^*(t^*)$. Bottom figure corresponds to the relative velocity $U^* - U_p^*$. Both depend on the relative position of the particle compared to the forehead position.	93

5.9	Relative velocity $U^* - U_p^*$ depending on the relative position of the particle for different particle diameters.	94
5.10	Scheme of the boundary layer of interest.	94
5.11	Left are the normalized velocity profiles. Right is the growth of δ_{BL} over the time.	96
5.12	Sketch of the tire location and the fluid particle location at three different instants with the distance $dist$ of traveling.	97
5.13	Left are the normalized velocity profiles for the blasius solution and the unsteady solution Equation.5.18. Right is the growth of δ_{BL} over the time.	97
5.14	Scheme of the transition zone where the two boundary layer shape should be joined.	97
5.15	Inputs profiles for the CCM in intensity, velocity and particle image diameter.	98
5.16	Velocity obtained depending on the boundary layer thickness $\delta_{BL}^* = \frac{\delta_{BL}}{h_{water}}$ and the standard deviation for the $N_{im} = 10000$ snapshots averaged.	99
5.17	Velocity predicted by the model as a function of the boundary layer thickness $\delta_{BL}^* = \frac{\delta_{BL}}{h_{water}}$ and the standard deviation.	99
5.18	Images of bubble columns with their size in the PCY4 tire grooves.	100
5.19	Problem considered for the tire groove flow analysis.	101
5.20	Scheme of the components of the electromagnetic field for a bubble.	102
5.21	Scattering section function of the bubble diameter.	103
5.22	Sketch of the problem studied.	103
5.23	Scheme of the bubble column.	104
5.24	Scheme of the bubble column with a particle above.	105
5.25	Transmission coefficient map as a function of bubble density and the bubble diameter with a bubble column thickness $L = 1.5$ mm.	105
5.26	Particle image diameter function of the height in the groove for both configurations.	107
5.27	Spanwise velocity obtained with both CCM (left) and BCCM (right) models for the 2 reception optic configurations, $z_{OP}^* = 0$ (top) and $z_{OP}^* = 1$ (bottom).	108
5.28	Ensemble averaged spanwise velocity obtained with both CCM and BCCM models for the 2 reception optic configurations.	109
5.29	Spatially averaged velocity profiles obtained with the 4 configuration compared to the reference velocity field.	109
5.30	R-PIV image inside Type C grooves.	111
5.31	R-PIV image inside Type C grooves.	111
6.1	Instantaneous vector field measured for a new tire rolling at $V_0 = 50$ km/h through a puddle with $h_{water} = 8$ mm.	115
6.2	Ensemble averaged velocity component maps for new (top) and worn (bottom) tires.	116
6.3	RMS velocity component maps for for new (top) and worn (bottom) tires.	117
6.4	Spatially averaged velocity profiles in the WB U_{WB}^* in front of the tire. Red lines represents the integration limits in x to obtain a global parameter $\langle \overline{U_{WB}} \rangle$	118
6.5	Spatially averaged velocity profiles at the shoulder V_s^* in front of the tire.	119
6.6	Spatially averaged velocity profiles at the shoulder V_s^* in front of the tire.	119

6.7	Ensemble averaged velocity component maps inside longitudinal grooves for both configurations.	122
6.8	RMS velocity component maps for both configurations.	122
6.9	Ensemble averaged longitudinal velocity profiles along the tire grooves. (new tire)	122
6.10	Instantaneous and ensemble averaged longitudinal velocity profiles along the tire grooves. (new tire)	123
6.11	Instantaneous and ensemble averaged longitudinal velocity profiles along the tire grooves (worn tire).	124
6.12	Velocity in the streamwise direction inside Type A and Type B tire grooves function of the wear indicator position in the image (worn tire).	125
6.13	Instantaneous and ensemble averaged transverse velocity profiles in the spanwise direction inside Type A grooves.	126
6.14	Instantaneous and ensemble averaged transverse velocity profiles in the spanwise direction inside Type B grooves.	127
6.15	Spatially and ensemble averaged velocity profiles obtained with both 2D2C and 2D3C configurations in the streamwise and spanwise directions.	127
6.16	Velocity map W inside longitudinal grooves.	128
6.17	Spatially and ensemble averaged velocity component W profiles inside A and B Type grooves (new tire).	128
6.18	A scheme of the tire grooves with their corresponding averaged transverse velocity component profiles for the new tire.	129
6.19	A scheme of the tire grooves with their corresponding averaged velocity profiles for the worn tire.	129
6.20	Instantaneous velocity maps V for new (left) and worn (right) tires.	130
6.21	Spatially averaged velocity in every Type C grooves in both cases.	131
6.22	Sketch of an example illustrating the position of Type C grooves in the contact patch area in percentage.	131
6.23	Velocity profiles in every the Type C grooves in both cases.	131
6.24	Ensemble averaged velocity component maps for CCP tire.	132
6.25	RMS velocity component maps for CCP tire.	133
6.26	Averaged longitudinal velocity profiles in the WB U_{WB}^* in front of the tire.	133
6.27	Averaged transverse velocity profiles at the shoulder V_s^* in front of the tire.	134
6.29	Sketch of the velocity components projected on the zigzag groove axis.	135
6.30	Velocity component $U_{//}$ and U_{\perp} profiles along the contact patch area. Orange lines represents the weld positions.	135
6.28	Velocity map $V^* = V/V_0$ in the Type zigzag groove.	135
6.31	Velocity map $V^* = V/V_0$ in the Type W grooves.	136
6.32	Scheme of the projection of velocity vectors on the axes of the grooves with $\vec{U}_{//}$, the velocity in the groove direction and \vec{U}_{\perp} transverse velocity in the groove.	136
6.33	Mean velocity projected in the grooves a) in the groove axis and b) perpendicularly to the groove axis.	137
6.34	Sketch of the position determination of the groove parts position in the contact patch. . .	137

6.35	Averaged $U_{//}$ velocity component in a groove segment versus the location of its geometric barycentre of the groove inside the contact patch area.	138
6.36	Inclination of the groove portions compared to the car rolling direction.	138
7.1	Spatially averaged velocity in the WB $\overline{U_{WB}}$ in front of the tire for different passes (left). Ensemble averaged $\langle \overline{U_{WB}} \rangle$ versus the vehicle speed (right).	142
7.2	Maximum velocity in the shoulder $max.V_s$ in front of the tire for different passes (Left). Maximum velocity $max.V_s$ and averaged velocity $\overline{V_s}$ function of the vehicle speed (Right).	143
7.3	Spatially averaged velocity in the WB $\overline{U_{WB}}$ in front of the tire for different passes (Left). Ensemble averaged $\langle \overline{U_{WB}} \rangle$ function of the vehicle speed (Right).	144
7.4	Maximum velocity in the shoulder $max.V_s$ in front of the tire for different passes (Left). Maximum velocity $max.V_s$ and averaged velocity $\overline{V_s}$ function of the vehicle speed (Right).	145
7.6	L_{WB} for every measurements and its evolution function of the vehicle speed.	146
7.5	Measurement of the length of the water-bank for two single shot PIV measurements.	146
7.7	Normalized ensemble averaged velocity component maps for cases with $V_0 \in [30; 80]$ km/h.	147
7.8	Isolines $\langle U^* \rangle = 0.4$ of the normalised velocity component maps (from Fig.7.7) at each vehicle speed.	148
7.9	Normalised velocity component profiles in the water-bank and at the shoulder for $V_0 \in [30; 80]$ km/h.	148
7.10	Shape of the contact patch area with an increasing speed according to Todoroff et al. 2018 [72].	149
7.11	Scheme of the hypothesis proposed for the loss of linearity in the velocity at high speed.	149
7.12	Velocity in the streamwise direction inside Type A grooves function of the vehicle speed.	150
7.13	Velocity in the streamwise direction inside Type B grooves for the worn tire function of the vehicle speed.	151
7.14	Ensemble averaged velocity profiles obtained at different vehicle speed.	152
7.15	Ensemble averaged velocity profiles obtained at different vehicle speed.	152
7.16	Velocity component map extracted from Fig.6.7 (up right) with the representation of the external and central part of both grooves.	153
7.17	Ensemble averaged velocity profiles in spanwise direction.	153
7.18	Lobes amplitudes as a function of the vehicle speed (left). Lobe amplitude definition with the case $V_0 = 50$ km/h (right)	154
7.19	Sketch of the effect of Type D grooves linking longitudinal grooves with arrows highlighting their expulsion direction.	154
7.20	Sketch of the differences in the boundary layer structure between Launay et al. 2017 [41] case and the tire rolling puddle flow case.	155
7.21	Visualisation of the bubble column creation zone in Type A grooves.	156
7.22	Sketch of the tire case with the vortex creation evolution between cross-section 1 and 5.	157
7.23	Sketch of the squishing effect to create a second vortex in Type A grooves.	157
7.24	F^* with the corresponding deformation sketched in the contact patch area.	158
7.25	Visualisation of the link between Type B and Type C grooves.	159
B.1	Raw image and preprocessed image comparison in Type A grooves.	176

B.2 Correlation map for a single interrogation window, right for raw images, left for treated images.	177
B.3 Velocity maps for both raw images and preprocessed images.	177
B.4 Velocity profiles obtained for both raw images and preprocessed images.	177
C.1 Velocity maps for a decreasing interrogation window size.	179
C.2 Velocity profiles for a decreasing interrogation window size.	180
C.3 Velocity maps for a decreasing interrogation window size.	181
C.4 two velocity component, $U_{//}$ and U_{\perp} profiles for a decreasing interrogation window size.	181
D.1 Velocity component maps $\langle V^* \rangle$ for both object plane positions.	182
D.2 Transverse velocity component profiles $\langle V_{A1}^* \rangle$ for both object plane locations.	183
E.1 Hydraulic loop in laboratory for tire preliminary tests.	184
E.2 Profiles obtained for different Reynolds number.	185

List of Tables

3.1	Number of statistical independent samples.	75
7.1	Table of the standard deviation in $\langle \overline{U_{WB}} \rangle$ normalised by the vehicle speed.	143
7.2	Table of the standard deviation in $max.V_s$ normalised by the vehicle speed.	144
7.3	Table of the standard deviation in $\overline{V_s}$ normalised by vehicle speed.	144
7.4	Table of the standard deviation in $\overline{U_{WB}}$ as a percentage of the vehicle speed.	144
7.5	Table of the standard deviation in $mean.V_s$ and $max.V_s$ in percentage of the vehicle speed.	145

Tire Specific Vocabulary :

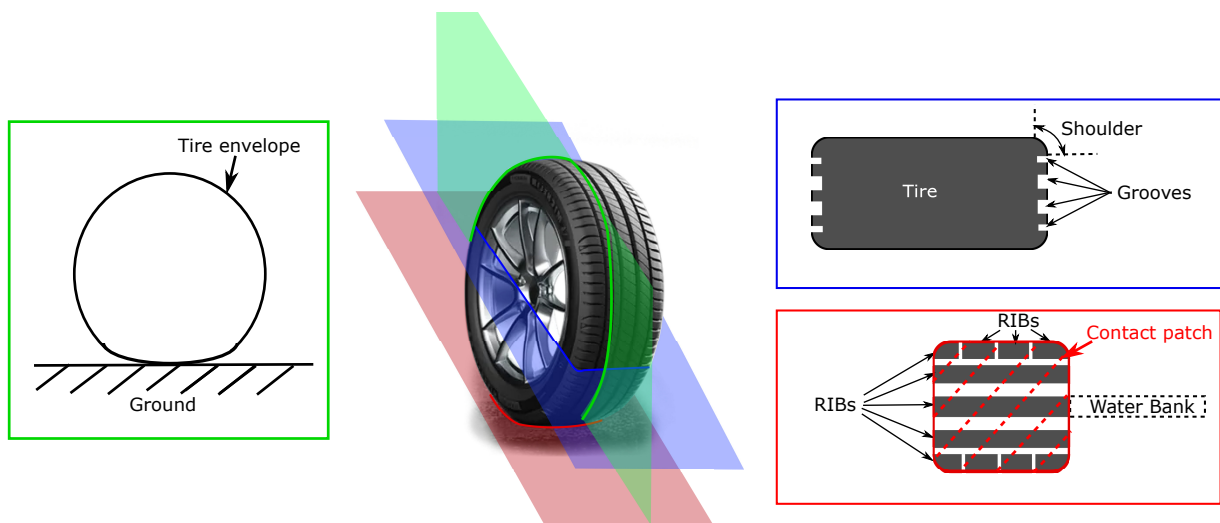


Figure 1: Sketch of the tire specific vocabulary used in the PhD.

1 Introduction and State of the Art

1.1 Context and Motivations.

The tire is one element of a vehicle that is of first importance for adhesion of a vehicle on the ground it is rolling on and at a less important level for aerodynamic drag. It insures the contact with the road as an interface between a static domain, the road, and a dynamic object, the vehicle. At this interface the tire could be submitted to different conditions of adhesion, wet or dry, rough or smooth roads. This of primary importance for the car security and car performance. The global adhesion and the aerodynamic drags are functions of the car speed and the geometry design of the tire external shape.

The tire material and shape geometry constitution lead to different behaviours as a function of the previous parameters that pilot the global safety and drag of the vehicle. Fluid mechanics is a key point to improve the tire performances (safety, drag).

Concerning the influence on the aerodynamic drag force exerted on the vehicle, Croner et al. 2013 [22] showed that it is a function of the tire geometry for an isolated tire in a wind tunnel. Croner et al. 2013 [22] studied with both URANS (Unsteady Random Averaged Navier-Stokes) CFD (Computational Fluid Dynamics) simulations and experiments (Particle Image Velocimetry and hot wire) in a wind tunnel, the structure of the flow around an isolated wheel. This study allows to characterise the origin of vortical structures in the wake of the wheel as well as their unsteady behaviour. This improved the knowledge of the general structure of the air flow around a wheel without directly quantifying the effect on the total drag of a car/wheel system.

Different studies are focused on this aerodynamics drag from the system *vehicle/tire* studying the influence of the tires as Wang 2020 [76]. Wang conducted experimental PIV measurements on a system car/wheel in a wind tunnel. The general wake of the car can be influenced by many characteristics of the wheel as the tire pattern. The optimised pattern and the exact influence of the tire pattern on the drag was not quantified. However this study highlighted the direct influence of the tire design on the car total drag.

The hydrodynamic behaviour of the tire at the interface with the road is another interest. By ensuring the grip of a tire on wet ground, the safety is improved. Many studies have been performed in order to analyse such a grip in presence of a wet ground as Beautre 2012 [9]. His study was focussed on the influence of thin water films between the road and the tire on the slippage of the car. The influence of the tire properties as well as the asphalt ones were investigated by quantifying the solid/solid contact between the tire and the road in order to determine the optimal conditions to ensure grip. They have done an experimental work based on DFT (Dynamic Frictional Tester) measurements in order to quantify the friction between the road and the rubber with small water height. This analysis highlighted the relation of

the friction coefficient as a function of the water height and the texture of the road. However, hydroplaning situation was not investigated.

In the present work, we aim to improve our knowledge concerning the aquaplaning phenomenon. This phenomenon is of a primary importance to ensure the grip properties on a wet road. The main requisite made to conceive a tire geometry is that the water has to be evacuated from below the tire when it is rolling on wet road (and a fortiori on a puddle). This has to be insured for maintaining a maximum tire shape/road contact area. For this the shape geometry contains grooves disposed to optimise the water evacuation whatever is the water presence. When a tire is rolling on a water puddle, whatever is this shape geometry, an high proportion of the incoming amount of water on the tire remains in front of it without evacuation. This imposes a pressure load in this zone that has to be minimised. Allbert 1968 [4], proposed in his paper a separation of the problem in three different zones as sketched on the figure 1.1 : the hydrodynamic zone, the viscodynamic zone and the dry zone.

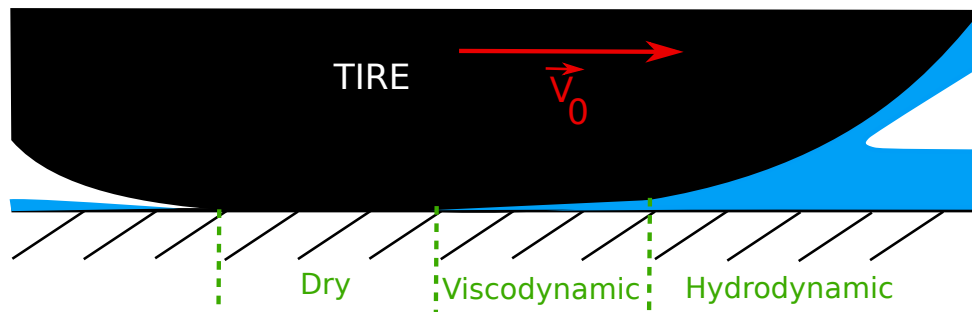


Figure 1.1: Aquaplaning sketch of the 3 different zones.

The hydrodynamic zone is the zone where a strong pressure is developing in front of the tire when the amount of the drained water by the grooves or by the side of the tire is not sufficient. In their works (Horne and Dreher 1963 [32]) summarized the overall knowledge on the hydroplaning phenomenon in 1963. They discussed in this paper, the hydrodynamic pressure which increases proportionally to the square of the vehicle speed.

They shown that this hydrodynamic pressure lifts up the tire reducing the contact patch area between the tire and the road. This reduction of the contact patch area induces a reduction of the tire grip on the road. When the tire is totally lifted off and does not touch the road any more, the aquaplaning situation appears. More recently, they studied the speed limit to reach aquaplaning situation as a function of different parameters as the inflation pressure, tire footprint aspect ratio (see Horne and Dreher 1963 [32] and Horne et al. 1986 [33]).

The viscodynamic zone corresponds to a zone where the flow is mainly driven by the tire shape sculpture. This zone is limited to where the distance between the tire and the ground is of a few microns up to 0.1 mm. In this PhD work, the viscous effects in this micronic water zone between the rubber and the road are not addressed due to metrological issues. Nevertheless in this zone the tire is submitted to a viscous slippage and not to the aquaplaning phenomenon. The preponderant physical effects in the water flow around the tire is here due to viscous forces more than pressure load. In the following study, this zone will be considered as the contact patch area, where the water flow is driven by the tire groove pattern.

In the dry contact zone, the water storage is mainly inside the tire grooves. Whatever is the dry contact

zone inside the contact patch area, grooves have the objective to evacuate water. Small drops of water can remain between the tire and the road surface which influences the total grip of the tire. However, this zone will be considered in the whole study as the contact patch area and the effect of these drops is not addressed.

As a first point of view, the hydroplaning situation appears when the hydrodynamic pressure in the hydrodynamic zone is greater than the averaged load exerted on the tire by the total car in its aerodynamic movement. In order to minimise this situation and to produce tire with high performance on water, the amount of water drained by the tire should be maximised. The water is drained by two different mechanisms : 1) The amount of water driven off the tire path, by the side that is linked to the tire general contact patch area shape; and 2) the amount of water flowing in the tire grooves, drained through the contact patch area as a function of the tire sculptures. Thus, tread design has an impact on wet ground tire performances as during braking. Maycock 1965 [45] and Meades 1967 [46] showed the significant effect of the presence of tire tread compared to smooth tire on a wet ground. In his work, Maycock quantified the grip ability of a tire with the deceleration of the car during wet braking. A Braking force coefficient is calculated from this deceleration and is maximum when the grip is maximized because the deceleration during braking is directly linked to the grip of the tire. This allows them to highlight the importance of a patterned tire compared to smooth tire on different types of rough asphalt.

In terms of hydroplaning situation, the optimisation of tire pattern is subject to few studies as the numerical fluid/structure simulations (k-epsilon model for the fluid) made by Fwa et al. 2009 [26] where the hydrodynamic speed limit is studied as a function of different "non-realistic" tread design in order to quantify the influence of fully longitudinal, fully transverse or angled tread. This study demonstrated that a change of tread can lead to a change of hydroplaning critical speed up to 30 km/h. This study was made with smooth ground with different water film thicknesses from 1 mm up to 10 mm.

The tire design is of primary importance for the safety of the user and to increase the span life of the tires. Two main types of studies can be leaded in order to analyse the hydroplaning situation, numerical simulations and experimental works. Some studies are summarised in the following section.

1.2 Analysis of the flow in a puddle with a rolling tire.

In this section, we discuss the results and limitations of the different studies in the literature which attempted to quantify the hydroplaning process and to study the effect of the tire grooves geometries regarding its wet ground performance.

Experimental observations were the first to allow the gathering of informations for a better understanding of the hydroplaning phenomena. Further and mainly during this last decade numerical simulations, even not able to account for all flow scales or two phase flow phenomena, provide now a complementary information to experimental one.

1.2.1 Experimental studies of the phenomenon.

The first attempt was qualitative estimation done using visualisations of the contact patch area using VLIF (Volume Laser Induced Fluorescence) as a contrast enhancement between the complete ground contact and the water around. Such technique was recently used to obtain quantitative results as function of car velocities (Todoroff et al. 2019 [72]).

1.2.1.1 Visualisation of the Contact patch area.

To perform these visualisations, fluorescent dye is placed in the water puddle. Images of the tire contact patch are taken with a high speed camera while a source of light illuminates the water puddle. This visualisation technique was first used by Yeager 1974 [81] and more recently by Todoroff et al. 2019 [72]. For both studies, the experimental measurements proposed take place on facilities where a glass plate covered with water is embedded into the road and allows the visualisations of the tire contact patch for true rolling conditions. The contact patch analysis is based on the contrast between the contact and the dyed water. The dye used to colour water is a fluorescein species. In Todoroff et al. 2019, images of the tire contact patch are recorded with a high speed camera. Thus the analysis of the contact patch area evolution with a growing vehicle speed V_0 can be performed. Usually, Todoroff used a water height 1 mm for both worn and new tire configurations. The vehicle speeds used range from $V_0 = 8$ km/h to $V_0 = 90$ km/h.

From this last study we can see instantaneous images on the figure 1.2. This was recorded on the Michelin's test facility with a summer tire at $V_0 = 50$ km/h. More details on the test facility are given in the chapter 3. The main problem is a correct detection of the contact patch area. This necessitates the use of digital image treatment tools to first increase the signal to noise ratio and secondly to have automatic criteria to treat the different samples obtained for a same case and to be able to do the best geometrical coincidence as possible for each sample in order to perform ensemble averaged of the measured quantities.

From the recorded images a Michelin's in-house treatment algorithm improves the contrast between the dry zone (black part from RIBs/road contact) and the water zone (green fluorescence from dyed water). This clearly allows to determine the boundary of the contact patch area of the tire. In so the study was able to furnish the evolution of the contact patch area as a function of the vehicle speed V_0 . In the work by Todoroff et al. 2019 [72] this is done for a summer tire but it can also be done for different tire sculptures. From this kind of observations it is supposed that the contact patch area have to be maintained the most important as possible compare to the initial null velocity of the vehicle. In so this kind of study is of first importance to furnish a global parameter to characterise a tire shape.

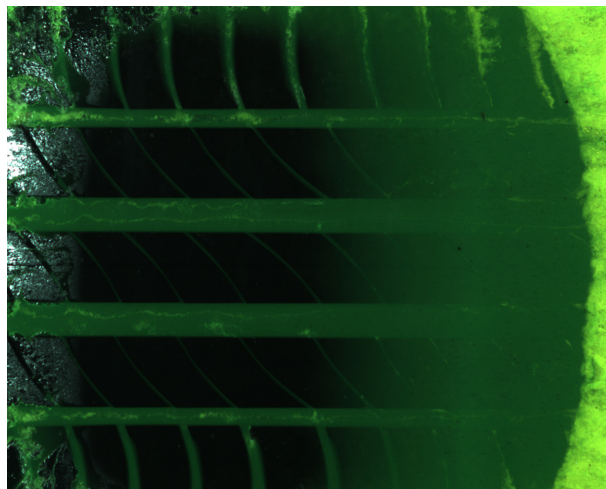


Figure 1.2: Images obtained for the contact patch determination from Todoroff et al. 2019 [72].

1.2.1.2 Velocity measurements in presence of water

The literature velocity measurements of the water flow around and below a rolling tire through a puddle is very sparse. To our knowledge, quantitative measurements have only been performed by Suzuki and Fujikama 2001 [69]. In this work, the experimental method proposed is based on a facility where a glass plate covered with water is embedded into the road and allows the visualisations of the tire contact patch area for true rolling conditions, as used by Todoroff for visualisations. Solid particles of Millet (of diameter 1 to 1.5 mm) seeded the water as tracers and some images were recorded with an high speed camera at 1500 Hz and illuminated by 4, 500 W, continuous light sources. With long exposure time images, the particles appeared as strikes on the images. From the length of these strikes, the displacement of the particles during the exposure time was calculated. Thus, the velocity can be deduced from these displacements.

This method allowed the authors to determine the velocity field in front of the tire on a grid whose random location of vector origin is inherent to the technique. The influence of the angle of the grooves on a cornering effect of the tire was discussed. This technique allowed the authors to produce very interesting experimental information about the velocity in front of the tire. However, the velocity inside the tire grooves was not addressed with this technique and the velocity vectors density obtained in front of the tire remained low and could be improved.

1.2.2 Some Numerical studies of the hydroplaning phenomenon.

The use of numerical simulation to analyse the flow induced during an hydroplaning phenomenon is largely more difficult to obtain as explained before and very rare work are existing on the subject with such tool. Nevertheless, the recent improvements of computational power allows now to envisage such hydroplaning simulation even more taking into account for fluid/structure deformations. Main part of the numerical simulation use an Eulerian point of view.

The tire deformation is simulated by Finite Element method (FE) in every work described in the following. For the fluid, different methods can be used as Finite Difference (FD), Finite Element (FE) and Finite Volumes (FV). For FD method, two main works can be found in the literature with the same characteristics for the simulations. Oh et al. 2008 [59] and Kim and Jeong 2010 [36] present simulation results for a tire rolling using single phase RANS (Random Averaged Navier Stokes) simulations. Oh et al. 2006 [59] showed in their simulations the effect of the increase of the vehicle rolling speed (from 0 km/h to 90 km/h) on the hydrodynamic pressure load on the tire. The water height in this study is set to different heights from 5mm to 20 mm with a straight-grooved tire on a smooth ground. In Kim and Jeong 2010 [36], the same simulations are performed but with an increase of the fluid-structure coupling performance allowing the analysis of a patterned tire. This highlighted the importance of a fully patterned tire on wet grounds. The hydrodynamic pressure exerted on the tire is lower for a patterned tire than for a smooth tire.

For FE method, one work is by Koishi et al. 2001 [38] where simulations of hydroplaning situations are performed for 10 mm water height with a patterned tire (V-shaped grooves) on smooth ground. This study allows to highlight the difference in the hydroplaning critical speed (vehicle speed needed to lose all contact between the tire and the road) between a V-shaped tire mounted in the good way and reversely. The hydroplaning critical speed is quantified as the speed for which the contact force between the tire and

the road becomes null.

Few works can be cited using the FV method for the fluid as the one by Cho et al. 2006 [18], where RANS simulations are performed for an inviscid fluid and a 10 mm water height puddle with a fully straight-grooved tire and a patterned tire on smooth ground. These simulations shows differences on the hydrodynamic load exerted on the tire for both tire model with vehicle speed from 40 km/h to 80 km/h. In Vincent et al. 2011 [75], LES simulations are performed with a 8 mm water height. In this study, the hydrodynamic load on the tire is presented together with the contact patch area for three different tire models with a fixed speed at 50 km/h. One is smooth, and the two others are patterned on smooth ground. This shows the importance of the pattern of the tire with a drastically decreased load with patterned tires. Finally, Kumar et al. 2012 [40] also performed simulations for smooth tire on smooth ground in a 10 mm water height puddle. Various inflation pressures were tested showing that the hydroplaning speed is increased with the increase of the inflation pressure.

All these simulations have been significant advances in the understanding of hydroplaning. They also highlight limitations of the simulation in such complex issues. Particularly, except for Vincent et al. 2011 [75] study, all the numerical studies of hydroplaning phenomenon do not deal with the multiphase aspect of the flow even if it can have an influence on the flow inside the tire grooves. These studies also show difficulties to determine the flow inside fully patterned tire grooves because of the computational time cost if a sufficient refined meshing inside the groove is accounted. Therefore, simplified geometries are often used.

This is one of the reasons why the importance of tire pattern compared to smooth tire is highlighted by these studies, but the differences between two patterned tires is difficult to determine.

Finally, simulations are always proposed for high water height which are not realistic conditions. In real road situations, the range of such height is about 1 mm during heavy raining events (see Hermange 2017 [30] page 26).

A different approach has been recently proposed by Hermange 2017 [30] with a Smoothed Particles Hydrodynamics (SPH) Lagrangian method for the fluid displacement. Simulations were here performed for a vehicle speed of 80 km/h with a water height of 1 mm. This method shows advantages for free surface flows and in term of computational cost as refinement could be compensated by selecting preferential zones for which more particles are accounted. This method also allows to perform calculations with rough grounds which are more similar to the real asphalt. However some difficulties still exists as soon as turbulence or multiphase flow have to be accounted.

Numerical simulations have been extensively used to gather informations on the hydroplaning phenomenon. Nevertheless, detailed quantitative descriptions of real flow situation were never addressed particularly in the tire grooves.

1.2.3 Purpose of this work.

Facing all the interrogations and missing informations as pointed out from the previous review a main purpose of the present PhD work is to provide an experimental method based on Particle Image Velocimetry (PIV) which allows In-Situ measurements of the water flow in the puddle with a real car rolling through it.

If this objective is respected more precision and information will be given for water flow in front of the tire, in some tire grooves. One objective is also to obtain the better as possible repeatability, precision

and a vector density high enough to describe in details the flow structure.

Before focusing on the description and characterisation of the new PIV extension that is developed in this work to fulfil the objective (Chapter2), let's summarize the knowledge of the flow structure that we just deduce from the previous literature review.

1.3 The flow structure.

1.3.1 Different zones of the flow.

We have previously indicated that it is difficult to measure the fluid flow in the viscous zone due to dimension of the thin film (Fig.1.1). In this work the flow analysis is focused on the two other zones described in Section.1. The first one is the hydrodynamic zone in front of the tire. In this work we split this specific zone with the one of the flow in front of the tire (water-bank zone) and an other one on the sides, the shoulder zone. In the first subpart, a certain amount of water is driven off the tire path at the shoulder zone (by a mean symmetry 2 parts) and a certain amount is accumulated in front of the tire. The second is the dry contact zone. In this zone, the ribs are supposed to be the part constituting the adhesion (along the constant rolling) with the ground. In the grooves, the water is stored and drained by the tire groove flow. Specific flow behaviours are present for every subparts (in the water-bank, at the shoulder and inside the grooves) of the flow and will be discussed here.

1.3.2 Flow in front of the tire.

In front of the tire (in the water-bank), the structure of the flow can be decomposed in three parts. (i) far from the tire a free-surface flow appears. (ii) the flow is subject to an acceleration phase with an increase of the water height. (iii) when we get closer to the tire, the flow becomes confined between the tire envelope and the ground (Fig.1.3). Based on literature and especially Hermange 2019 private communication [31] simulations, it appears (Fig.1.3) that the velocity of the fluid in the first part (i) is null (in the figure the velocity is normalised by the vehicle speed).

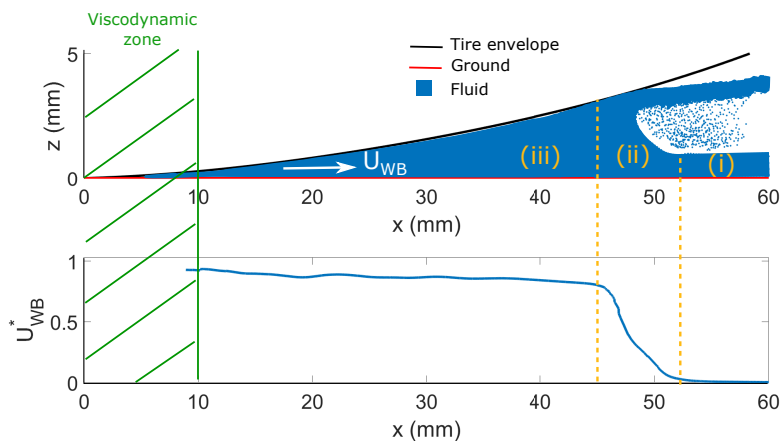


Figure 1.3: Scheme of the geometry of the flow in the Hydrodynamic zone (with the three parts highlighted) with the corresponding averaged velocity profile over the water height in z.

The flow studied in front of the tire is channelled between the tire and the ground ((i) zone). The flow

in this zone could be associated to a flow at velocity U_{WB}^* in a divergent channel in the ground referential with a flow coming from the contact patch area in the x direction.

In the referential of the tire, the flow arrives on the tire. This can be associated to a water flow past an obstacle. From a schematic point of view, it can be considered as an obstacle with a rectangle shape. The free-surface flow passing a rectangular or cubic obstacle is extensively studied in the literature. Thus a part of the water arriving on the tire will be driven off the tire path by the side at the shoulder of the tire. Nevertheless it is clear here that free surface can add complexities as the formation of a hydraulic jump surrounding the obstacle and the formation of a horseshoe vortex. Mignot and Rivière 2010 [52], showed with visualisations that two flow regimes can be distinguished for this last case. For high Reynolds number, the "breaking type" of flow appears with a length of the hydraulic jump greater than the length of the horseshoe vortex. For low Reynolds numbers, the "separation type" of flow appears with a greater length for the horseshoe vortex than the hydraulic jump. The critical Reynolds number between both types depends on the Froude number and the ratio water height/obstacle width. They also showed that three parameters can influence the length of the hydraulic jump and the horseshoe vortex, the Reynolds number, the Froude number and the ratio water height/obstacle width. The horseshoe vortex presence can be interesting knowing the presence of vortices in the tire grooves. The conditions of creation of these grooves depend on the separation of the boundary layer on the ground near the obstacle. This was especially observed by Launay 2017 [41].

In some specific conditions of low water height/obstacle width ratio, the bow-like wave in front of the tire becomes a wall-jet-like bow-wave. This jet height depends on the Froude number and the water height/obstacle width ratio as observed with visualisations by Rivière et al. 2017 [63]. For the rolling tire conditions, the water height/obstacle width ratio is approximately 0.04 which is lower than 1 for a whole tire. Therefore, the creation of a wall-jet-like bow-wave in the tire vicinity at the free surface can be assumed as sketched Fig.1.4. According to Equation 9 in Rivière et al. 2017 [63], the dimensionless jet height normalised by the kinetic height $h_{jet}^* = h_{jet}/(U^2/2g) = 4$ (where U is the fluid velocity in the obstacle referential and g is the gravity acceleration) with tire conditions. The maximum value encountered by the authors is $h_{jet}^* = 1.4$. Therefore, the tire flow conditions are extreme and can slightly diverge from the results of the literature.

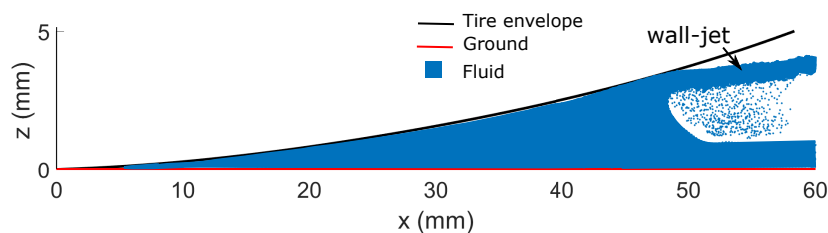


Figure 1.4: Sketch of the wall-jet in front of the tire.

1.3.3 Flow in tire groove.

Two different levels of description are interesting inside the tire grooves. A primary flow is considered as the flow in the longitudinal groove direction whatever the groove axis is in the longitudinal car direction or in the transverse car direction. This primary flow corresponds to the amount of water driven through the contact patch area by the grooves and evacuated down the tire or on the sides of the dry zone. A

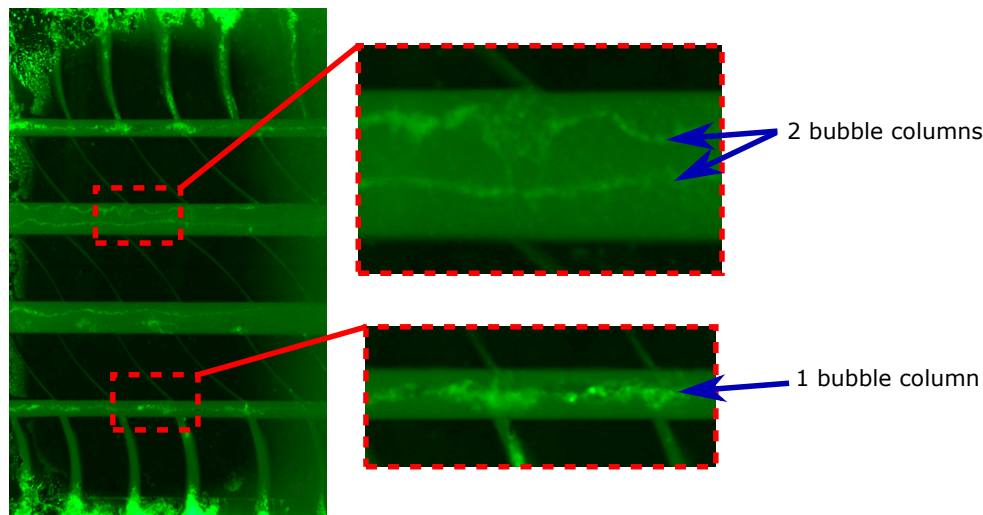


Figure 1.5: Zoom on tire grooves from Todoroff et al. 2019 [72].

secondary flow is detailed in this work considering transverse vortex structures of the flow all along the longitudinal tire groove direction.

The velocity of the tire envelope in the ground referential in the contact patch area with no slip condition is $V_e = 0$. Thus the wall displacement velocity of the channel formed by the groove is quasi-null in the ground referential. If we consider the channel flow with a fluid velocity $U = 0.1.V_0$ in the ground referential (see Chapter6, Fig6.10) with the following definition for the Reynolds number $Re = \frac{U.D_H}{\nu}$ (where D_H is the hydraulic diameter and ν is the kinematic viscosity of the water), for a car rolling at $V_0 = 50$ km/h, the Reynolds number is about $Re = 3000$.

This Reynolds number is high enough to consider a potential presence of turbulence. However in this highly unsteady phenomenon with a short contact patch area length (90 mm approximately for $V_0 = 50$ km/h for a new tire configuration according to Todoroff et al 2019 [72]), the flow regime can not be established and the real presence of turbulence remains to be discussed.

The second interesting feature of the flow is its 3D structure inside the grooves. If we now get back on Todoroff et al. 2019 [72] visualisations and take a closer look inside the tire grooves (Fig.1.2), there are rich information on the flow structure inside the tire grooves. For example we can observe the existence of multiphase flow with straight bubble columns inside the tire grooves. This observation in longitudinal grooves can be observed also for an other tire on the figure 1.5.

From this last image the bigger grooves contain 2 bubble columns whereas there is only one bubble column in the smaller grooves. Note that these grooves have respectively an aspect ratio of 2 and 1. These bubble columns seems generally straight inside the tire grooves. An apparent concentration of bubble lets think that they participate to a structure that could be due to some flow vortices in the grooves. Multiple forces are involved in a bubble displacement inside a rotating flow as the drag and lift forces which are subject to many research (see Rastello et al. 2009[62] and Rastello et al. 2011[61]). Considering centrifugal forces, bubbles, lighter than the water, will converge to the core of the vortices after some time (as demonstrated with experimental visualisations by Chahine 1995[16] in Figure 18.6.1). This convergence was also discussed by Caridi et al. 2017 [15]. In their paper, they discussed the influence on the particles distribution of heavier or lighter particles in vortices. This was made in order to quantify the good density ratio between their particles and the air flow studied to obtain homogeneous partition

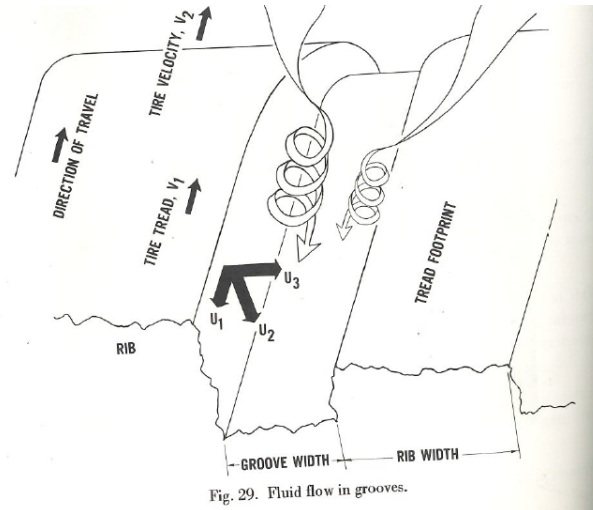


Figure 1.6: Sketch of the vortices inside the tire grooves from Yeager 1974 [81].

of particles for PIV. They showed that when the particles are way lighter than the fluid, the particles will converge to the core and the density of particles outside the vortex core will be too low to perform PIV measurements. In our case, air bubbles are 1000 times lighter than the water. Therefore, bubbles will converge to the core of the vortices.

While the visualisations shown in this reference clearly identify the presence of elongated filaments probably related to local two-phase flow (bubble column or bubble cluster), the author do not highlight especially this feature of the flow. On the other hand, Yeager implicitly relates these filaments to hypothetical longitudinal vortices like those depicted in Fig.1.6

More recently these vortices inside the flow tire grooves are observed but with only an air flow surrounding the tire for an aerodynamics study by Croner 2014 [21] and for which the creation mechanism may be similar. Croner's PhD is focused on the analysis on the air flow surrounding a tire based on numerical simulations and experimental measurements presented in Croner et al. 2013 [22] (already presented in Section.1.1). The vortices inside tire grooves were mentioned in the numerical simulation results without focusing on it. The main purpose of her PhD. being the analysis of the wake for drag reduction.

Nevertheless, the vortex presence in the groove and with a water flow due to tire rolling on a water puddle for example, was neither quantitatively measured nor simulated before the present work. It is thus one challenge for this work to be able to prove their existence. This will be presented in the Chapter 5 and further with quantitative original PIV measurements.

As a first approach, before measuring quantitatively these vortices, the analysis of the visualisations from Todoroff et al. 2019 [72] allows us to determine differences of the flow structure from worn to new tire configurations. In the summer tire grooves we can observe the number of bubble columns to determine the number of vortices per grooves. The largest tire grooves have an aspect ratio (width/height) of 2 and the smallest grooves at the shoulder have an aspect ratio of 1. For the worn tire case, the corresponding value of the aspect ratio is respectively 6 and 3. Thus the number of vortices can be analysed in both cases Fig.1.7.

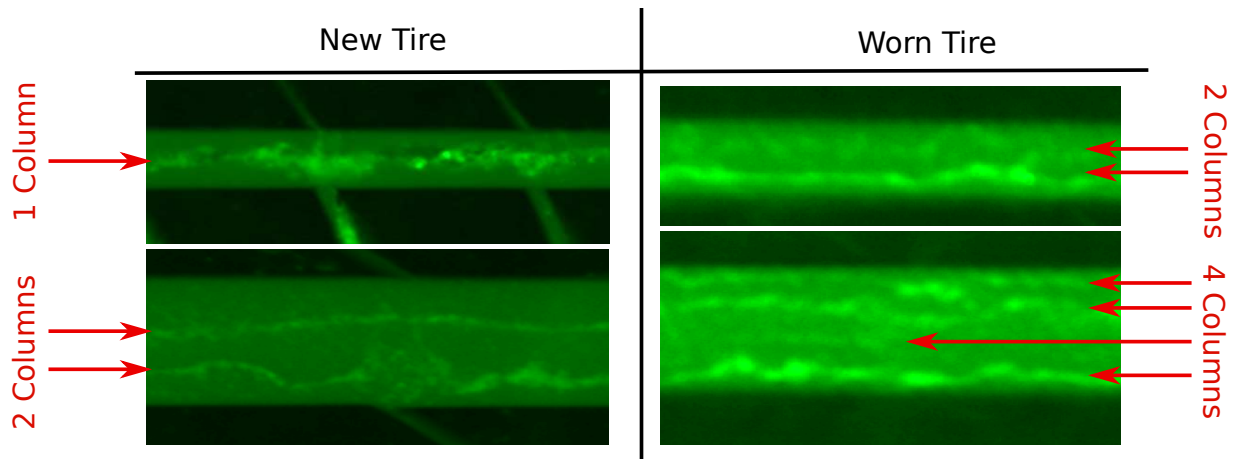


Figure 1.7: Groove images for both new and worn tires. Upper image is the smallest groove and lower image is the largest groove (from Todoroff et al. 2019 [72])

We can observe here a difference in the number of bubble columns that are visible in both cases. This number seems to depend on the aspect ratio of the tire grooves. This hypothesis is accounting and have to be ascertained by the present measurements which are performed inside the tire grooves (6).

1.3.4 Conclusion.

A first idea of the flow structure allows us to identify a priori the general behaviour in the different parts of the flow. In front of the tire, the tire constitutes an obstacle and thus a part of the flow will be driven off the tire path at the shoulders. An other part of the flow, in front of the central RIBs of the tire, is pushed forward by the tire and is not a free-surface flow but more a channelled flow between the ground and the tire. Inside the tire grooves, the flow seems to be a high Reynolds number flow with a too short distance to establish in a net regime. The secondary flow constituted by the vortices depends on the configuration of the longitudinal groove and its aspect ratio.

1.4 Thesis organisation.

As we have seen at the best of our knowledge there is no existing quantitative velocity field measurements in the different zones described above. The purpose of this work is first to develop an experimental method based on PIV before adapting this method to the tire measurements. Therefore the Chapter 2 introduces, the experimental method developed here and called R-PIV and that is an extension of the more classic Planar PIV. It is described and validated with a laboratory channel flow study. In this chapter, the specific optical properties of the method will be discussed with their effects on the PIV field calculations. This will lead us to revisit the PIV optical models for classic PIV as we adapt them to particular illumination technique. An experimental validation is proposed from the test bench results as analytic solutions are known and classic PIV measurements are further done.

In the Chapter 3, the adaptation of the set-up to IN SITU tire measurements is described with the optical properties associated to the tire measurements. The tire models tested are also described with the digital image processes necessary to use to coincide the coordinate system as soon as a fixed tire case

study needs several measurement repetition to ensure a statistical convergence. Then description of the image processing and velocity field calculations are described with the flow zone studied in the tire case.

The Chapter 4 is dedicated to the analysis of the different sources of variability for the application of the R-PIV to the IN SITU tire flow. In this chapter, the main different sources of bias are discussed, from the control parameter associated to the set-up to the hydrodynamic and metrological variations from a measurement to an other.

The Chapter 5 is dedicated to a metrological discussion. In this chapter, a discussion about the tracer ability is conducted to precise the uncertainty associated to the particles used for seeding the flow. In a second part, a discussion on the effect of a probable boundary layer on the R-PIV measurements in front of the tire is proposed. Finally the complex case of the effect of the multiphase flow (inclusion of micro bubbles inside the vortex cores) on R-PIV measurements is discussed in order to show what part (in height) of the velocity field is described in this zone.

Finally, a presentation of the results in every parts of the flow is shown in Chapter 6 with a discussion, on the hypothesis proposed and on the origin of the different phenomenons that are described, in the Chapter 7.

2 The refracted PIV (R-PIV) technique.

2.1 The Particle Image Velocimetry (PIV).

2.1.1 planar PIV technique.

The particle image velocimetry (PIV) is a well known technique used in fluid mechanics to measure velocity fields in fluid flows. In PIV, particles are seeding the fluid flow of interest and are illuminated by a double pulsed laser light sheet. Images of these particles are recorded on a camera at two successive instants, t and $t + dt$, and the velocity field is calculated from correlation techniques, as cross-correlation, between two successive images.

2.1.1.1 Description of a planar PIV set-up.

For planar PIV measurements (denoted as P-PIV, in the following), the working distance is usually of a macroscopic scale. The working distance could range typically between 50 mm to 1000 mm. With these conditions, the depth of focus of the camera, which is proportional to the working distance, is large compared to the light sheet thickness (at least few millimeters). Therefore, the depth over which particles contribute to the cross-correlation is driven by the thickness of the laser sheet illuminating the particles.

For P-PIV measurements in a channel flow, the laser sheet should be as thin as possible and ideally perfectly parallel to the camera recording plane to avoid distortion of the images (Fig.2.1). A constraint to use this technique is that the laser sheet should be, most of the time, perpendicular to the camera axis. This could be difficult to respect in particular cases where the flow does not possess two optical accesses.

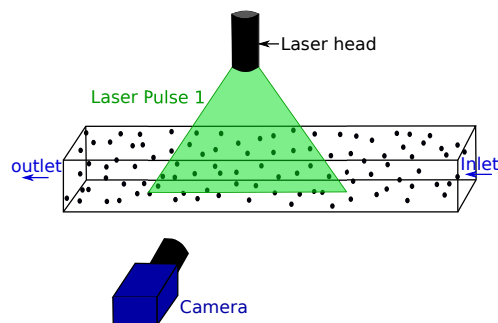


Figure 2.1: Scheme of a light sheet illuminating particles for P-PIV measurements.

When these prerequisites are respected, two successive laser pulses illuminate particles with a time

delay dt and two images are recorded. The displacement of particles between both images (dx, dy) can be calculated using a cross-correlation algorithm. Therefore the velocity field is determined with ($U = \frac{dx}{dt}$, $V = \frac{dy}{dt}$).

2.1.1.2 Description of the cross correlation.

After recording, images are matrices of pixel whose grey levels describe the intensity re emitted from the field of view. The cross-correlation is applied to small areas of the images called interrogation windows with a size ($\delta w_x, \delta w_y$) in pixels ($(\Delta w_x, \Delta w_y)$ in mm) depending on the displacement of particles. These windows must be small enough to consider that all the particles in the window have the same velocity. The cross-correlation algorithm consists in finding the pattern produced by the particles in image one interrogation window at time t , in the second image at time $t + dt$ (Fig.2.2) (Adrian and Yao 1985 [3] and Adrian 1991 [2]).

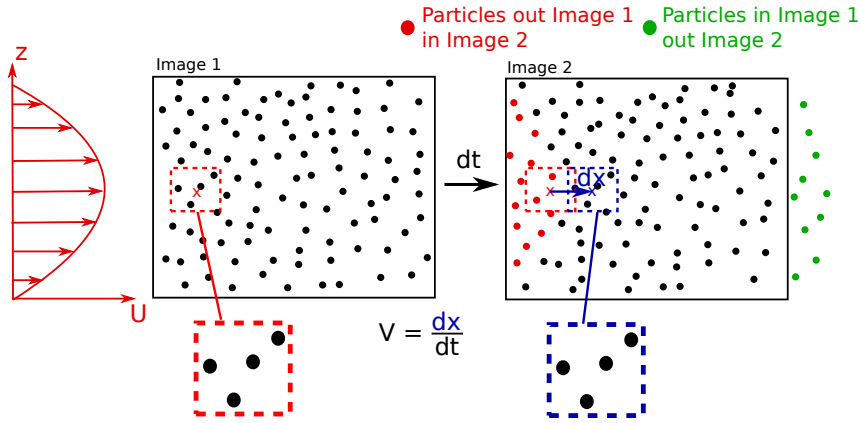


Figure 2.2: Scheme of the two images recorded with the interrogation windows represented.

If $I_1(X, Y)$ is the intensity pattern in the interrogation window centred in (X, Y) in image 1 and $I_2(X + \delta x, Y + \delta y)$ the intensity pattern of a window centred in $(X + \delta x, Y + \delta y)$ in image 2, the cross-correlation between I_1 and I_2 is calculated according to Scarano and Riethmuller 2000 [64] :

$$R_{12}(\delta x, \delta y) = \int_{X-\Delta w_x/2}^{X+\Delta w_x/2} \int_{Y-\Delta w_y/2}^{Y+\Delta w_y/2} I_1(X+x, Y+y) \cdot I_2(X+x+\delta x, Y+y+\delta y) dx dy \quad (2.1)$$

In this work, the cross-correlation is calculated with a commercial Software (Davis from Lavision). With a discrete intensity distribution in pixels on the camera sensors, the discrete cross-correlation function is calculated as expressed by Willert and Gharib 1991 [79] :

$$R_{12}(\delta x, \delta y) = \sum_{i=-\delta w_x}^{\delta w_x} \sum_{j=-\delta w_y}^{\delta w_y} I_1(i, j) \cdot I_2(i + \delta x_{px}, j + \delta y_{py}) \quad (2.2)$$

where δx_{px} and δy_{py} are the displacement components between image 1 and 2 in pixels for an interrogation window centered in $(0, 0)$ in image 1.

To determine the particle displacement in such an interrogation window, the displacement $(\delta x_{px}, \delta y_{py})$ maximising the cross-correlation function is found. According to Kean and Adrian 1992 [34], the cross-correlation function can be decomposed into 3 parts. R_C is between backgrounds of image 1 and image 2. R_F takes into account the correlation of image of particles in image 1 with image of particles that are different from them in image 2. R_D is the displacement component which corresponds to the correlation of particles in the image 1 with their own images on image 2. These components are sketched in Fig.2.3 :

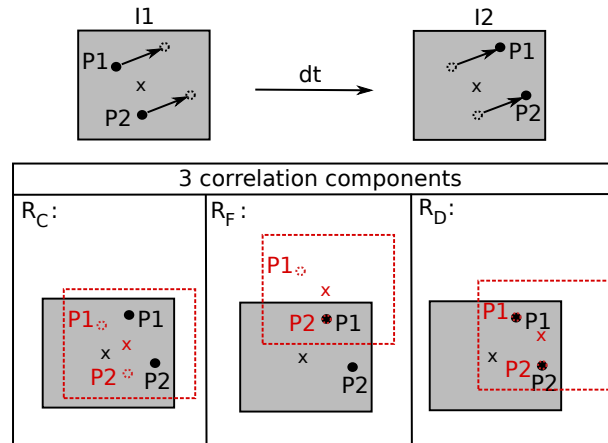


Figure 2.3: Scheme of the decomposition of the cross-correlation function.

This leads to a cross-correlation function between image 1 and 2 that is the sum of these 3 components (Adrian 1988 [1]) :

$$R_{12} = R_{C12} + R_{F12} + R_{D12} \quad (2.3)$$

An example of the cross-correlation and its components is displayed in Fig.2.4 :

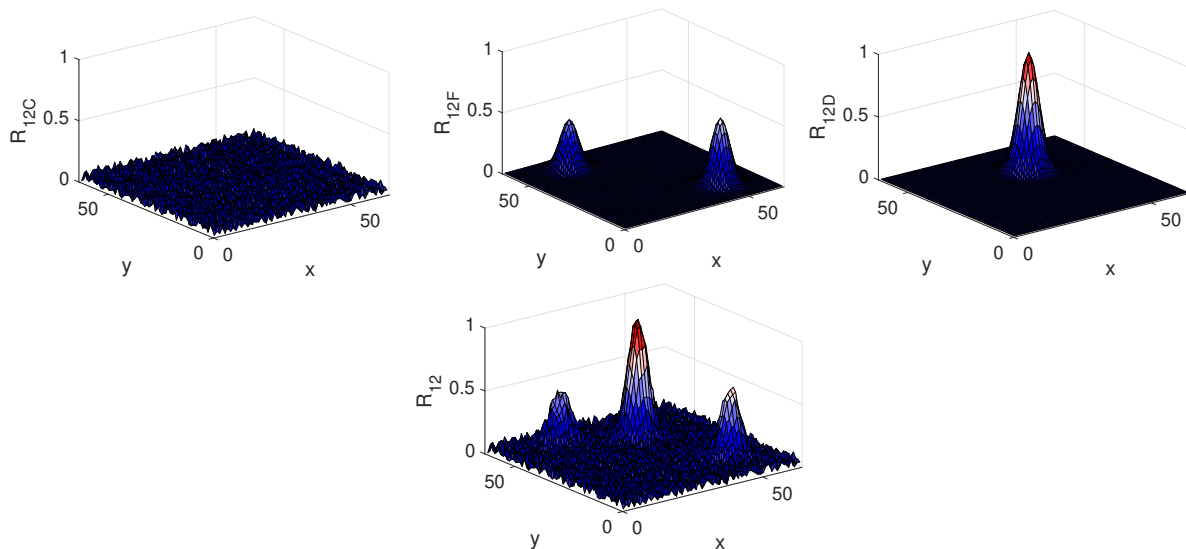


Figure 2.4: Illustration of the 3 components contributions to the total cross-correlation.

In the example of Fig.2.3 and Fig.2.4, the two particles have the same displacement. They both contributes to the same part in R_{D12} . On the contrary, the correlation between image of particles 1 and 2 contributes to two different peaks in R_{F12} . With two particles, the ratio of the R_{D12} peak over the R_{F12} is 2. If we consider a higher number of particles in the interrogation window in image 1, the ratio between R_{D12} and R_{F12} will grow proportionally.

With P-PIV, the laser sheet is considered thin enough to consider all the illuminated particles at the same location in depth (in a 2D plane). Therefore, the maximum of the cross-correlation is the displacement of the particles at the position of the laser sheet in the flow.

2.1.2 Microscopic PIV (μ -PIV) technique.

2.1.2.1 Description of a μ -PIV set-up.

For μ -PIV, the scale of the flow under investigation is of a sub-millimeter range. Therefore, it is difficult to obtain thin light sheets compared to the scale of the flow. However, for such a configuration, microscopic lenses with large magnification are used. Both working distance and depth of focus are then very small. In μ -PIV the selection of the measured position in the flow is then driven by the collection optic instead of the laser sheet, as for P-PIV (Vetrano et al. 2008 [74]). A sketch of a μ -PIV set-up is presented in Fig.2.5.

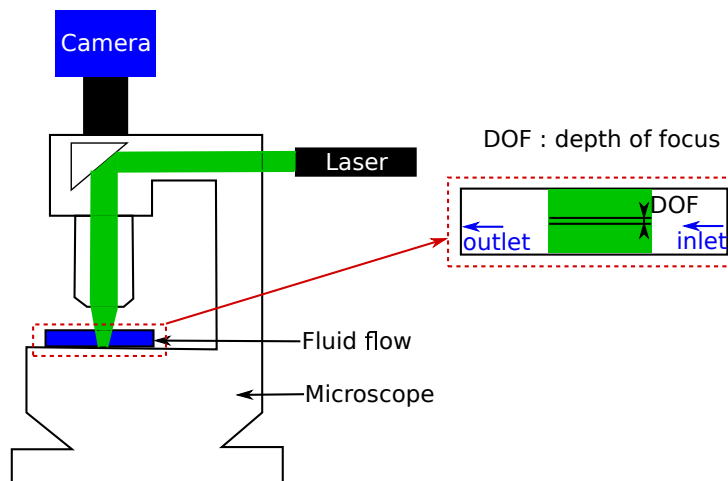


Figure 2.5: Scheme of the set-up configuration for a μ -PIV experiment.

In confined configurations as for μ -PIV, with low velocities, fluorescent particles are often used (as used by Brücker 2000 [13]). When the fluid illumination is global, interfering reflections introduce background noise which can be reduced by the use of fluorescence. However, fluorescent particles are re-emitting less light which makes it more complex to use in high speed cases.

2.1.2.2 Cross-correlation and integration effect.

With this setting, the depth over which particles appear on the images is driven by the reception optic. Therefore, if the depth of focus is of the order of magnitude of the particle diameters, the particles appearing on the images are only particles at the specific location of the object plane and the cross-correlation

properties are the same as used for the P-PIV.

Many studies focus on the effect of a thick depth of focus for μ -PIV configuration (Olsen and Adrian 2000 [60], Meinhart et al. 2000 [50]). These studies take into account, the integration effect due to the fact that particles at different heights appear on the images. The cross-correlation takes into consideration the contribution of the particles in the whole illuminated volume depending on their focusing. This effect is studied by Kloosterman et al. 2011 [37].

2.1.3 R-PIV a hybrid technique adapted to confined spaces.

The main purpose of the present work is to measure the velocity field in a puddle with a rolling tire. The targeted size of the field of view is therefore around 200 mm large with a working distance in the range 500 mm to 1000 mm. Therefore, the macroscopic scale of the flow does not allow the reduction of the depth of focus as for μ -PIV. For our measurement configuration, the main limitation is that neither the laser head nor the camera can be placed at the ground level on the road surface due to the rolling car. Moreover, a single optical window is available for both emitting and receiving optic. It is not possible to perform P-PIV for this type of confined flow. Therefore a method should be developed in order to perform PIV measurements in macroscopic scale flows with only one optical access from below the road.

The solution chosen to perform PIV measurements with one optical access at macroscopic scales is based on the refraction of the laser beam at the window/flow interface to illuminate the particles (Fig.2.6). This extension of the PIV with a refraction of the light sheet is here called R-PIV. This refraction has been used by Minami et al. 2012 [53] to study a water droplet behaviour in a rubber/window contact patch area with a global illumination.

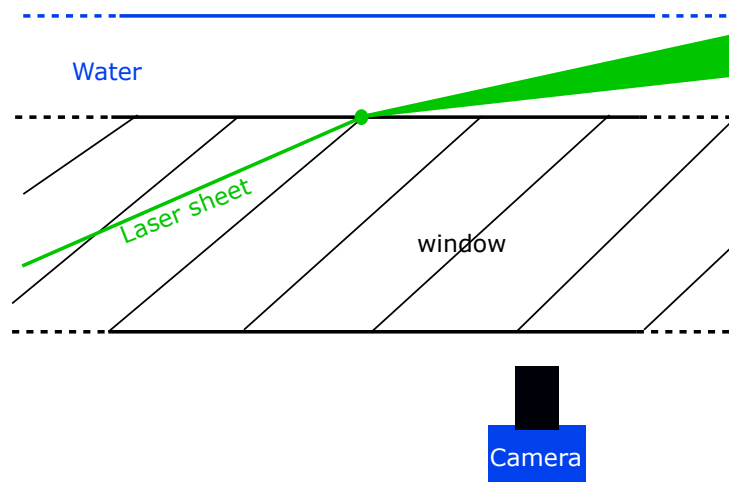


Figure 2.6: Scheme of the illumination method for velocity measurements inside a liquid film using refraction.

In this chapter, an academic flow is studied in order to characterize the illumination after refraction and to identify and quantify the measurement bias induced by this technique. The academic flow has been chosen to allow 1) comparison with an analytic solution in laminar regime and 2) comparison with standard P-PIV measurements.

2.2 Experimental set-up for R-PIV testing.

2.2.1 The bench and operating conditions

In order to characterize this extension of PIV, a square channel flow is investigated. The flow is developing in a square channel inside a hydraulic loop depicted in Fig.2.7. This loop is composed of a water tank which delivers with a pump, water in the hydraulic loop. This loop is composed of two parts, the test section with a flowmeter to quantify the flow rate and a by-pass channel in order to regulate the flow rate.

The test channel is composed of PMMA transparent top and side walls. The channel is mounted on a PMMA block with a prismatic shape (Fig.2.7 c)) constituting the bottom part. The height of the square cross-section of the channel is $h = 8$ mm. The thickness of the prismatic PMMA block is 49 mm. This block has an inclined face near the channel exit with an inclination of $\theta_p = 64^\circ$ (Fig.2.7). This angle is chosen to be close to the critical angle given by Snell-Descartes Laws (equation. 2.6) for a total reflection at the interface PMMA/water with $n^{PMMA} = 1.49$ and $n^{water} = 1.33$.

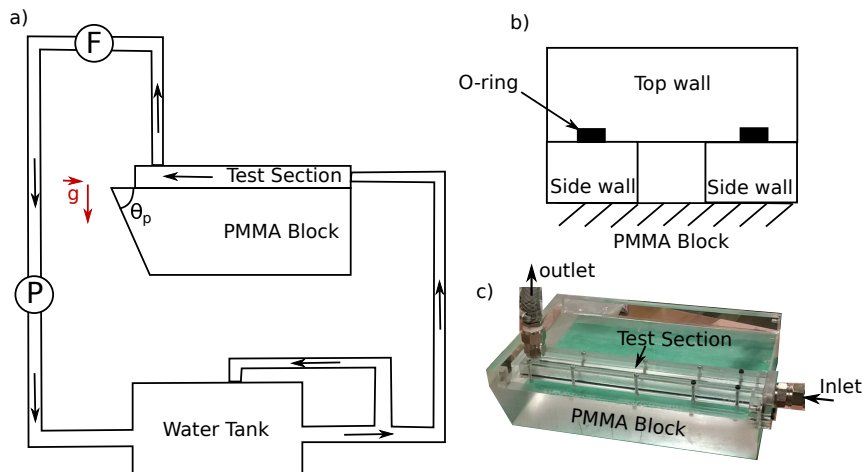


Figure 2.7: a) Scheme of the hydraulic loop with P for the pump and F for the flow-meter. b) Scheme of a cross-section of the channel. c) Picture of the channel mounted on the PMMA block.

The outlet of the test section is perpendicular to the main flow direction in order to allow illumination through the end wall of the channel (as sketched Fig.2.8 a)). The upper plate of the channel is removable to perform specific optical measurements inside the channel, when the fluid is at rest. All the coordinates are normalized by the height of the channel h (respectively $x^* = \frac{x}{h}$, $y^* = \frac{y}{h}$ and $z^* = \frac{z}{h}$). x and y are respectively the horizontal streamwise and spanwise directions while z is the vertical direction.

The origin of the coordinate system is considered at a distance $x_0^* = 7$ upstream the end of the channel. This distance corresponds to the distance between the end of the channel and the emerging point of the laser beam in the water in refracted configuration (Fig2.8b)).

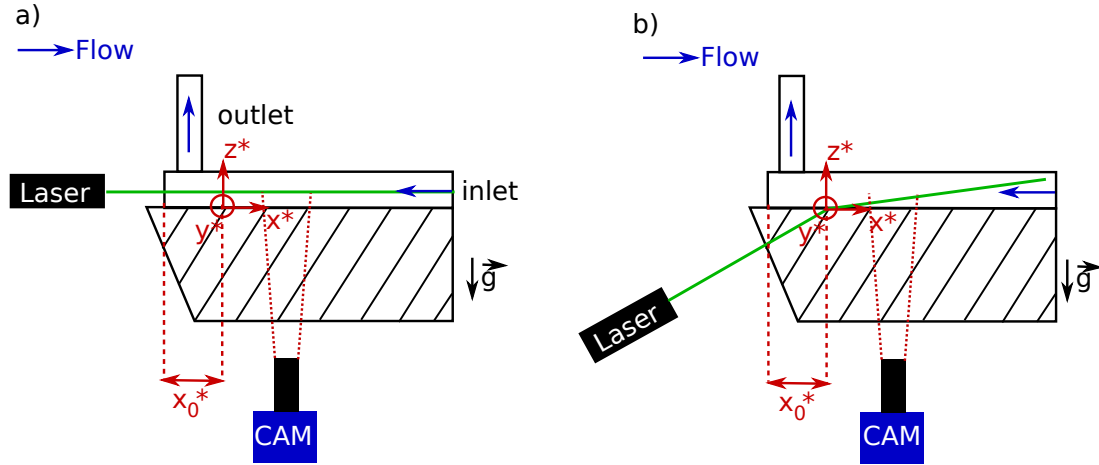


Figure 2.8: Side view of the experimental setup for a) P-PIV, b) R-PIV. In all the following study, $x^* = \frac{x}{h}$, $y^* = \frac{y}{h}$, $z^* = \frac{z}{h}$.

Measurements described here are performed for a Reynolds number based on the bulk velocity, U_b , deduced from the flow rate, and the channel height, h , equal to 465. This value is small enough for the flow to be laminar. An analytic solution of the streamwise velocity component U ($V = 0$ and $W = 0$) for a fully developed steady laminar flow in a square channel is given, in F.M. White and Corfield 2006 [78]. Coordinates, velocity and pressure are normalized respectively by h , U_b and $1/2 \cdot \rho U_b^2$ as : $x^* = x/h$, $y^* = y/h$, $z^* = z/h$, $U^* = U/U_b$ and $\hat{p}^* = \hat{p}/((1/2) \cdot (\rho U_b^2))$. The analytic solution writes :

$$\begin{cases} U^*(y^*, z^*) = \frac{2\rho h U_b}{\mu \pi^3} \left(\frac{-d\hat{p}^*}{dx} \right) \\ \sum_{i=1,3,5,\dots}^{\infty} \left((-1)^{(i-1)/2} \left[1 - \frac{\cosh(i\pi(z^*-0.5))}{\cosh(i\pi/2)} \right] \frac{\cos(i\pi(y^*-0.5))}{i^3} \right) \end{cases} \quad (2.4)$$

and :

$$\frac{d\hat{p}^*}{dx^*} = \frac{24\mu}{\rho U_b h} \frac{1}{\left[1 - \frac{192}{\pi^5} \sum_{i=1,3,5,\dots}^{\infty} \frac{\tanh(i\pi/2)}{i^5} \right]}$$

with $V^* = 0$ and $W^* = 0$, μ is the dynamic viscosity and $\cosh(\cdot)$ and $\tanh(\cdot)$ respectively the cosinus and tangent hyperbolic functions.

2.2.2 Emitting Optics

The test bench is designed in order to allow the use of both P-PIV (Fig.2.8a)) and R-PIV (Fig.2.8b)). The P-PIV is performed with a laser sheet parallel to the bottom wall of the channel and entering the channel by the transparent end wall. The camera in this configuration is placed perpendicular to the light sheet and below the prismatic shaped block. In the refracted configuration (Fig.2.8b)), the incident light sheet is inclined with a small offset from the normal of the inclined face of the PMMA block. After the refraction at the bottom wall (flow/window interface), the purpose is to obtain a slightly inclined laser beam (around 5° in this chapter) with the horizontal.

The laser source used is a double cavity pulsed Nd:Yag Laser (Litron Bernouilli) emitting a wave length of 532 nm with a maximum frequency of 15 Hz. The output diameter of the laser beam is 6 mm with a divergence angle of about 3.5 mrad. The laser sheet is generated with a specific optical device composed of a beam-expander, with an expansion factor of 2, a spherical converging lens with $f = 500$ mm and a cylindrical diverging lens with $f = 400$ mm to spread the laser sheet in y^* direction. In planar configuration (Fig2.8a)), the spherical lens allows us to focus the laser beam in the measurement area to minimise the thickness of the laser sheet.

For both optical configurations, the laser head is placed on translation stages to set the axial and vertical (x^* and z^*) positions of the laser head with a precision of 0.01 mm. The emitting optic is also placed on a rotation stage with a precision 0.01° in order to precisely tune the inclination of the laser sheet for the refracted configuration (Fig.2.8b)).

The distance used here between the emission optic and the inclined face of the prism is approximately 270 mm. The total thickness of the prism being 49 mm, the impingement of the leaser sheet with the water/PMMA interface is in the converging propagation part of the beam.

2.2.3 Seeding

With this refracted illumination technique, spurious background light is generated by multiple reflections and refractions at the different PMMA/air and PMMA/water interfaces. To remove this spurious background light, flow seeding is achieved using fluorescent particles homogeneously mixed to the water in the water tank. The particles used here are Lefranc et Bourgeois paint as characterized by Strubel et al. 2017 [68] and Nogueira et al. 2003 [57], with a particle mean diameter $d_p = 10 \pm 4 \mu\text{m}$. The relaxation time of these particles is $\tau_v = \frac{\rho_p d_p^2}{18\rho\nu} = 6.10^{-6}$ s. For the laminar flow in the channel studied here, the characteristic time of the flow is considered as the convection time from the channel inlet to the measurement area $\tau_0 = \frac{L_c}{U_b} = 2.55$ s (with $L_c = 148$ mm, distance between the measurement area and the channel inlet). Therefore the Stokes number of these particles in this channel flow is $St = \frac{\tau_v}{\tau_0} = 2.35 \cdot 10^{-6}$. This small value ensure a good agreement between the particle velocities and the fluid flow velocity.

When these fluorescent particles are illuminated by a 532 nm light sheet, the fluorescence spectrum is centered around 570 nm. The lens of the camera is equipped with an optical band-pass filter centred around 586 nm with a width of ± 20 nm to record the fluorescing particle images free from reflected noise at the laser wavelength (532 nm).

2.2.4 Image acquisition and processing

Image acquisitions are made with a double frame sCMOS camera. The camera sensor, of size 14x16.6 mm, has 2160x2560 pixels. The maximum acquisition frequency of the camera is 50 Hz. The synchronisation of the laser pulses and the camera acquisitions is achieved with a synchronisation unit (PTU). The acquisition is made with a commercial software (Lavision, Davis 8). The maximal acquisition rate is limited by the laser frequency at 15 Hz.

For these measurements, a NIKKOR-NIKON lens of $f = 135$ mm focal length is used with two extension rings of length 12 mm and 32 mm. The dimensions of the field of view, normalised by h , are $\Delta_x^* = 5.28$ and $\Delta_y^* = 4.46$ for a magnification factor of $M = 0.39$. This measurement area is placed 148

mm downstream the channel inlet as mentioned previously and 80 mm upstream the channel outlet.

In order to improve the signal/noise ratio 500 independent image pairs are recorded. In this chapter, the individual cross-correlation functions are averaged instead of the instantaneous velocities during the iterative process for the cross-correlation computation. The size of the interrogation windows used here is decreasing from 64x64 pixels to 32x32 pixels. Therefore the size of the interrogation windows normalized by the channel height is $d_{wx}^* \times d_{wy}^* = 0.066 \times 0.066$.

2.3 Optical properties for R-PIV.

2.3.1 The laser sheet propagation.

2.3.1.1 Measurement of the laser sheet intensity after the refraction.

With this specific R-PIV technique, the propagation characteristics of the laser sheet after refraction is unknown. An intensity profile measurement technique is developed in order to quantify the thickness of the laser beam and its structure in the channel. The measurements are done when the fluid is at rest by positioning in the light sheet path a fluorescent target with a flat face inclined at 45° with the horizontal (Fig2.9). Fluorescent light emitted by the impingement of the laser sheet on the plate is collected by the camera placed below the PMMA block (Fig2.9). The spatially averaged intensity in y^* direction is studied along the plate in x^* direction to determine the intensity profile $I_0^*(z^*)$ due to the inclination of the plate. To know the evolution of the intensity profile in the channel, the measurement is repeated at different positions x^* of the plate.

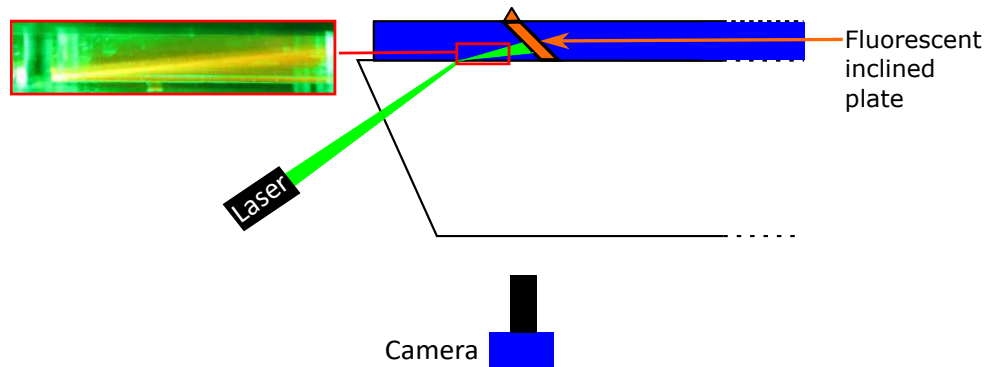


Figure 2.9: Set-up for the in-situ measurement of the inclined light sheet intensity profile. Left picture is a photo of the emerging light sheet.

This measurement technique is used for both optical configurations (Fig.2.8 a) and b)) in this chapter. This allows us to quantify the thickness of the planar laser sheet for Fig.2.8a). A typical normalized intensity profile $I_0^*(z^*)$ is presented for both optical configurations (P-PIV and R-PIV) (Fig.2.10).

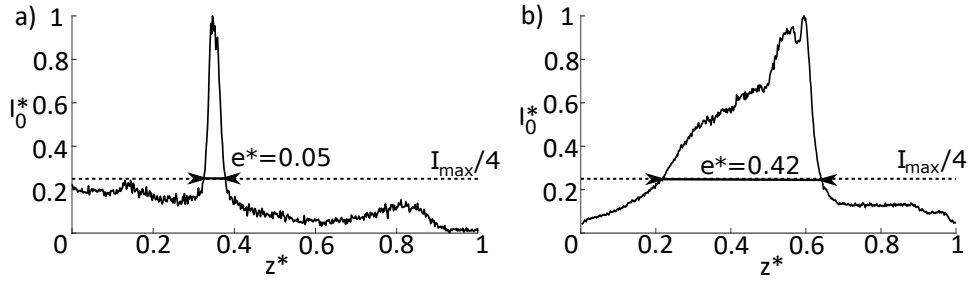


Figure 2.10: Light sheet profile $I_0^*(z^*)$ a) near the beam-waist for P-PIV, b) at $x^* = 8$ for the R-PIV.

For the P-PIV configuration the measurement is made at $x^* = 6$ (near the beam-waist (thinner part of the laser sheet) position in Fig.2.8 a)). The profile appears to be sharp as expected and nearly symmetric around its peak (Fig.2.10a)). The light sheet thickness e is arbitrarily defined as the profile width at height $I_0^* = 0.25$. Its value is here $e = 0.4$ mm which corresponds to $e^* = 0.05$ in its normalised form which is small enough to consider the laser sheet thickness negligible facing the characteristic length scale h of the channel.

For the R-PIV technique, the measurement presented Fig.2.10b) is made at $x^* = 6.5$. This profile shows two main features, a much larger thickness and a strong asymmetry. Using the same definition for the thickness of the peak, its value is here $e^* = 0.42$. Therefore, the large thickness of the laser sheet can introduce a larger bias in the measurements compared to the P-PIV arrangement.

For the R-PIV technique, the measurement of the intensity profile is repeated at four different positions x^* along the measurement area. This allows to study the evolution with x^* of the laser sheet edges, z_{inf}^* and z_{sup}^* (defined as height $I_0^* = 0.25$) and the maximum intensity of the laser sheet z_{max}^* (Fig.2.11).

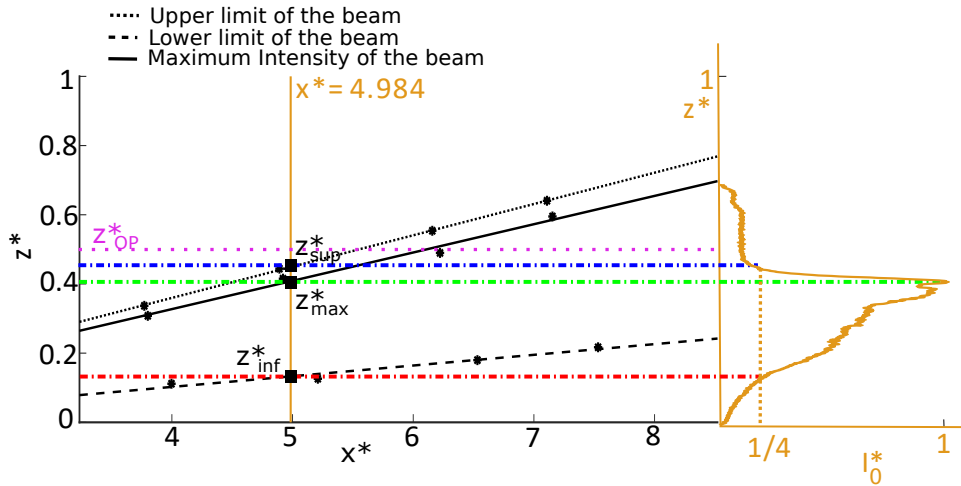


Figure 2.11: Dashed-dotted colored lines are planar horizontal light sheets corresponding to z_{sup}^*, z_{max}^* and z_{inf}^* . Purple dotted line is the position of the camera object plane (Fig.2.17). The normalized intensity profile function of the height (right) is also presented to show the correspondence between limit lines and the intensity distribution, in the case $x^* = 4.984$.

The laser sheet appears to propagate with a small inclination with respect to the channel floor (approximately 5°) and a growing thickness along the measurement area $e^*(x^*)$. The normalized intensity profile $I_0^*(z^+)$ (with $z^+ = \frac{z^*}{e^*(x^*)}$) appears to be self-similar at every position x^* (Fig.2.11).

2.3.1.2 Ray tracing model.

A ray tracing model is used here to explain the results obtained for the measurements of the laser sheet thickness. The propagation problem is here simplified as a 2D problem in the (x^*, z^*) plane. In this ray model, the initial cross-section shape of the laser beam is modeled as a set of 100000 rays equally spaced. The intensity distribution is set with respect to a Gaussian intensity profile of width 19 mm.

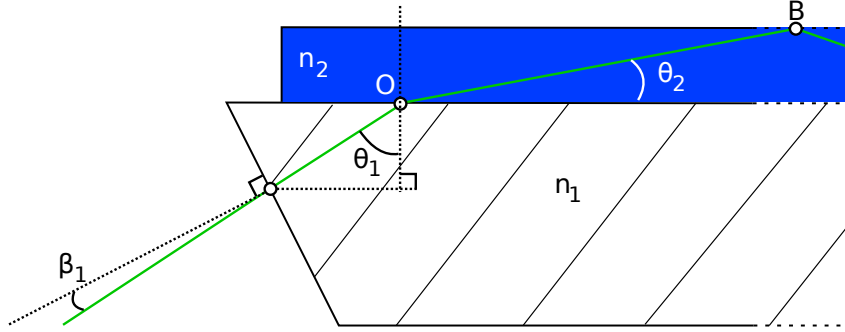


Figure 2.12: Scheme of the propagation of a single ray.

All the rays are converging with respect to a spherical convex lens of focal length $f = 500$ mm. Each ray independently crosses two interfaces air/PMMA and PMMA/water (Fig.2.12). The calculation of the ray trajectory and intensity at both interface is made with respect to Descartes Laws :

$$\theta_t(\eta) = \arcsin(\eta \sin(\theta_i)) \quad (2.5)$$

$$T(\eta) = 1 - R = 1 - \left| \frac{\tan(\arcsin(\eta \sin(\theta_i)) - \theta_i)}{\tan(\arcsin(\eta \sin(\theta_i)) + \theta_i)} \right|^2 \quad (2.6)$$

where η is the ratio between the refractive index of the incident medium and the refractive index of the transmission medium ($\eta = \frac{n^{air}}{n^{PMMA}}$ for the entry of the ray in the PMMA block and $\eta = \frac{n^{PMMA}}{n^{water}}$ for the O interface Fig.2.12). θ_i is the incident angle at the interface and θ_t is the transmitted angle. T is the transmission coefficient at the interface.

The theoretical value, at 532 nm, of the refractive index of the PMMA and the water are respectively $n_0^{PMMA} = 1.49$ and $n_0^{water} = 1.33$ (at $20^\circ C$). However, actual values of these refractive indices can vary depending on the manufacturing process for the PMMA ($n^{PMMA} = n_0^{PMMA} \pm 0.01$ according to Beadie et al. 2015 [8]) and depending on the temperature for the water ($n^{water} = n_0^{water} \pm 0.01$ according to Bashkatov and Gemina 2003 [7]). Therefore the reference ratio between refractive indices is expressed as $\eta_0 = \frac{n_0^{PMMA}}{n_0^{water}}$. The actual ratio is written as $\eta = \eta_0 + \delta\eta$. The variations in the transmitted angle and the transmission coefficient depend on η as $\theta_t(\eta) = \theta_{t0} + \delta\theta_t$ and $T(\eta) = T_0 + \delta T$ (where $\theta_{t0} = \theta_t(\eta_0)$ and $T_0 = T(\eta_0)$). The relative variations of both T and δ_t can be calculated depending on $\delta\eta$ as $\frac{\delta\theta_t}{\theta_{t0}} = \frac{\theta_t(\eta_0 + \delta\eta)}{\theta_{t0}} - 1$ and $\frac{\delta T}{T_0} = \frac{T(\eta_0 + \delta\eta)}{T_0} - 1$.

With the uncertainty considered as $n^{PMMA} = n_0^{PMMA} \pm 0.01$ and $n^{water} = n_0^{water} \pm 0.01$, the variation of the ratio $\delta\eta$ lies in the range $[-0.016; 0.016]$. The influence of this variation on $\frac{\delta\theta_t}{\theta_{t0}}$ and $\frac{\delta T}{T_0}$, for a single ray with an incidence $\beta_1 = 1.5^\circ$ on the prism, is shown in Fig.2.13.

This highlights the effect of a small variation of refractive index on a ray transmission properties. For an error of $\delta\eta = -0.016$, the error is approximately 6% for the transmitted angle θ_t and around 35%

for the transmission coefficient T . For $\delta\eta > 0.006$ the ray is not transmitted in the water. Therefore, it is important for the experimental set-up to allow an adaptation of the incident angle to compensate the uncertainty on the actual values of refractive indices.

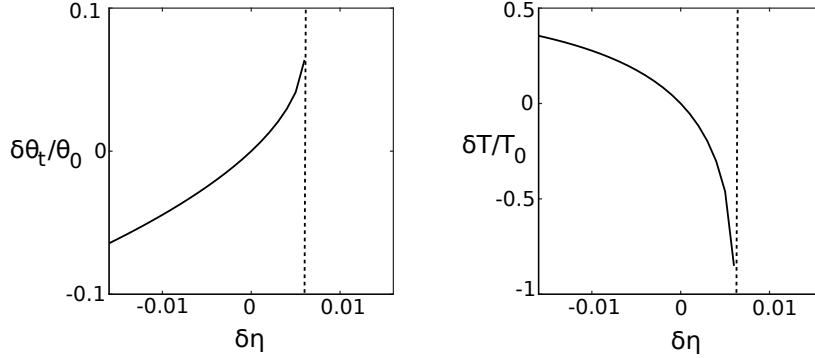


Figure 2.13: Relative error in the transmission angle (Left) and in the transmission coefficient (Right) as a function of the error in the refractive index ratio.

With this ray tracing model, the incident angle β_1 of the laser beam from the normal of the PMMA block inclined face can be modified. Therefore, the sensitivity of the method is studied with the evolution of the intensity profile at a fixed position $x^* = 4.455$ for different incident angles (Fig.2.14).

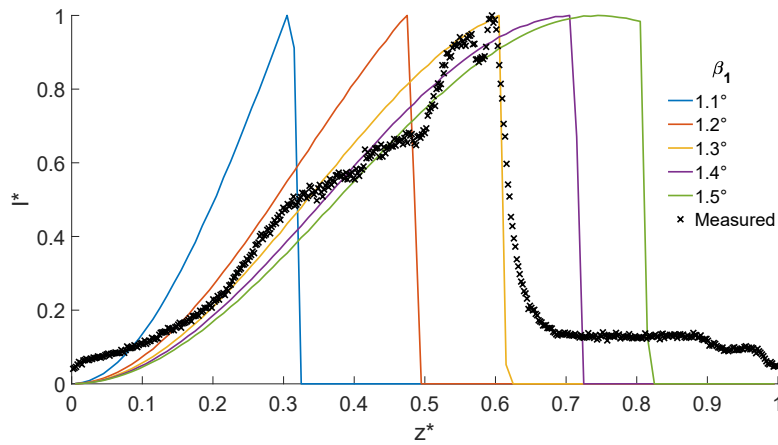


Figure 2.14: Normalized light intensity profile versus β_1 (Fig.2.12).

This analysis confirms the asymmetry of the intensity profile measured in Section 2.3.1.1, with a good agreement of the shape of the intensity profile measured and the intensity profile obtained with the simulation with $\beta_1 = 1.3^\circ$. The profiles obtained for low incident angle (around 1°) are thinner with a sharper peak, which is closer to the P-PIV. Therefore, the precision of the measurement technique increases at lower incident angles. In order to analyse the intensity of the sheet transmitted, two parameters can be analysed. The first one is the intensity peak value normalised by the intensity of the peak at $\beta_1 = 2^\circ$ as $I_{peak}^* = \frac{I_{peak}(\beta_1)}{I_{peak}(\beta_1=2^\circ)}$. The second is the percentage of the incident Gaussian beam transmitted in the water I_t/I_g (where I_t is the total intensity of the transmitted beam and I_g is the total intensity of the incident Gaussian beam). These two parameters are presented Fig.2.15.

Fig.2.15 highlights the increase of the total transmitted intensity and the intensity of the peak with

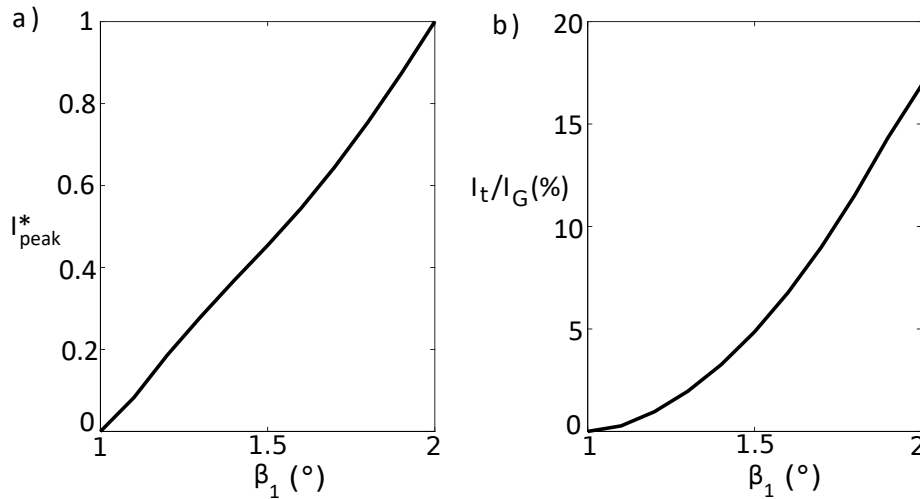


Figure 2.15: a) Value of the intensity peak depending on the incident angle β_1 (Fig.2.12). b) Percentage of the total transmitted intensity in the fluid function of β_1 .

the incident angle β_1 . This ray tracing model shows us that the incident angle is a key parameter in the intensity profile shape and propagation. Considering the evolution of the thickness of the laser sheet (Fig.2.14) with β_1 , the incident angle should be low enough in order to increase the precision. On the other hand, considering the evolution of the intensity of the laser sheet (Fig.2.15) with β_1 , the incident angle should be high enough to ensure sufficient particle illumination and enhance the signal/noise ratio. Therefore, the chosen β_1 is a compromise between intensity and precision. This ray tracing model also highlights the high sensitivity of the method to optical default of the transparent window.

2.3.1.3 Long range propagation for tire application.

For tire applications, the field of view is larger than the one for the channel experiment and the water thickness can be smaller (down to 1.5 mm). Therefore, it is important for future analysis to allow the simulation of the laser sheet propagation with reflections at the free surface. With this feature, the analysis of the intensity profile after multiple reflections (around 5 reflections) at the free surface is possible (after B Fig.2.12). The intensity profile at $x^* = 100$ is here presented to illustrate the behaviour for long propagation ranges (Fig.2.16).

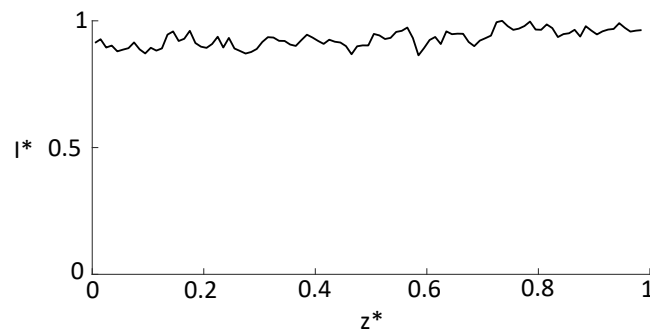


Figure 2.16: Normalized light intensity profile at $x^* = 100$.

After few reflections, a mix of the ray trajectories generates a volume illumination with a flat intensity profile in height. This situation of long range propagation is studied more extensively in chapter 3. Nevertheless, the following analysis of the technique is made with an arbitrary specified intensity profile $I_0^*(z^*)$. The influence of the profile on the bias of R-PIV measurements is important and is discussed in more detail in the following.

2.3.2 Depth of focus.

The optical parameter of interest for the collecting optic is the depth of focus. It defines the sharpness of particle images and therefore influences their contributions to the cross-correlation. To quantify this parameter, the knowledge of the object plane position of the camera is needed. A measurement technique is developed in order to quantify the position of the object plane in the fluid at rest. A dotted target (white background plate with 0.0625 mm diameter black dots and 0.125 mm distance between them) is placed on an inclined plate of 45° inclination with the horizontal. Images of this dotted target are recorded to determine the positions of best focused dots. Focused dots are smaller and darker. Therefore, the focusing quality of a dot can be calculated with these two parameters. Due to the small size of the dot images (diameter 0.024 mm ~ 2 px), the analysis of the dots focusing is made based on their gray level. Due to the inclination of the plate the analysis of the inverse intensity of the dots ($1/I^*$) along the x^* axis gives us the grey level in the z^* direction (Fig.2.17).

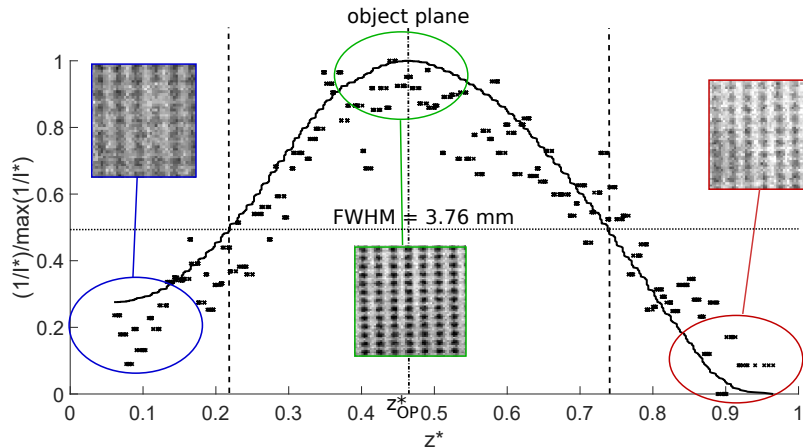


Figure 2.17: Normalized gray level profile for an aperture number of 5.6.

For the 5.6 aperture number used here, the order of magnitude of the depth of focus can be defined by the full width at half maximum of the gray level of the dots (Fig.2.17). This normalized depth of focus is $DOF^* = 0.43$, which is in the same order of magnitude than the laser sheet thickness measured and shown Fig.2.10 b). With larger depth of focus, the ambient light due to the reflections of the laser sheet at the different interfaces is more intense and the signal/noise ratio is lowered. For thinner depth of focus, due to the inclination of the light sheet, the maximum intensity of the laser beam is out of the depth of focus near the images edges. Therefore, most illuminated particles are blurred and the signal/noise ratio in those parts is lowered. These are the reasons why an aperture number of 5.6 is chosen here to ensure a good focus in the whole volume while limiting refractive noise. The object plane position (z_{OP}^*) can therefore be measured with the maximum gray level (Fig.2.17) (here $z_{OP}^* = 0.45$).

2.3.3 Conclusions.

To conclude on optical properties of the technique, we can say that the intensity profile illumination is initially thick. This profile can take two main shapes depending on the propagation zone studied. Close to the impingement point at the flow window interface, the profile is thick with an asymmetrical intensity distribution. After few reflections of the laser sheet at the free surface, the intensity profile becomes nearly homogeneous in the volume. In this characterization of the technique, the study will be focused on the first laser sheet structure (asymmetrical) which is more specific. The homogeneous illumination is considered as a particular case where $I_0^*(z^*) = cste$, which corresponds to a μ -PIV like illumination.

2.4 Cross-correlation statistical model for R-PIV

2.4.1 Cross correlation model (CCM).

2.4.1.1 The cross-correlation general form.

In this Section, the main calculation steps are presented in order to drive the reader through the reasoning for the cross-correlation model construction. Calculation details are presented in Appendix A.

As seen in section 2.1.2.2, the influence of the thickness of the depth of focus (DOF) with a volume illumination has been addressed in the past revisiting the original PIV cross-correlation model of Kean and Adrian 1992 [34]. In this section, the model is revisited in order to take into account the in-homogeneous light sheet intensity profile highlighted in the previous section 2.3.1.1. To understand the behaviour of the cross-correlation with the R-PIV optical set-up, images of individual particles are considered as a normal distribution as expressed by Olsen and Adrian 2000 [60]. If we consider a particle i at the position (μ_{1X_i}, μ_{1Y_i}) in image 1 and $(\mu_{2X_i} = \mu_{1X_i} + DX_i, \mu_{2Y_i} = \mu_{1Y_i} + DY_i)$ in image 2 with (DX, DY) displacement of the particle image on the camera sensor between both images is :

$$\begin{aligned} I_{1i}(X, Y) &= \frac{I_{p1i} Da^2 \beta^2}{4\pi d_{e1i}^2 (s_0 + z_{1i}')^2} \cdot e^{-\frac{4\beta^2}{d_{e1i}^2} ((X - \mu_{1X_i})^2 + (Y - \mu_{1Y_i})^2)} \\ I_{2i}(X, Y) &= \frac{I_{p2i} Da^2 \beta^2}{4\pi d_{e2i}^2 (s_0 + z_{2i}')^2} \cdot e^{-\frac{4\beta^2}{d_{e2i}^2} ((X - \mu_{2X_i})^2 + (Y - \mu_{2Y_i})^2)} \end{aligned} \quad (2.7)$$

where I_{p1i} is the intensity emitted by the particle for image 1 (with fluorescence $I_{p1i} \propto I_{01i} \cdot d_{p_i}^3$, with I_{01i} the intensity of the incident laser sheet on particle i and d_{p_i} is the geometrical diameter of the particle). Da is the aperture diameter of the lens, β^2 is a constant value set to 3.67 to best approximate the Airy diffraction (according to Olsen and Adrian 2000 [60]). s_0 is the distance between the camera and the object plane and $z_{1i}' = |z_{1i}^* - z_{OP}^*|$ is the distance between the particle and the object plane. d_{e1i} is the particle image diameter on the sensor for image 1 calculated according to Olsen and Adrian 2000 [60] as :

$$d_{e1i} = \sqrt{M^2 d_{p_i}^2 + 5.95(M+1)^2 \lambda_p^2 f^{\#2} + \frac{M^2 z_{1i}'^2 Da^2}{(s_0 + z_{1i}')^2}} \quad (2.8)$$

where λ_p is the wavelength of the light fluoresced by the particle and $f^\#$ is the aperture number of the camera lens. All those optical parameters are represented Fig.2.18.

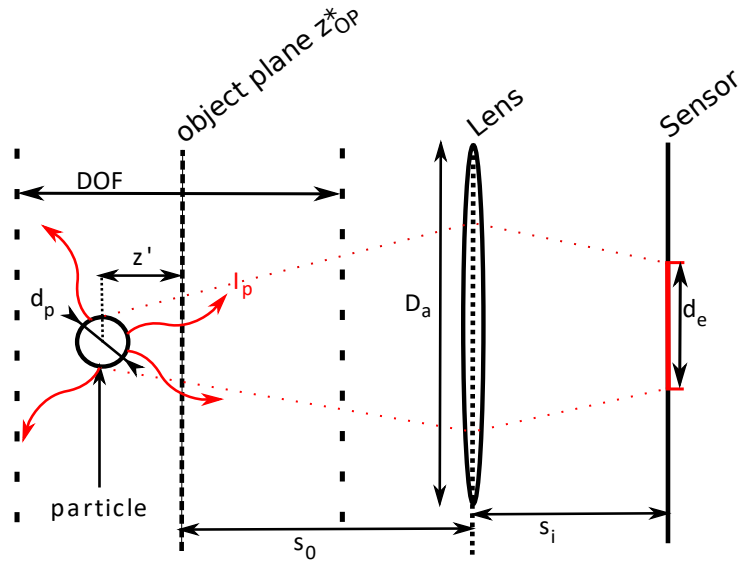


Figure 2.18: Scheme of the optic parameters involved to calculate a particle image diameter.

For an image with N particles, and a background noise B , the total image intensity pattern is the summation of all the particles and the background as :

$$I_1(X, Y) = \sum_{i=1}^N I_{1i}(X, Y) + B_1 \quad (2.9)$$

with the same reasoning, the second image of the image pair is :

$$I_2(X, Y) = \sum_{i=1}^N I_{2i}(X, Y) + B_2 \quad (2.10)$$

Therefore, the intensity pattern of both images can be added to the equation of the cross-correlation presented Eq.2.1.

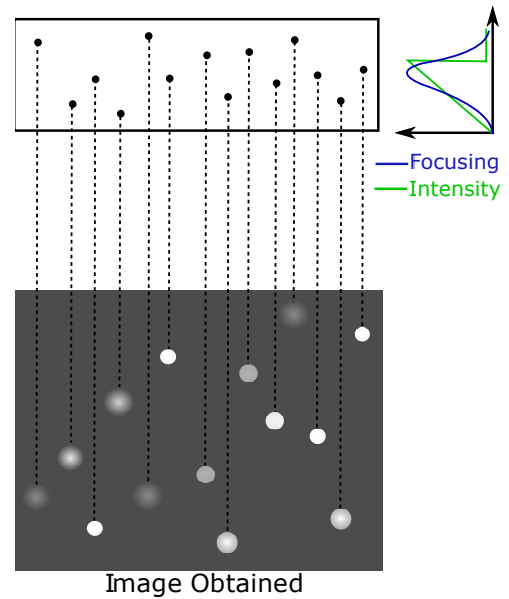


Figure 2.19: Scheme of the particle images depending on their relative location inside the light sheet thickness and with respect to the object plane altitude.

$$R_{12}(\delta x, \delta y) = \int_S \left(\sum_{i=1}^N I_{1i}(X+x, Y+y) + B_1 \right) \cdot \left(\sum_{i=1}^N I_{2i}(X+x+\delta x, Y+y+\delta y) + B_2 \right) dS \quad (2.11)$$

Therefore by developing the expression (Appendix A) we obtain :

$$\begin{aligned}
 R_{12}(\delta x, \delta y) &= \overbrace{\int_S \sum_{i=j=1}^N I_{1i}(X+x, Y+y) I_{2j}(X+x+\delta x, Y+y+\delta y) dS}^{R_{D12}} \\
 &\quad + \overbrace{\int_S \sum_{i \neq j}^N I_{1i}(X+x, Y+y) I_{2j}(X+x+\delta x, Y+y+\delta y) dS}^{R_{F12}} \\
 &\quad + \overbrace{\int_S \left(B_1 \cdot \sum_{i=1}^N I_{2i}(X+x+\delta x, Y+y+\delta y) + \sum_{i=1}^N I_{1i}(X+x, Y+y) \cdot B_2 + B_1 \cdot B_2 \right) dS}^{R_{C12}} \quad (2.12)
 \end{aligned}$$

This highlights the expression of the different components of the decomposition of the cross-correlation (according to Adrian 1988 [1]) as defined Fig.2.3 and Eq.2.3. If we make the hypothesis that the displacement component R_D is of a higher magnitude than the fluctuating R_F and the background R_C components, we can focus our analysis on R_D as :

$$R_{D12} = \int_S \sum_{i=j=1}^N I_{1i}(X+x, Y+y) I_{2j}(X+x+\delta x, Y+y+\delta y) dS \quad (2.13)$$

This cross-correlation can be calculated using the Fourier transforms of I_{1i} and I_{2j} as described in Appendix A. Thus the expression of the cross-correlation can be defined as the summation of the individual cross-correlations of each particles as $R_{D12} = \sum_{i=1}^N (R_{12})_{i,i}$, where $(R_{12})_{i,i}$ is the cross-correlation of a particle i in image 1 with its own image in image 2.

This single particle cross-correlation function can be calculated following the calculations in Appendix A. Therefore, the expression of the displacement component of the cross-correlation function is written as :

$$R_{D12}(\delta x, \delta y) = \sum_{i=1}^N \frac{I_{01i} \cdot I_{02i} \cdot d_{pi}^6 \cdot Da^2 \cdot \beta^2}{16\pi(d_{e1i}^2 + d_{e2i}^2) \cdot (s_0 + z_{1i}')^2 \cdot (s_0 + z_{2i}')^2} \cdot e^{-4\beta^2 \frac{(\mu_{2x} - \mu_{1x} - \delta_x)^2 + (\mu_{2y} - \mu_{1y} - \delta_y)^2}{d_{e1i}^2 + d_{e2i}^2}} \quad (2.14)$$

to reduce the equation, let's consider $A_i = \frac{d_{pi}^4 \cdot Da^2 \cdot \beta^2}{16 \cdot \pi}$.

Usually in PIV, the displacement of particles between both images should be smaller than the interrogation window size (generally, $DX_i \leq \frac{\Delta w_x}{4}$, where, Δw_x interrogation window size). For a refracted light sheet as presented Fig.2.11, the inclination of the maximum intensity line (solid line) $z_{max}^*(x^*)$ is approximately 4.6° . Therefore, between both boundaries of the interrogation window, the difference of maximum intensity height is $\Delta z_{max}^* = z_{max}^*(x^* + dw_x) - z_{max}^*(x^*) = 0.005$, which is low. Therefore, the light sheet intensity profile is locally considered as horizontal at the scale of an interrogation window. Thus, if the vertical velocity (W) of a particle is negligible, the particle is illuminated with the same intensity for both images depending its altitude z_i^* ($I_{01i} = I_{02i} = I_0(z_i^*)$). Due to the horizontal object plane, the focus of a particle is also the same inside both images depending on its height z_i^* ($d_{e1i} = d_{e2i} = d_e(z_i^*)$) and if the distance between the object plane and the particle is constant ($z_{1i}' = z_{2i}' = z_i'$). Finally, if the ve-

locity is considered as independent of (x^*, y^*) locally in an interrogation window, the particle velocity is determined by its height in the interrogation volume ($U(z_i^*) = DX(z_i^*)/(M.dt)$, $V(z_i^*) = DY(z_i^*)/(M.dt)$). Therefore, the simplified form of the cross-correlation displacement component becomes :

$$R_{D12}(\delta_x, \delta_y) = \sum_{i=1}^N \frac{A_i \cdot I_0^2(z_i^*)}{2 \cdot d_e^2(z_i^*) \cdot (s_0 + z_i^*)^4} \cdot e^{-4\beta^2 \frac{(DX(z_i^*) - \delta_x)^2 + (DY(z_i^*) - \delta_y)^2}{2 \cdot d_e^2(z_i^*)}} = \sum_{i=1}^N R_{Dz}(z_i^*) \quad (2.15)$$

In conclusion, the general form of the cross-correlation displacement component is given by the equation 2.14. This equation can be simplified for the low inclination light sheet measurements for R-PIV with negligible velocity in z direction. Therefore, the simplified form (equation 2.15) is used for the channel flow studied for R-PIV testing using the model.

Finally, to calculate the cross-correlation function for an interrogation window for a given optical set-up, the inputs needed are :

- An intensity profile $I_0(z)$
- A particle image diameter profile $d_e(z)$ (only dependant on the object plane position)
- A velocity profile ($U(z) = DX(z)/(M.dt)$, $V(z) = DY(z)/(M.dt)$).

2.4.1.2 Statistical convergence.

As shown by equation 2.15, the cross-correlation displacement component for a single image pair is the summation of the individual cross-correlation of each particles within the interrogation volume. Thus the cross-correlation function obtained for a single image pair is highly dependent on the random distribution of the N particle altitudes (z_1, z_2, \dots, z_N) . Therefore, this measurement technique can be highly variable for one single image pair to an other.

Therefore, to ensure the convergence of the R-PIV technique, a statistical averaging over numerous image pairs should be done. In PIV, the velocity is given by finding the displacement corresponding to the position of the cross-correlation peak. For a fixed number N_{im} of image pairs, two different averaging strategies are used, based on the same correlation model equation 2.15. Let's consider that the velocity finally obtained at the end of the averaging process is (U, V) with $U = \frac{\delta_x^{(f)}}{M.dt}$ and $V = \frac{\delta_y^{(f)}}{M.dt}$. Here $(\delta_x^{(f)}, \delta_y^{(f)})$ are the final displacements obtained after the averaging process.

The first one consists in finding the peak value of the averaged cross-correlation function over N_{im} image pairs. This corresponds to the sum of correlation cross-correlation method :

$$\begin{aligned} (\delta_x^{(f)}, \delta_y^{(f)}), \text{ as } < R_{D12}(\delta_x^{(f)}, \delta_y^{(f)}) > = \max\{ < R_{D12}(\delta x, \delta y) > : \delta x, \delta y \} \\ < R_{D12}(\delta x, \delta y) > = \frac{1}{N_{im}} \sum_{i=1}^{N_{im}} R_{D12}(\delta x, \delta y) \end{aligned} \quad (2.16)$$

For this first averaging method, if we consider a probability law $P(z)$ of presence of a particle at a height z , the mean displacement component of the cross-correlation $< R_{D12}(\delta x, \delta y) >$ converges to the integral of the contributions of every z when the number of particles tend to the infinity.

$$\langle R_{D12}(\delta x, \delta y) \rangle = \lim_{N_{im} \rightarrow \infty} \frac{1}{N_{im}} \sum_{i=1}^{N_{im}} R_{D12}(\delta x, \delta y) = \int_{z_{min}}^{z_{max}} P(z) R_{Dz}(z) dz \quad (2.17)$$

The second averaging process consists in calculating the average of each displacement, deduced from the peak location of each independent cross-correlation function. This corresponds to the averaging of the measured velocities :

$$\begin{aligned} (\delta x^{(f)}, \delta y^{(f)}) &= \frac{1}{N_{im}} \sum_{i=1}^{N_{im}} (\delta x_i, \delta y_i) \\ (\delta x_i, \delta y_i), \text{ as } R_{D12}((\delta x_i, \delta y_i)) &= \max\{R_{D12}(\delta x, \delta y) : \delta x, \delta y\} \end{aligned} \quad (2.18)$$

To test both cross-correlations and velocities averaging, an interrogation volume is considered with $N = 15$ particles in this volume (approximately the number of particles per interrogation windows for measurements). The intensity profile considered is a simplified inhomogeneous profile to approximate the actual one measured in the channel (Fig.2.10b)). The velocity profile is the one given by Eq.2.4 for $y^* = 0.5$. The particle image diameter profile is calculated from Eq.2.8 with an object plane $z_{OP}^* = 0.45$ to well simulate experimental conditions. The input profiles are presented Fig.2.20.

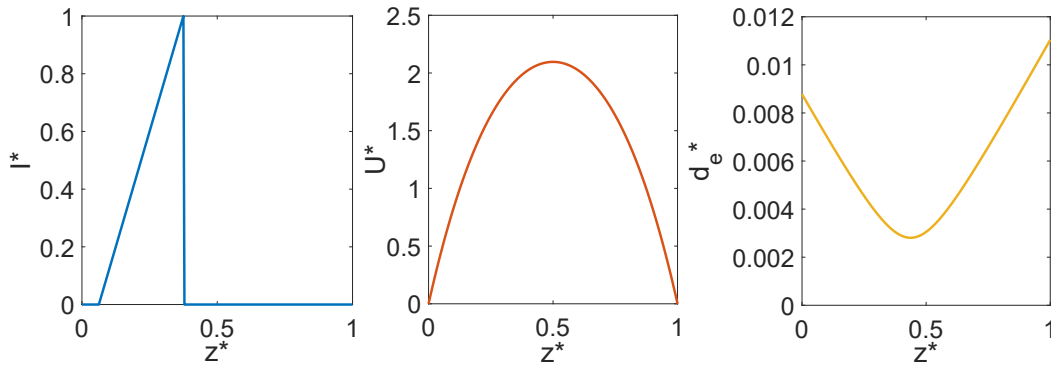


Figure 2.20: Inputs profiles for the CCM intensity, velocity and particle image diameter.

Simulations with the models Eq.2.16 and Eq.2.18 considering an increasing number of image pairs (N_{im}) are made in order to study the convergence of these models. The algorithm used to compare those averaging models is sketched Fig.2.21. To quantify the standard deviations, simulations are repeated 20 times with different particle random positions for every N_{im} in order to quantify the standard deviation of the velocities given by the models depending on N_{im} .

With this analysis, we observe in Fig.2.22, that the velocity obtained with the model with the averaging process corresponding to the sum of correlation (Eq.2.16), does converge to the integral given value (Eq.2.17). However, velocity predicted with the averaging process Eq.2.18, converges to a lower velocity. This is explained by the fact that for each independent image pair, the Eq.2.18 consists in calculating a velocity for every image pairs and then averaging the velocities obtained. This includes velocities in the high velocity part and low velocity part.

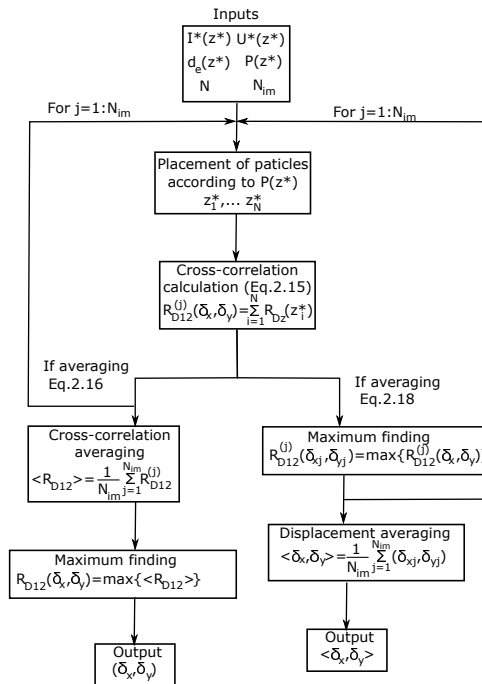


Figure 2.21: Scheme of the chart of the algorithm.

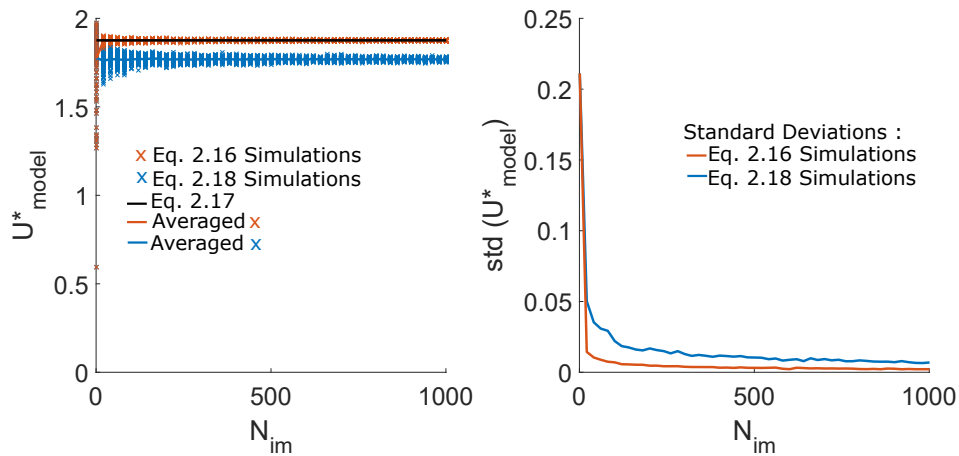


Figure 2.22: Simulations performed with both averaging methods and their standard deviations for $N = 15$.

In conclusion, the measured velocity predicted by the CCM Eq.2.15 depends on the averaging process used for the statistical analysis (Eq.2.16 or Eq.2.18). Eq.2.16 (sum of correlation) converges faster with a lower dispersion in general (Fig.2.22 (right)) than Eq.2.18 (sum of velocities). Eq.2.16 converges, when the number of image pairs tend to infinity, to Eq.2.17. In the next section, for this study of the R-PIV, the validation of the CCM model Eq.2.15 will be done comparing the results obtained with measurements using the sum of correlation averaging process and the one predicted with Eq.2.17.

2.4.2 Analysis of the illumination methods with the CCM

In this section the model is used in its integral form (Eq.2.17) to predict the velocity (U_{model}^*) in a square channel flow if we apply measurements with either P-PIV or R-PIV. As described previously, the inputs needed are :

- The reference velocity profile U_{ref}^* .
- The intensity profile $I_0^*(z^*)$.
- The object plane position z_{OP}^* .
- The probability distribution of particles in height $P(z^*)$.

The reference velocity field U_{ref}^* is chosen as the analytic solution Eq.2.4 of the studied flow for $y^* = 0.5$ in this specific section. For this experimental set-up, the particles are homogeneously distributed in the water tank and then the probability distribution of particles positions is homogeneous in the flow. The velocity U_{comp}^* is then compared to the reference velocity U_{ref}^* for both illumination methods (in this specific section, $U_{comp}^* = U_{model}^*$).

The relative errors are quantified to compare velocity profiles ($E_{1\alpha}$) or velocity 2D maps ($E_{2\alpha,\gamma}$). These errors are defined as follows :

$$E_{1\alpha} = \frac{\sqrt{\int_0^1 (U_{ref}^*(\alpha) - U_{comp}^*(\alpha))^2 d\alpha}}{\int_0^1 U_{ref}^*(\alpha) d\alpha} \quad (2.19)$$

where α is a coordinate that could be either x^* , y^* or z^* .

2.4.2.1 Model Prediction for P-PIV.

In the case of P-PIV, the measured perfectly horizontal laser sheet intensity profile (Fig.2.10a) is close to a Gaussian distribution. In this example, the thickness measured at $I_{max}^*/4$ is $e^* \simeq 0.05$.

P-PIV is simulated with the model with a position of the object plane z_{OP}^* corresponding to the position of the center of the laser beam $z_B^* = z_{OP}^*$ (maximum intensity of the Gaussian profile). For a fixed position x^* , calculations are made with Eq.2.17 with different laser beam and object plane positions from $z_B^* = z_{OP}^* = 0.0625$ to $z_B^* = z_{OP}^* = 0.9375$. Those simulations were made with two different light sheet thickness ($e^* = 0.05$ and $e^* = 0.19$) in order to quantify the effect of a large light sheet. The errors between the model profiles and the analytic solution are calculated according to Eq.2.19.

This shows that with $z_B^* = z_{OP}^*$, the measurement bias introduced by the laser sheet thickness is limited. For a thick laser sheet ($e^* = 0.19$) the error remains below 2.5%. For the thin laser sheet ($e^* = 0.05$, as measured for the experiment), the maximum error is approximately 0.1%. Therefore, the P-PIV with a thin laser sheet with $z_B^* = z_{OP}^*$ can be considered as a reference measurement of the flow of interest.

The same illumination profiles ($e^* = 0.05$ and $e^* = 0.19$) are studied with a fixed position of the object plane $z_{OP}^* = 0.5$, while varying the position of the light sheet from $z_B^* = 0.0625$ up to $z_B^* = 0.9375$. Those calculations are presented Fig.2.24 with the error between profiles calculated according to Eq.2.19.

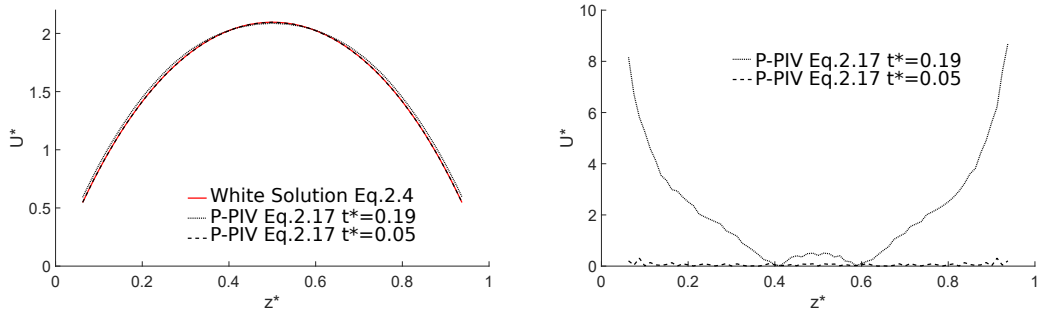


Figure 2.23: Left is the velocity profile $U^*(z^*)$ at $y^* = 0.5$ with the White[78] solution (Eq.2.4) compared to the profile predicted by the model with different laser sheet thickness. Right is the relative error (eq.2.19) between the White[78] and the velocities predicted by the model.

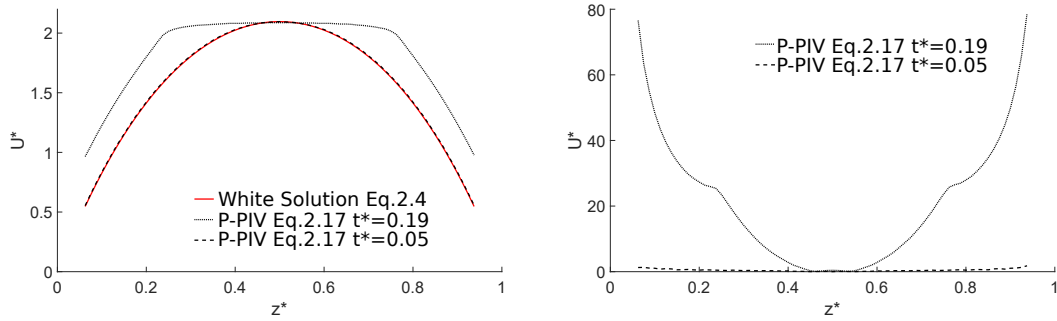


Figure 2.24: Left is the velocity profile $U^*(z^*)$ at $y^* = 0.5$ with the White[78] solution (Eq.2.4) compared to the profile predicted by the model with different laser sheet thickness. Right is the relative error (eq.2.19) between White[78] and the velocities predicted by the model.

In this configuration, the error with the thin laser sheet ($e^* = 0.05$) remains lower than 1.5%. However, with the thick laser sheet ($e^* = 0.19$) the error grows up to 70%. This highlights the importance in P-PIV to reduce the laser sheet thickness to increase precision. When the laser sheet thickness increases, particles at different height with different velocities contributes to the cross-correlation. Therefore, the bias introduced in the measurements is increased. These preliminary results also show that the accuracy of P-PIV is increased when the object plane is aligned with the laser sheet ($z_B^* = z_{OP}^*$).

2.4.2.2 Model Prediction for R-PIV.

In the case of R-PIV, the measured laser sheet intensity profiles during propagation (Fig.2.11) are used. For any x^* the computed velocity is associated to an altitude $z_{max}^*(x^*)$ (Fig.2.11) corresponding to the maximum intensity on the vertical. We fix the object plane at $z_{OP}^* = 0.5$. For any x^* , CCM is used to predict the velocity obtained with Eq.2.17 with inputs as :

- The reference velocity profile U_{ref}^* from the analytic solution Eq.2.4.
- The intensity profile $I_0^*(z^*)$ at the specific location x^* .
- The object plane position z_{OP}^* .
- The homogeneous probability distribution of particles in height $P(z^*) = constant$.

The CCM simulations are repeated from $x^* = 3$ (left edge of the field of view) to $x^* = 6.3$ (location x^* where $z_{max}^*(x^*) = 0.5$). At each x^* , the velocity predicted by the model is associated to the location $z_{max}^*(x^*)$ as $U_{model}(z_{max}^*(x^*))$. For $z_{max}^* > 0.5$, symmetry of the profiles is assumed.

Afterwards, the reference velocity profile $U_{ref}^*(z_{max}^*(x^*))$ is compared to $U_{model}^*(z_{max}^*(x^*))$ in Fig.2.25. The relative error is given by Eq.2.19 with $U_{ref}^* = U_{ref}^*(z_{max}^*(x^*))$ and $U_{com}^* = U_{model}^*(z_{max}^*(x^*))$.

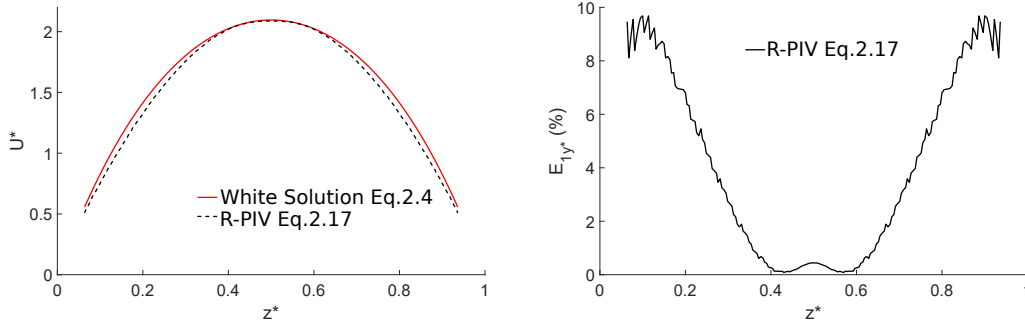


Figure 2.25: Left is the velocity profile $U_{ref}^*(z_{max}^*(x^*))$ at $y^* = 0.5$ with the White and Corfield 2006 [78] solution (Eq.2.4) compared to the profile predicted by the model with refracted laser beam. Right is the error (eq.2.19) between White and Corfield 2006 [78] at $z_{max}^*(x^*)$ and the velocity predicted by the correlation model for R-PIV.

With a refracted light sheet and a fixed object plane $z_{OP}^* = 0.5$, the error between profiles obtained by the model and the reference (analytic solution) is below 1 % in the low velocity gradient part of the flow. However, the error grows rapidly near the walls with an error of approximately 8.5% at $z^* = 0.0625$. It is thus interesting to note that this bias is due to the velocity gradient that is accounted in the model. Thus R-PIV induces an intrinsic (due to optical-correlation process of analysis) error that is not negligible, contrarily to P-PIV, as soon as the studied flow shows large gradient.

Now, the model can be used to analyse the R-PIV measurements in the whole work.

2.5 Results and validation of the model

2.5.1 Flow Structure.

Due to the geometry constraints of the set-up (presented Fig.2.7), the measurement area is placed 148 mm downstream the inlet of the channel. This distance is too short to consider a fully developed channel flow. In these conditions, P-PIV measurements can show locally different velocities than the analytic solution (Eq.2.4). The three main reasons that can explain these differences are : 1) The bias introduced by the laser sheet thickness, 2) the disturbance of the flow due to the set-up imperfections as the adjustment of the connector at the entry of the channel and 3) the not fully developed flow. Here for the P-PIV measurements, the laser light sheet used is as presented Fig.2.10a) with a thickness $e^* = 0.05$ and with an object plane aligned with the laser sheet ($z_{OP}^* = z_B^*$). As shown previously, for these conditions, the bias introduced by the laser sheet thickness is negligible. Therefore, the small differences between P-PIV measurements and the analytic solution for such flow are due to flow disturbances.

P-PIV is here used first to characterize the flow field in the channel. This measurement method is considered as a reference as its robustness and limitations were extensively demonstrated in the literature

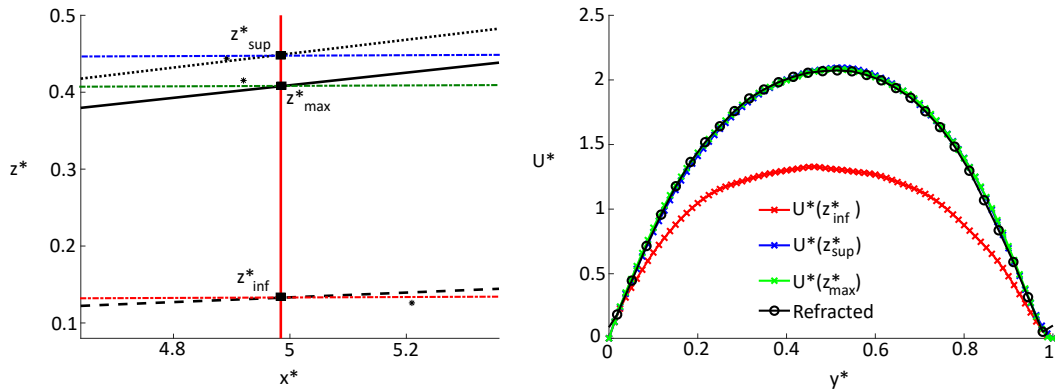


Figure 2.27: Left : Zoom on the section $x^*=4.984$ from Fig.2.11. Right : Colored line with cross markers are profiles obtained with P-PIV at fixed z^* , colors corresponding to the color of various z^* horizontal sheets in the left figure. The black line with circle markers represents profile measured with R-PIV.

for similar flows. To obtain the most complete velocity field representation of the channel flow, P-PIV measurements are repeated by step of 0.5 mm from $z^*_B = 0.0625$ to $z^*_B = 0.9375$. The object plane position is adjusted for every measurements in order to ensure $z^*_{OP} = z^*_B$. A spatial interpolation is finally made to obtain the complete 3D2C velocity field in the channel (Fig.2.26) (interpolation with cubic spline method).

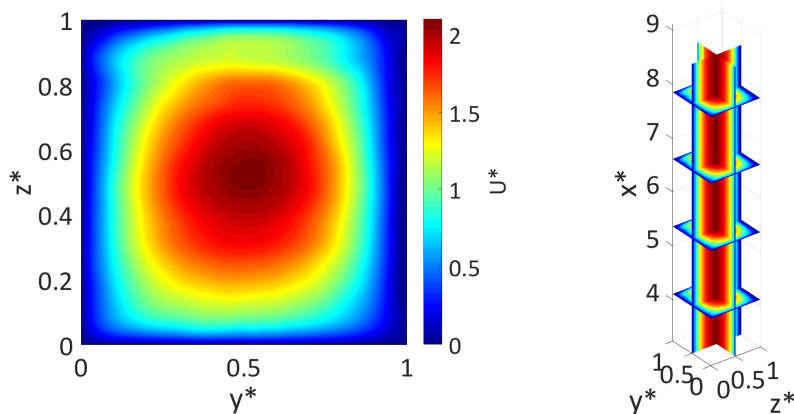


Figure 2.26: Measured velocity field in the channel (cubic spline interpolation from 2D slices obtained with P-PIV).

2.5.2 R-PIV results.

With a refracted light sheet illumination as presented Fig.2.11, PIV analysis is led with a sum of correlation processing over 500 recorded image pairs in order to converge to the integral formulation (Eq.2.17). The velocity is then determined by finding the peak location of this averaged correlation. The object plane for these measurements is measured at $z^*_{OP} = 0.45$ (Fig.2.17). The velocity profile in y^* direction obtained with the R-PIV is compared to the P-PIV reference profiles at the specific heights z^*_{inf} , z^*_{max} and z^*_{sup} (Fig.2.11). This comparison was made for every sections x^* in the measurement area. An example is presented Fig.2.27 for the section $x^* = 4.984$ already highlighted Fig.2.11.

Such comparisons demonstrate that the velocities measured with R-PIV are in good agreement with

the P-PIV horizontal measurements at the height z_{max}^* . This demonstrates that with an inhomogeneous and asymmetrical light sheet, the particles which are the most illuminated contribute more to the cross-correlation. To quantify the validity of this conclusion over the whole measurement area, the global error indicator E_{1y^*} between the reference profiles (z_{inf}^* , z_{max}^* and z_{sup}^*) and R-PIV measurements is calculated according to Eq.2.19 at every section x^* (Fig.2.28).

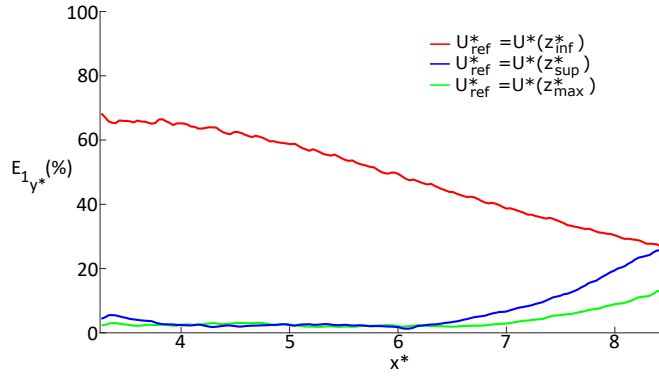


Figure 2.28: The error Eq.2.19 is represented with U_{ref}^* the velocity measured with R-PIV and $U_{comp}^* = U^*(z_{inf}^*)$ (Red), $U_{comp}^* = U^*(z_{sup}^*)$ (Blue) and $U_{comp}^* = U^*(z_{max}^*)$ (Green).

Fig.2.28 confirms that the R-PIV measurements are close to the velocity obtained with P-PIV at z_{max}^* . Fig.2.28 (green curve) shows that for $x^* \geq 6$ the error between the R-PIV velocity measurements and P-PIV velocity measurements at z_{max}^* grows. Remember that every x^* is associated a unique z_{max}^* . For $x^* \geq 6$, the particles at z_{max}^* are not the closest of the object plane. Thus, some particles at lower altitude are illuminated due to the asymmetry of the intensity profile and are best focused. Therefore the contribution of these particles is more important than the ones at z_{max}^* and the velocity measured will correspond to the velocity at best focused height.

We have further ran the model Eq.2.15 with the averaging integral formulation Eq.2.17 considering the present experimental parameters (Intensity profile, object plane position and reference velocity profile). With this model we obtain the predicted velocity with the R-PIV optical configuration. This predicted velocity and the velocity obtained from R-PIV measurements (with the sum of correlation over the 500 image pairs) are compared all along the measurement zone (x^*) at a fixed $y^* = 0.5$ in Fig.2.29.

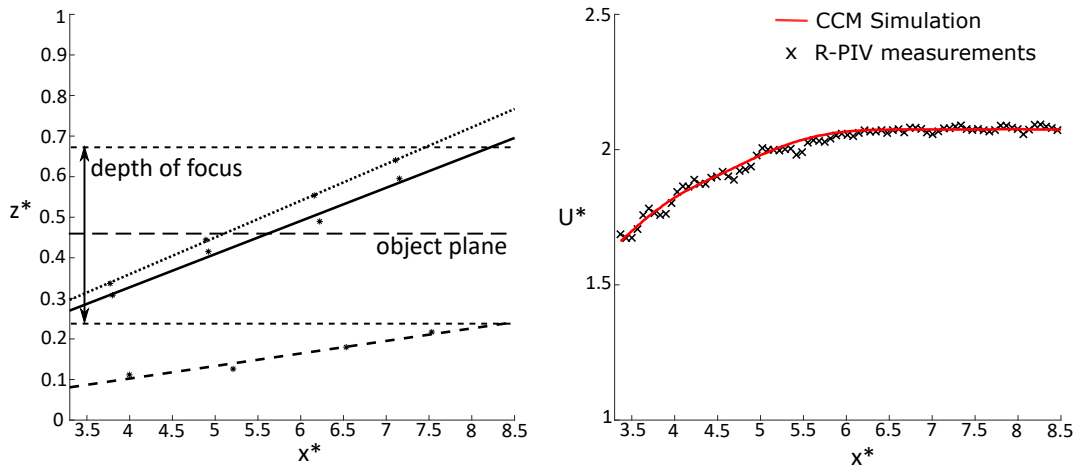


Figure 2.29: Left side is the laser sheet evolution in x^* with the object plane (z_{OP}^*) and the depth of focus shown. Right side is the velocity at $y^* = 0.5$ for the R-PIV measurement (black points) and the velocity obtained with the model for the same position (red line).

This shows a good agreement between the R-PIV measurements and the predicted velocity by the model. Therefore, the optical model Eq.2.15 can be used with the proper averaging process (here Eq.2.17) to describe the bias in the R-PIV measurements depending on the optical parameters of the experiment.

As discussed in the Section 2.4.1.2, the averaging process Eq.2.17 is a statistical interpretation of the sum of correlation when the number of image pairs considered tend to infinity. To verify this statistical convergence with measurements, the R-PIV image pairs are cross-correlated with the exact same process considering a number of image pairs growing from 1 to 500. To quantify the error between the R-PIV measured velocity with the prediction of the CCM, the relative error is calculated according to Eq.2.19 using the velocity predicted by the CCM model as U_{ref}^* (red line Fig.2.29) and the velocity from R-PIV measurements for various number of image pairs as U_{comp}^* (black crosses Fig.2.29). This error is represented as a function of the number of image pairs considered Fig.2.30.

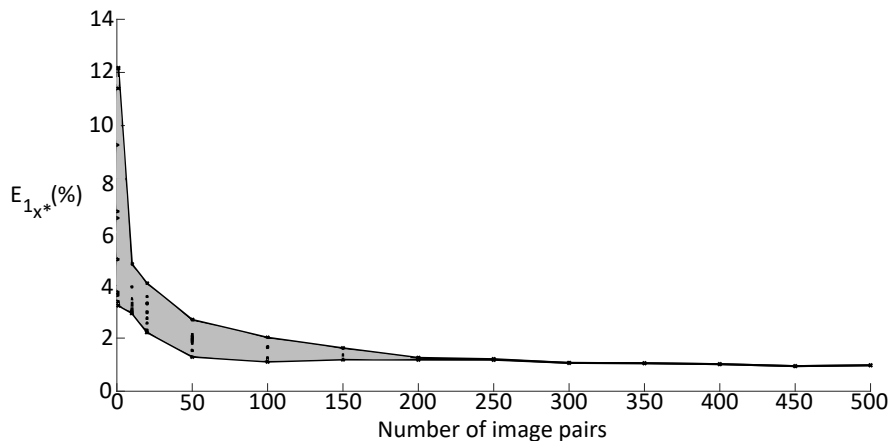


Figure 2.30: Error eq.2.19 is represented with U_{ref}^* the velocity measured with R-PIV and U_{comp}^* the velocity predicted by the model.

This shows the convergence of the measurements to the model predicted velocity with the increase

of the number of image pairs considered. To obtain measurements that can be interpreted and predicted by the model, the number of image pairs to consider for measurements should ideally be over 200 image pairs.

2.6 Conclusions

2.6.1 Optical properties of R-PIV

In this chapter, the R-PIV technique based on the refraction of the laser sheet at the flow window interface has been described. This technique is adapted for measurements of the velocity in a water puddle with a rolling tire. A configuration for which only one optical access is available.

With this technique, the optical properties are specific and should be measured in order to determine the precision of measurements. A measurement technique of the laser light sheet profile after refraction at the solid/liquid interface was proposed in addition to a ray tracing model in order to characterize the light sheet propagation in the liquid phase. This propagation is decomposed in two zones. Right after the refraction of the laser sheet at the solid/fluid interface, the laser sheet emerges with a low inclination. It is characterized by a large thickness growing with the propagation of the laser sheet in x^* and by an asymmetrical form that remains unchanged while it grows. After the impingement of the laser sheet at the free-surface for a long range propagation, the intensity profile in the flow tends to become uniform.

2.6.2 Prediction of the measured velocity using a cross-correlation model

This specific illumination together with the positioning of the object plane of the camera influences the shape of the cross-correlation in PIV analysis. An extension of the cross-correlation models proposed in the literature for μ -PIV accounting for large depth of focus is proposed here at macroscopic scale with an inhomogeneous incident intensity light sheet. This model helps us to understand the integration effect intrinsic of this R-PIV technique. This CCM model allows to study the PIV cross-correlation with an intensity profile $I_0^*(z^*)$ to be determined experimentally for the specific optical configuration. This model also allow to study the effect of different averaging processes as the sum of correlation and the averaged velocity. To conclude, whenever it is possible, the use of the sum of correlation for the velocity field calculation is recommended due to the lower standard deviation of this averaging method (Eq.2.16) when compared with the CCM model. However, when the sum of correlation is not usable, the averaged velocity field can be used with the averaging process Eq.2.18. for the CCM model.

The use of R-PIV technique is then appropriated to measure velocity field in confined space as for the tire flow measurements targeted in this thesis. The cross-correlation model can then be used to determine the integration effect, for every configurations.

3 Application to tire flow measurements.

3.1 Experimental set-up for tire measurements.

3.1.1 Measurement pit.

3.1.1.1 2D2C R-PIV measurement set-up

To study the water flow under a rolling tire, measurements are performed at a dedicated track at Michelin©Ladoux site (Clermont-Ferrand, France). This track is composed of a straight road which can be locally filled with a water puddle. The water height h_{water} of the puddle can be regulated between 1.5 and 8 mm with an ultrasound probe which controls the valves of the hydraulic loop at the inlet and the outlet of the puddle. A prismatic shaped PMMA block with a thickness of 500 mm is embedded in the road allowing an optical access from a room below the track (as sketched Fig.3.1). The inclination angle of the prism inclined face is approximately $\theta_p = 66^\circ$. Therefore, a refracted light sheet can be generated inside the water puddle thanks to a slight offset from the normal to the inclined face (as described Chapter 2).

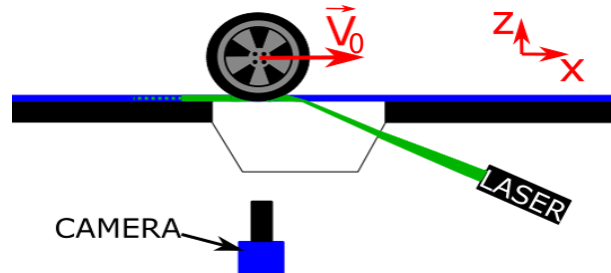


Figure 3.1: Set-up for in-situ measurement of the velocity field in the water puddle.

As for the laboratory experiments Chapter 2, fluorescent particles are used in order to enhance the signal/noise ratio for R-PIV measurements. In this whole work, the coordinate system is chosen in order to have the x axis in the rolling direction of the car, y in the transverse direction and the z axis in the vertical axis. The origin of the coordinate system will be discussed in Section.3.4.

3.1.1.2 2D3C Stereoscopic R-PIV measurement set-up

To investigate the 3D structure of the flow inside tire grooves, stereoscopic measurements are performed giving us access to the third component of the water flow (W). For 2D3C (2 dimensions 3 components) stereoscopic measurements, the same setup is used with two cameras (Arroyo et al. 1991 [6] and Van

Doorne et al. 2007 [73]) Fig.3.2 where both cameras are aligned in the car rolling direction. The two lenses in front of each cameras are placed on Scheimpflug arrangement in order to optimize the recovering of both depth of focus.

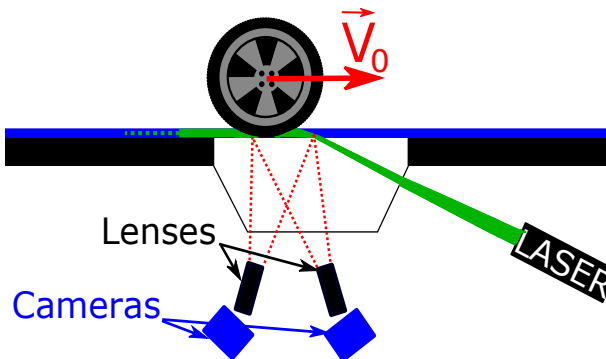


Figure 3.2: Scheme of the experimental setup for stereoscopic measurements.

In this configuration, the 3D position of the particles can be determined after a calibration based on triangulation polynomials that transforms the 2D displacement on both camera sensors (X_j, Y_j) into the real displacement in (x, y, z) (j is the camera index). This calibration is done with the help of a 3D calibration matrix composed of white dots on a black plate. These dots are placed in two different planes, one at $z = 0$ mm and $z = 3$ mm. Based on the position of each dots on both camera sensors, the software calculates polynomial coefficients needed to transform coordinates into 3D coordinates (Fig.3.3).

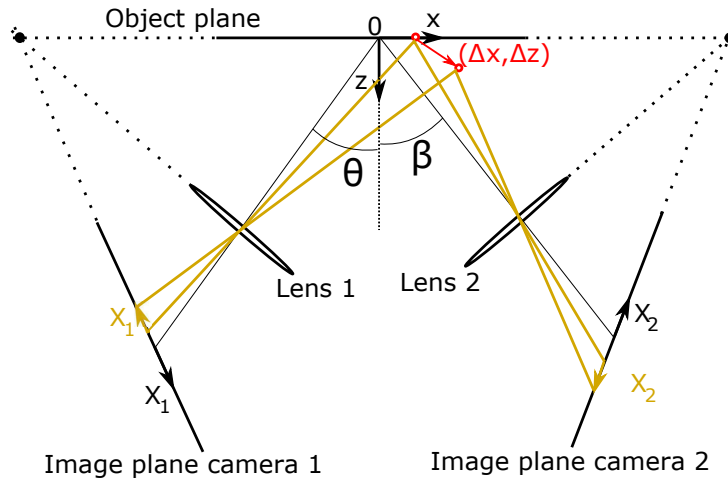


Figure 3.3: Scheme of the stereoscopic PIV principle with Scheimpflug settlement.

The triangulation function used is a direct polynomial third order fit.

$$\begin{pmatrix} X_1 \\ Y_1 \end{pmatrix} = \begin{pmatrix} F_1^{(j)}(x, y, z) \\ F_2^{(j)}(x, y, z) \end{pmatrix} \quad (3.1)$$

where $F_1^{(j)}$ and $F_2^{(j)}$ are functions which associate x and X .

Those functions can be approximated with a polynomial form :

$$F_i^{(j)} \simeq \hat{F}_i^{(j)} = a_{0,i}^{(j)} + a_{1,i}^{(j)}x + a_{2,i}^{(j)}y + a_{3,i}^{(j)}z + a_{4,i}^{(j)}x^2 + a_{5,i}^{(j)}xy + a_{6,i}^{(j)}y^2 + a_{7,i}^{(j)}xz + a_{8,i}^{(j)}yz + a_{9,i}^{(j)}z^2 \quad (3.2)$$

$$+ a_{10,i}^{(j)}x^3 + a_{11,i}^{(j)}x^2y + a_{12,i}^{(j)}xy^2 + a_{13,i}^{(j)}y^3 + a_{14,i}^{(j)}x^2z + a_{15,i}^{(j)}xyz + a_{16,i}^{(j)}y^2z + a_{17,i}^{(j)}xz^2 + a_{18,i}^{(j)}yz^2$$

Where $a_{k,i}^{(j)}$ are factors of the triangulation functions to be determined by a least square approach. j represents the camera index and i the function index.

We determine the displacement with this triangulation :

$$\begin{pmatrix} DX_j \\ DY_j \end{pmatrix} = \begin{pmatrix} F_1^{(j)}(x + \Delta x, y + \Delta y, z + \Delta z) \\ F_2^{(j)}(x + \Delta x, y + \Delta y, z + \Delta z) \end{pmatrix} - \begin{pmatrix} F_1^{(j)}(x, y, z) \\ F_2^{(j)}(x, y, z) \end{pmatrix} \quad (3.3)$$

The root mean square error of the triangulation function obtained with this calibration method is around 0.6 pixels for the first camera and 0.8 pixels for the second camera.

3.1.2 Reception Optic.

Images of the fluorescent particles are recorded with sCMOS cameras of 2160x2560 pixels (2560 in the streamwise direction and 2160 in the spanwise direction). An optical filter with a band-pass width of ± 20 nm centred at 590 nm is used for filtering all wavelengths out of interest. The objective for tire measurements is to obtain velocity fields in all the tire grooves and also in front of the tire. Therefore the field of view targeted is approximately 240x200 mm (with a camera sensor size of 16.6x14 mm which correspond to a pixel size of $d_{pix} \simeq 6.5 \cdot 10^{-3}$ mm). Thus the magnification in this configuration is $M = \frac{14}{200} = 0.07$. To obtain this field of view a $f = 100$ mm lens is used with a distance between the lens and the PMMA block of $d = 1150$ mm. For this configuration, the thickness of the PMMA window (e_{PMMA}) can not be neglected. Therefore a corrected working distance $s_0^{(eff)} = \frac{f}{M} - f$ is calculated to consider the equivalent working distance without the PMMA block to be in the conditions of Eq.2.8. The aperture number chosen for measurements is 5.6. The wavelength fluoresced by particles is $\lambda_p = 584$ nm and their diameter is between 20 – 50 μ m (as described in Section 3.1.3). Considering an object plane on the floor $z_{OP}^* = \frac{z_{OP}}{h_{water}} = 0$, the evolution with the normalised vertical coordinate z^* of the apparent particle image diameter calculated from Eq.2.8 is shown in Fig.3.4 for $h_{water} = 2$ and $h_{water} = 8$ mm.

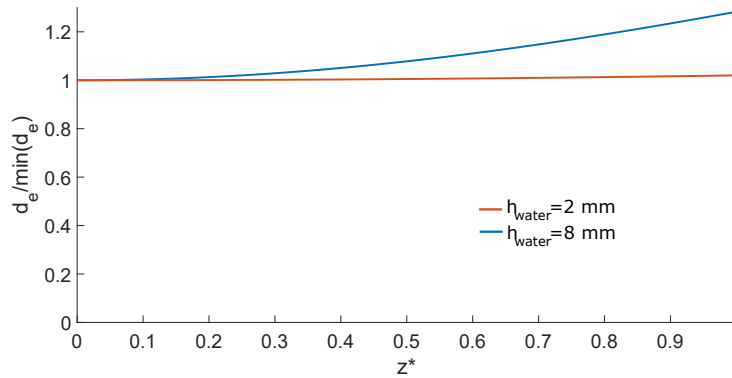


Figure 3.4: diameter of the image of a particle depending on its height in the puddle.

This shows that for $h_{water} = 2$ mm, the apparent particle image diameters profile is nearly uniform between the floor and the free surface. For a puddle of $h_{water} = 8$ mm, the difference is more visible with a difference of approximately 20% in the particle image diameter between the floor and the free surface. However, for particles of size around 2 pixels on the image, this difference corresponds to less than 1 pixel. Therefore, this difference is difficult to see on the images but will be taken into consideration in the CCM.

To conclude, altitude selection with the depth of focus is not possible and particles contribute to the cross correlation within the whole puddle with a slightly different weight depending on their image diameter. This bias can be important if velocity profiles are not uniform with the altitude z^* .

3.1.3 Seeding particles.

As previously indicated, in order to increase the signal to noise ratio, fluorescent particles are used for the measurements. These particles are Lavision PMMA spheres with a density $\rho_p = 1190$ g/m³. Images of these particles have been recorded with a microscope proving their spherical aspect as presented in Fig.3.5.

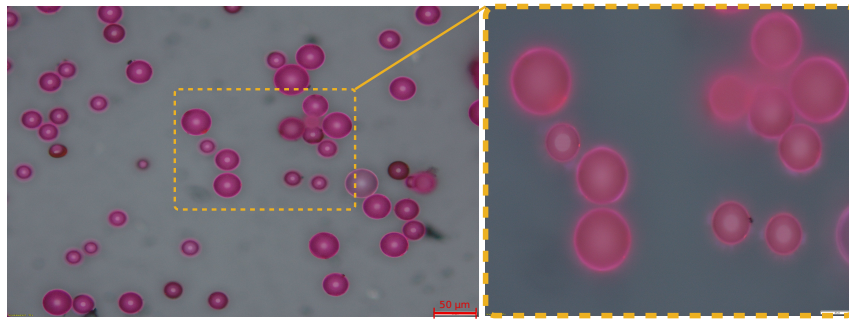


Figure 3.5: Images taken of particles.

The fluorescence is due to included Rhodamine B molecules whose fluorescent wavelength of maximum intensity is $\lambda_p = 584$ nm (according to Kubin and Fletcher 1982 [39]) and with a maximum excitation at $\lambda = 532$ nm. The diameter of the spheres lies in the range $20 - 50$ μm with a normal distribution centered around 35 μm and a standard deviation ~ 5 μm . The probability $P(d_p)$ for a particle to be of diameter d_p is sketched on Fig.3.6.

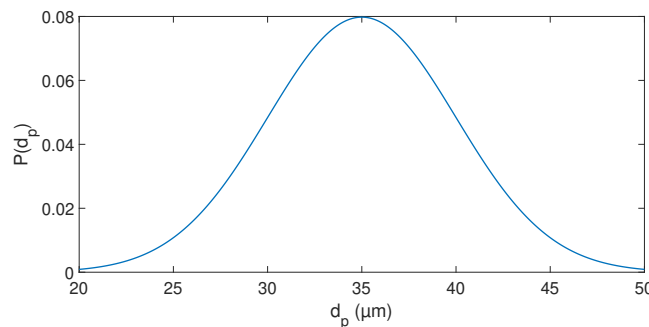


Figure 3.6: Sketch of the shape of the diameter distribution of particles.

The size of the particle images on the sensor are calculated with Eq.2.8. These particle image sizes

are between 1 and 2 pixels for the best focused particles. Therefore the particle image areas are between 1 up to 4 pixels maximum. Thus the particles can not be chosen with lower diameter in order to obtain enough resolution to describe the image of the individual particles on the sensor.

3.1.4 Emission Optic.

The laser sheet is generated with the same double pulsed laser Nd:Yag as used in Chapter 2. The light sheet is here generated with an optical device composed of a spherical divergent lens that enlarges the laser beam and a spherical convergent lens at an adjustable distance to focus the beam. These elements are followed by a cylindrical divergent lens to spread the laser sheet in one direction. This adjustable distance allows the user to adjust the position of the beam-waist with a fixed optical device. This produces a laser sheet with a thicker beam-waist than the device used Chapter 2. However, this allows an higher degree of freedom which makes it more adaptable to the measurement on the pit. The light sheet optical set is placed on a rotation stage to finely tune the incident angle of the laser sheet impinging the prism inlet face. The precision of this angle is approximately equal to 0.1° .

In order to quantify the intensity profile in the water puddle, a combination of measurements, as used Section 2.3.1.1, and ray tracing simulations, as described Section 2.3.1.2, are used. The configuration for those measurements and simulations is described Fig.3.7.

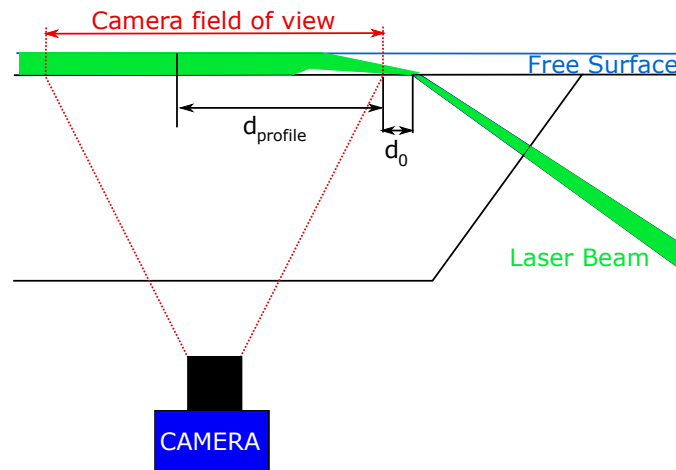


Figure 3.7: Scheme of the configuration for intensity profiles determination.

On this scheme, the chosen intensity profile location is defined via $d_{profile}$ relatively to the camera field of view (red) and is the distance between the image boundary and the profile location. We can see on this figure that the light sheet emerges at d_0 from the right edge of the camera field of view. At the impingement point of the laser sheet at the PMMA/water interface, a part of the laser sheet is reflected inside PMMA. This load of reflected light could generate an high intensity spot on the camera image. Therefore d_0 should be at least 60 mm in order to avoid this high intensity zone on the image.

In a first step, simulations are performed with the ray tracing model to obtain the intensity profile at 3 different locations in the puddle. These profiles are chosen at $d_{profile} = 10, 100, 190$ mm. The other parameters are $d_0 = 60$ mm with a water puddle of $h_{water} = 8$ mm and an incident angle $\beta_1 \simeq 3^\circ$ (see Fig.2.12) which is the minimum angle allowing to ensure 2% of transmission of the total laser beam in the water. The intensity profiles obtained for this simulation are shown Fig.3.8.

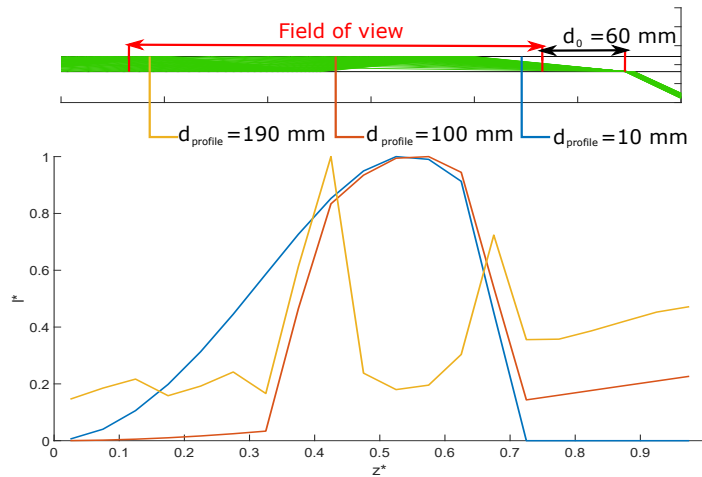


Figure 3.8: Intensity profiles obtained with the ray tracing model in the inhomogeneous configuration (vertical sticks orange, brown and blue show locations of chosen profiles).

A first profile (at $d_{profile} = 10$ mm) shows an asymmetric shape before the impact at the free surface as studied in the Chapter.2. The second profile (at $d_{profile} = 100$ mm) represents a typical profile after one reflection at the free surface and one reflection at the water/PMMA interface. The last profile (at $d_{profile} = 190$ mm), show a mixing of the rays more important with an almost uniform profile except for two peaks which represent nodes with many rays crossing from different incidences. These profiles show a non-homogeneous intensity in the water puddle as seen in Chapter.2. However, the profiles show complex behaviours after few reflections. Therefore, to use this kind of illumination for R-PIV measurements, a 3D mapping of the whole field of view is needed to quantify the intensity in the whole measurement area. This real situation can also be disturbed by the disturbances of the free surface generated by the tire rolling through the puddle.

A second simulation is performed in order to quantify the intensity profiles at the same position in the field of view but further from the light sheet emergence in the water with $d_0 = 400$ mm. An higher incident angle is also used $\beta_1 = 6^\circ$ in order to increase the total intensity transmitted in the water puddle up to 30% to illuminate particles. The intensity profiles obtained for this simulation are shown Fig.3.9.

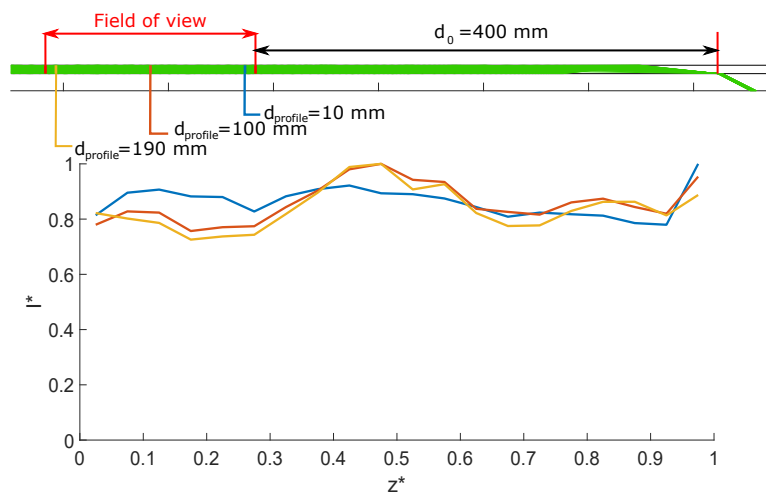


Figure 3.9: Intensity profiles obtained with the ray tracing model in the homogeneous configuration.

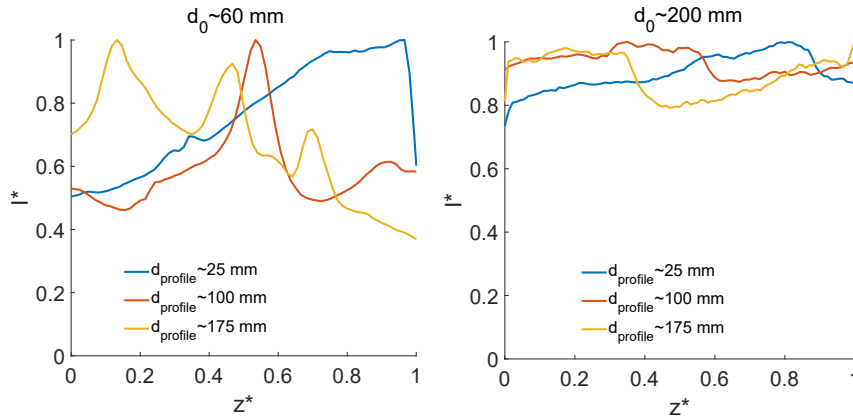


Figure 3.10: Intensity profiles obtained for two different distances, from the emerging laser point, at $d_0 = 60$ and 200 mm.

With these parameters, the intensity profiles appear to be almost uniform in the whole measurement area. This parameter configuration makes easier the characterization of the illumination of the flow.

Considering the importance of the intensity profile knowledge necessary for R-PIV as seen with the CCM model in Chapter.2, the uncertainties and the complexity of the intensity profile in the first case (with $d_0 = 60$ mm) can be a problem for measurement interpretations. Therefore in this study the preferred configuration will be the second one with $d_0 = 400$ mm.

For the second step, in order to check for the distribution of the illumination in the water puddle, intensity profile measurements are performed before PIV measurements in order to validate the configuration. These measurements are done as the ones done and described in Section 2.3.1.1.

Note that for this In-Situ configuration, the car is placed on the window during the recording of images for obtaining the intensity profile measurements. This allows to reproduce in a static manner the elastic deformation (that is a supplementary problem compare to laboratory preliminary tests) of the PMMA window which will be present during PIV measurements under unsteady loading of the window. Measurements of the intensity profiles are made at three different positions in the field of view $d_{profile} \sim 25$ mm, $d_{profile} \sim 100$ mm and $d_{profile} \sim 175$ mm. These values are approximative, due to the complexity to precisely place the inclined plate inside the tire grooves. The emergence of the laser sheet in the water is at two different distances $d_0 \sim 60, 200$ mm from the right edge of the measurement area. Intensity profile measurements along the fluorescent plate at each position $d_{profile}$ for each d_0 are presented Fig.3.10.

These measurements highlight the differences between both configurations (short d_0 and long d_0) as discussed for the first step using for the ray tracing simulations. This highlights the structure of the laser sheet with $d_0 \sim 60$ mm with a complex form and peaks which represent nodes with many ray crossings from different incidences. For long range propagation $d_0 \sim 200$ mm, the profile becomes flatter as a function of height as expected with the ray tracing model. Remember that both measurement zones are, consequently to the presence of car on the window, made in the tire grooves.

For the two long propagations, at $d_{profile} \sim 100$ mm and $d_{profile} \sim 175$ mm, a small step is visible along the intensity profiles at high height. If we consider the tire envelope as a black material with no possible reflection on it, we can consider that the rays hitting the top of the grooves are not reflected which can explain the lower intensity in the upper part of the profiles.

3.1.5 Conclusions.

For the reception optic (as discussed Sec.3.1.2) the difference of focus between the floor and the free surface is low. Therefore, it is complicated (especially for a $h_{water} = 2$ mm puddle) to place the object plane with precision at a specific height. To optimise the precision of the object plane position, the focusing is made on a ruler placed at the window surface. To account for the real In-Situ conditions of PIV measurements, the car is placed on the window during the focusing in order to exert a static load on the window which will reproduce the deformation of the PMMA block during PIV measurements and car rolling. Therefore, for tire measurements, the object plane will be considered at $z_{OP}^* = 0$, except for a specific study in Sec.5.2.

For the emission optic, two types of illumination depending on the propagation distance were discussed in Sec.3.1.4. In the first one, the profile is not homogeneous with high intensity zones in the puddle. This case could be interesting in order to give more weight to a specific height for the measurements. However, due to the sensitivity of the R-PIV technique, this inhomogeneous intensity profile is difficult to precisely tune. Therefore, to know exactly the evolution of the laser sheet intensity profile, measurements should be done at every location x in the field of view. In the second configuration, after many reflections of the laser beam, the intensity profile becomes almost homogeneous in the whole puddle. This gives us a better knowledge of the structure of the illumination in the water puddle for measurement interpretations. This is why, for all the In-Situ trials, measurements are made with the second configuration with a close to homogeneous intensity profile in height.

3.2 Measurement protocol for R-PIV measurements.

All In-situ R-PIV measurements are made during the night, for safety considerations but also in order to avoid background sun light. Fluorescent particles are used in this work in order to record only filtered particle wavelength and to reduce background light due to the laser emitting wavelength. The protocol is the same for every measurements. When the puddle water height is regulated at the expected value h_{water} , particles are mixed in the puddle. Fluorescent particles are not introduced inside the whole closed-loop hydraulic system in order to prevent trapping of a large amount of fluorescent particles inside the hydraulic system and to avoid to seed all the water necessary for the puddle. A last point is to avoid sedimentation between two car rolling events. After mixing particles with water the car starts and rolls on the track at a constant speed in direction of the window. Sensors detect the car, calculate its speed and derive the delay for the tire to reach the area of interest above the window, in the camera field of view. The computer sends a trigger to a timing unit (PTU) system which synchronise the laser pulses and the camera acquisitions, taking into account the intrinsic delay of the PIV system. Time interval dt between both laser pulses is chosen depending on the vehicle rolling speed ($dt = 330 \mu s$ for $V_0 = 30$ km/h, $dt = 225 \mu s$ for $V_0 = 40$ km/h, $dt = 180 \mu s$ for $V_0 = 50$ km/h, $dt = 150 \mu s$ for $V_0 = 60$ km/h, $dt = 130 \mu s$ for $V_0 = 70$ km/h, $dt = 115 \mu s$ for $V_0 = 80$ km/h).

Image acquisitions is possible with a low frequency only (limited by the 15 Hz laser frequency). At this frequency level, only one image pair can be recorded for each run (the vehicle displacement is approximately 0.9 m between two laser repetitions with a vehicle speed at $V_0 = 50$ km/h and the frequency 15 Hz). Therefore cross-correlation is made with only one image pair for every measurements. In order to obtain multiple vector fields for different vehicle speed, the whole process is repeated over several

runs.

Cross-correlation is then made with different analysis parameters depending on the flow zone studied. These cross-correlation calculation parameters are presented Section.3.4. It is first necessary to present the used tire geometries that will induce flow geometry domains and will conditioned the PIV analysis precision in some parts.

3.3 Tire models studied.

In this work, R-PIV measurements are made with two different types of tires with two different wear states. In this section we will describe the tire specific patterns of each tire and the definition of both wear states. For both tires the coordinate system presented (Fig.3.11 and Fig.3.12) is defined in a similar manner. The origin is placed at the beginning of the contact patch area in the x direction and at the center of the tire in the y direction. This coordinate system will be used for the rest of the work.

3.3.1 Primacy 4 (PCY 4) (commercial summer tire).

The summer tire is the most extensively used in this PhD. For this tire model, both wear states are studied. This tire pattern is mainly composed of four different types of grooves described Fig.3.11.

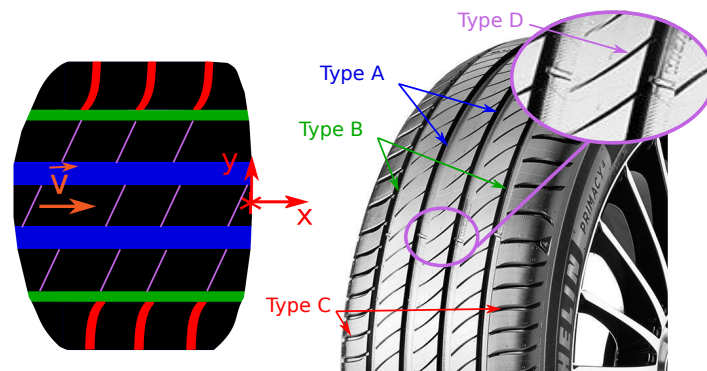


Figure 3.11: Scheme of the tire sculpture pattern for the PCY4.

Two main classes of grooves can be defined. The longitudinal grooves (blue and green) and the transverse grooves (red and purple). The longitudinal grooves are found in two different dimensions. The blue grooves (further called Type A) are approximately 12 mm large with a depth depending on the wear state. The green grooves (further called Type B) are approximately 6 mm large and the red grooves (further called Type C) are of various width around 3 mm. We can also see in the picture, smaller transverse grooves (further called Type D) in the RIBs linking Type A grooves together and linking Type A grooves with Type B grooves. These smaller grooves are not visible in PIV images so PIV can not be performed inside. However, these grooves can have an influence on the flow which will be discussed in Section.4.2.2.

The winter tire (CCP) is tested in this work only in new state only. This tire is composed of only one type of transverse complex grooves sketched Fig.3.12.



Figure 3.12: Scheme of the tire sculpture pattern for the CCP.

Those grooves (further called Type W) are composed of 3 portions with different orientations, the center zone, the mid-zone and the shoulder zone. The cross-section of these grooves varies from one to another. However their width remain around 6 mm.

3.3.2 Wear state.

The wear state of the tire defines the depth of the tire sculpture. At the new state, the depth of the tire grooves are 6 mm. At the worn state, the tire is worn up to the wear indicator of the tire. According to legislations, the height of a wear indicator is 1.6 mm which impose a depth of tire grooves of 1.6 mm at the worn state. The water height h_{water} for R-PIV measurements is adjusted depending on the wear state of the tire studied. In this work, for a new tire, the water height chosen is $h_{water} = 8$ mm and for a worn tire, the water height is regulated at $h_{water} = 1.5$ mm.

Details of the tire structure can be modified with the wear state. In their new states, for the PCY4 tire, the Type C and Type B grooves are geometrically connected. This is not the case for the worn tire for which Type C and Type B grooves are independent. For new state and PCY4, in every RIBS (rubber part between longitudinal grooves), small transverse grooves (Type D) of width 0.5 mm connects the longitudinal grooves (Type A and B and both Type A together). Nevertheless, these grooves are too small to perform PIV measurements. However, their presence influences the flow in longitudinal grooves. These small grooves disappear for worn PCY4 tires.

3.4 Coordinate system and contact patch.

Depending on the control parameters, as the vehicle speed (V_0) and the water height (h_{water}), some geometrical aspects of the flow domain can vary with variation of the dimensions of the contact patch area between the tire and the ground. Therefore, a common criterion should be defined in order to place the origin of the coordinate system independently of the control parameter and the tire configuration.

For both tire types, the origin of the coordinate system is defined as the beginning of the contact patch area in the x direction and at the center of the tire contact patch in the y direction (Fig.3.11 and Fig.3.12). In this section the example of the coordinate system origin determination is performed for a specific case with a water height $h_{water} = 8$ mm with a new tire rolling at $V_0 = 50$ km/h for both tire models.

To determine the location of the coordinate system origin, an analysis based on the gray level of images is made for both tire models. The gray level analysis is also made on a normalised gray level value NGL . This normalisation is made from a gray level in the contact patch area. To define this normalisation value, the user defines a zone in the contact patch area, as sketched in Fig.3.13, where the mean gray level is calculated GL_{cont} . Thus the normalised gray level is calculated as : $NGL = GL/GL_{cont}$.

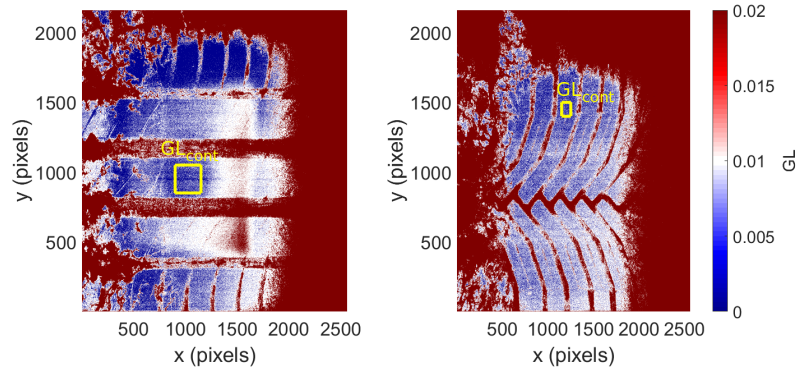


Figure 3.13: Maps of GL with the zone of calculation for GL_{cont} .

3.4.1 PCY4 tire.

This analysis of the tire location in the image is based on the study of the contact patch between the tire and the window. Out of this work, the contact patch area is usually determined by Michelin with the analysis of PLIF images (without particles inside the puddle) done for contrast enhancement as used by Todoroff et al. [72]. From PLIF images, location analysis is based on a specific image treatment. This analysis is well fitted for continuous intensity evolution as for PLIF images. However, for PIV images with discontinuous intensity pattern, this treatment is complex. Therefore, a different contact patch area location determination is finally chosen here.

For the summer tire (PCY4) the center of the contact patch area in the y direction is determined by the center of the central RIB. To quantify its position, an analysis of the spatially averaged gray level in the x direction is studied in a box containing the pair of type A grooves (Fig.3.14).

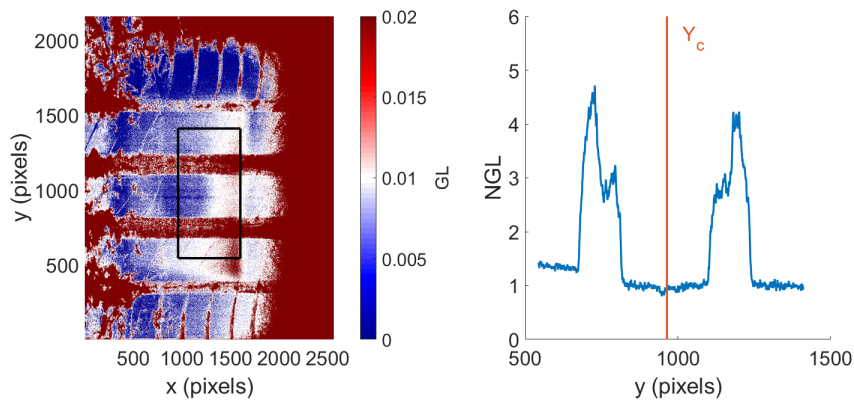


Figure 3.14: On left : Gray level map with the averaging border zone in black. On right : mean Gray level profile in y .

On the Fig.3.14 the location of the two Type A tire grooves can easily be pointed out with an higher gray level in the grooves. On right the center plateau profile with a normalized gray level of approximately $NGL = 1$ represents the central RIB. Thus the location (y_c) of the coordinate system origin in the y direction is defined as the center of this plateau. If we define a threshold at $NGL = 2$, the profile takes this value at four different positions (y_1, y_2, y_3 and y_4) the center of the RIB is then defined as $y_c = \frac{y_2 + y_3}{2}$.

To determine the front edge location x_c of the contact patch area in front of the central RIB, the gray level is spatially averaged in the y direction and over the central RIB width (Fig.3.15).

Form the spatially averaged profile over y , it can be seen that in front of the central RIB, the gray level is growing fast with the loss of the contact between the tire and the road. Thus the beginning of the contact patch area can be determined with a threshold (here set at $NGL = 1.05$). Thus the origin of the coordinate system in (x, y) can be determined with a gray level analysis of the PIV images.

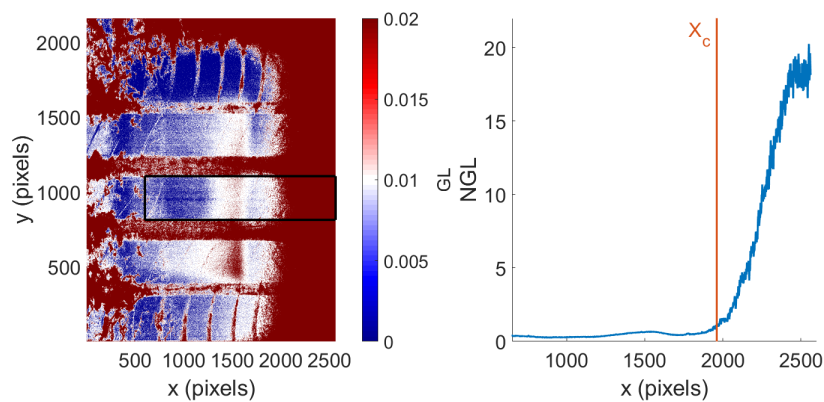


Figure 3.15: On left : Gray level map with the averaging zone in black. On right : spatially averaged Gray level over y profile as a function of x .

3.4.2 CCP tire.

For the winter tire (CCP) the center of the contact patch area in the y direction is determined by the center of the "zigzag" pattern. To quantify its location, an analysis of the averaged gray level in the x direction is made in a box containing the "zigzag" pattern (border of such box are shown on Fig.3.16 in black).

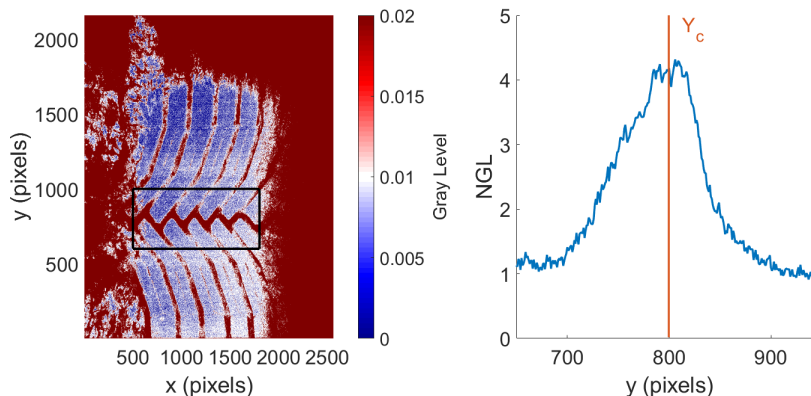


Figure 3.16: On left : Gray level map with the averaging zone in black. On right : mean Gray level profile in y (y mean profile).

For this tire model, the gray level grows near the center of the "zigzag" where a small plateau is visible at a normalized gray level around 4.25. Therefore, the center of the tire (y_c) is determined by the center of this small plateau. If we define a threshold at $NGL = 3.75$ around the peak value, the profile takes this value at two different positions (y_1 and y_2) the center of the RIB is then defined as $y_c = \frac{y_1 + y_2}{2}$.

For the location of the front edge of the contact patch area, the same analysis is made than for the PCY4 tire but the width for the averaging process in the y direction is set to $y \in [y_c - 200; y_c + 200]$ in pixels.

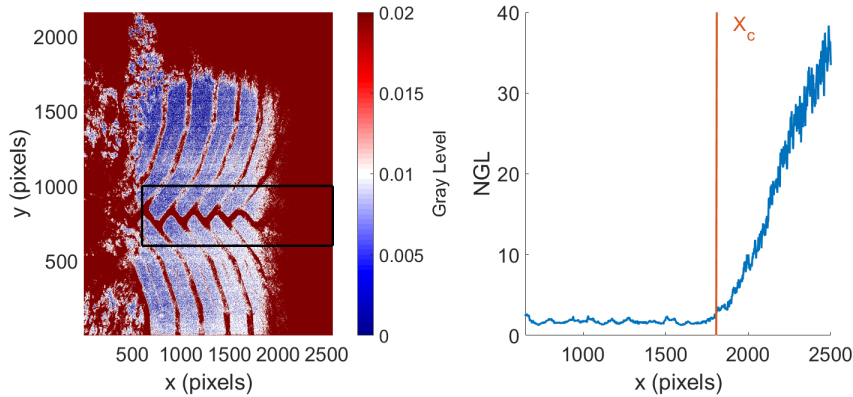


Figure 3.17: On left : Gray level map with the averaging zone in black. On right : Spatially averaged Gray level profile over y as a function of x .

With the same process than for the PCY4 tire, the beginning of the contact patch area (x_c) can thus be determined from a gray level analysis for the CCP tire with a threshold set here to $NGL = 2.5$.

3.5 Flow zones and velocity fields processing.

In this PhD work the analysis of the flow is focussed on different zones in order to quantify the velocity of the water in front of the tire but also inside the tire grooves.

To avoid calculation of vectors in the contact patch area, a masking strategy is used and sketched in Fig.3.18 for both tires.

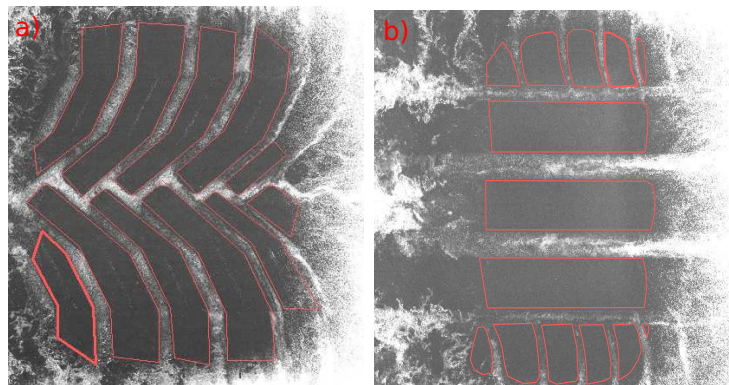


Figure 3.18: R-PIV images of the contact patch area with the mask superimposed in red thin lines.

Before the vector calculations, image processing can be performed as image normalization to deal

with uneven illumination as suggested by [77]. Here, the subtraction of the sliding minimum (as discussed by [23]) which consists in subtracting locally the minimum gray level in order to enhance the signal/noise ratio is used. The effect of this image processing is discussed in Appendix B.

In both parts (in front and inside the grooves) the velocity range is drastically different. Therefore, the displacement of particles in pixels is different and the size of the interrogation windows varies between the zones. We will here discuss the definition of the different zones and the parameters chosen to calculate the cross-correlation in these zones.

3.5.1 In front of the tire.

For quantitative analysis, in front of the tire, two main zones are studied. If we take for the example the PCY4 tire model, the first zone studied is the water-bank. This zone corresponds to the flow in front of the central RIB of the tire where the water is pushed forward. The second zone of interest is the shoulder zone. This corresponds to the amount of water driven off the tire path by the side. Those two zones (violet and brown lines) are sketched Fig.3.19.

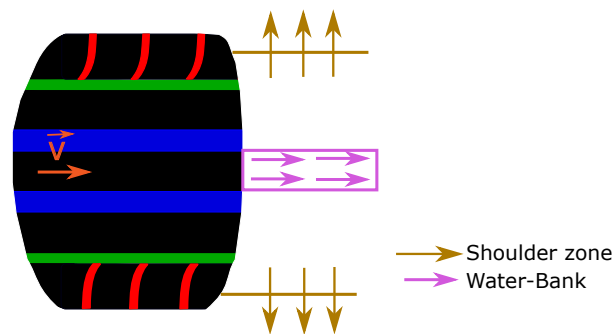


Figure 3.19: Description of the two flow zones (violet and brown lines) in front of the tire.

In these zones, the order of magnitude of the flow velocity is approximately the vehicle speed. The time instant between two pulses is chosen in order, in these areas, to have a displacement of particles between two successive images (from a pair for PIV analysis) of typically 15 pixels. Therefore, the treatment used for the cross-correlation is a calculation with 64pixels x64 pixels interrogation windows for the first step of the iterative process, followed by a 2 calculations with 32 pixels x32 pixels windows to improve the resolution in front of the tire (a 32pixels x32 pixels window correspond to 2.7 mm x2.7 mm).

The two zones defined here are the zones where the quantitative analysis is the most extensive. However, a quantitative analysis of the flow in the whole area in front of the tire will be presented here

3.5.2 Inside tire grooves.

Inside tire grooves, the flow velocity is smaller than vehicle speed. The particle displacement between images inside the grooves is approximately between 5 to 8 pixels if take the same the time separation between pulses than for the front of tire. Therefore, the initial size of the interrogation windows chosen here is 32x32 pixels for the first step and is decreased down to 12x12 pixels (note that 12x12 pixels sampling corresponds to one vector every millimeter inside the 12 mm Type A grooves).

Appendix C presents the results of a parametric analysis with a varying size of interrogation area for both tire models.

3.5.3 Repetition strategy and ensemble averaging.

Since measurements are not time resolved, the analysis of time dependant phenomenon is not possible with the frequency of our apparatus. Further a repetition of single shot measurements is performed without changing control parameters for statistical and convergence considerations. The number of repetitions for each tire configuration and vehicle speed is given in Table3.1.

Case	30 km/h	40 km/h	50 km/h	60 km/h	70 km/h	80 km/h
CCP New	8	8	8	8	8	0
PCY4 New	20	8	16	12	16	2
PCY4 worn	28	28	28	28	28	8

Table 3.1: Number of statistical independent samples.

These samples at every configuration will allow to evaluate and analyse the repeatability of the measurement technique relatively to different zones. In the zones where the structure of the flow is similar for each sample, an ensemble averaging allows us to determine the averaged velocity field. This can also be useful to use the CCM averaging process described Sec.2.4.1.2. Due to the random distribution of particles, the velocity obtained with R-PIV with snapshots can vary from a measurement to an other for the same operating conditions. To study these variations and perform an ensemble averaging, the protocol should be repeated multiple times to obtain a sample of measurements with the same operating conditions.

This repetition strategy also allows us to analyse localised events. In some zones as in Type C grooves or inside longitudinal grooves of worn tire, as discussed Sec.6.1.2.3 and Sec.4.3.2, the phase in the rotation cycle of the tire is presumed to be important for the velocity inside the grooves. Therefore, the repetition strategy allows to perform conditional "phase-locked" measurements in order to quantify the influence of these time dependant parameters as the position of the wear indicator and the location of transversal grooves inside the contact patch area.

4 Sources of Variabilities.

4.1 Influence of control parameters.

In this section precisions of the control parameters as, the water height, the vehicle speed, the tire centring in the measurement area and the masking protocol for images, are discussed in order to quantify the variability sources for the repeatability of the measurement protocol.

4.1.1 The water height.

The water height is a key parameter and set the amount of water which should be drained by the tire. We have seen that in this work two main tire wear state are tested with two different water heights. When measurements are made with a new tire, the water height is set to $h_{water} = 8$ mm. For worn tire configuration, the water height is set to $h_{water} = 1.5$ mm. $h_{water} = 8$ mm is not representative of the real road conditions. However, this water height is important to better understand the draining effect with new tires. For both configurations, the ultrasound probe regulating the water height in the puddle has a high precision (around 0.01 mm) and does not introduce variability in water height measurements. However, in-situ measurements are performed on a track where the wind is present. In such conditions, the free-surface of the puddle is oscillating with waves. These oscillations introduce a variability in water height measurements. For a water puddle of $h_{water} = 1.5$ mm, those oscillations are generally around ± 0.1 mm. In new tire configuration, with $h_{water} = 8$ mm, those oscillations are greater. For high wind conditions, measurements sessions are cancelled in order to ensure a satisfying water height control. With $h_{water} = 8$ mm measurements are allowed for wind conditions that allows to respect $h_{water} = 8 \pm 0.2$ mm.

Therefore, the water height can vary up to $\pm 2.5\%$ for a new tire and 6.6% for a worn tire.

4.1.2 Vehicle speed.

A second possible source of variability for PIV measurements is the car speed. In the protocol, the car rolls over the track at a constant speed in direction of the window as described Sec.3.2. To ensure a constant speed the driver switch on the autonomous car cruise control. This control has a precision around 1 km/h. This was controlled with the track sensors which calculate the vehicle speed along the track for the synchronisation. This variation represents a variation between two successive measurements of $\pm 3.3\%$ for measurements at $V_0 = 30$ km/h and a variation of $\pm 1.5\%$ for measurements at $V_0 = 70$ km/h.

4.1.3 Tire location identification.

As discussed in Sec.3.2, measurements are made by night. The field of view of the camera is around 200 mm wide. Thus for measurements, the driver must target a 200 mm area with the front left tire of the car by night at $V_0 = 30$ up to $V_0 = 70$ km/h. This complex task is achieved by a professional driver but quite understandably a variability of the tire positioning in the images can be seen from one measurement to another. For example images for two successive measurements with a rolling tire at $V_0 = 50$ km/h are presented Fig.4.1.

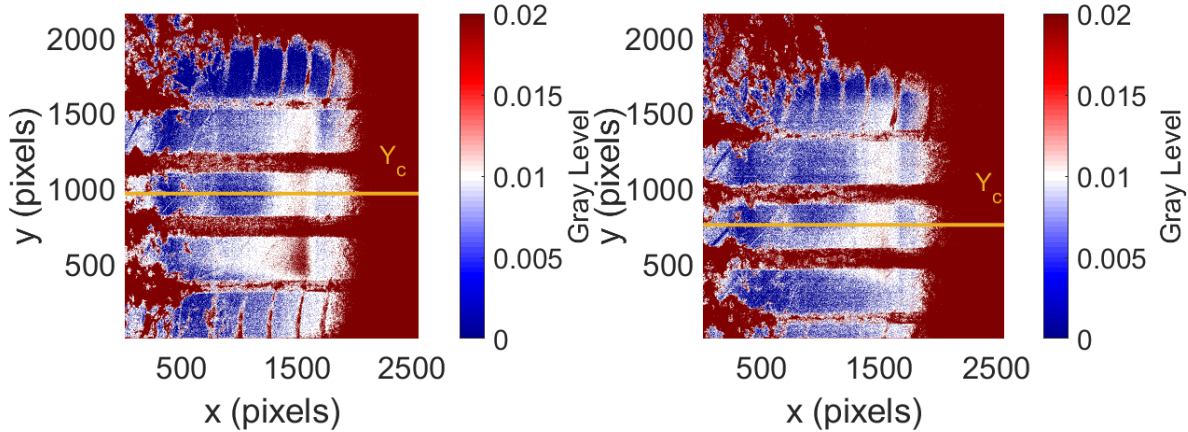


Figure 4.1: Contact patch of the tire for two successive measurements at $V_0 = 50$ km/h.

In Fig.4.1, we can see the determined central axis of the tire (y_c) represented in yellow. The center of the image in the y direction is at $y_{pix} = 1080$ pixels. For the left image the tire axis is at $y_c = 964$ which corresponds to a difference $\delta y_c^{(pixels)} = |y_{pix} - y_c| = 116$ pixels and thus $\delta y_c = 10.7$ mm. For the right image case, the tire axis is located at $y_c = 756$ which corresponds to a difference $\delta y_c^{(pixels)} = |y_{pix} - y_c| = 324$ pixels and thus $\delta y_c = 30$ mm. For the present PIV measurements, images with an offset with the center of the image of more than $\delta y_c = 50$ mm are not kept.

The averaged difference δy_c between the center of the image and the center of the tire is $\delta y_c \sim 20$ mm for the PCY4 tire and $\delta y_c \sim 30$ mm for the CCP tire.

4.1.4 Contact patch position.

As seen in Sec.3.4, the contact patch area location is determined using a gray level analysis. Small scale gray level fluctuations visible in the profile sketched in Fig.4.2 are a source of incertitude in the determination of the contact patch front edge.

We can see here (for a case of a rolling speed $V_0 = 50$ km/h with a new tire) an uncertainty due to gray level fluctuations of approximately $\delta x_c^{(pixels)} = 34$ pixels. This corresponds to $\delta x_c = 3.1$ mm. For an higher vehicle speed of $V_0 = 70 - 80$ km/h this uncertainty can grow up to $\delta x_c = 5$ mm. Thus the coordinate system origin and the placement of the mask can vary up to 5 mm in the x direction from one measurement to another at high vehicle speed.

This contact patch position determination technique based on gray scale presents some variability. However, we chose in this work to use this technique in order to fix our coordinate system to a geometrical point of the tire to analyse the variabilities of the flow in the different zones.

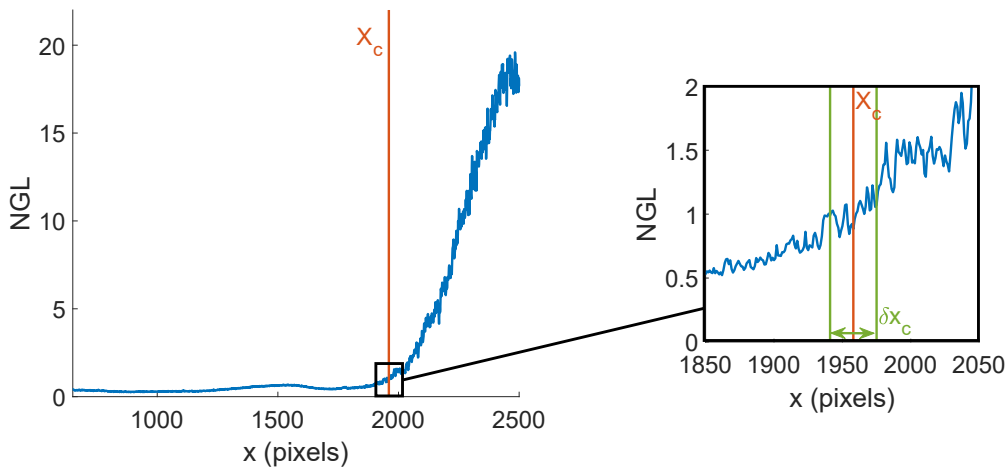


Figure 4.2: Fig.3.15 with a zoom in the contact patch area front edge (x_c) with an uncertainty δx_c .

4.1.5 Mask positioning.

The masking used in order to avoid calculations of vectors in the contact patch area (presented Sec.3.5) can also be a source of variability. Due to the complexity of the structure of our images that have not an high contrast near the side of the tire and also behind, it is difficult to create an algorithm to produce automatically masks. Therefore, the strategy here for a first approach of the problem is to use a user defined masked zones. This strategy introduce a variability due to the precision of the human eye and the appreciation of the user. Therefore, the mask is in this work produced always with the same user in order to keep this human driven parameter the less variable as possible.

The automated masking strategy has been made with different strategies like the one using boundary detection as used by Dussol et al. 2016 [24] or with the analysis of the probability of a pixel to belong of the mask Massulo and Theunissen 2017 [43]. For tire measurements, the automated masking is a complex task which has not been studied here but which can be an interesting challenge for future work.

4.2 Metrological sources of variability.

In this section the differences from one measurement to an other will be discussed in a metrological point of view based on the gray level on images in different zones in front of the tire or inside the tire grooves.

4.2.1 In front of the tire.

In front of the tire, we can take a look at the gray level evolution in front of the central RIB for successive measurements for a set of single shot measurements without changing the control parameters. Here the case of a worn tire with $h_{water} = 1.5$ mm at a vehicle speed of $V_0 = 50$ km/h is considered. The choice of a worn tire is made because, as we will see in Chapter 5, the water-bank is shorter for the worn tire case which makes it more interesting for the gray level analysis with the presence of the full water-bank flow. The spatially averaged gray level profile in front of the central RIB is presented in Fig.4.3 for 8 successive measurement runs.

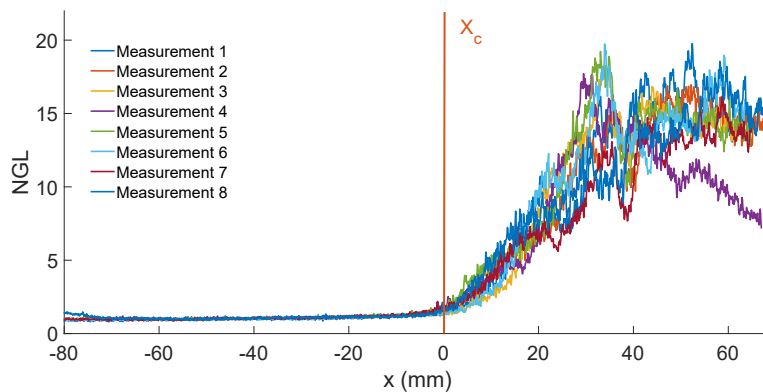


Figure 4.3: Evolution of the gray level in front of the central RIB for 8 measurements with a worn tire at $v = 50$ km/h.

This shows that in front of the contact patch area, the gray level can vary locally of 50% from a measurement to another (especially between $x = 30$ mm and $x = 65$ mm). Therefore, even if the protocol for seeding is the same, the number of particles in front of the tire can vary locally. These variations can be due to a different amount of particles placed in the puddle or to a difference of mixing of particles between measurements. These variations can be a source of differences in the cross-correlation calculation with a different number of particles locally for two successive measurement runs. Therefore, these variations of the number of particles/m³ can introduce variations in the PIV results as highlighted by Wilson and Smith 2013 [80] with an increase of the precision with the increase of the number of particles for P-PIV.

4.2.2 Inside tire grooves.

As seen Sec.1.3, some bubble columns are present inside the tire grooves. Those bubble columns remain straight through the longitudinal grooves at the groove scale as discussed previously. However, disturbances on the bubble columns shape can be observed locally. More precisely, small transverse grooves linking longitudinal Type A and Type B grooves are the source of small jets that can be visible with visualisations as used in Sec.1.3. These jets disturb the trajectory of the bubble columns in longitudinal grooves (Fig.4.4) which influence the optical effect of bubbles inside the grooves.

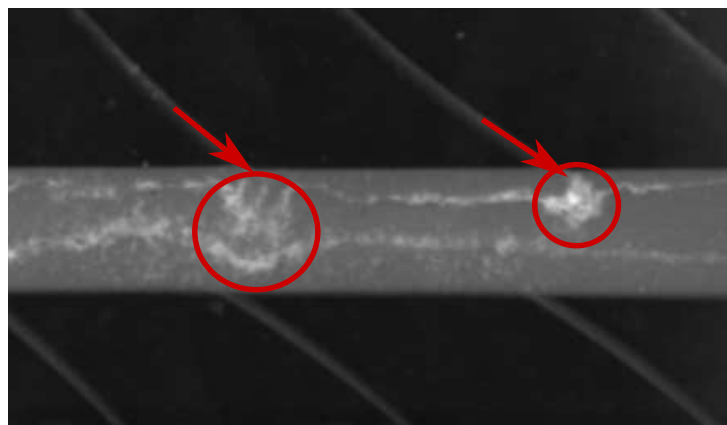


Figure 4.4: Disturbances of the bubble column trajectory with the position of transverse small grooves.

These bubble column disturbances and jet appears in raw PIV images (Fig.4.5). An image processing is used with the enhancement of the contrast and a saturation of the particles image gray level to highlight the bubble columns (Fig.4.5). The gray level of these bubbles are actually lower than the particles gray level. However these bubbles have an effect on the cross correlation function with their optical influence on the images and this effect will not be the same on every image pairs. These small transverse grooves are at different positions in the contact patch area for every measurements. Thus the location of these disturbances of the bubble column structures will be a source of optical variability between measurements.

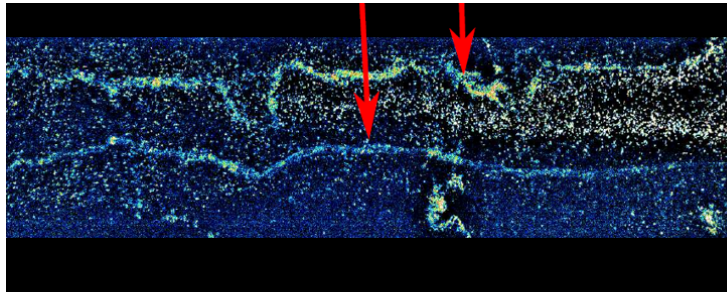


Figure 4.5: Disturbances of the bubble column trajectory in PIV images.

4.3 Hydrodynamic source of variabilities.

In this section the variabilities will be discussed from an hydrodynamic point of view. We will here focus on the parameters that can influence the flow for different measurements in the same operating conditions.

4.3.1 Transverse grooves position.

For transverse grooves as Type C, the deformation of the grooves with the stress on the RIB can influence the shape and the flow inside the tire grooves themselves. This deformation depends on the location of the tire groove in the contact patch area. For PIV measurements, the location of the transverse tire grooves in the contact patch area can not be handled. Therefore, for every cases, these positions are different. The flow through the transverse grooves will depend, for every measurement, on the position of the tire grooves in the contact patch area.

Those transverse tire grooves are separated from longitudinal Type B grooves for the worn tire case. However, for new tire configuration Type B grooves and Type C grooves communicate. Therefore, the flow in Type B grooves may also be influenced by Type C grooves position in the contact patch area.

Finally, the position of this type of grooves will also influence the flow at the shoulder of the tire. The presence or not of a tire groove in the vicinity of the contact patch near the tire shoulder can influence the velocity profile measured. Two configurations are presented Fig.4.6.

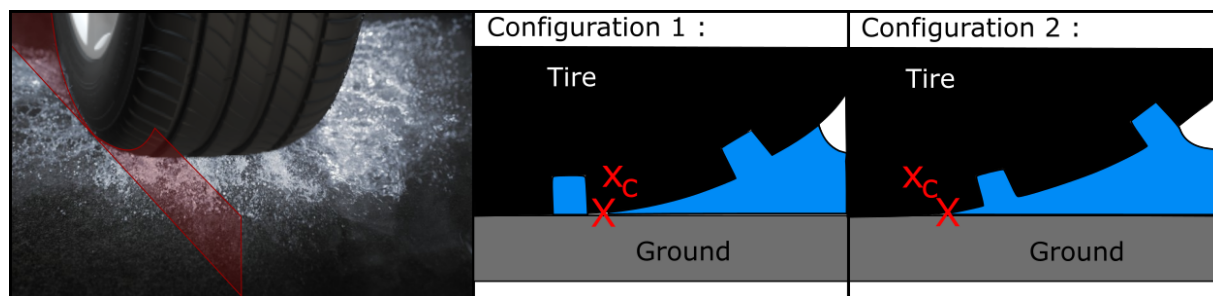


Figure 4.6: Scheme of two different configurations of position of Type C grooves near the shoulder.

The influence of the position of the transverse grooves will be discussed in details in the PIV measurement results analysis Sec.6.1.

4.3.2 Wear indicator position.

For every tire, the legislation places a clear obligation to position wear indicators inside tire grooves to inform the user of the wear state of his tire. Those wear indicators are present all around the tire (at 8 positions) inside Type A and Type B grooves for the PCY4 tire model. These indicators are 1.6 mm height. For a new tire, this represents approximately 25% of the total tire groove height. For worn tire this represents 100% of the tire groove height. Therefore, it seems obvious that these indicators will influence the flow inside the tire grooves.

However, as for the position of Type C grooves in the contact patch area, the period of the rotation cycle of the tire is not handled for measurement. Therefore for two successive measurements with the same operating conditions, a wear indicator can be present or not in the contact patch area (Fig.4.7). This source of flow variability inside the longitudinal tire grooves (Type A and B) for the PCY4 tire is discussed in Sec.6.1.

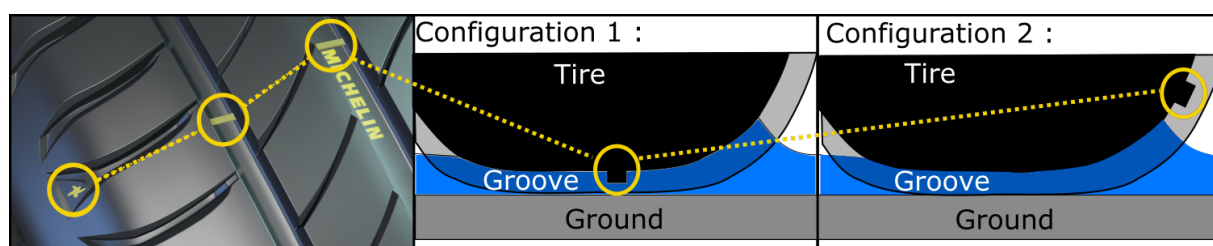


Figure 4.7: Scheme of two different configurations of position of wear indicators in the grooves.

4.3.3 Turbulence.

In this tire flow, different zones were differentiated Sec.3.5. Results for velocity measurements are presented in Chapter6. Based on our knowledge and numerical simulations performed by Hermange 2019 private communication[31], we can in a first approach consider the velocity in the water-bank as approximately 70% of the vehicle speed. If we consider a water height of $h_{water} = 8$ mm and the width of the central RIB of $w_{RIB} = 25$ mm for the width of the water-bank as sketched on Fig.3.19. For a vehicle rolling at $V_0 = 50$ km/h, the corresponding Reynolds number is about Re 30000. In the water-bank, the flow is highly complex and unsteady. Therefore, there is no reason why turbulent flow can be fully es-

ablished in front of the tire. However with this range of Reynolds number, the presence of turbulent structures can be possible.

For tire grooves, the water flow through the grooves is approximately 10% of the vehicle speed in the opposite direction in the ground referential. Thus the Reynolds number value was previously discussed in Section 1.3.3. Thus, for new tire the Reynolds number is approximately $Re = 3000$ which is sufficient to consider the potential presence of turbulence in new tire grooves.

In PIV in general, the integration over the interrogation area induces the necessity to obtain a small interrogation area in order to measure the local temporal fluctuations of the flow. In 2D PIV the integration is mainly in the (x, y) directions and needed to be small facing the turbulence scales as studied by Lavoie et al. 2007 [42] or used by Tanaka and Eaton 2010 [70]. For the field of view targeted in this study, the size of interrogation area in the (x, y) direction is approximately 1x1 mm which is too large to quantitatively measure turbulence. For R-PIV, the integration in z direction is even greater with an integration over the whole groove height. Therefore, quantitative measurements of the turbulence is impossible for our tire R-PIV configurations. However, the mean velocity $\bar{U}(x, y, z)$ in the flow can be measured even if the fluctuations $u'(x, y, z, t)$ can not be quantified according to the Reynolds decomposition $U(x, y, z, t) = \bar{U}(x, y, z) + u'(x, y, z, t)$.

4.4 Conclusions.

Finally, for R-PIV use to tire application, many different sources of variability can be possible. In terms of fluid mechanics, with the repetition strategy described Sec. 3.5, conditional events should be detected as a function of the wear indicator location or as a function of the position of Type C grooves inside the contact patch area.

5 Metrological discussion.

5.1 Metrological sources of bias in front of the tire.

5.1.1 Geometry of the flow in front of the tire.

A high acceleration zone at the forehead of the water bank could be deduced from SPH numerical simulations performed by Hermange 2019 private communication [31] and our measurements described in Chap.6. The fluid being set into movement from rest to approximately 0.75 times the vehicle speed V_0 as the car arrives on the area of interest. This produces a longitudinal spatial gradient as shown on Fig.5.1 for a SPH simulation with a worn PCY4 tire rolling at $V_0 = 70$ km/h.

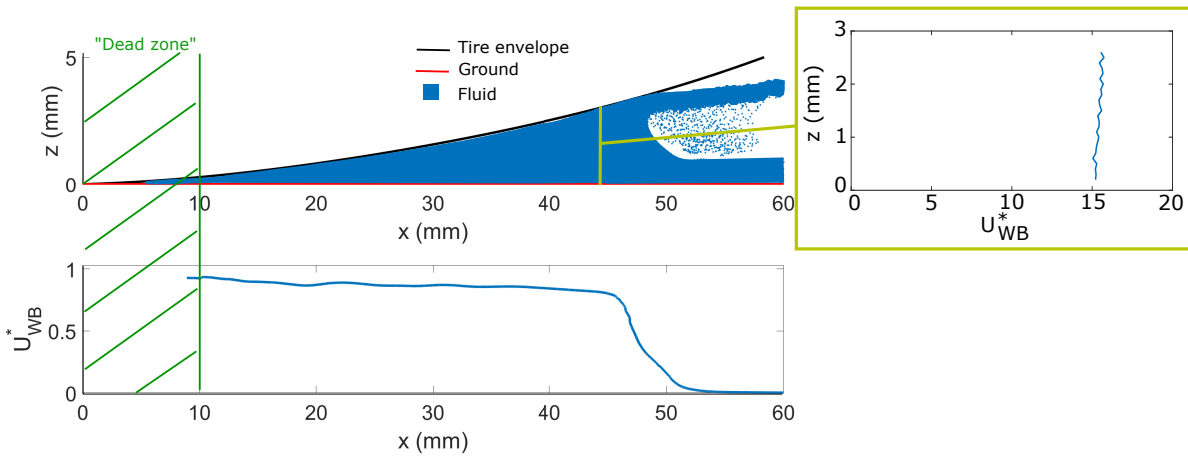


Figure 5.1: Scheme of the tire envelope with the fluid below and the corresponding velocity in the water bank.

The velocity profile $U_{WB}^*(x)$ presented in the bottom figure in Fig.5.1 is calculated by averaging the velocity over the whole water height between the ground and the tire envelope.

As discussed previously, the origin of the coordinate systems corresponds to the beginning of the contact patch area in x direction. Thus the zone between $x = 0$ to $x = 10$ mm in the water-bank will be considered as a "viscodynamic zone" (VZ). In the simulation example, in this VZ, the distance between the tire envelope and the ground is less than 0.2 mm which corresponds to $4.d_p$ for the largest particles used for PIV measurements. Therefore, in this VZ, particles are too large to interpret their velocities. After this zone, the high velocity flow in front of the tire corresponds to a zone where the water is trapped between the tire and the ground (until $x = 50$ mm on Fig.5.1). In the zone after around $x = 55$ mm is

a free surface flow probably complex (with two phase occlusions, waves, etc...), where the velocity is quasi-null $U_{WB}^* \sim 0$. Between these zones occurs an acceleration inducing a higher flow velocity.

5.1.2 Fluorescent Particle motion in the fluid.

In this section we will focus on the displacement properties of particles in the flow. We first analyse the falling properties of particles when the water is at rest (before the arrival of the car in the puddle) in order to quantify a potential sedimentation and determine the particle distribution in the puddle for R-PIV measurements. In a second part, the ability of particles to follow the fluid velocity during the high acceleration phenomenon when the tire arrives on the window is questioned. In order to quantify these two properties, the equation of the motion of a sphere in a moving fluid is used based on second Newton law (according to Maxey and Riley 1983 [44]):

$$\frac{d\vec{U}_p}{dt} = \underbrace{\vec{g}}_{\text{Gravity (G)}} - \underbrace{\frac{\rho_f}{\rho_p} \vec{g}}_{\text{Buoyancy (B)}} + \underbrace{\frac{3}{4} \frac{\mu Re C_D(Re)}{d_p^2 \rho_p} [\vec{U} - \vec{U}_p]}_{\text{Drag (D)}} + \underbrace{\frac{1}{2} \frac{\rho_f}{\rho_p} \left(\frac{D\vec{U}}{Dt} - \frac{d\vec{U}_p}{dt} \right)}_{\text{Added Mass (AM)}} + \underbrace{\frac{\rho_f}{\rho_p} \frac{D\vec{U}}{Dt}}_{\text{Pressure Gradient (Pr)}} + \underbrace{c \frac{\rho_f}{\rho_p} \int_0^t K(t-\tau) \left(\frac{D\vec{U}}{D\tau} - \frac{d\vec{U}_p}{d\tau} \right) d\tau}_{\text{Basset History term (BH)}} \quad (5.1)$$

where $\vec{g} = (0, 0, g)$ is the gravity acceleration vector, $C_D(Re)$ is the drag coefficient, $\vec{U} = (U, V, W)$ is the fluid velocity, $\vec{U}_p = (U_p, V_p, W_p)$ is the particle velocity, $\frac{D}{Dt}$ is the material derivative as $\frac{D\vec{U}}{Dt} = \frac{\partial \vec{U}}{\partial t} + (\vec{U} \cdot \nabla) \vec{U}$, c is a constant coefficient and K is the Basset Kernel which was described by Mei and Adrian 1992 [48] (according to Moreno-Casas and Bombardelli 2016[54]) as $K(t-\tau) = \left[(t-\tau)^{1/(2c_1)} + \left(\sqrt{\frac{\pi}{v}} \frac{|\vec{U}-\vec{U}_p|^3 (t-\tau)^2}{2vf_h} \right)^{1/c_1} \right]^{-c_1}$,

with $f_h = \left[0.75 + c_2 \left(\frac{d_p |\vec{U}-\vec{U}_p|}{v} \right) \right]^3$, $c_1 = 2$ and $c_2 = 0.105$.

In this equation each term represents a physical phenomenon. G and B are basic gravitational force and the opposed Buoyancy exerted on the particle.

The term D represents the drag exerted on the particle by the relative velocity between the fluid and the solid phase. This term is driven by the drag coefficient C_D which is a function of the Reynolds number. This term takes into account both viscous and pressure drags. The first standard formulation valid for low Reynolds numbers (creeping steady flow, $Re < 1$) is the Stokes drag formulation with $C_D = 24/Re$. For higher Reynolds numbers, different formulations have been proposed as summarized by Clift, Grace and Weber 2005[20] page 111 where a table summarize the range of validity of the different drag formulations. Current works still try to go deeper in the Reynolds validity range as the work proposed by Morrisson 2013 [55] where the validity range go from $Re = 0.1$ up to $Re = 10^6$. However, large range formulations are more complex and the chosen formulation in calculations should be limited to the useful Reynolds range in order to simplify the calculation.

The fourth right term AM corresponds to the added mass. As well described by Fackrell 2011 [25], this added mass corresponds to the inertial effect of the mass of the fluid displaced by the presence of the particle. This term has a high influence in the early time where the acceleration of the particle is null and the acceleration of the fluid is not. Odar et al. 1964 [58] described this force as $AM =$

$C_{AM} \cdot \frac{1}{2} \cdot \frac{\rho_f}{\rho_p} \left(\frac{D\vec{U}}{Dt} - \frac{d\vec{U}_p}{dt} \right)$ with C_{AM} a coefficient to be experimentally or numerically determine. $C_{AM} = 1/2$ is considered for creeping, potential flows. As Kim et al. 1998 [35] and Mei et al. 1991 [49] explained, the added mass is the same at finite Reynolds number than in creeping flow and potential flow and the coefficient $C_{AM} = 1$. Mei 1996 [47] highlighted that no correction is needed for the added mass at finite Reynolds number since it is purely inertial and non viscous.

The fifth term represents the pressure gradient effect. It corresponds to the effect of a pressure gradient in the fluid in the particle moving direction. As highlighted by Maxey and Riley 1983 [44], for an incompressible flow, the pressure gradient should satisfy $\frac{DU}{Dt} = -\frac{1}{\rho_f} \frac{\partial p}{\partial x} + g_x + \nu \nabla^2 U$. However, based on Buevich and Yu 1970 [14] change of frame to the coordinate system moving with the particle, Maxey and Riley show that the pressure gradient term can be expressed as $\rho_f \cdot \frac{\pi}{6} d_p^3$.

Analysis of the movement of particles in the water puddle is performed in this section. This movement is separated in two main phases where some terms of the equation 5.1 can be neglected. In the first phase, particles are falling in the steady puddle during the time between the particles mixing and the car arrival to determine the distribution of particles in height for measurements. In a second phase, particles are suddenly accelerated at the forehead of the water-bank and the analysis of the deviation between particles and fluid velocity is made. In both parts the Basset History force is neglected.

5.1.2.1 Falling time before acquisition.

As discussed in chapter 3 in the protocol description, particles are placed in the water puddle approximately 30 seconds before the image acquisition (the time needed by the car to reach the window). Therefore during this time particles can fall in the water puddle. In this problem, the fluid is at rest therefore $\vec{U} = \vec{0}$ and $\frac{D\vec{U}}{Dt} = \vec{0}$. Therefore (Pr) term in Eq.5.1 vanishes. The acceleration of the particle is negligible. Therefore (AM) and (BH) terms are not considered. Finally the falling movement of particles is described by the vertical velocity component W_p . Therefore equation 5.1 becomes :

$$\frac{dW_p}{dt} = \overbrace{\frac{(\rho_f - \rho_p)}{\rho_p} g}^{\Pi_g} - \overbrace{\frac{3 \mu Re C_D(Re)}{4 d_p^2 \rho_p} W_p}^D - \overbrace{\frac{1}{2} \frac{\rho_f}{\rho_p} \frac{dW_p}{dt}}^{AM} \quad (5.2)$$

At low Reynolds number ($Re < 1$), the drag coefficient is considered as $C_D = \frac{24}{Re}$ (Cheng 2009 [17]). The added mass is usually neglected at low Reynolds number (Armenio 2001 [5]). However, in this case, the formulations with and without added mass are considered in order to study the importance of this term.

$$\begin{cases} \frac{dW_{p1}}{dt} + \frac{18\mu}{\rho_p d_p^2} W_{p1} = \Pi_g \Rightarrow \frac{dW_{p1}}{dt} + \frac{1}{\tau_{p1}} W_{p1} = \Pi_{g1} \\ \left(1 + \frac{1}{2} \frac{\rho_f}{\rho_p}\right) \frac{dW_{p2}}{dt} + \frac{18\mu}{\rho_p d_p^2} W_{p2} = \Pi_g \Rightarrow \frac{dW_{p2}}{dt} + \frac{18\mu}{(\rho_p + \frac{1}{2}\rho_f) d_p^2} W_{p2} = \frac{(\rho_f - \rho_p)}{(\rho_p + \frac{1}{2}\rho_f)} \Pi_g \Rightarrow \frac{dW_{p2}}{dt} + \frac{1}{\tau_{p2}} W_{p2} = \Pi_{g2} \end{cases} \quad (5.3)$$

where $\tau_{p1} = \frac{\rho_p d_p^2}{18\mu}$ and $\tau_{p2} = \frac{(\rho_p + \frac{1}{2}\rho_f) d_p^2}{18\mu}$ are the relaxation times for both formulations.

The differential equation without added mass is presented in the formulation 1 of Eq.5.3 and the one with the added mass is presented in the formulation 2 of Eq.5.3. Both differential equations pos-

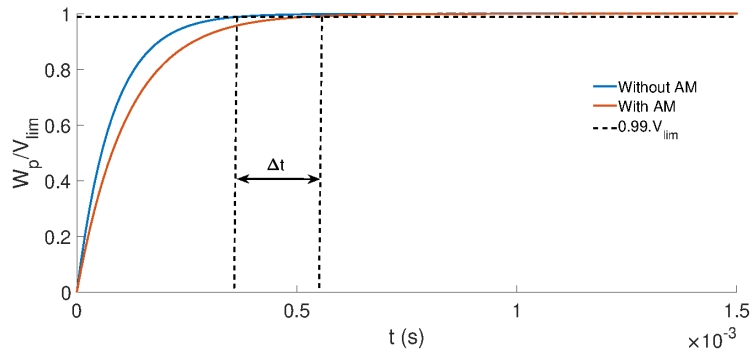


Figure 5.2: Normalized falling velocity of particles of diameter $d_p = 35 \mu\text{m}$ over the time with both formulations.

sess the same form as $\frac{dW_p}{dt} + \frac{1}{\tau_p}W_p = \Pi g$. The solution for both formulations are of the same form $W_p(t) = \Pi g \tau_p (1 - e^{-t/\tau_p}) = V_{lim} (1 - e^{-t/\tau_p})$. Let's note that $\Pi_{g1} \tau_{p1} = \frac{(\rho_f - \rho_p)}{\rho_p} g \frac{\rho_p d_p^2}{18\mu} = \frac{(\rho_f - \rho_p) g d_p^2}{18\mu} = \frac{(\rho_f - \rho_p)}{(\rho_p + \frac{1}{2}\rho_f)} g \frac{(\rho_p + \frac{1}{2}\rho_f) d_p^2}{18\mu} = \Pi_{g2} \tau_{p2} = V_{lim}$. Therefore, for both formulations, the maximum falling velocity V_{lim} is the same. The only difference between an analysis with or without the added mass consideration is the characteristic time (τ_{p1} or τ_{p2}) to reach $V_{lim} = \frac{(\rho_f - \rho_p) g d_p^2}{18\mu}$. Thus the solution for both formulations is :

$$\begin{cases} W_{p1}(t) = V_{lim} (1 - e^{-t/\tau_{p1}}) \\ W_{p2}(t) = V_{lim} (1 - e^{-t/\tau_{p2}}) \end{cases} \quad (5.4)$$

For the most represented particle size according to Section.3.1.3 ($d_p = 35 \mu\text{m}$), $V_{lim} \sim 1.27 \cdot 10^{-4}$ m/s which corresponds to a Reynolds number of $Re = 0.0044$. The relaxation times are $\tau_{p1} = 0.81 \cdot 10^{-4}$ s and $\tau_{p2} = 1.15 \cdot 10^{-4}$ s. Therefore, the hypothesis $Re < 1$ is validated.

As discussed previously, the difference between both formulations is the time needed for a particle to reach the maximum velocity. This is quantified as the difference of time needed to reach $W_p = 0.99 \cdot V_{lim}$ approximately $\Delta t = 0.00007$ s which is negligible compared to the 30 s falling time before R-PIV measurements. Thus the first formulation is considered for the falling velocity of a particle and then the position of a particle can be calculated with the integration of Eq.5.4.

$$\begin{aligned} W_{p1}(t) &= \frac{dz_p}{dt} = V_{lim} (1 - e^{-t/\tau_{p1}}) \\ \Rightarrow \Delta z_p(t) &= z_p(t) - z_p(t=0) = V_{lim} \left(t + \left[\tau_{p1} (e^{-t/\tau_{p1}} - 1) \right] \right) \end{aligned} \quad (5.5)$$

The falling distance of a particle $\Delta z_p(t)$ can be studied over the time and compared to the linear evolution $V_{lim} \cdot t$ if a particle falls at constant speed V_{lim} (Fig.5.3).

The particles at the first instants ($t \leq 0.0005$ s) is accelerated and then moves away from the linear evolution $V_{lim} \cdot t$ due to the inertia of the particle. After this time, the particle reaches the limit velocity V_{lim} and then falls at a constant speed. The curve $\Delta z_p(t)$ is then parallel to $V_{lim} \cdot t$ with a slight offset $z_{offset} \simeq 10$ nm which is negligible. Therefore, particles can be considered as falling at a constant speed

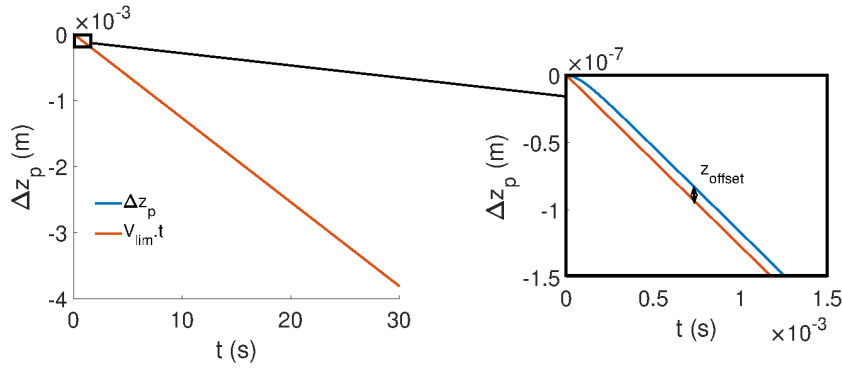


Figure 5.3: Falling distance of a $d_p = 35 \mu\text{m}$ particle over the time (Right is a zoom on the early times).

V_{lim} in the water puddle ($\Delta z_p(t) \simeq v_{lim} \cdot t$).

For a fixed falling time t_{fall} , the final altitude of a particle in the puddle is a function of its diameter d_p and its original position $z_0 = z_p(t = 0)$. The specific falling distance can be calculated as a function of the diameter of the particle $\Delta z_p(d_p, t_{fall}) = \frac{(\rho_f - \rho_p)d_p^2}{18\mu} \cdot t_{fall}$.

If we consider here a homogeneous partition of particles in the puddle of height h_{water} at $t = 0$ ($P_{in}(z) = 1/h_{water}$). All particles of a specific diameter d_p fall of the same distance $\Delta z_p(d_p, t_{fall})$. Therefore, the probability distribution in height of particles of diameter d_p at $t = t_{fall}$:

$$\begin{cases} a) P_{d_p}(z = 0) = \int_0^{\Delta z_p(d_p, t_{fall})} P_{in}(z) dz \\ b) P_{d_p}(z \in]0; h_{water} - \Delta z_p(d_p, t_{fall})]) = P_{in}(z + \Delta z_p(d_p, t_{fall})) \\ c) P_{d_p}(z > h_{water} - \Delta z_p(d_p, t_{fall})) = 0 \end{cases}$$

a) All the particles below Δz_p at the initial instant fall on the floor. b) All particles at the height $z + \Delta z_p(d_p, t_{fall})$ fall of a distance $\Delta z_p(d_p, t_{fall})$ to reach z . c) All the particles over $h_{water} + \Delta z_p(d_p, t_{fall})$ are not replaced by upper particles.

The particle diameter range is $d_p = 20 - 50 \mu\text{m}$ with a normal distribution centered at $d_p = 35 \mu\text{m}$ and a standard deviation $\sigma = 5 \mu\text{m}$ as described in Section.3.1.3. Therefore the probability of presence of particles in altitude will be the mean probability over all the diameter range :

$$P(z) = \frac{1}{d_{p_{max}} - d_{p_{min}}} \int_{d_{p_{min}}}^{d_{p_{max}}} P_{d_p} dd_p \quad (5.6)$$

For a water height $h_{water} = 8 \text{ mm}$, the probability of presence of particles in the height is shown in Fig.5.4.

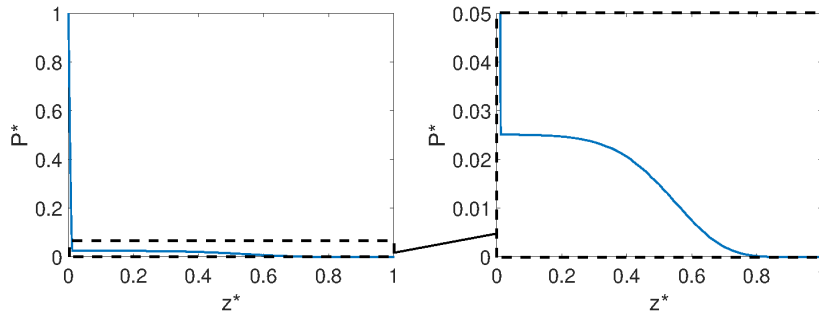


Figure 5.4: Probability of presence in height of particles in the puddle.

Therefore, for a $h_{water} = 8$ mm puddle, particles are not present in the 0.8 higher millimetres of the puddle. Particles are mainly present in the lower part of the puddle. Therefore this information should be taken into account for the interpretation of R-PIV measurements with the CCM.

5.1.2.2 Particle behaviour submitted to highly accelerated flows.

After the falling time, the car arrives on the window and particle images are recorded. Between two successive images, particles move and their displacement are determined using cross-correlation. The particles are considered as moving at the same velocity than the water puddle. The purpose of this section is to check this assumption especially for the highly accelerated flow at the water-bank forehead (Fig.5.1).

In front of the tire, the fluid is considered at rest until the water-bank forehead arrives. This forehead is assumed to be convected with the tire rolling speed V_0 . The thickness of the forehead is noted δ . Based on numerical simulation results (Hermange 2019 private communication [31]) and PIV measurement results presented in Chapter 6, velocities in y and z direction in the water-bank in front of the central RIB are negligible ($V = 0$ and $W = 0$) and the maximum velocity in x direction is considered as $U = \lambda V_0$ with $\lambda \simeq 0.75$ (Fig.5.5).

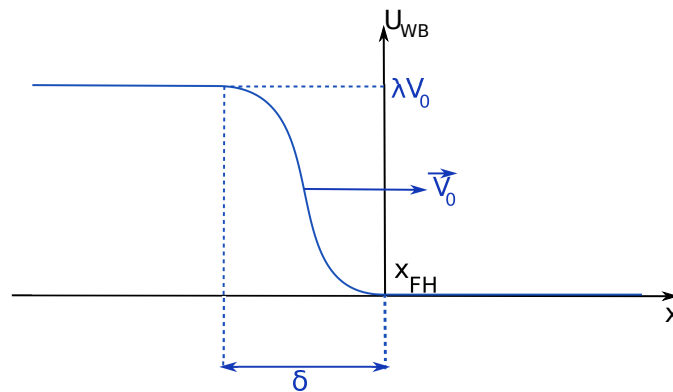


Figure 5.5: Scheme of the convected forehead of the water-bank. With $x_{FH}(t) = V_0.t$ position of the forehead over the time

Thus an analytic formula allows to well approximate the fluid velocity in the forehead and in the water-bank in Eulerian coordinates:

$$\begin{cases} U(x,t) = 0, \text{ for } x - V_0 t > 0 \\ U(x,t) = \frac{\lambda V_0}{2} \left[1 - \cos\left(\frac{\pi(x - V_0 t)}{\delta}\right) \right], \text{ for } -\delta \geq x - V_0 t \geq 0 \\ U(x,t) = \lambda V_0, \text{ for } x - V_0 t < -\delta \end{cases} \quad (5.7)$$

Let's consider normalized variables as $x^* = \frac{x}{\delta}$, $U^* = \frac{U}{V_0}$ and $t^* = \frac{t}{T}$, with $T = \frac{\delta}{V_0}$. Thus, the fluid equation for the forehead (Eq.5.7) becomes :

$$\begin{cases} U^*(x^*, t^*) = 0, \text{ for } x^* - t^* > 0 \\ U^*(x^*, t^*) = \frac{\lambda}{2} [1 - \cos(\pi(x^* - t^*))], \text{ for } -1 \geq x^* - t^* \geq 0 \\ U^*(x^*, t^*) = \lambda, \text{ for } x^* - t^* < -1 \end{cases} \quad (5.8)$$

To calculate the velocity of a solid particle in this accelerated fluid flow Eq.5.1 is used. Here we consider $V = 0$ and $W = 0$. Therefore the equation of the movement of a particle reduces, in its normalized form, to :

$$\frac{dU_p^*}{dt^*} = \overbrace{\frac{3}{4} \frac{\delta}{V_0} \frac{\mu Re C_D(Re)}{d_p^2 \rho_p}}^{D^*} (U^* - U_p^*) + \overbrace{\frac{1}{2} \frac{\rho_f}{\rho_p} \left(\frac{DU^*}{Dt^*} - \frac{dU_p^*}{dt^*} \right)}^{AM^*} + \overbrace{\frac{\rho_f}{\rho_p} \frac{DU^*}{Dt^*}}^{Pr^*} \quad (5.9)$$

With this acceleration, if we consider a fluid at the velocity $U = \lambda V_0$ and a solid particle at rest $U_p = 0$, the maximum possible Reynolds number is $Re_{max} = \frac{|U - U_p| d_p \rho_f}{\mu} = 510$ for a car rolling at $V_0 = 70$ km/h with a particle of diameter $d_p = 35 \mu\text{m}$. Therefore, here $Re_{max} > 1$ and the drag coefficient can not be considered as $C_D = \frac{24}{Re}$ as used in the previous Section. The expression of the drag coefficient chosen here is the formulation of Naumann and Schiller 1935 [56] as $C_D = \frac{24}{Re} (1 + 0.15 Re^{0.687})$ adapted for a Reynolds number under 800 as defined by Clift, Grace and Weber 2005 [20].

With this drag coefficient, the normalized drag (D^*) in equation Eq.5.9 becomes :

$$D^* = \frac{\delta}{V_0} \frac{18\mu}{d_p^2 \rho_p} (U^* - U_p^*) + \frac{\delta}{V_0} \frac{2.7\mu Re^{0.687}}{d_p^2 \rho_p} (U^* - U_p^*) \quad (5.10)$$

If we consider the Reynolds number as $Re = \frac{|U - U_p| d_p \rho_f}{\mu}$ with $U > U_p \Rightarrow |U - U_p| = [U - U_p]$. And considering the characteristic time $T = \frac{\delta}{V_0}$:

$$D^* = \frac{1}{\tau_1^*} (U^* - U_p^*) + \frac{1}{\tau_2^*} (U - U_p^*)^{1.687} \quad (5.11)$$

where $\frac{1}{\tau_1^*} = \frac{T}{\tau_1}$, with $\tau_1 = \frac{d_p^2 \rho_p}{18\mu}$ and $\frac{1}{\tau_2^*} = \frac{T}{\tau_2}$, with $\tau_2 = \frac{d_p^{1.313} \rho_p}{2.7 V_0^{0.687} \mu^{0.313} \rho_f^{0.687}}$.

If we inject Eq.5.11 in the equation Eq.5.9, the equation of the movement for a particle becomes :

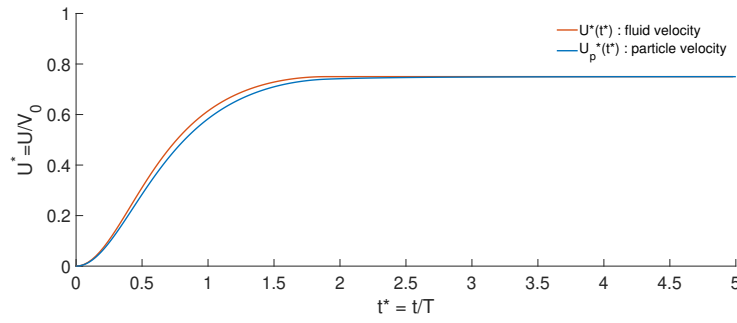


Figure 5.6: Evolution of the velocity of the fluid at $x^*(t^*)$ compared to the velocity of the solid particle.

$$\begin{aligned}
 \frac{dU_p^*}{dt^*} &= \frac{1}{\tau_1^*}(U^* - U_p^*) + \frac{1}{\tau_2^*}(U^* - U_p^*)^{1.687} + \frac{1}{2} \frac{\rho_f}{\rho_p} \left(\frac{DU^*}{Dt^*} - \frac{dU_p^*}{dt^*} \right) + \frac{\rho_f}{\rho_p} \frac{DU^*}{Dt^*} \\
 \Rightarrow \frac{dU_p^*}{dt^*} &= \frac{\rho^*}{\tau_1^*}(U^* - U_p^*) + \frac{\rho^*}{\tau_2^*}(U^* - U_p^*)^{1.687} + \frac{3}{2} \rho^* \frac{\rho_f}{\rho_p} \frac{DU^*}{Dt^*}
 \end{aligned} \quad (5.12)$$

where $\rho^* = \frac{\rho_p}{\rho_p + \frac{1}{2}\rho_f}$.

Considering the particle position $X_p^*(t^*)$ over the time. The equations system to solve is :

$$\begin{cases} \frac{dX_p^*}{dt^*} = U_p^* \\ \frac{dU_p^*}{dt^*} = \frac{\rho^*}{\tau_1^*}(U^* - U_p^*) + \frac{\rho^*}{\tau_2^*}(U^* - U_p^*)^{1.687} + \frac{3}{2} \rho^* \frac{\rho_f}{\rho_p} \frac{DU^*}{Dt^*} \end{cases}, \text{ with } \begin{cases} X_p^*(0) = 0 \\ U_p^*(0) = 0 \end{cases} \quad (5.13)$$

This system equations Eq.5.13 is solved using a Runge-Kutta scheme of fourth order in time and allows to determine the location and the velocity of a particle at every time step $\Delta t^* = \frac{\Delta t}{T} = 10^{-6}$. For the thickness of the WB forehead about $\delta = 0.004$ m and determined as shown on figure 5.5 from real curve (shown on figure 5.1) for a car rolling at the speed $V_0 = 70$ km/h, $T = 2.10^{-4}$ s, we have $\Delta t = 2.10^{-10}$ s. The evolution of the velocity of a fluid particle and a solid particle are presented on Fig.5.6 for a particle diameter $d_p = 35 \mu\text{m}$ (mean particle diameter as presented in Chapter3.1).

This shows the effect of the inertia of the particle. During the acceleration phase of the flow, the particle takes a small delay. When the particle reaches the maximum water velocity zone (where $U^* = \lambda$), the particle velocity catches up with the fluid velocity in the water-bank. To visualise the position of the particle in the acceleration phase, the relative position of the particle compared to x_{FH}^* over the time is represented in Fig.5.7 for $d_p = 35 \mu\text{m}$.

In this figure we can see that the particle remains in the acceleration phase (in the forehead) of the water-bank until $t^* 1.8$. Then the particle reaches the part of the flow where $U^* = \lambda$ is constant. Thus the velocity of the particle and its relative velocity compared to the fluid velocity can be represented function of the relative position of the particle in the forehead (Fig.5.8) for $d_p = 35 \mu\text{m}$.

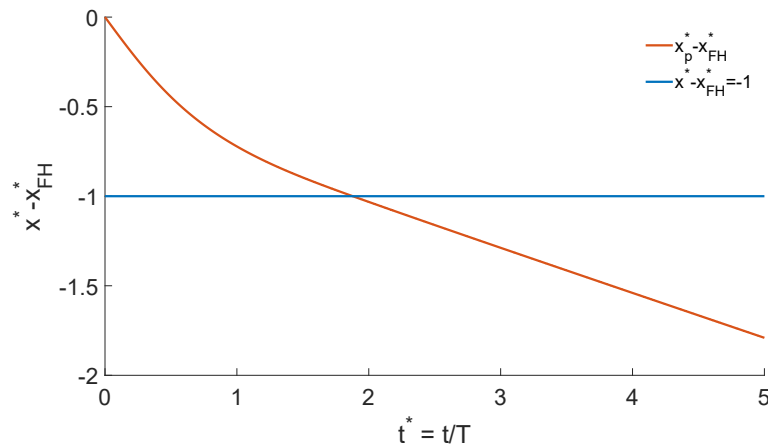


Figure 5.7: Evolution of the relative position of a solid particle compared to the water bank forehead position.

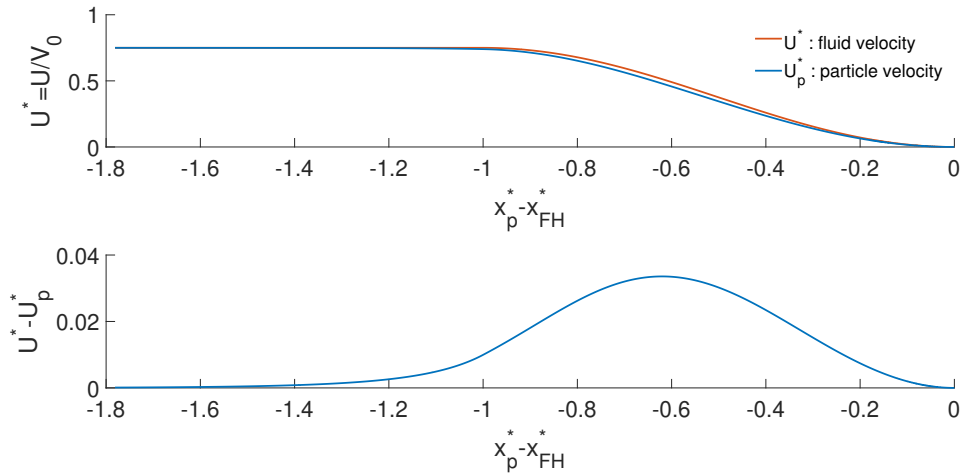


Figure 5.8: Top figure is the fluid velocity and the particle velocity at $x = X_p^*(t^*)$. Bottom figure corresponds to the relative velocity $U^* - U_p^*$. Both depend on the relative position of the particle compared to the forehead position.

This illustrates the offset between the velocity of a particle compared to the fluid velocity in the high acceleration phase of the fluid. The maximum difference between the particle velocity and the fluid velocity is approximately $U^* - U_p^* = 0.04$ which corresponds to 4% of the car rolling speed V_0 . This difference is not negligible. However, when the particle reaches the top of the velocity front, the velocity of the particle catches up with the velocity of the fluid. Therefore, these particles can introduce a small bias by smoothing the velocity front profile of the water-bank but the velocity of the particles in the water-bank corresponds to the velocity of the fluid.

The same analysis is made for different particle diameters in order to quantify the range available for this type of measurements. Simulations are repeated for particles diameter of $d_p = 10 \mu\text{m}$, $d_p = 20 \mu\text{m}$, $d_p = 50 \mu\text{m}$, $d_p = 100 \mu\text{m}$ and $d_p = 500 \mu\text{m}$. The relative velocities of these particles compared to the fluid velocity are represented on Fig.5.9.

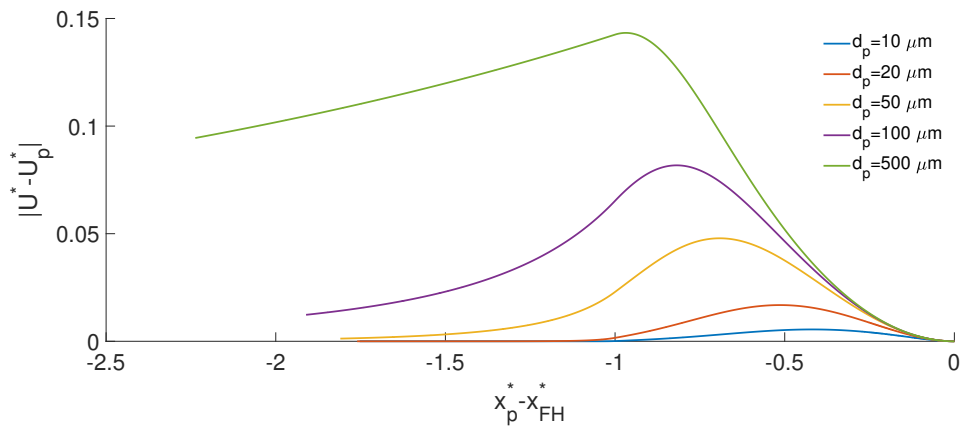


Figure 5.9: Relative velocity $U^* - U_p^*$ depending on the relative position of the particle for different particle diameters.

This shows that with small particles ($d_p = 10 \mu\text{m}$), the difference between the particle velocity and the fluid velocity is under 1% of the vehicle speed which is negligible. Thus, small particles are good tracers of the flow. However, this particle diameter is too small to measure velocity field for a whole rolling tire with particle images too small for PIV. For particles with a diameter $d_p > 100 \mu\text{m}$, the particle velocity never catches up with the fluid velocity in the water-bank and then are not good tracers for the flow.

In conclusion, the chosen particle diameter for PIV measurements ($d_p \in [20; 50] \mu\text{m}$) is the best combination between particle image diameters high enough to perform cross-correlation and low enough to consider fluorescent particles as tracers in the liquid phase.

5.1.3 Boundary Layer presence.

5.1.3.1 Mechanisms of boundary layer creation.

Based on SPH simulation results in Hermange 2017 [30], the velocity profile $U_{WB}^*(z)$ can be considered as flat in a first approach (Fig.5.1). However, the creation of a boundary layer on the floor and on the tire surface can be discussed. The complexity of the case of the tire surface with a rotating tire envelope combined with the fact that particle are not present in the upper part of the flow (near the tire envelope), leads us to focus our analysis on the boundary layer present on the floor (Fig.5.10)).

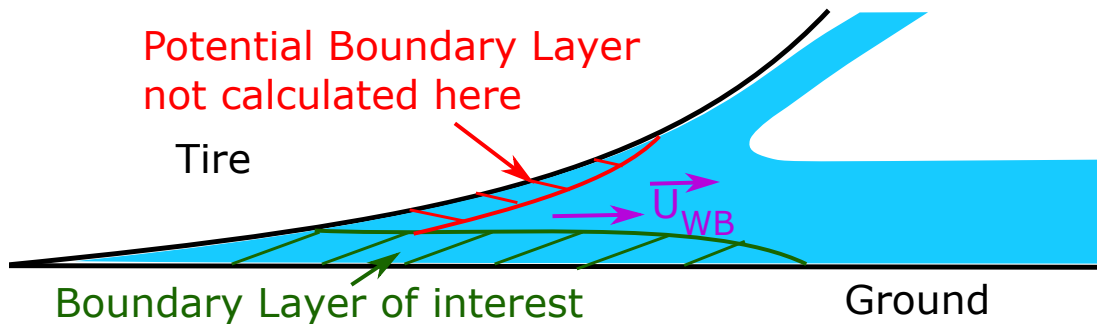


Figure 5.10: Scheme of the boundary layer of interest.

In this case, the flow in front of the tire can be decomposed in two different zones. The first one is the

unsteady zone where the flow is accelerated in front of the tire. The second one is considered as a steady flow developing over a flat plate.

To begin, let us consider firstly the case of a First Stokes Problem with a flow at a wall suddenly set into motion as presented by Schlichting and Gersten 2016 [65]. These problem was firstly studied by Stokes 1856 [67]. In our case, the fluid is set into movement and the ground does not move. The main hypothesis made here is the consideration that the flow is uniformly set into movement in x direction. Therefore, the velocity gradient in x direction is not taken into account which is not the case in the forehead of the water-bank. However, this analysis with $\frac{\partial U}{\partial x} = 0$ is a quantitative first approach of the boundary layer creation in the forehead. For a two dimensional flow in the plane (x, z) in front of the central RIB and with the hypothesis $\frac{\partial W}{\partial x} = 0$ and $W = 0$, which is coherent with the tire flow. The pressure is here considered as constant in the whole space. Thus Navier-Stokes equation in the x direction becomes :

$$\frac{\partial U}{\partial t} = \nu \frac{\partial^2 U}{\partial y^2} \quad (5.14)$$

If we consider here a fluid accelerated over a steady plate, the boundary conditions are :

$$\begin{aligned} t &= 0 : \forall z : U = 0 \\ t &> 0 : \begin{cases} z = 0 : U = 0 \\ z \rightarrow \infty : U = U_{\infty} \end{cases} \end{aligned} \quad (5.15)$$

From the Π theorem, the dimensionless similarity variable can be introduced as $\eta = \frac{z}{2\sqrt{\nu t}}$. Thus, with $U/U_{\infty} = f(\eta)$ the differential equation becomes :

$$f'' + 2\eta f' = 0 \quad (5.16)$$

with the boundary conditions $f(0) = 0$ and $f(\infty) = 1$.

The solution is then :

$$\frac{U}{U_{\infty}} = \frac{2}{\sqrt{\pi}} \int_0^{\eta} e^{-\mu^2} d\mu = erf(\eta) \quad (5.17)$$

Let us now consider an unsteady acceleration of the flow above the boundary layer as described in Equation.5.7 with $U_{\infty}(t) = \frac{\lambda V_0}{2} [1 - \cos(\pi t/T)]$, with $T = \delta/V_0$. Due to the linearity of the differential equation Eq.5.16, we can consider $U_{\infty}(t)$, as an summation of infinitesimal increments dU_{∞} for which Equation.5.17 is valid. The general structure of the boundary layer can be considered as the integration of the effects of each increment as :

$$\begin{aligned}
 U(z,t) &= \int_{-\infty}^t dU_{\infty} \cdot \text{erf} \left(\frac{z}{2\sqrt{\nu(t-\tau)}} \right) = \int_{-\infty}^t \frac{dU_{\infty}}{d\tau} \cdot \text{erf} \left(\frac{z}{2\sqrt{\nu(t-\tau)}} \right) d\tau \\
 &\rightarrow \frac{U(z,t)}{\lambda V_0} = \frac{\pi}{2T} \int_{-\infty}^t \sin \left(\frac{\pi\tau}{T} \right) \text{erf} \left(\frac{z}{2\sqrt{\nu(t-\tau)}} \right) d\tau
 \end{aligned} \quad (5.18)$$

In this calculation, the velocity gradient in x direction ($\partial U_{\infty}/\partial x$) is neglected. Thus strong approximations are made but this calculation allows us to quantify the order of magnitude of the boundary layer thickness for an accelerated flow. The boundary layer thickness corresponds to altitude where $U(\delta_{BL}(t),t) = 0.99.U_{\infty}$. In Fig.5.11, the boundary layer profile is presented at three different times in the acceleration phase ($t/T = 0.01, 0.5$ and 1). The boundary layer thickness evolution is also presented here.

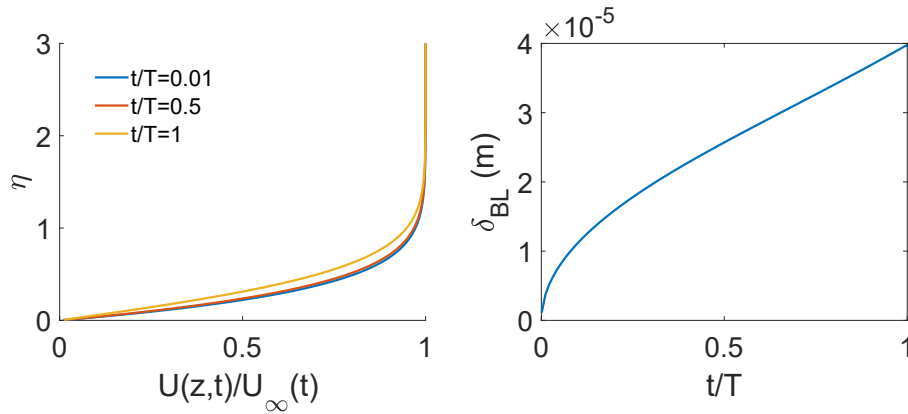


Figure 5.11: Left are the normalized velocity profiles. Right is the growth of δ_{BL} over the time.

The boundary layer at the end of this acceleration is approximately $\delta_{BL} = 0.04$ mm. This thickness is the one right after the acceleration phase. However, when the fluid reaches the water-bank velocity $U_{\infty} = \lambda V_0$, the boundary layer will continue to grow.

In this second phase, the situation is different with a boundary layer developing over a fixed plate (the ground) with a constant velocity $U_{\infty} = \lambda V_0$. If we consider a fluid particle in front of the tire, this particle is pushed forward at $U_{\infty} = \lambda V_0$. The tire and the forehead are convected at a fixed velocity V_0 . Therefore, the relative velocity of the fluid particle in the water-bank compared to the vehicle speed is $U_r = \lambda - 1 = -0.25$. For a water-bank length of approximately 30 mm long, the tire catches up the fluid particle after a time $t = 0.0062$ seconds. Thus the fluid particle traveling at a speed $U_{\infty} = \lambda V_0$, is displaced of a distance $dist = 90$ mm (sketched in Fig.5.12).

In this zone, the flow can be considered as developing over a fixed plate with a traveling distance $dist = 90$ mm and a traveling time $t = 0.0062$ seconds ($t/T = 30$). This boundary layer development over a flat plate is well known as Blasius 1908[10] formulation with a boundary layer thickness expression as expressed by White 2006 [78] :

$$\delta_{BL} = 3.5 \sqrt{\frac{2\nu x}{U_{\infty}}} \quad (5.19)$$

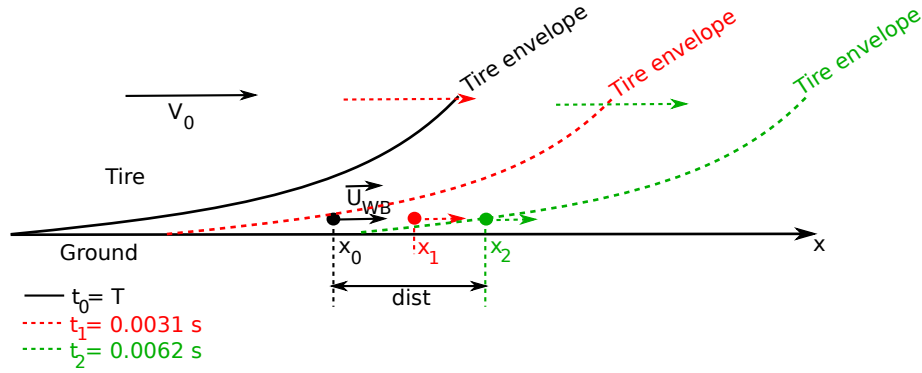


Figure 5.12: Sketch of the tire location and the fluid particle location at three different instants with the distance *dist* of traveling.

The growth of the boundary layer in this zone is represented with the velocity profile Fig.5.13.

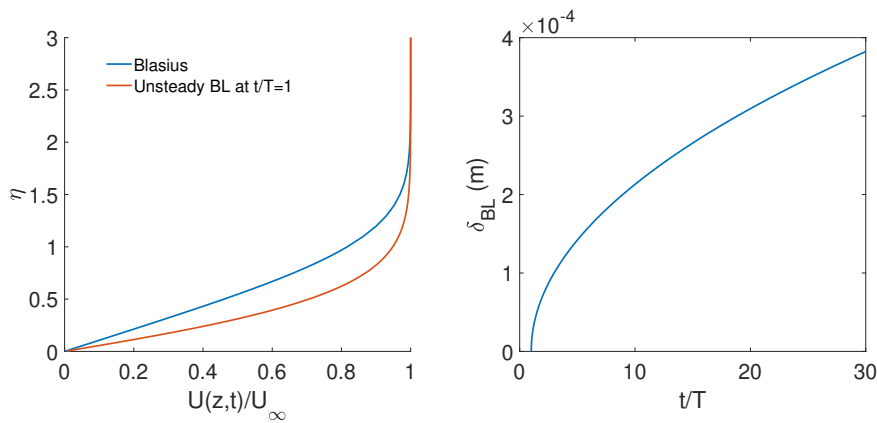


Figure 5.13: Left are the normalized velocity profiles for the blasius solution and the unsteady solution Equation.5.18. Right is the growth of δ_{BL} over the time.

This shows that the growth of the boundary layer during the passage of the water-bank leads to a boundary layer up to $\delta_{BL} = 0.4$ mm. This also highlight the difference between the Blasius profile and the velocity profile obtained for the first part in the accelerated zone. This difference makes it difficult to transition from the first zone to the second zone. This difference is sketched in Fig.5.14.

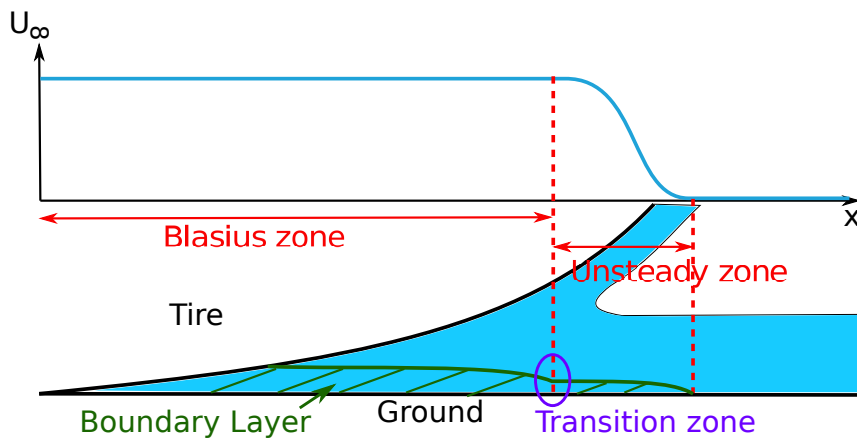


Figure 5.14: Scheme of the transition zone where the two boundary layer shape should be joined.

With this transition zone, the continuity between the two zones can not be ensured. This first approach calculation does not gives us the precise structure of the boundary layer due to the approximations made in the accelerated phase of the flow with the velocity gradient neglected and due to the transition between the two zones. However, the first calculations made in this section allows us to quantify the order of magnitude of the boundary layer in the case of the tire which can be considered in the range $\delta_{BL} \in [10^{-1}; 1]$ mm in the water bank.

5.1.3.2 Boundary layer and cross-correlation model.

In this section, we use the CCM developed in Chapter.2 in order to quantify the effect of a boundary layer on the R-PIV results. Let's assume here the presence of a boundary layer of thickness δ_{BL} on the ground. The boundary layer velocity profile is here considered of the same form than the one in the water-bank with a Blasius equation form.

With this assumption, the CCM Eq.2.15 described in Section.2.4 can be used in order to quantify the effect of a boundary layer on the R-PIV measurements in the water-bank. To run the model, the probability of particles presence in the altitude is considered as Fig.5.4 after the falling time of the particles. As discussed in Sec.3.1, the intensity profile ($I^*(z^*)$) is considered as homogeneous and the object plane is placed on the floor. The optical parameters are then chosen to reproduce R-PIV measurement conditions at the pit. The velocity profile is calculated with different boundary layer thickness (Eq.5.19). The inputs parameters in this case are represented Fig.5.15.

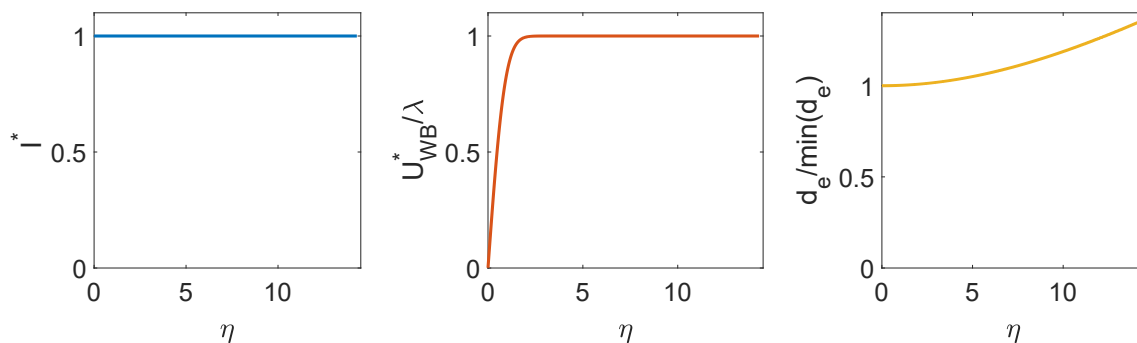


Figure 5.15: Inputs profiles for the CCM in intensity, velocity and particle image diameter.

As described in Section.2.4, the CCM for R-PIV converge to a measured value for N_{im} independent snapshots. To focus on the influence of the boundary layer on measurements and avoid fluctuations, a large number of snapshots are considered ($N_{im} = 10000$). As discussed in Sec.3.5.3, the averaging process used for tire measurement is the averaging of the velocities Eq.2.18. Finally, this CCM model depends on the number of particles in an interrogation window. Thus the simulation is repeated for 3 different number of particle images in the interrogation window : $N = 5$, $N = 20$ and $N = 30$. The evolution of the CCM velocity prevision for R-PIV function of the boundary layer thickness δ_{BL} is presented in Fig.5.16.

This shows the strong influence of the boundary layer thickness on the measured velocity predicted by the CCM. This also shows that the influence of the boundary layer grows when the number of particles per interrogation window grows. Therefore, it is important to well quantify the number of particles per interrogation window to use the model for the boundary layer thickness quantification. With the growth of the boundary layer thickness, the averaged velocity given by the model decrease and the standard

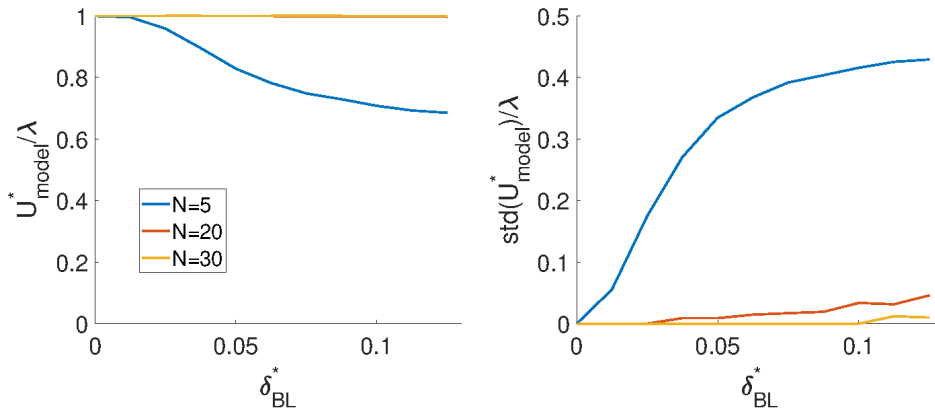


Figure 5.16: Velocity obtained depending on the boundary layer thickness $\delta_{BL}^* = \frac{\delta_{BL}}{h_{water}}$ and the standard deviation for the $N_{im} = 10000$ snapshots averaged.

deviation grows. Therefore, for a sample of $N_{im} = 10000$ snapshots, a combination of the averaged velocity and the standard deviation can locally give an information on the boundary layer thickness in the flow.

However, for tire measurements, the number of sample available is lower. Therefore, the same analysis is made here with different number of snapshots to study the behaviour for $N_{im} = 50$, $N_{im} = 100$ and $N_{im} = 1000$ snapshots. The number of particle images per interrogation window is here fixed at $N = 20$ which approximately corresponds to the number of particles in interrogation windows of 32×32 pixels in PIV images. The evolution of the averaged model given velocity U_{model}^* and the standard deviation are represented Fig.5.17.

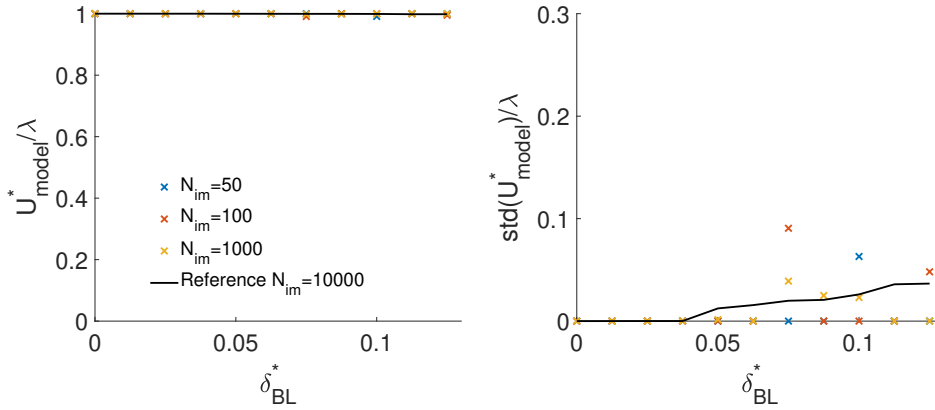


Figure 5.17: Velocity predicted by the model as a function of the boundary layer thickness $\delta_{BL}^* = \frac{\delta_{BL}}{h_{water}}$ and the standard deviation.

The averaged velocity and the standard deviation converge to the evolution for $N_{im} = 10000$ with a growing number of snapshot considered. This shows that for smaller samples of image pairs (as $N_{im} = 50$), the behaviour of U_{model}^* and $std(U_{model}^*)$ follows the evolution for $N_{im} = 10000$ with a higher dispersion. However, with $N = 20$ particles per interrogation window, even with a low number of image pairs, the effect of the boundary layer on the R-PIV measurement will be negligible for a boundary layer from 0 up to 0.8 mm for a $h_{water} = 8$ mm puddle.

In conclusion, we can say that this R-PIV technique can allow the determination of a boundary layer thickness with the help of the CCM if the number of samples is large enough and if the boundary layer is thick. However, for tire measurements, the number of snapshot is not sufficient to determine the exact thickness of the boundary layer and its effect can be considered as negligible in this study.

5.2 Metrological sources of bias inside longitudinal grooves.

As discussed in the Sec.1.3, fluorescent visualisations allow to highlight bubble columns inside the tire grooves. The number of bubble columns depends on the wear state of the tire. Yeager 1974 [81] made an hypothesis of a flow in tire grooves with two bubble columns concentrated in straight line by double helical vortices. This section will then be focused on the analysis of the behaviour of the R-PIV technique with the CCM in the case of double rotating vortices with or without bubble columns on their cores. The counter-rotating vortices will be modelled as Taylor-Green like vortices (Brachet 1990 [12]).

In the whole section, the configuration studied is a Type A tire groove of section 6x12 mm as for new PCY4 tire configuration (Here the height of the groove is noted $h_g = 6$ mm and the width of the groove is noted $w_g = 6$). For a vehicle speed $V_0 = 50$ km/h, the contact patch length is approximately $L_{cont} \sim 90$ mm. Therefore, the geometry studied is a 6x12 mm cross-section channel of length L_{cont} with Taylor-Green like double vortices convected in x direction.

$$\begin{cases} U(x,y,z) = A.V_0 \\ V(x,y,z) = B.V_0.\sin(2\pi y/w_g).\cos(\pi z/h_g) \\ W(x,y,z) = -B.V_0.\cos(2\pi y/w_g).\sin(\pi z/h_g) \end{cases} \quad (5.20)$$

A and B are constants.

Bubble columns are assumed to be concentrated in the core of the vortices. To determine the diameter of the bubble columns, we based our analysis on visualisations of the flow Fig.5.18 for a tire rolling at $V_0 = 50$ km/h.

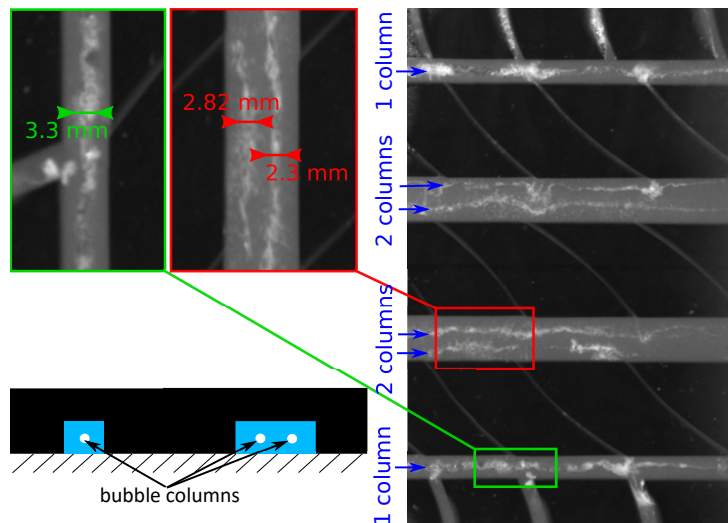


Figure 5.18: Images of bubble columns with their size in the PCY4 tire grooves.

These bubble columns are parametrised with a column diameter d_c as sketched Fig.5.18, but also with a bubble density ρ_b and a bubble diameter d_b as the column can be composed of multiple independent bubbles. Thus the general problem of interest is sketched Fig.5.19. It should be noticed that the velocity field is a model of a pair of counter rotating vortices in the groove, satisfying a no slip condition at the walls, but not the real adherence condition imposed by viscous effects.

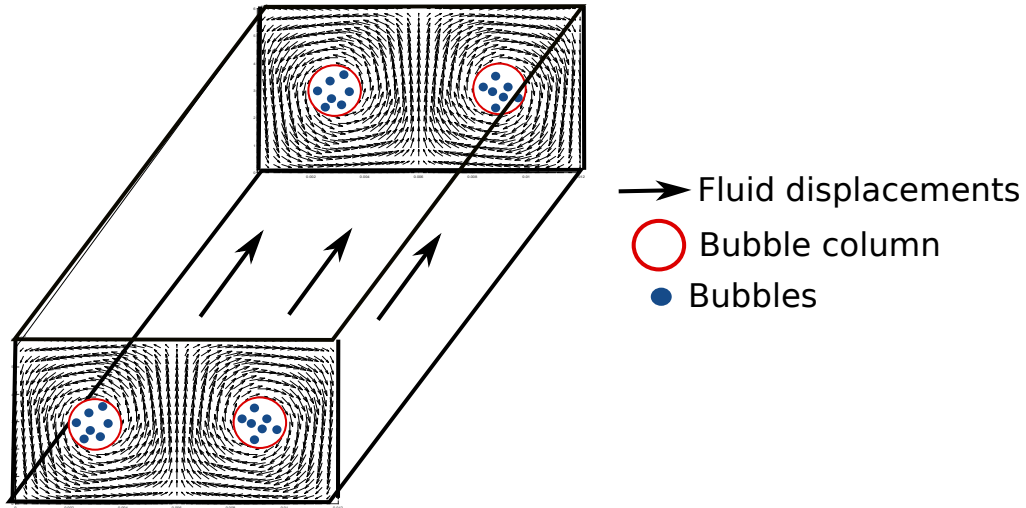


Figure 5.19: Problem considered for the tire groove flow analysis.

Intuitively, the particles behind the bubble column for the camera can be considered as hidden by the bubbles and will not contribute to the cross-correlation for PIV images. However, we will propose here a more rigorous approach in order to determine whether or not the particles will appear on the images.

5.2.1 Optical influence of the bubbles in the model.

We will focus our analysis on the optical effect of bubbles on the image of a fluorescent particle placed above the bubble column. Let's remind that the camera is placed below the prism, below the tire. Therefore, we will study the case where the bubbles are between the camera and the particle of interest in order to estimate the bubbles influence on image formation.

In a first approach, the "shadow" generated by the bubbles could be considered as the physical section of the bubbles ($S_b = \pi d_b^2/4$). A more suitable analysis consists in calculating the scattering cross-section of the bubbles which is an effective section for light/bubbles interactions and can be drastically different from the geometrical section S_b of the bubble. As an example, in the limit of very large bubbles, the scattering cross section is twice the geometric section.

A full resolution of this problem is extremely complicated. It would require a light propagation model, an image formation model and an interaction model between light and bubble of various sizes, shapes and relative positions that are time dependent. Such an approach is far beyond the scope of this work. However, we will try to estimate in average, the influence of bubbles on image formation in terms of extinction/transmission of the light.

In order to quantify the extinction associated to a bubble, a simple configuration is considered here with an isolated single spheric bubble.

The resolution of the problem is made according to Bohren and Huffman 1983 [11] calculations (Chapter 4 : Absorption and scattering by a sphere). To calculate the scattering section of the bubbles we can consider a single spheric bubble in an incident plane wave electromagnetic field (E_i, H_i) . The general electromagnetic field is composed of the incident field, the field scattered by the bubble (E_s, H_s) and the internal field of the bubble (E_1, H_1) (see Fig.5.20).

The calculations made here are according to Mie's theory considering each medium (the water and the bubble) as local, linear, homogeneous and isotropic.

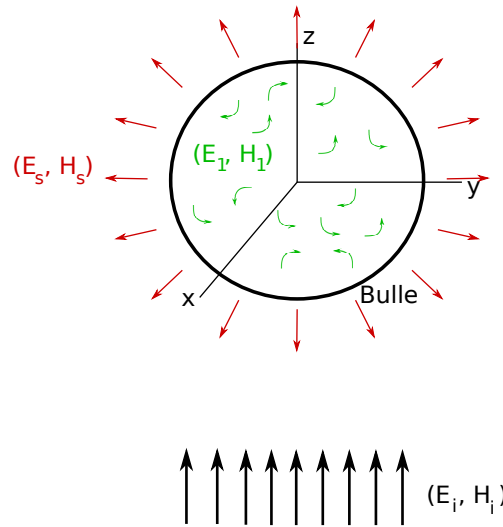


Figure 5.20: Scheme of the components of the electromagnetic field for a bubble.

The cross section is a summation of the scattered and absorbed components : $C_{ext} = C_s + C_a$. C_s is the scattering component (proportion of the incident intensity scattered) and C_a is the absorption component (proportion of the incident intensity attenuated inside the bubble). The attenuation of the light in air is negligible. Therefore, inside the bubble $C_a = 0$ and $C_{ext} = C_s$ for an air bubble inside water.

According to Bohren and Huffman 1983 [11], the scattering component corresponds to the ratio of the incident energy that is scattered by the bubble. To quantify this factor, the Poynting vector of the scattered field is integrated at the surface of a sphere surrounding the bubble in the far field. Following the calculations of Bohren and Huffman 1983 [11] (Chapter 4), the resolution of Maxwell equations allows the calculation of the scattered field (E_s, H_s) equation 4.45 in Bohren and Huffman 1983 [11]. Thus the scattering cross section can be calculated based on the equation 4.61 in the Bohren and Huffman 1983 [11]. A Matlab code has been written in order to calculate a_n, b_n coefficients necessary to calculate the scattered cross-section according to equations 4.56 and 4.57 in the Bohren and Huffman 1983 [11].

Let us assume that the distance between the particle and the bubble is far enough to consider that the light fluoresced by the particle is a plane wave. For a fluoresced light emitted by the particles at $\lambda_p = 586$ nm, the evolution of the scattering cross-section normalised by the physical section of the bubble ($S_b = \pi \left(\frac{d_b}{2}\right)^2$) with d_b the diameter of the bubble can be studied Fig.5.21.

For this wavelength, the cross-section converges to value of approximately $C_{ext}/S_b = 2$. For small bubbles (below 10 μm), the value of the scattering cross-section oscillates between 0 and 2.5 times the geometrical section.

Now with the calculated scattering section of a bubble, two different cases can be studied, the case of single bubble of millimeter range diameter, or the case of a slab of micro bubbles (in the range $d_b \in [1; 100]$ μm).

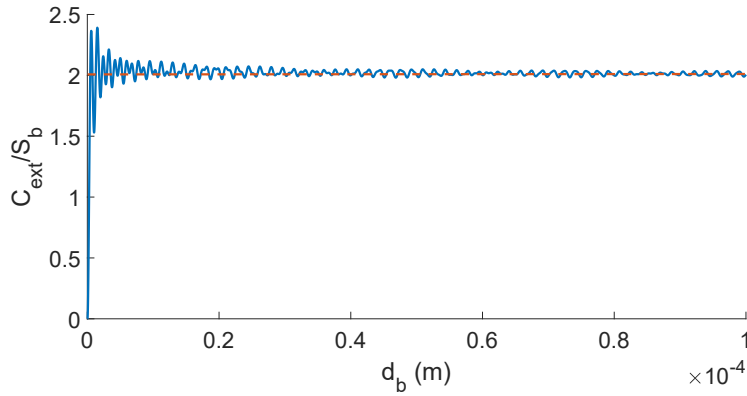


Figure 5.21: Scattering section function of the bubble diameter.

5.2.1.1 Single millimetric bubble.

According to Bohren and Huffman 1983 [11], the power \square incident on a detector without bubble is $\square = \square_i = I_i \cdot A$, where A is the collection surface. If a bubble is placed between the sensor and the light source, when the incident light is a plane-wave and the camera is in the far field, the power collected by the sensor is $\square = \square_i - \square_{ext} = I_i \cdot A - I_i \cdot C_{ext}$. Thus, the power perceived by the sensor is $\square = I_i \cdot (A - C_{ext})$. If $C_{ext} > A$, $\square = 0$. In the present case the problem is sketched Fig.5.22.

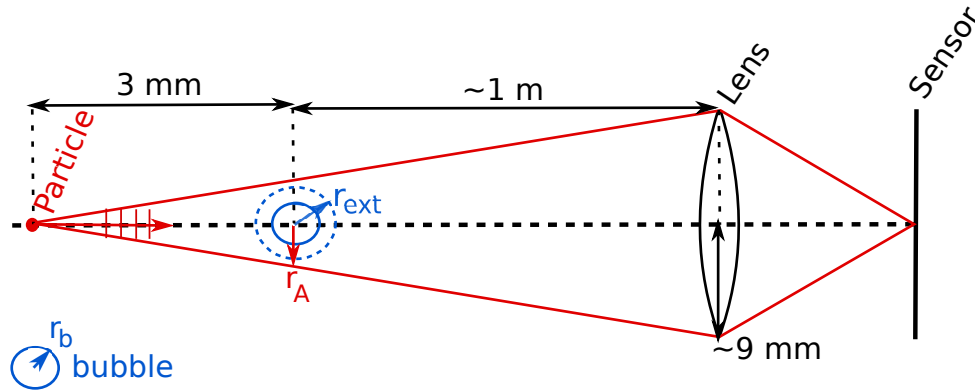


Figure 5.22: Sketch of the problem studied.

As sketched here, r_A is the collection radius at the bubble level as $A = \pi r_A^2$ and r_{ext} is the scattering radius as $C_{ext} = \pi r_{ext}^2$. As shown previously with the study of C_{ext}/S_b , with big diameter bubbles as $d_b = 1$ mm, the scattering section converges to $C_{ext} = 2 \cdot S_b$. With these considerations, $r_{ext} = \sqrt{2} \cdot r_b$ and $U = I_i \cdot \pi (r_A^2 - 2 \cdot r_b^2)$. A critical bubble diameter can be calculated as $r_c = r_a / \sqrt{2}$, which is the minimum bubble diameter which totally hides a particle over it and perfectly aligned. In the experimental conditions, $r_A \sim 0.03$ mm and therefore, $r_c \sim 0.02$ mm. Thus, for bubbles with a diameter of more than $d_b = 0.04$ mm, the image of a particle above them will not appear on the camera sensor and the transmission coefficient is $Tr = 0$.

5.2.1.2 Slab of small bubbles.

In the case of a slab of bubbles, a statistical approach is more suitable. The bubble medium which is composed of a load of bubbles is statistically considered as an homogeneous medium. More rigorously, at an instant t , a particle can have a bubble between itself and the camera or not depending on the medium but statistically it has a probability to be hidden which is taken into consideration with this approach. Multiple scattering (from bubbles to bubbles) effect are negligible. Thus the light scattered by a given bubble is not considered as a secondary source of light for the other bubble. The attenuation of an incident light propagation through the bubble slab is considered as a continuous change of medium, the attenuation of the light through the medium is calculated based on the Beer-Lambert law as $I_t = I_i \cdot e^{-\alpha \cdot L}$, where α is an attenuation coefficient, L the thickness of the medium crossed by the incident light I_i and I_t is the transmitted intensity.

In the case of a bubble column composed of multiple bubbles, the attenuation coefficient of the bubbly medium is calculated as the averaged attenuation generated by single bubbles multiplied by the density of bubbles as $\alpha_{ext} = N_b \cdot \overline{C_{ext}}$, with $\overline{C_{ext}}$ the averaged efficient cross section of bubbles.

Leading to :

$$Tr = \frac{I_t}{I_i} = e^{-N_b \overline{C_{ext}} \cdot L} \quad (5.21)$$

where L is the thickness of the bubble column, N_b is the bubble density (in bubbles/m³).

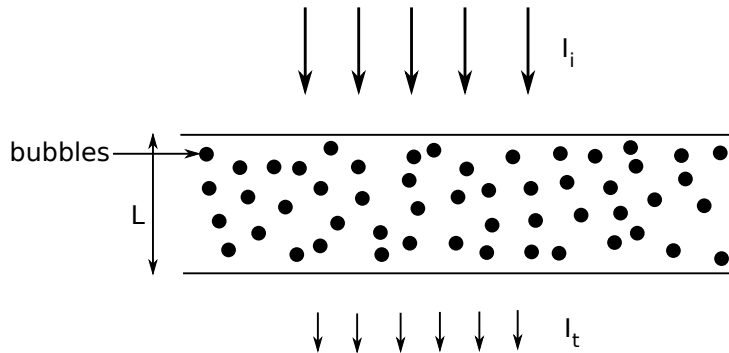


Figure 5.23: Scheme of the bubble column.

If we consider that the bubble diameters (d_b) are randomly distributed following a normal distribution in the column centered around the mean value $d_b^{(c)}$ with a standard deviation σ_b , the probability $P(d_b)$ for a bubble to have a diameter d_b written as $P(d_b) = \frac{1}{\sigma_b \sqrt{2\pi}} e^{-\frac{(d_b - d_b^{(c)})^2}{2\sigma_b^2}}$.

Thus, the averaged extinction coefficient in the bubble column is calculated as :

$$\overline{C_{ext}} = \int_0^{\infty} P(d_b) C_{ext}(d_b) dd_b \quad (5.22)$$

Therefore, the transmission coefficient can be calculated as a function of bubble diameter and bubble density. This transmission also depends on the thickness of the bubble column. In this geometric configuration, a thickness (L) of bubble column crossed by the particle light is determined depending on the position of the particle in the cross-section as sketched on Fig.5.24.

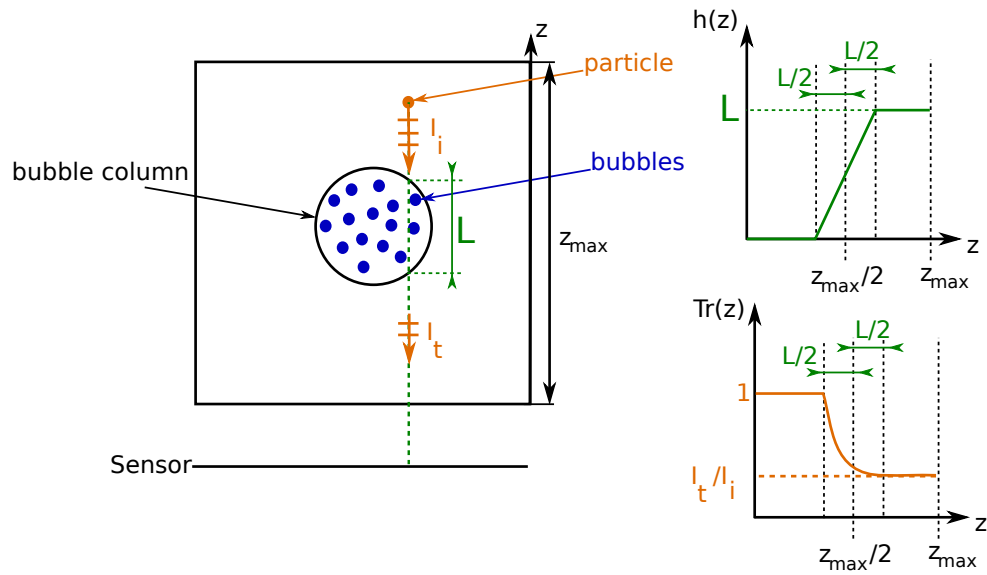
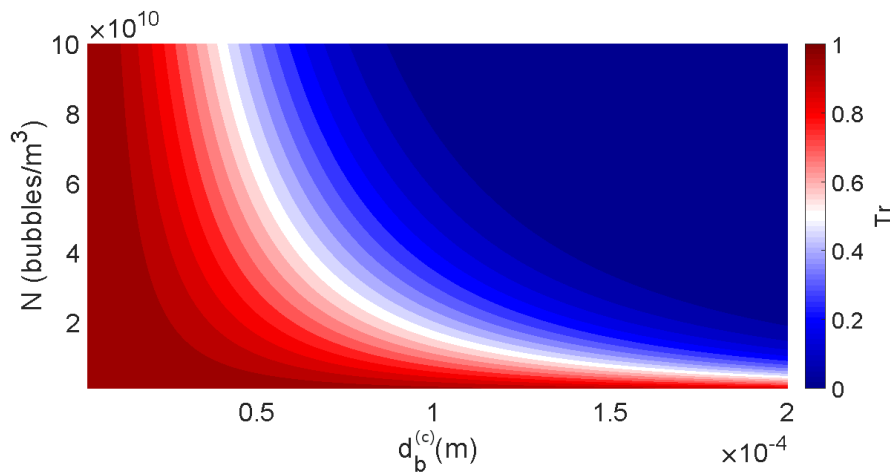


Figure 5.24: Scheme of the bubble column with a particle above.

Depending on the position in (y,z) of the particle in the groove, a certain thickness (L) of bubble column will be present below this particle. If we consider for the example a thickness of bubble column $L = 1.5$ mm between a particle and the camera sensor, the transmission of intensity through the column can be calculated depending on N , $d_b^{(c)}$ and σ_b . The standard deviation considered here is 10% of the mean particle diameter $\sigma_b = 0.1 \cdot d_b^{(c)}$. The calculation of the transmission coefficient Tr is represented in Fig.5.25.


 Figure 5.25: Transmission coefficient map as a function of bubble density and the bubble diameter with a bubble column thickness $L = 1.5$ mm.

This map shows that for bubble diameters over $d_b^{(c)} = 0.1$ mm, the transmission coefficient can be considered as null for more than twenty bubbles per mm^3 .

5.2.1.3 Conclusions

Whether the bubble columns are composed of millimeter bubbles in line or of a slab of smaller bubbles of size $d_b \sim 0.1$ mm, the masking effect of the bubble columns is important. Therefore, in the case of a particle above the bubble column in tire grooves, the light emitted by the particle will not reach the sensor and the particle will not appear on the PIV image.

In previous calculations of Tr , hypothesis are made. This calculation is performed considering an incident plane wave. For the light emitted by a particle, the plane wave consideration can be made in the far field. This far field hypothesis is not truly verified. However, with a spherical wave front, the main difference in the scattered field will be the directivity and not the total amount of scattered energy. If we consider that the Poynting vector is integrated over the whole sphere for C_{ext} calculation, at a first order the value of C_{ext} considering a plane wave is similar as the one with a spherical front wave. A second hypothesis is the neglected influence of the optical interaction of the bubbles. We here consider that the intensity scattered by a bubble impacting an other bubble is neglected. Finally the last hypothesis is based on the fact that the whole scattered light is not transmitted to the camera. To be perfectly rigorous, the collection angle of the camera should be excluded of the integration of the Poynting vector in the calculation of C_{ext} . Due to the large distance between the camera and the bubble (approximately 1 m), the proportion of the total surface of the sphere of radius $r = 1$ m ($S = 4\pi.r^2$) taken by the surface of the lens aperture (S_L) is calculated as $Ratio = \frac{S_L}{S} = 2.10^{-5} = 2.10^{-3}\%$. Therefore, the amount of the total scattered field captured by the camera is negligible.

Finally, the results obtained through this section highlight the fact that the particle image of a particle behind the bubble column will not appear on the camera sensor. Therefore, in the following, the value of the transmission coefficient Tr is a binary value, 0 or 1.

5.2.2 Cross-correlation model analysis in case of counter-rotating vortices.

Knowing the masking effect of bubbles, we can now analyse the influence of these bubble columns hiding effect on the cross-correlation to determine the bias introduced with the specific R-PIV technique. As seen in the previous section, the intensity transmitted through the bubble column by a particle placed above it is expressed as $I_t = I_i.Tr$. As discussed in Sec.2.4, the intensity of the image of a particle i is described by Eq.5.23 as proportional to the intensity emitted through the particle surface (I_{p1i}). However as seen previously, the intensity reaching the sensor depends on the position of a particle compared to bubble column. Therefore, the intensity of the image of a particle (i) is calculated according to Eq.5.23 with a transmission coefficient depending on the position of the particle in the flow (above or below bubble column).

$$\begin{aligned} I_{1i}(X,Y) &= Tr_{1i} \cdot \frac{I_{p1i} Da^2 \beta^2}{4\pi d_{e1i}^2 (s_0 + z_{1i}')^2} \cdot e^{-\frac{4\beta^2}{d_{e1i}^2} ((X-\mu_{1Xi})^2 + (Y-\mu_{1Yi})^2)} \\ I_{2i}(X,Y) &= Tr_{2i} \cdot \frac{I_{p2i} Da^2 \beta^2}{4\pi d_{e2i}^2 (s_0 + z_{2i}')^2} \cdot e^{-\frac{4\beta^2}{d_{e2i}^2} ((X-\mu_{2Xi})^2 + (Y-\mu_{2Yi})^2)} \end{aligned} \quad (5.23)$$

If we consider a fixed interrogation window in x and y direction and if we assume a constant thickness of the bubble column in the whole interrogation window, the transmission coefficient associated to a

particle in the interrogation window only depends on its altitude z^* (above or below the bubble column, $Tr_{1i} = Tr_1(z_i^*)$). If we consider that a particle above the bubble column in the first image will not be below the bubble column in the second image, we can consider $Tr_1(z_i^*) = Tr_2(z_i^*) = Tr(z_i^*)$.

With these considerations, going through calculations presented Sec.2.4, we can now consider a corrected bubbly cross-correlation model (BCCM) similar to the CCM Eq.2.15 with the consideration of the transmission coefficient :

$$R_{D12}(\delta_x, \delta_y) = \sum_{i=1}^N \frac{A_i \cdot Tr^2(z_i^*) \cdot I_0^2(z_i^*)}{2 \cdot d_e^2(z_i^*) \cdot (s_0 + z_i^*)^4} \cdot e^{-4\beta^2 \frac{(DX(z_i^*) - \delta_x)^2 + (DY(z_i^*) - \delta_y)^2}{2 \cdot d_e^2(z_i^*)}} = \sum_{i=1}^N Tr^2(z_i^*) \cdot R_{Dz}(z_i^*) \quad (5.24)$$

With these considerations, simulations with the BCCM can be performed in order to analyse the behaviour of the R-PIV technique as used for tire measurement for a flow with a structure as described in Fig.5.19.

To perform these simulations, inputs are needed. The probability of presence of particles in this case is considered as constant in height. In the grooves the Taylor-Green structure of the flow is distributing the particles all over the groove height and thus the effect of the fall of particles before measurements is not considered in the grooves. The intensity profile is considered as presented on Fig.5.15 as homogeneous in the tire configuration. In this section two main configurations of reception optics are considered. In a first set-up, the object plane is considered as Fig.5.15 on the ground ($z_{OP}^* = \frac{z_{OP}}{h_{grooves}} = 0$). In the second one, the object plane is considered at the top of the groove ($z_{OP}^* = 1$) (Fig.5.26).

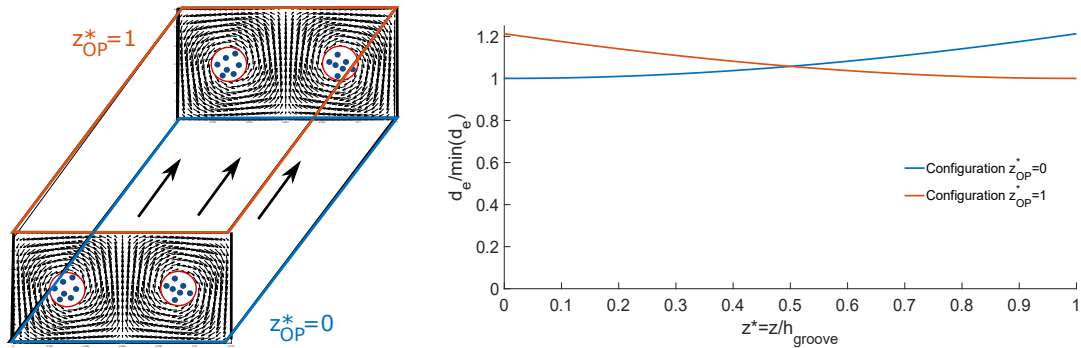


Figure 5.26: Particle image diameter function of the height in the groove for both configurations.

In this study, the BCCM model is used with interrogation windows of size $dw_x = 1 \times dw_y = 1$ mm (12x12 pixels) in the grooves in order to best reproduce the configuration of R-PIV measurements analysed Chap.6. The BCCM model calculation is repeated for every interrogation window in the geometry studied with an independent random particle distribution Fig.5.19. Therefore, for every interrogation window centered in (X, Y) , the velocity profile considered as an input of the model is calculated from Eq.5.20.

The bubble column is considered as straight, the bubble column position is independent of x . With this consideration, simulations can be performed with both models :

- The CCM model does not take into account the bubble presence
- The BCCM model take into account two bubble columns of diameter $d_c = 2.5$ mm in the core of

the vortices (Fig.5.18).

Results of these simulations for a single snapshot are presented in Fig.5.27 for $N = 10$ particles per interrogation window. This value is representative of R-PIV measurements.

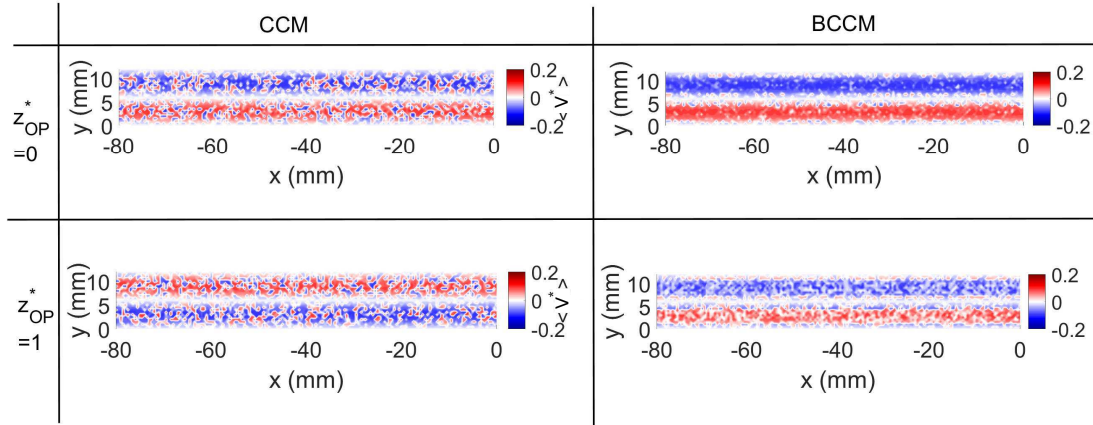


Figure 5.27: Spanwise velocity obtained with both CCM (left) and BCCM (right) models for the 2 reception optic configurations, $z_{OP}^* = 0$ (top) and $z_{OP}^* = 1$ (bottom).

The use of the CCM (left column in Fig.5.27), shows that depending on the position of the object plane z_{OP}^* , the particles that contributes the most to the cross-correlation changes. For $z_{OP}^* = 0$, the particles near the ground contributes more to the cross-correlation and therefore between $y = 0$ and $y = 6$ mm, the velocity obtained is generally positive and between $y = 6$ and $y = 12$ mm, the velocity obtained is generally negative. Otherwise, for $z_{OP}^* = 1$, the particles at the top of the groove contributes more to the cross-correlation. Therefore, with $z_{OP}^* = 1$, the general behaviour is the opposite of the one for $z_{OP}^* = 0$. For both configurations, the CCM shows that without the consideration of bubbles the velocity obtained is noisy.

With the BCCM (right column in Fig.5.27), shows that the consideration of bubble changes the general behaviour for $z_{OP}^* = 1$. In this case both positions of the object plane give the same general behaviour with a positive velocity between $y = 0$ and $y = 6$ mm and a negative velocity between $y = 6$ and $y = 12$ mm. This is explained by the masking effect of the bubbles. In the zone where the spanwise velocity is maximum (around $y = 3$ mm for one vortex and around $y = 9$ mm for the other), the bubbles hide the particles in the upper part of the flow. Therefore, for both configurations, the particles that appears on the camera sensor are the ones in the lower part of the flow. This also shows that the bubble will have a reduction effect on the spanwise velocity measured inside tire grooves.

The R-PIV measurements in the tire case are repeated several times in order to study the reproducibility of the measurements and to obtain statistical samples. Thus, as for the CCM, the BCCM can be averaged with the process described in Eq.2.18 in order to take into consideration a multiple number of image pairs. Thus, the same simulations presented in Fig.5.27, are reproduced with the averaging Eq.2.18 over $N_{im} = 10$ image pairs. The results are presented on Fig.5.28.

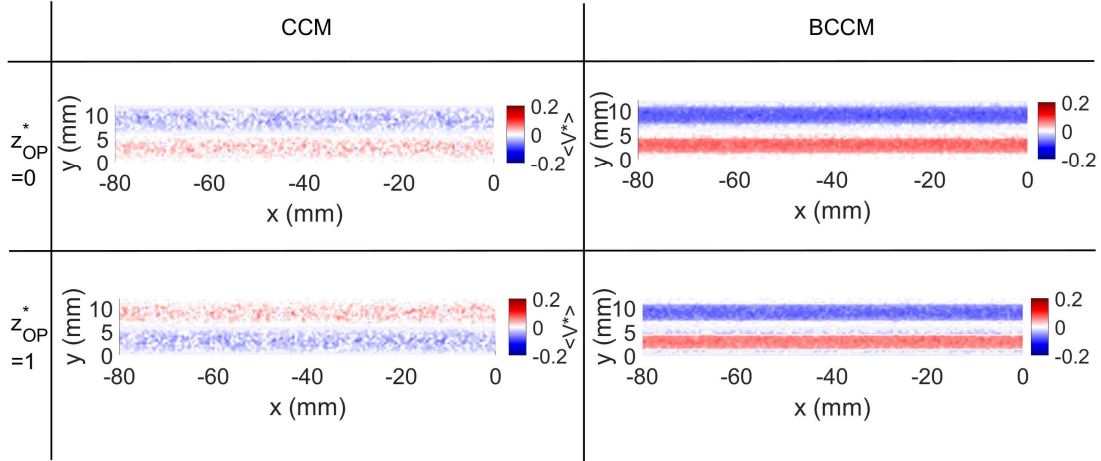


Figure 5.28: Ensemble averaged spanwise velocity obtained with both CCM and BCCM models for the 2 reception optic configurations.

The averaging process over samples allows to validate the general behaviour of the CCM model without bubbles with a vertical mirror symmetry inversion of the $\langle V^* \rangle (y)$ profile if we change the object plane position (especially considering measurement results for both z_{OP}^* positions presented Appendix.D). For the BCCM model, the inversion is not possible. This latter prediction of the BCCM model is in concordance with measurements given in Appendix.D.

In order to highlight the differences between every configuration, the spatially averaged velocity V/V_0 profiles are calculated along x direction and are compared to the velocity of the Taylor-Green vortices at $z^* = 0$ and $z^* = 1$. This figure is presented Fig.5.29.

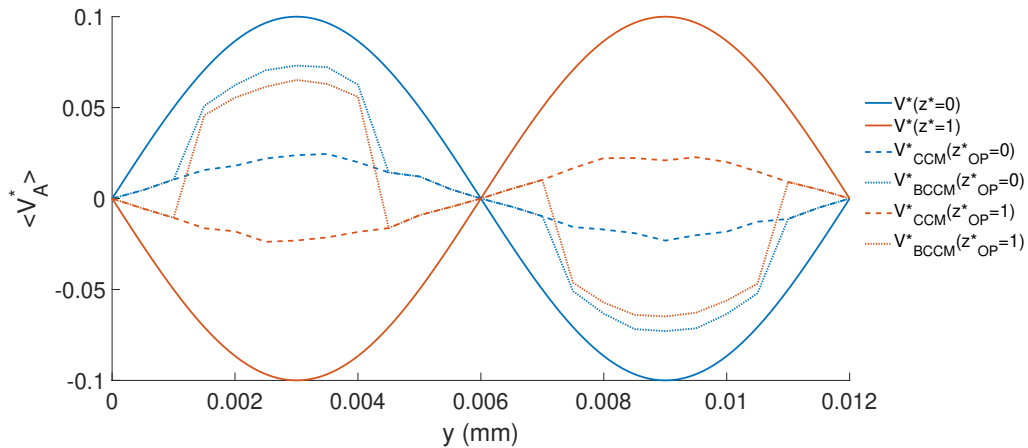


Figure 5.29: Spatially averaged velocity profiles obtained with the 4 configuration compared to the reference velocity field.

With this figure we can observe that the bubbles are hiding the particles in the upper part of the flow. Therefore, even with an object plane position at the top of the groove, the measured velocity will be the one in the lower part of the groove (below bubbles). Which is confirmed by measurements in Appendix.D. We can also observe that the velocity predicted with the BCCM is lower for an object plane $z_{OP}^* = 1$ than for $z_{OP}^* = 0$.

5.2.3 Discussion on the streamwise velocity.

For the streamwise velocity the effect of integration of the R-PIV can be discussed on the boundary layers at the walls of the grooves. As seen previously the masking effect of bubble will hide the upper wall boundary layer particles which will not contribute to the cross-correlation. Thus the structure of the velocity profile in the streamwise direction will only depend on the boundary layer on the ground. Thus, the structure of the velocity profile will be similar than the one used for the water-bank analysis in Section.5.1.3. Therefore, if the boundary layer thickness $\delta_{BL}^* \leq 0.1$ the effect of the boundary layer on the R-PIV measurement will be negligible. An estimation of the order of magnitude of the boundary layer thickness based on laboratory measurements is proposed in Appendix.E.

At the side wall, the boundary layers could be present as well. However, the size of the interrogation window 1x1 mm does not allow to catch the boundary layer at the wall if they are under the millimeter.

5.2.4 Conclusions.

In this Section, the masking effect of bubble was investigated to highlight the fact that particles above the bubble columns will not appear on the camera sensor. With this consideration, the CCM model was modified to take into account the effect of bubbles in the BCCM model. This model was used in order to compare what is the predicted velocity obtained with the model if we apply R-PIV on a specific Taylor-Green like vortices flow. This shows that with bubble consideration (contrary to the case without bubbles), wherever the object plane is placed, the velocity obtained correspond to the velocity in the lower part of the flow due to the masking effect of bubbles.

In the case of the R-PIV in-situ snapshot measurements presented in Chap.6, the object plane is placed on the ground ($z_{OP}^* = 0$) as discussed previously and the bubble columns are present. Therefore the configuration which correspond the most to the measurements is the one presented Fig.5.27 on the top right corner. Therefore, if Yeager 1974 [81] hypothesis of double counter rotating vortices is true inside tire grooves, the R-PIV measurements should look like this Fig.5.27 with $z_{OP}^* = 0$ and the BCCM.

The structure and nature of the potential vortices is yet unknown. Thus the Taylor-Green structure of the vortices used in this study can differ from the nature of the real tire groove vortices. Furthermore, the exact structure of the bubble columns in terms of bubble sizes and density is also unknown. Finally, this whole section is a discussion on the effect of bubble columns and what should happened in the case of Yeager 1974 [81] hypothesis in terms of general behaviour (qualitative study). However, quantitative conclusions can not be made from this analysis.

5.3 Illumination in transverse grooves.

In this work, the illumination method was discussed to determine the way the laser sheet propagates inside the puddle. This explains the structure of the light sheet and the illumination profile in front of the tire and inside longitudinal grooves. However, the light sheet propagates straight in the x direction. Therefore, the this light sheet propagation as studied by the ray tracing model in Sec.3.1.4 can not explain the illumination inside transverse grooves (as shown for Type C grooves on Fig.5.30).

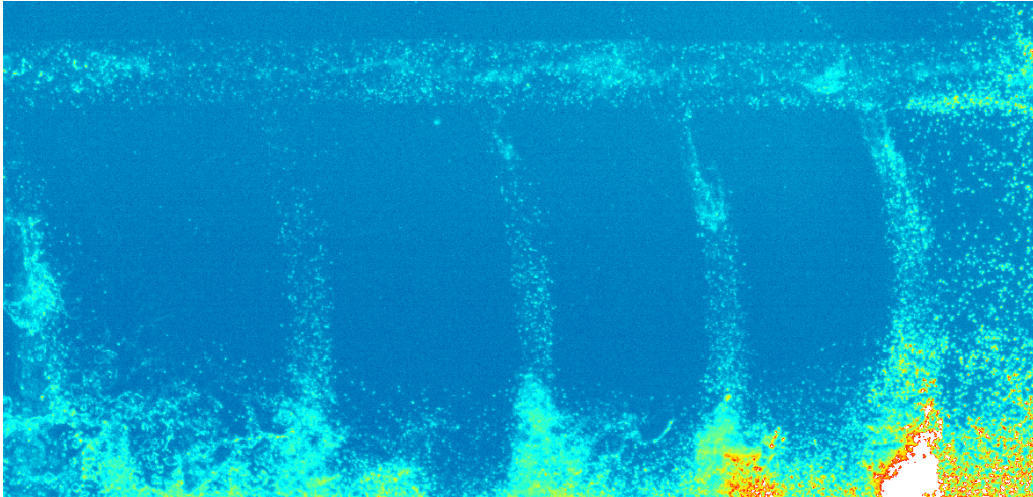


Figure 5.30: R-PIV image inside Type C grooves.

This illumination of the transverse grooves can be explained by the illumination coming from the quantity of light imprisoned in the prism. In the ray tracing model used in Sec.3.1.4, the analysis was focussed on the light transmitted into the water at the first laser sheet impingement at the interface. However, at this interface in the configuration Fig.3.9, appropriately 30% of the laser sheet is transmitted. This means that 70% remains on the prism. This rest of light can emerge in the water after some reflections inside the prism and can illuminate the flow from below the puddle as for the μ -PIV configurations (see Fig.5.31).

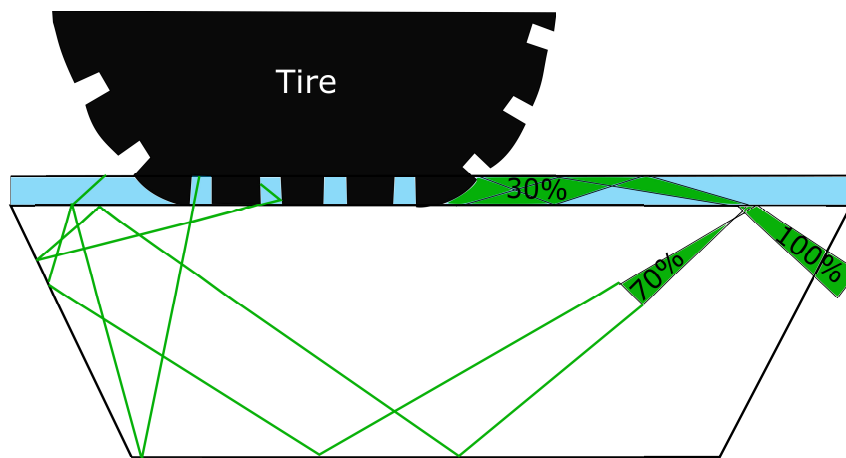


Figure 5.31: R-PIV image inside Type C grooves.

This scheme illustrates the proportion of the incident beam that is reflected inside the prism. Two example of travelling rays in the prism are shown to illustrate how transverse grooves are illuminated. Finally, this light illuminating the transverse grooves is equivalent to the background light generated in the rest of the tire. This shows how important is the background light due to the quantity of light trapped inside the prism in the whole tire measurement.

This background light can be considered as homogeneous in the whole domain due to the homogeneous structure of the light intensity profile in longitudinal grooves Fig.3.10. We decomposed the light intensity profile as $I(z^*) = I_0(z^*) + I_b(z^*)$, with $I_0(z^*)$ incident light intensity (from direct illumination) as studied with the ray tracing model Fig.3.9 and $I_b(z^*)$ the background intensity. Therefore, if

$I(z^*) = \text{constant}$ as measured Fig.3.10 and $I_0(z^*) = \text{constant}$ as calculated Fig.3.9, thus the background light profile $I_b(z^*) = \text{constant}$.

In conclusion, the transverse grooves illumination is generated by the background ambient light illumination and not directly from the refracted light sheet. However, due to the large proportion of the laser beam which is reflected and not refracted at the first interface, the illumination of transverse grooves is sufficient to obtain particle images in those grooves and to perform PIV.

6 Tire R-PIV measurement results.

In this chapter, results of PIV measurements will be presented. This chapter is segmented into two parts. The first one is focused on the PCY4 summer tire study. In which is the most extensively studied tire and in a second section, the results are presented for the CCP tire. This structure is chosen in order to present the tire flow analysis for the best known and the most extensively studied tire model, the PCY4 one. For both comparison between new and wear state is done. CCP tire is studied to confirm efficiency of the technique on a differently patterned tire. A second interest of this comparison is to understand if the conclusions drawn concerning the PCY4 tire are supported by an other tire model.

All the results shown in this chapter are performed for a single vehicle speed, $V_0 = 50$ km/h, for both tire models. Firstly, the flow in front of the tire in the water-bank and the shoulder is analysed with the velocity profiles obtained at $V_0 = 50$ km/h. The same analysis protocol is proposed for both tire models.

In a first step, for the PCY4 tire, the flow in the longitudinal grooves will be analysed, firstly for the primary flow (flow parallel to the groove direction) structure along the groove and secondly for the secondary vortex flow inside the grooves. In a second step, the analysis of the flow in transverse Type C grooves of the PCY4 tire is proposed. For the CCP tire, the analysis of the structure of the flow inside its transverse grooves is proposed which is comparable to the Type C grooves analysis. Then the study of the structure of the flow in "zigzag" groove is proposed.

In conclusion, an analysis of the flow is proposed here for 2 different tire models to highlight the capacity of the method to be adapted to tire sculptures and configurations for a fixed vehicle speed $V_0 = 50$ km/h.

6.1 PCY4 Tire.

In this section, results of tire measurements are presented for PCY4 tire model. This section is separated into two subsections, one focussed on the flow in front of the tire and one focussed on the flow inside the grooves.

6.1.1 Flow in front of the Tire.

The vector field obtained for a single measurement with a vehicle speed of $V_0 = 50$ km/h for a new tire with $h_{water} = 8$ mm is presented in Fig.6.1 as an example.

This figure highlights three different zones of the flow in front of the tire. In front of the ribs and especially in front of the central RIB (red rectangle Fig.6.1), the flow is straight forward in the rolling

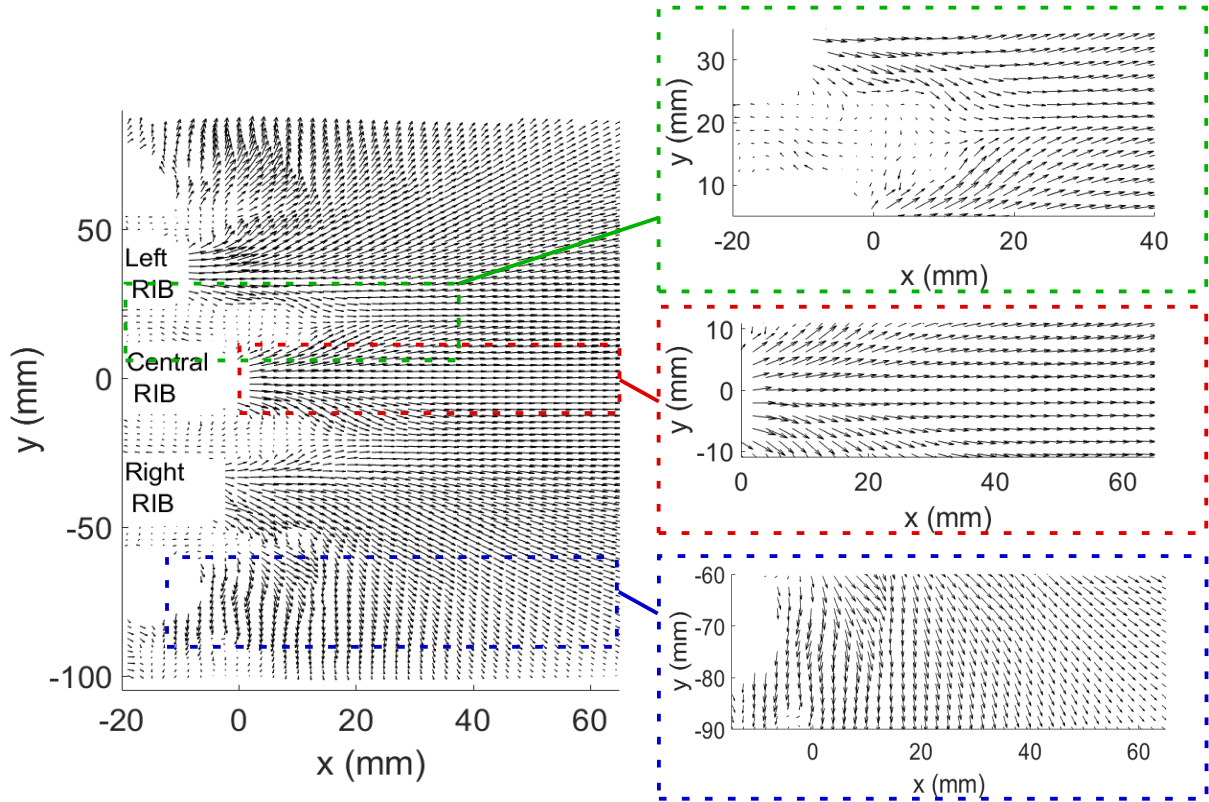


Figure 6.1: Instantaneous vector field measured for a new tire rolling at $V_0 = 50$ km/h through a puddle with $h_{water} = 8$ mm.

direction of the tire. This zone is called the water-bank (WB). In front of the tire grooves (green rectangle in Fig.6.1), the disturbance generated by the groove entry can be observed, with vectors in the direction of the grooves showing the potential flow around the RIB which goes inside the grooves. In this region, the vectors are pointing to the center of the groove. At the shoulder, (blue rectangle Fig.6.1), the flow is mainly in the transverse direction with a large amount of water driven off the car path. In this first analysis of the flow in front of the tire, we will focus on the flow in the WB and near the shoulder.

The velocity component maps obtained for every independent measurement are repositioned according to the coordinate system origin defined in Section 3.4. The resulting ensemble averaged velocity field computed over the independent measurements is presented in Fig.6.2, for both new and worn tires.

These maps confirm the observations made from the snapshot vector field. In front of the central RIB, the velocity is mainly in the rolling direction. The maximum velocity in the spanwise direction can be observed at the shoulder of the tire. What we can observe is the presence of the velocity front as described in Fig.5.1 for the worn tire configuration. This velocity front also exists in the new tire configuration. However, for the new tire, the WB is longer than for worn tire and is out of the field of view.

We can observe here, that the magnitude of the normalised averaged velocity $\langle U^* \rangle = \langle U \rangle / V_0$ in the water-bank which seems to be greater in the case of the worn tire than for the new tire. In the meantime, the normalised averaged spanwise velocity $\langle V^* \rangle = \langle V \rangle / V_0$ seems to be of a higher magnitude at the shoulder for the new tire configuration than for the worn tire configuration.

The standard deviation maps of both velocity components are shown in Fig.6.3.

This demonstrates that standard deviation is generally low in front of the tires RIB, especially in the WB. These RMS velocity component maps show a higher dispersion for low water height measurements with worn tire. The specific zones where the RMS of the velocity grows can be determined.

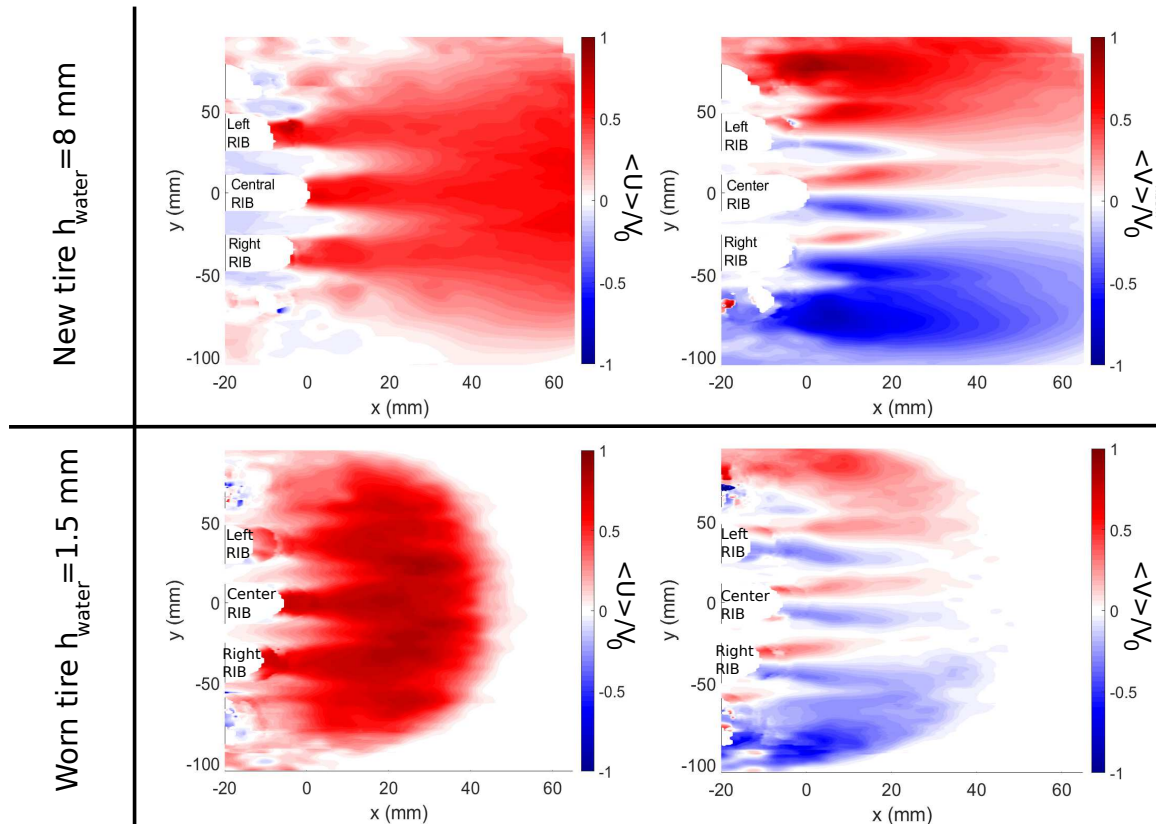


Figure 6.2: Ensemble averaged velocity component maps for new (top) and worn (bottom) tires.

In the case of $U_{RMS}^* = U_{RMS}/V_0$ for the worn tire case, a high dispersion zone appears between $x = 35$ to $x = 45$ mm. This zone corresponds to the forehead of the WB. As discussed in Section.5.1, in the forehead of the water bank, ability of particles to catch up the flow velocity highly depends on the particle diameters. The precision of the tire positioning as discussed in Section.4.1 can also explain an offset in the forehead position and then increase the standard deviation. In Section.4.1 the control of h_{water} was discussed. As shown on Fig.6.2, the water height, together with the wear state of the tire, seem to have an influence on the length of the WB. Therefore a variation in h_{water} can induce a variation of the length of the WB and then an offset in the forehead position and an increase of the standard deviation at the forehead of the water-bank. However, this variation can also be caused by an hydrodynamic source of variation with an oscillating length of the water-bank with the time which can explain the differences between measurements taken at an unknown instant in the rolling cycle.

For both, $U_{RMS}^* = U_{RMS}/V_0$ and $V_{RMS}^* = V_{RMS}/V_0$, the standard-deviation increases near the shoulder. This can be explained easily based on the discussion (Sec.4.3) on the effect of the Type C groove positions at the beginning of the contact patch area.

Finally, in front of the tire grooves, the $U_{RMS}^* = U_{RMS}/V_0$ grows in the case of the worn tire with a higher amplitude than for new tire. This can be explained by the effect of the wear indicator, as discussed in Section.4.3, on the flow inside the grooves and which influences the flow in front of the grooves.

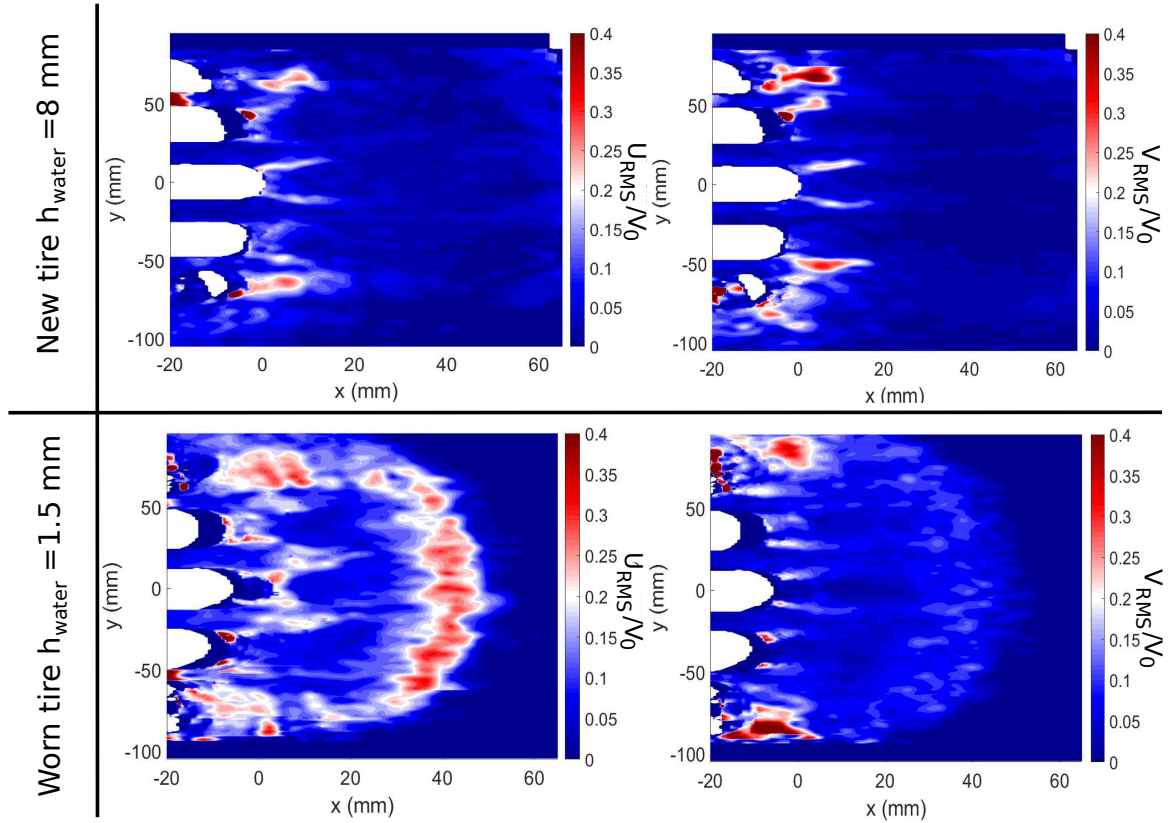


Figure 6.3: RMS velocity component maps for for new (top) and worn (bottom) tires.

6.1.1.1 Water-Bank

In this subsection, we will now focus on the velocity profiles and on the evolution of the velocity in the WB. For each run, the velocity is spatially averaged in the spanwise direction y over the central RIB (from $y = -11$ to $y = 11$ mm, red rectangle on Fig.6.1) for both tire state and is noted $U_{WB}(x) = \frac{1}{22} \int_{-11}^{11} U(x,y)dy$. The ensemble averaged velocity profile $\langle U_{WB}^* \rangle(x)$ in front of the tire is shown on Fig.6.4.

This highlights that the field of view used for our experiment allows to measure the water-bank forehead for the worn tire case but not for the new tire case. These profiles show similarities. After the contact patch area, the velocity slowly grows when we get further from the tire (from $x = 0$ to $x = 25$ mm for the worn tire and from $x = 0$ to $x = 65$ mm for the new tire). A characteristic velocity is defined as the spatially averaged velocity around the maximum of the profiles. This value is calculated as $\overline{U_{WB}^*} = \frac{1}{x_{max} - x_{min}} \int_{x_{min}}^{x_{max}} U_{WB}(x)dx$. For the worn tire, x_{min} is equal to 20 mm and $x_{max} = 30$ mm. For the new tire, the maximum velocity being reached at the right edge of the profile, x_{min} is equal to 55 mm and $x_{max} = 65$ mm. This characteristic velocity can be calculated for each run at $V_0 = 50$ km/h. For the new tire, the ensemble averaged value obtained, normalised by the vehicle speed, is $\langle \overline{U_{WB}^*} \rangle = 0.6$ with a standard deviation of $RMS(\overline{U_{WB}^*}) = 0.04$. For the worn tire, this value is $\langle \overline{U_{WB}^*} \rangle = 0.81$ with a standard deviation $RMS(\overline{U_{WB}^*}) = 0.05$.

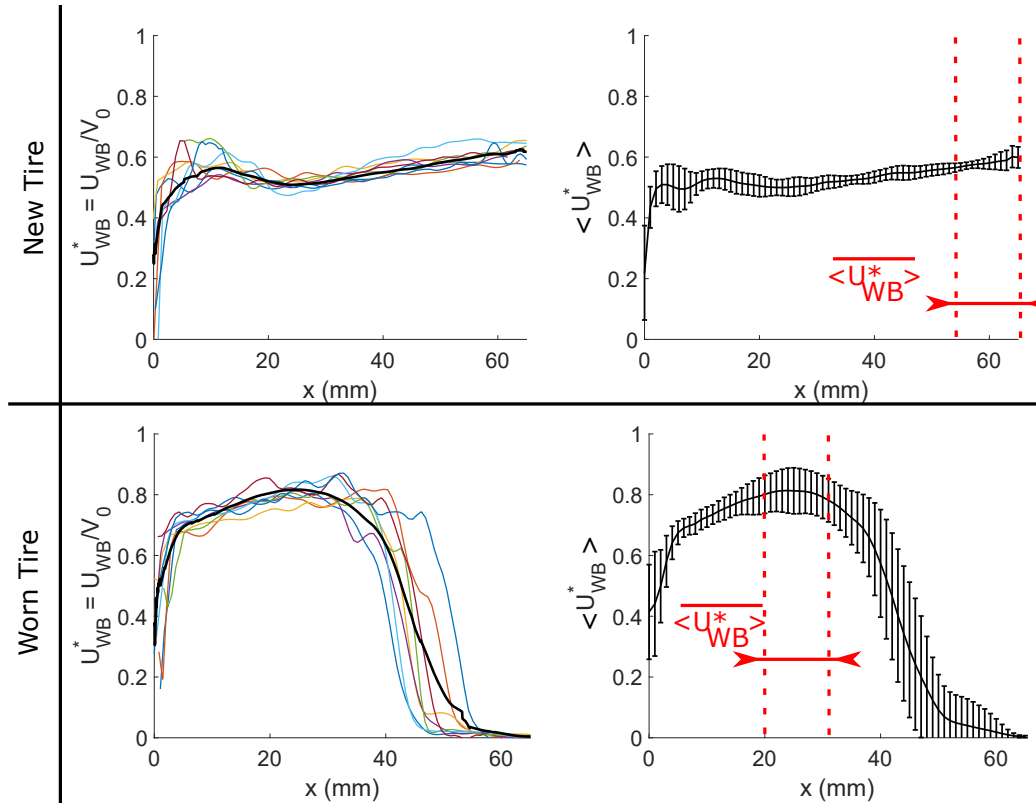


Figure 6.4: Spatially averaged velocity profiles in the WB U_{WB}^* in front of the tire. Red lines represents the integration limits in x to obtain a global parameter $\langle \overline{U_{WB}^*} \rangle$.

It appears that this characteristic value is higher for the worn tire than for the new tire case. The standard deviation for the worn tire is slightly higher than for the new tire. However these deviations are low and highlight the high repeatability of the measurement method in the water-bank. The same analysis is done for different vehicle speed in Chapter 7 and deeply analysed.

6.1.1.2 Shoulder

In this section, results are focused on the flow near the shoulder (blue rectangle in Fig.6.1). In this region, the water is driven off the tire rolling path by the side. Therefore, the velocity component of interest here is the velocity component V in the spanwise direction y . To analyse this value, the velocity V_s^* is spatially averaged over a narrow band of 2 mm thickness centred at $y = 75$ mm as $V_s(x) = \frac{1}{2} \int_{74}^{76} V(x,y) dy$. The evolution of this velocity in front of the tire is depicted in Fig.6.5.

These profiles show a low dispersion in the new tire case all along the velocity profile. For the worn tire case, with lower water height, the dispersion in the contact patch area vicinity is higher. This dispersion is mainly due to the high influence of the presence of a Type C groove or a RIB in the tire vicinity (see discussion Section 6.1.2.3). In order to visualise more in details the general structure of the profiles at the tire shoulder, the same profiles are presented with a superposition of the peak velocity in Fig.6.6.

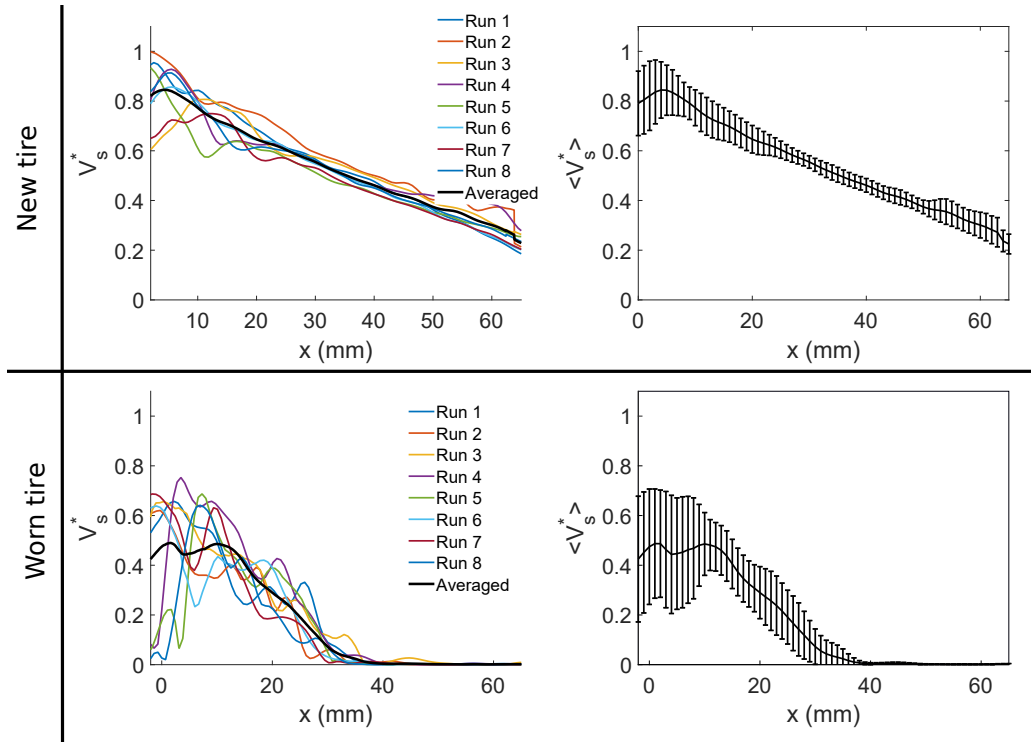


Figure 6.5: Spatially averaged velocity profiles at the shoulder V_s^* in front of the tire.

This superposition shows minor differences in the velocity profiles for the new tire. However, for the worn tire, it allows us to better analyse the similar structure of the profiles.

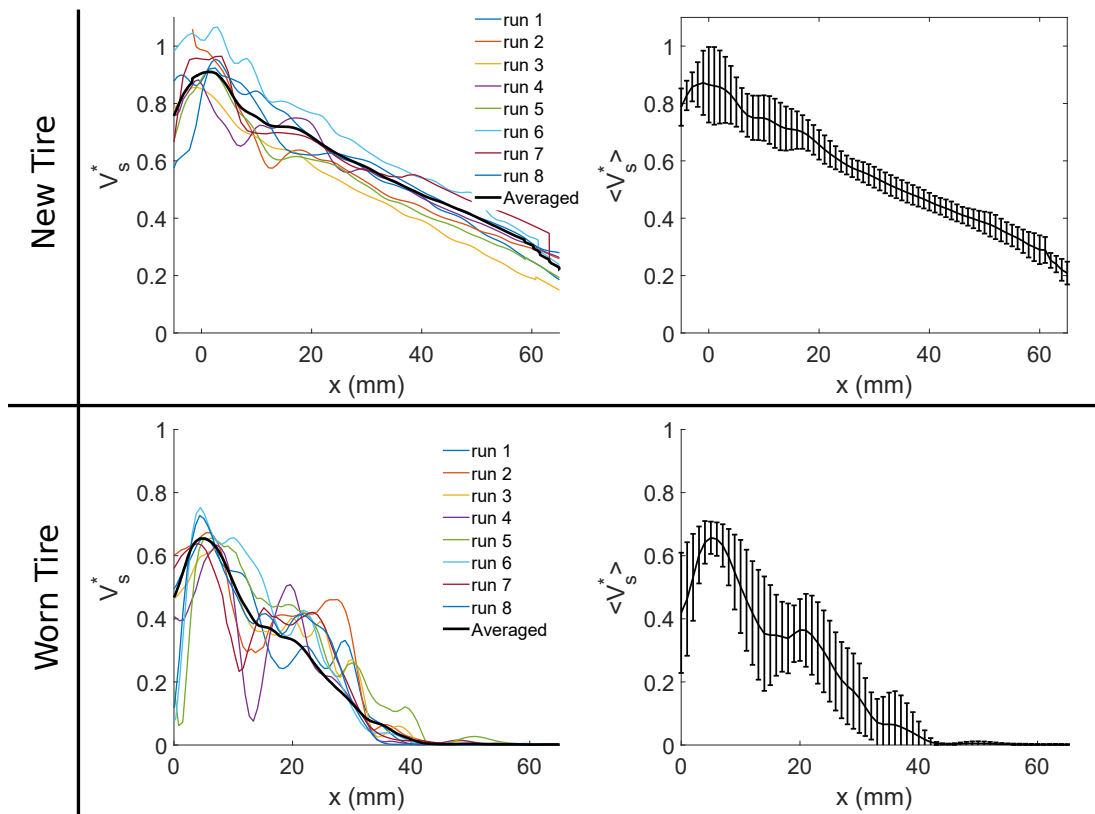


Figure 6.6: Spatially averaged velocity profiles at the shoulder V_s^* in front of the tire.

In this figure, the velocity profile V_s^* is presented for 8 independent runs before presenting the ensemble averaged profile with the standard deviation. In general, the structure of the flow is the same for every case with a maximum velocity at the shoulder and a decrease of this spanwise velocity with the distance from the tire. Nevertheless, for the worn tire, the dispersion appears to be much higher than for the new tire measurements. In this case, we can observe a valley in some profiles as for run 4 around $x = 15$ mm which corresponds to the arrival of a RIB between two Type C grooves near the contact patch area. This illustrates well the effect of the Type C grooves position on the shoulder velocity profile and can explain the higher dispersion for shoulder measurements compared to WB.

These profiles can be well described by the analysis of the maximum velocity at the shoulder $max.V_s$ by considering a structure of the flow with a maximum velocity at the shoulder and then a linear decrease down to zero with x . Having in mind the physical significance of the flowrate due to the spanwise motion of water around the shoulder, we also define a more global characteristic velocity \bar{V}_s , integrating the profiles from the tire until the last point of the shoulder zone : $\bar{V}_s = \frac{1}{L_x} \int_0^{L_x} V_s(x) dx$, with L the length of the shoulder line (length needed for the velocity to reach $V_s(x) = 0$). For the new tire L_x is 100 mm and for the worn tire L_x is 40 mm.

These values are calculated for both new and worn tires. The ensemble averaged characteristic velocities obtained for the new tire are $\langle max.V_s^* \rangle = 0.94$ and $\langle \bar{V}_s^* \rangle = 0.46$ with standard deviations of $RMS(max.V_s^*) = 0.09$ and $RMS(\bar{V}_s^*) = 0.05$ respectively. For the worn tire, the ensemble averaged values are $\langle max.V_s^* \rangle = 0.68$ and $\langle \bar{V}_s^* \rangle = 0.32$ with standard deviations of $RMS(max.V_s^*) = 0.06$ and $RMS(\bar{V}_s^*) = 0.07$.

It appears that $\langle \bar{V}_s^* \rangle$ is approximately equal to $\langle max.V_s^* \rangle$. Standard deviations are higher at the shoulder than in the water-bank due to the higher influence of Type C grooves locations. However, these standard deviations remain low and shows the good repeatability of the technique for shoulder measurements. This analysis shows that with the new tire, for which velocity profiles are less disturbed by the presence of Type C grooves, the standard deviation is reduced by the integration of the profiles ($RMS(max.V_s^*) > RMS(\bar{V}_s^*)$). For the worn tire, where the influence of Type C grooves is important, the disturbances of the profiles generate an increase of the standard deviation with the integration of the whole profile ($RMS(max.V_s^*) < RMS(\bar{V}_s^*)$).

6.1.1.3 Conclusions

In conclusions, with the two cases tested, it seems that the wear state induces a higher velocity in the water-bank and a lower velocity at the shoulder. The standard deviations for both cases are low which shows the high reproducibility of the measurement of the flow in front of the tire for the PCY4 tire.

6.1.2 Flow inside tire grooves.

In this Section, results of the fluid flow measurements inside the PCY4 tire grooves are presented. This Section will be spread in 3 different parts. One will be focused on the 2D flow inside longitudinal grooves. The second one will concern the 3D flow inside the longitudinal grooves and the last one will analyse the flow in the Type C transverse grooves.

6.1.2.1 Primary flow inside longitudinal grooves.

The flow obtained inside longitudinal grooves are presented. The velocity maps obtained for every independent measurement can be repositioned according to the coordinate system origin defined in Section.3.4. The results presented here are the ones for a vehicle speed of $V_0 = 50$ km/h. Thus, the ensemble averaged velocity field over all the independent measurements (12 for the new tire and 28 for the worn tire as already written in Section.3.5) is presented in Fig.6.7, for both new and worn tires as color maps of velocity components.

These velocity component maps show different behaviours. On one hand, the velocity in x direction appears to be generally uniform inside the Type A grooves. At a local scale, this flow through the Type A grooves varies in the case of the new tire and appears to be smoother in the case of the worn tire. In the Type B grooves, the general structure of the flow for the worn tire is similar to the one in the Type A grooves. For new tire, the structure of the flow is different in the Type B grooves. In these Type B grooves, the velocity seems to be generally negative in the first part of the grooves (from $x = 0$ down to $x = -40$ mm) and positive in the second part (from $x = -40$ down to $x = -100$ mm). The flow also appears to be locally highly variable.

For the velocity in the spanwise direction, it appears in Type A grooves a specific structure of the flow with one change of sign (negative sign in the upper part of the groove and positive sign in the lower part of the groove Fig.6.7 (top right)) for the new tire and 3 changes of sign in the case of the worn tire (Fig.6.7 (bottom right)). In Type B grooves, for the new tire, the velocity in the spanwise direction is positive in the upper groove and negative in the lower groove. For the worn tire, the structure of the flow in Type B grooves is the same than in Type A groove of the new tire with a change on sign in the groove (negative sign in the upper part of the groove and positive sign in the lower part of the groove Fig.6.7(bottom right)).

As for the flow in front of the tire, the standard deviation of the velocity components are presented Fig.6.8.

These standard deviation maps illustrate a high variability of the flow through the longitudinal grooves (Type A and Type B) for the worn tire case. For the new tire, the standard deviation shows locally high standard deviation spots in Type B grooves.

On the right bottom figure, the nomenclature for tire grooves is presented. Each groove is described by a name (A1, A2, B1 and B2) with its own referential in y, respectively (y_{A1} , y_{A2} , y_{B1} and y_{B2}). This nomenclature will be useful for the analysis of the velocity profiles inside each grooves.

In order to analyse more deeply the velocity field inside the longitudinal tire grooves, the velocity profiles in the streamwise direction are firstly extracted, as done previously in order to obtain global quantities related to the grooves (as for WB and Shoulder). To determine the velocity of the water through the grooves a spatial averaging is performed in a cross section of the groove. This averaged velocity is analysed along the tire grooves for a vehicle rolling at $V_0 = 50$ km/h for new tires. A comparison between the ensemble averaged velocity in A1 and A2 grooves and between B1 and B2 grooves is presented in Fig.6.9 to check for the symmetry.

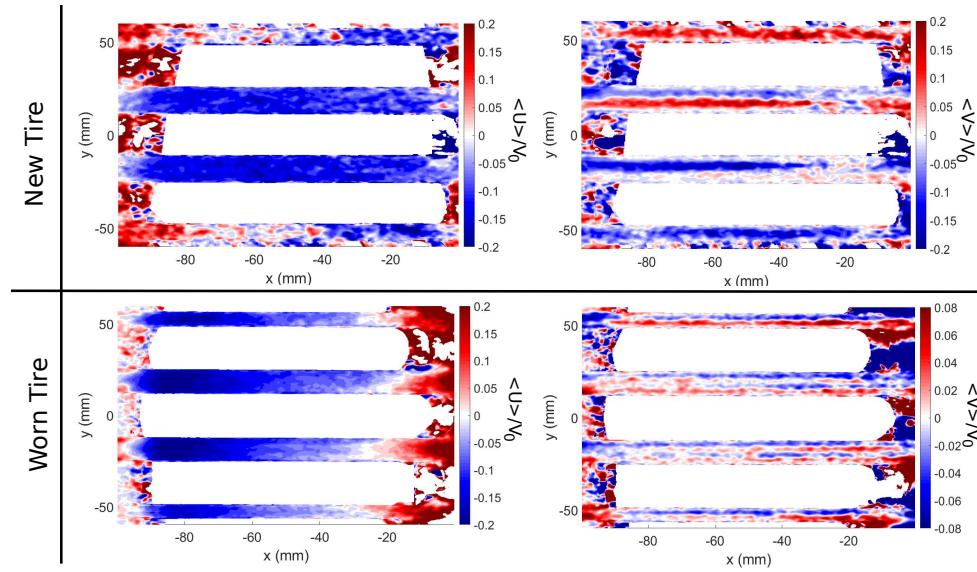


Figure 6.7: Ensemble averaged velocity component maps inside longitudinal grooves for both configurations.

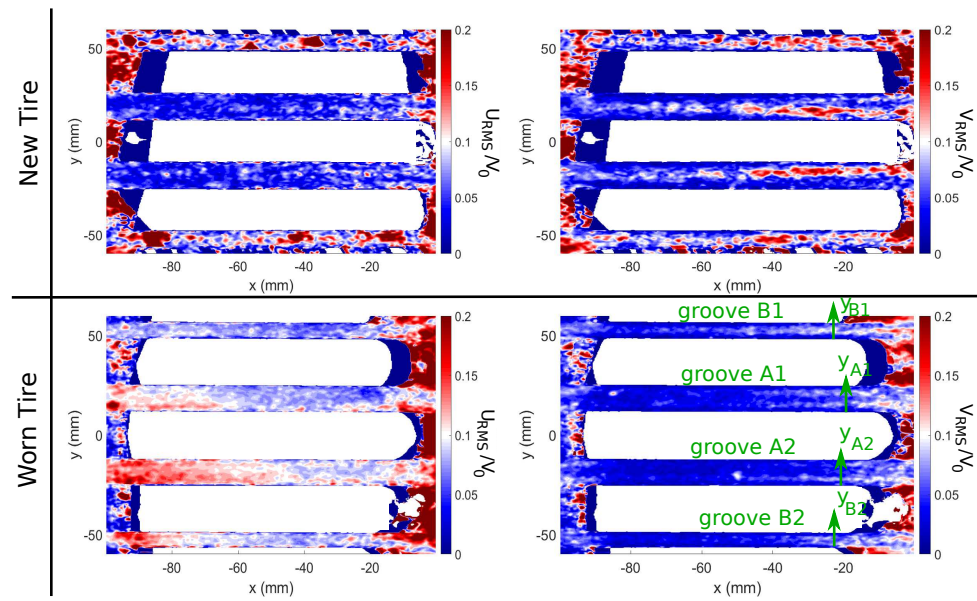


Figure 6.8: RMS velocity component maps for both configurations.

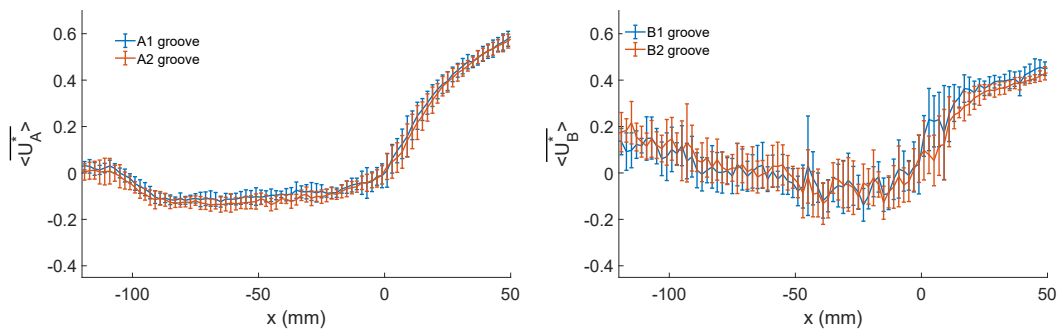


Figure 6.9: Ensemble averaged longitudinal velocity profiles along the tire grooves. (new tire)

Fig.6.9 shows a good agreement between A1 and A2 grooves and between B1 and B2 grooves. Therefore, the symmetry of the velocity component U can be assumed for this tire model. Thus, the velocity profiles obtained can be gathered for both Type A grooves and for both Type B grooves as presented in Fig.6.10. Velocity profiles obtained for different runs are presented additionally to the ensemble averaged profiles to observe local fluctuations for independent runs.

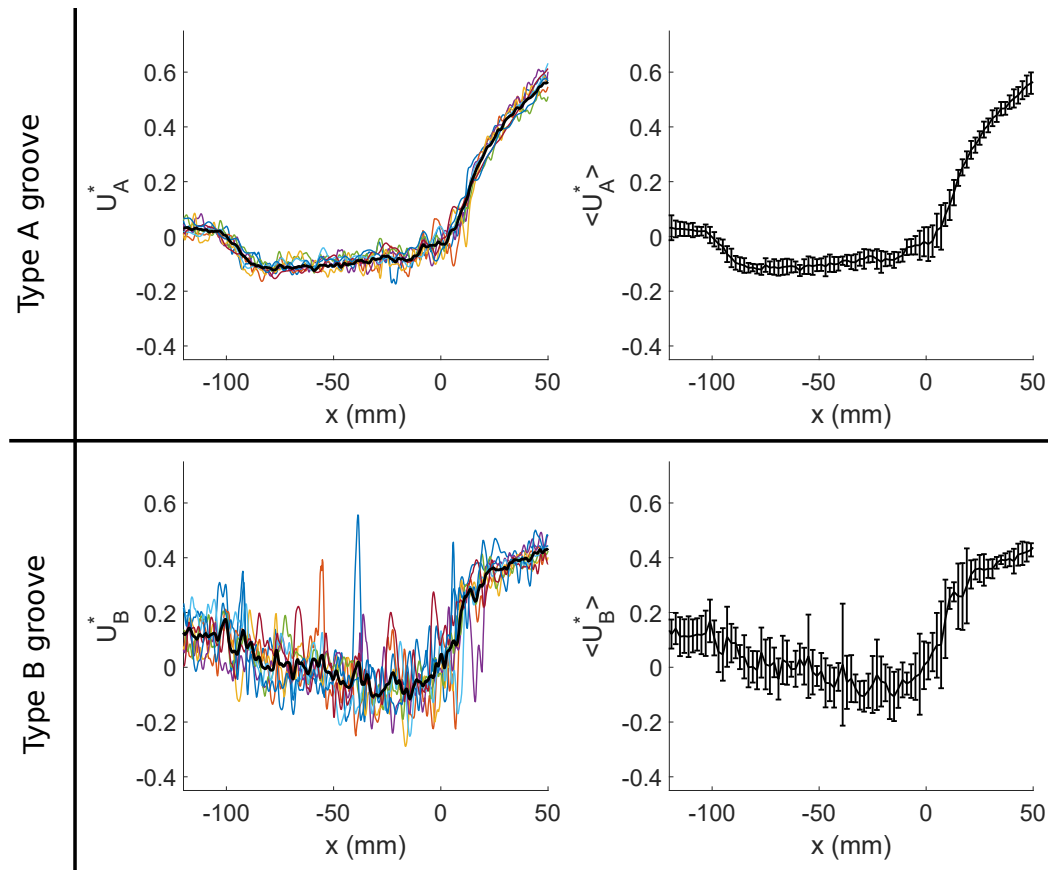


Figure 6.10: Instantaneous and ensemble averaged longitudinal velocity profiles along the tire grooves. (new tire)

If we take a look at the instantaneous and ensemble averaged longitudinal velocity profiles for the different runs, we can see small scale variations and oscillations of these profiles inside the groove (Fig.6.10). These local variations are of low amplitude in Type A grooves and can be linked possibly to :

- The presence of small scale turbulence in the flow in these grooves.
- The random altitude of the seeding particles below the bubbles.
- The deformation of the bubble columns and water velocity field which is different for every runs.

For type B grooves, the amplitude these local oscillations are way more important than in Type A grooves. The main difference is the geometrical connection between Type B and Type C grooves. This connection can locally disturb the flow inside Type B groove and explain the largest values of the small fluctuations in Fig.6.10.

For new tire measurements it appears that in Type A grooves, the fluid velocity decreases at the inlet of the groove down to a plateau. In the Type B grooves, the general structure of these profiles shows a

negative velocity in the first part of the contact patch area (between $x = 0$ and $x = -50$ mm) and a positive velocity in the end of the contact patch area (between $x = -50$ and $x = -100$ mm). This difference in the general shape of the profiles could be explained by the influence of Type C grooves on Type B grooves. As highlighted in for small fluctuations, variations of the flow in Type C grooves can influence the flow in Type B grooves due to the geometrical connection. Therefore, a change of sign of the flow in Type C grooves in the contact patch area can induce a change of sign in the Type B grooves.

The same analysis can be made for the worn tire in both types of grooves (Type A and Type B). The cases where the wear indicator is visible at the beginning of the contact patch area are plotted in dashed line. When the wear indicator is at the end of the contact patch area the profile is plotted in dotted line and solid line represents the cases without wear indicators in Fig.6.11.

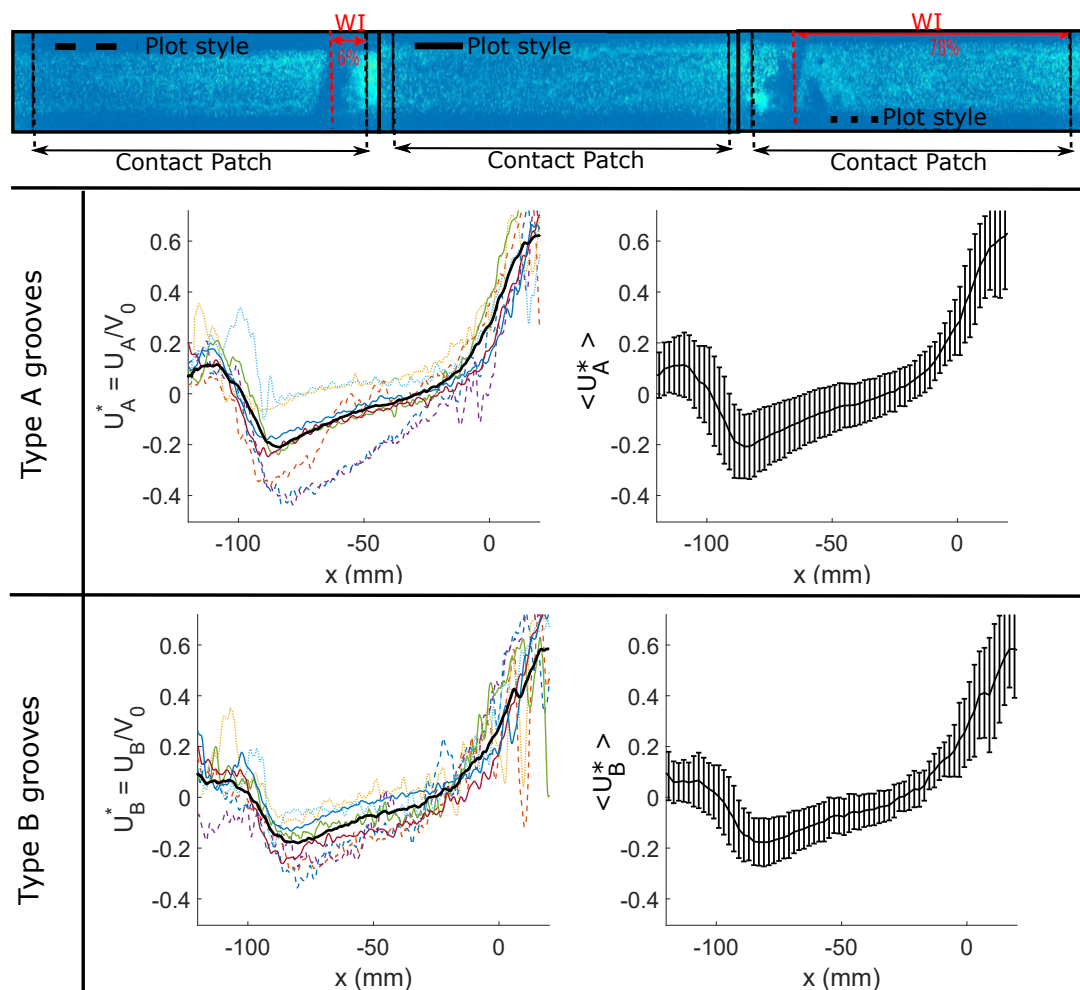


Figure 6.11: Instantaneous and ensemble averaged longitudinal velocity profiles along the tire grooves (worn tire).

In the worn tire grooves, the velocity profile structure is similar for both tire groove Types (Type A and Type B). Nevertheless, the overall feature of the profiles is quite different than for new tire. The small scale spatial fluctuations are strongly reduced, while fluctuations at the scale of the contact patch area length are increased. The general structure of the velocity profile consists in the decrease of the velocity down to a minimum. These profiles shows a high variability in their global amplitude. It appears that the magnitude of the fluid velocity inside the tire groove is greater when the wear indicator is at the

beginning of the contact patch area. This velocity is almost null when the wear indicator is at the end of the contact patch area.

Variations inside Type B grooves can also be discussed. It appears that in the case of the worn tire, where the Type B and Type C grooves are not linked, the velocity profile in Type B grooves has the same shape than in Type A grooves which was not the case for the new tire. Thus, the velocity profile general structure in Type B groove seems to be influenced by Type C groove. The same observation can be made for the local oscillations which are of the same amplitude than in the Type A groove for the worn tire which highlight the importance of the link between the Type C groove and the Type B groove flows.

To illustrate the influence of the wear indicator on the flow, the velocity is spatially averaged around the minimum velocity inside the tire grooves for every 28 independent measurements inside tire grooves. If we note x_{min} the location where is found the minimum velocity inside the tire groove, the averaged velocity \overline{U}_A is calculated between $[x_{min} - 5; x_{min} + 20]$. This velocity is shown in Fig.6.12 versus the location x_{WI} of the wear indicator inside the contact patch area. The location of the wear indicator is manually determined by the user based on raw PIV images. We consider here a location of the wear indicator of 0 % when $x_{WI} = 0$. The length of the contact patch at $V_0 = 50$ km/h being $L_C = 90$ mm (according to Todoroff et al. 2019[72]), $x_{WI} = -90$ mm corresponds to a location of the wear indicator of 100 %.

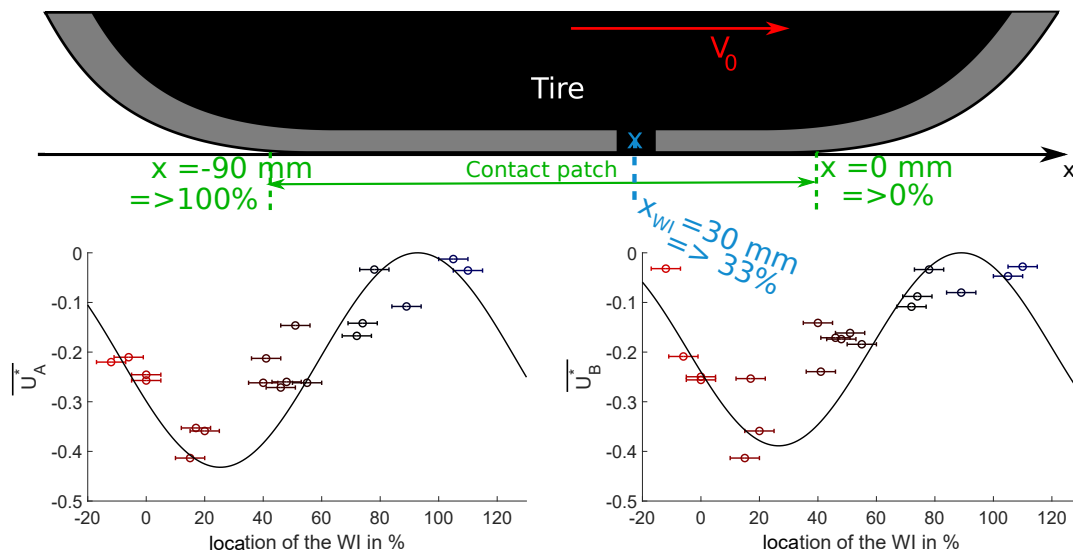


Figure 6.12: Velocity in the streamwise direction inside Type A and Type B tire grooves function of the wear indicator position in the image (worn tire).

This illustrates the influence of the wear indicator on the flow inside the tire grooves. It appears that the evolution of the velocity inside the tire grooves is quasi-sinusoidal as a function of the position of the wear indicator in the contact patch area.

6.1.2.2 Secondary flow inside longitudinal grooves.

We will now focus our analysis on the velocity in the spanwise direction in the tire grooves. In Fig.6.7, we already highlighted different flow behaviours between the Type A and the Type B grooves but also between worn and new states. To highlight the number of velocity sign changes in a cross section of the tire grooves, the spatially averaged spanwise velocity along the contact patch area is calculated. The

averaged velocity profiles are presented on Fig.6.13 for the Type A grooves. As for the previous results, the velocity profiles presented here are the profiles obtained for runs at $V_0 = 50$ km/h. The velocity profiles are presented here for the A1 groove on Fig.6.8. Velocity profiles are here spatially averaged in x between $x = -80$ mm and $x = -40$ mm.

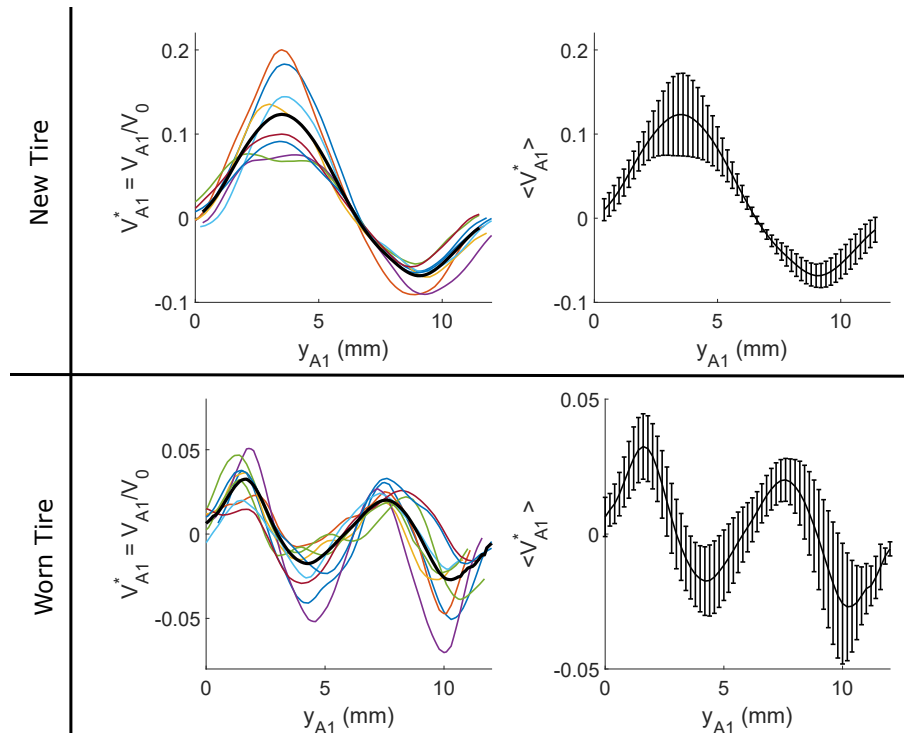


Figure 6.13: Instantaneous and ensemble averaged transverse velocity profiles in the spanwise direction inside Type A grooves.

This figure shows the specific structure of the flow in Type A grooves. For the new tire, the velocity profile in the spanwise direction inside the type A grooves is composed of three nodes (a node is a location for which $V = 0$) and two lobes (between the nodes), one with negative velocities and one with positive velocities. For the worn tire, the behaviour is different as there is five nodes and four lobes. There are two lobes with positive velocities and two lobes with negative velocities alternating in the transverse direction as for a sinusoidal curve (+ - + -)).

The same profile description can be performed inside Type B grooves for both tire configurations. The spanwise velocity profiles in these grooves are presented on Fig.6.14. Velocity profiles are presented here for the B1 groove (Fig.6.8).

In the case of the Type B grooves, the structure of the flow in these grooves is different than in the type A grooves. For the new tire, the velocity profiles show one lobe with two nodes at the walls. For the worn tire, the profiles are composed of three nodes and two lobes (one for positive velocities and one for negative velocities).

Thus the averaged profiles can be studied for both Type A and Type B grooves. Let's remember that for worn tire, 4 bubble columns are visible inside Type A grooves and 2 bubble columns are visible inside Type B grooves. For new tires, 2 bubble columns are visible inside Type A grooves and 1 bubble column is visible inside Type B grooves. Considering the masking effect of the bubbles discussed in Section.5.2, the velocity measured correspond to the velocity below the bubble columns. In order to

validate the helical vortex structure of the flow, the velocity in the third direction (z) is needed. Therefore, stereoscopic measurements were supplementary performed for the new tire state.

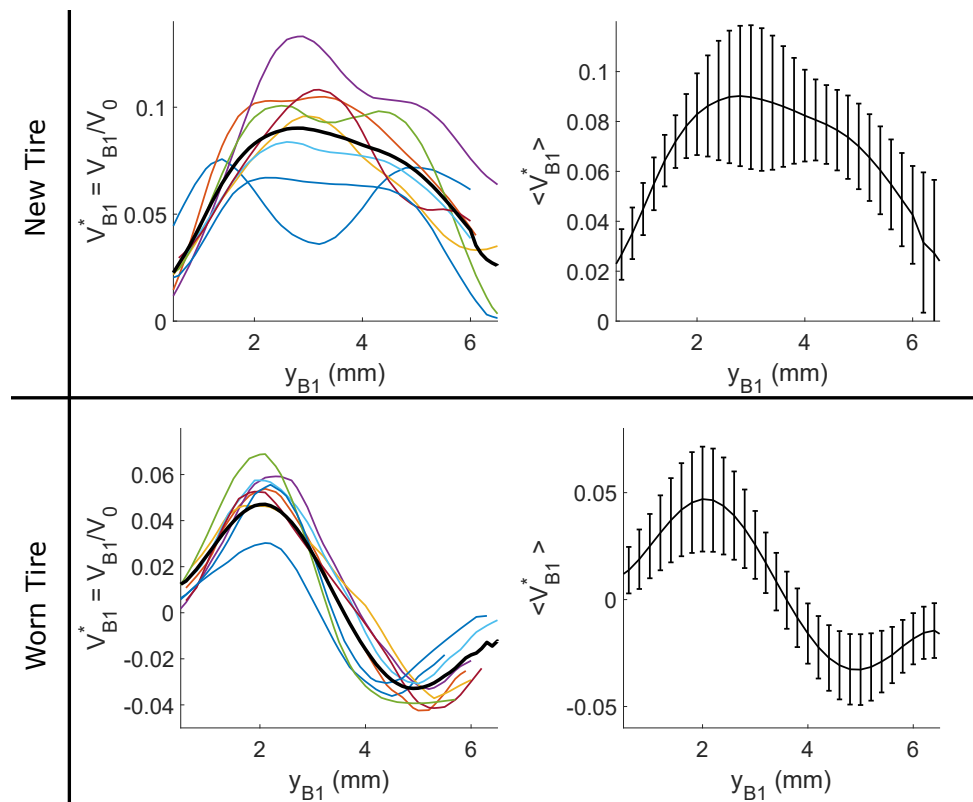


Figure 6.14: Instantaneous and ensemble averaged transverse velocity profiles in the spanwise direction inside Type B grooves.

The velocity profiles obtained with stereoscopic mounting inside the tire grooves are compared to the previous 2D measurements in the x and y directions in order to validate the results obtained from the stereoscopic R-PIV use (Fig.6.15). An example of comparison is presented for a vehicle speed at $V_0 = 50$ km/h.

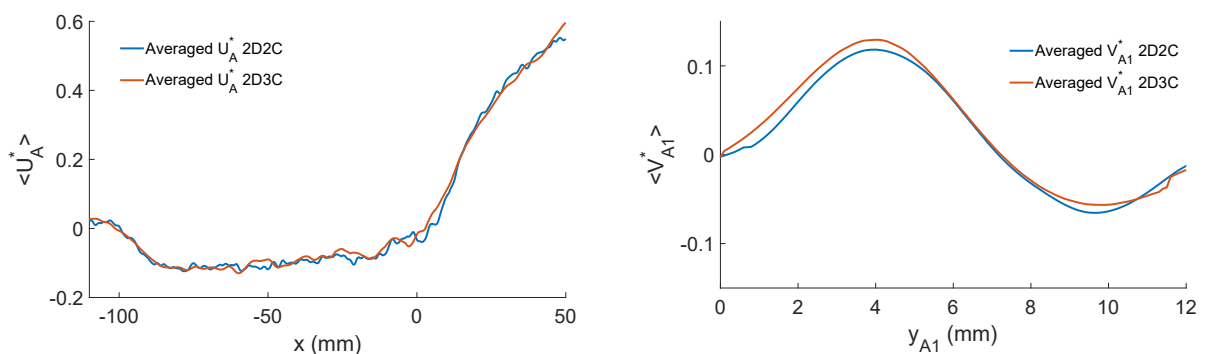


Figure 6.15: Spatially and ensemble averaged velocity profiles obtained with both 2D2C and 2D3C configurations in the streamwise and spanwise directions.

The comparison shows a good agreement between the 2D2C and 2D3C measurements inside tire grooves in x and y directions. Therefore, the stereoscopic setup is validated and the measured vertical

velocity W can be considered as trustworthy.

Considering this agreement for the velocities (U and V), the third component (W) can be studied in order to quantify the velocity in the z direction. Velocity map for $V_0 = 50$ km/h are shown on Fig.6.16.

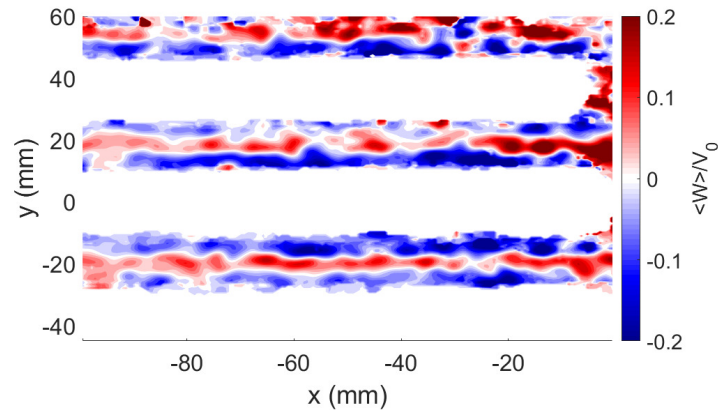


Figure 6.16: Velocity map W inside longitudinal grooves.

In spite of the large irregularities, this map shows a specific behaviour of the flow in z direction. It appears that in Type B grooves, half of the groove has positive velocity and half of the groove has negative velocity. In Type A grooves, the flow structure is composed of two negative lobes near the walls and one positive in the core of the groove.

To highlight this specific structure of the flow, spatially averaged velocity profiles along the contact patch area are studied in both Type A and Type B grooves (Fig.6.17).

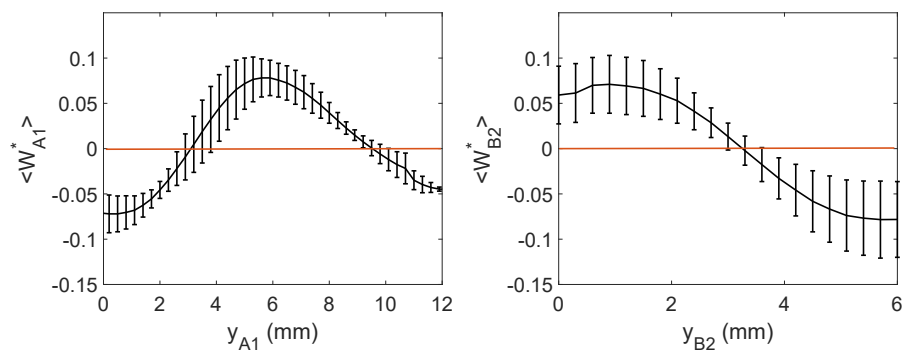


Figure 6.17: Spatially and ensemble averaged velocity component W profiles inside A and B Type grooves (new tire).

In this case, velocity profiles are presented for $B2$ tire grooves and not $B1$ because, in the case of stereoscopic measurements, only 4 measurements are available at $V_0 = 50$ km/h and none of them involve $B1$ grooves.

These velocity profiles highlight a specific shape of the velocity profile inside $A1$ and $B2$ grooves. In $A1$ grooves, the velocity profiles are composed of 2 nodes and 3 lobes in the order $(-, +, -)$. In $B2$ grooves, the profile is composed of one nodes and two lobes in the order $(+, -)$.

On the figure 6.18, a scheme of the tire groove flows with their corresponding averaged velocity profiles summarizes the transverse behaviour of the flow inside the tire grooves. Such deduction is only

possible because of the correlation between the profiles for W and the profiles for V .

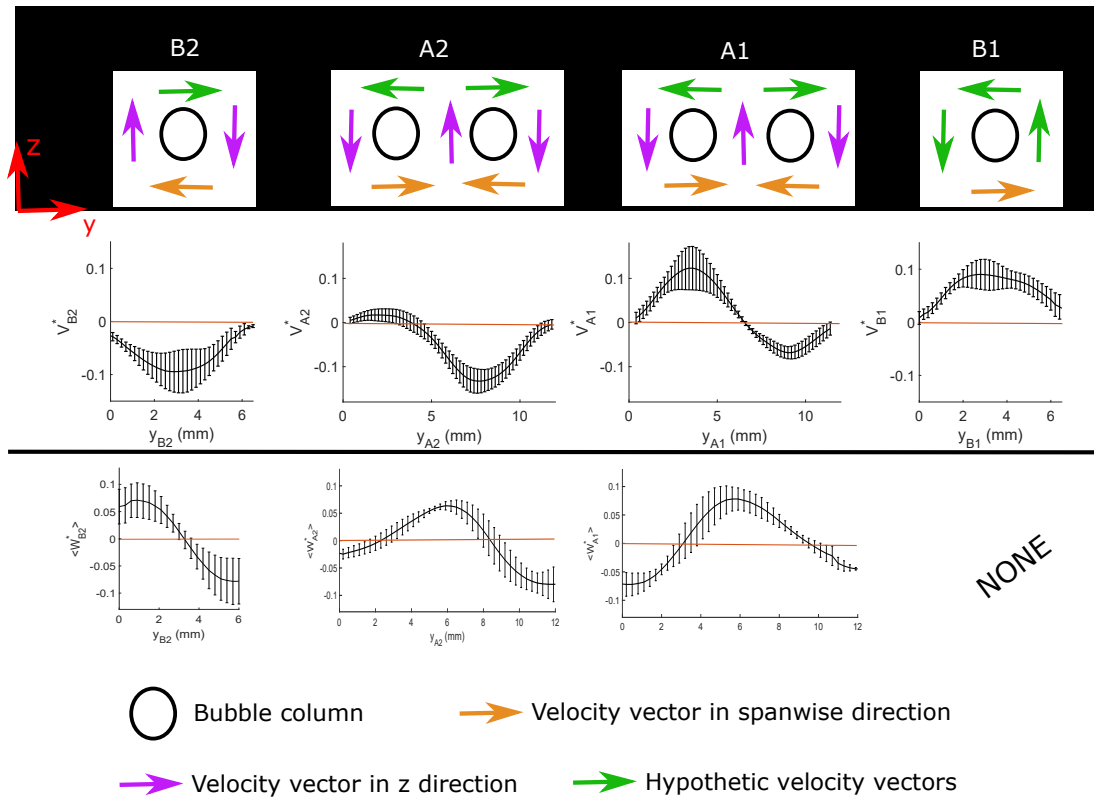


Figure 6.18: A scheme of the tire grooves with their corresponding averaged transverse velocity component profiles for the new tire.

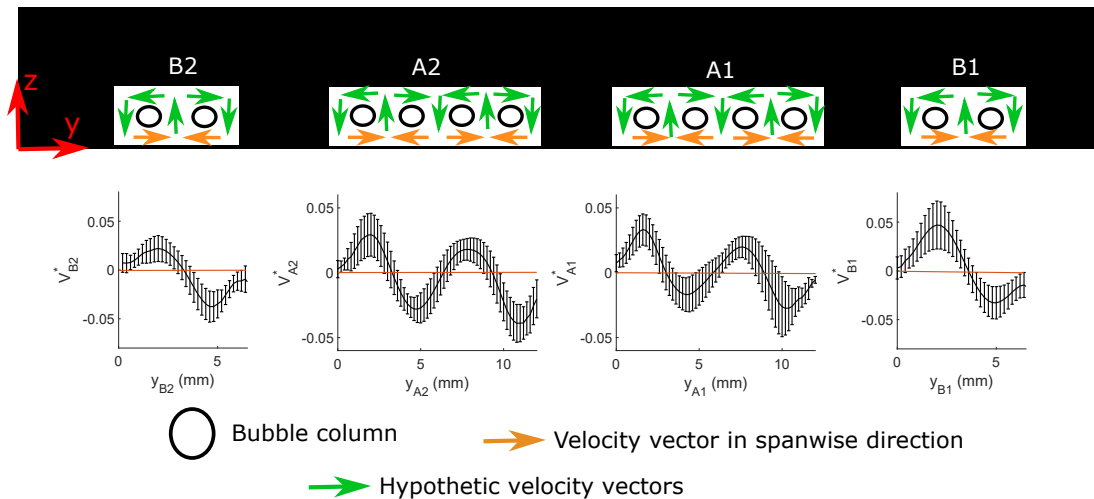


Figure 6.19: A scheme of the tire grooves with their corresponding averaged velocity profiles for the worn tire.

This stereoscopic analysis is not performed for worn tire. However, based on the V velocity profiles and the Fig.6.18 for the new tire, the structure of the 3D velocity field in the case of the worn tire can be assumed to contain vortices (Fig.6.19).

With these profiles, it appears that the measured spanwise velocity below bubbles can correspond to

the lower part (near the ground $z^* = 0$) of the vortices as predicted Section 5.2. These combined analysis of the velocity components V and W confirms the vortex like structure of the flow that have been supposed by Yeager 1974[81].

The interesting point is that the number of vortices is clearly related to the geometrical aspect ratio w_g/h_g of the grooves. This has to be regarded face to the cavity flows studied in the literature. Main part of these flows are for transverse upper flows and show the dependence of the maximum vortex coexistence inside a cavity as a function of the shape ratio (Simoëns et al. 2007[66]), even if here we have clearly a main longitudinal flow.

6.1.2.3 Flow inside transverse (Type C) grooves.

For the PCY4 tire, the only tire groove type that was not treated yet are the Type C grooves. From various runs, the location of the transverse Type C grooves vary inside the contact patch area. Therefore the analysis of an ensemble averaged velocity map is not possible. In this case, the velocity map in the spanwise direction is presented for a single snapshot at $V_0 = 50$ km/h (Fig.6.20). The velocity field is qualitatively similar from run to run.

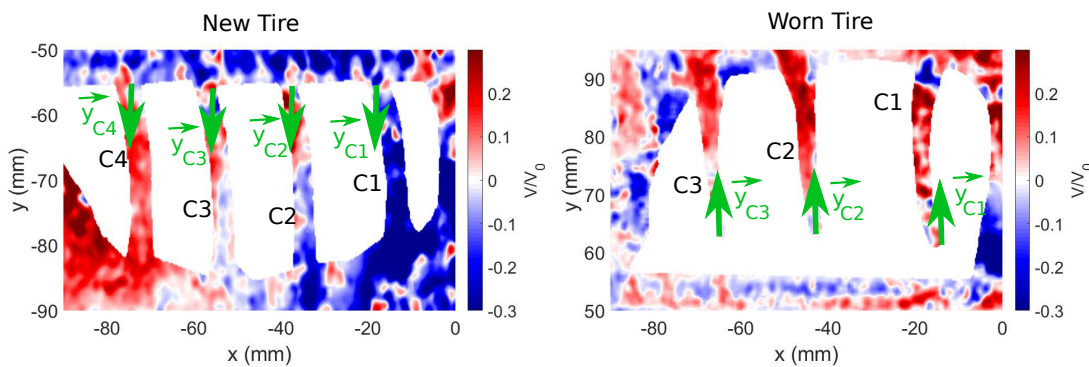


Figure 6.20: Instantaneous velocity maps V for new (left) and worn (right) tires.

We note the C grooves detected from the right to the left of an image as C1;C2;C3;C4. In the presented run, for new tire there are four grooves detected whereas only three are detected for the worn tire. Each groove has its own y axis (respectively $y_{C1}, y_{C2}, y_{C3}, y_{C4}$) oriented from the center of the tire to the side with an origin as sketched Fig.6.20 at the root of the Type C groove. In the case of the new tire, it appears that the velocity V in the C1 and C4 grooves are of opposite sign. This phenomenon does not appear for the worn tire case. In order to visualise this behaviour, the averaged velocity is calculated in every cross section (x) along the groove direction for both snapshots. To well compare these two cases in opposite direction, for each groove C , the velocities V_C^* are projected on the y_C direction Fig.6.21.

In the new tire case, we can observe that the velocity decreases with the position in the contact patch area. The velocity in C1 is greater than in C2 and so on for C3 and C4. For the worn tire, the velocity in C3 groove is sensitively lower than the one in C1 and C2 grooves. With these observations, it appears that the velocity inside the type C grooves decreases with the position of the groove inside the contact patch area. In the case of the new tire, the velocity in C4 groove even appears to be negative.

To illustrate these behaviours, the averaged velocity in the whole type C groove ($\overline{V_C^*}$) is calculated for every type C groove for every measurement at $V_0 = 50$ km/h. The averaged velocity for each groove is presented function of the groove location in the contact patch area according to the sketch in Fig.6.22.

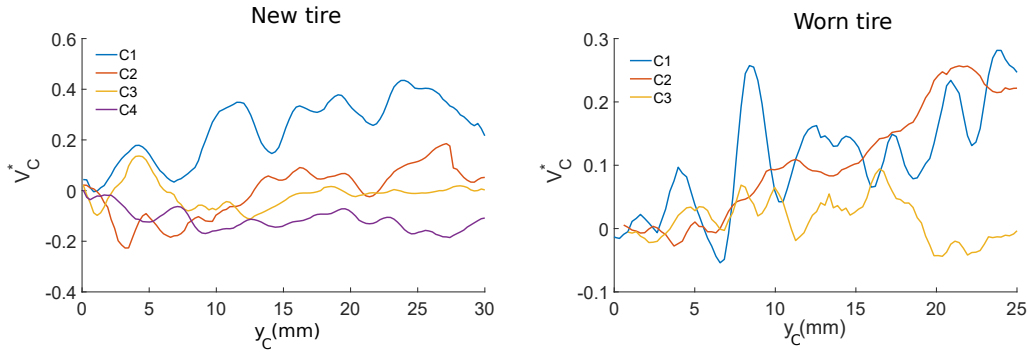


Figure 6.21: Spatially averaged velocity in every Type C grooves in both cases.

The locations of the Type C grooves are determined in percentage of the contact patch area as used for the wear indicator Fig.6.12.

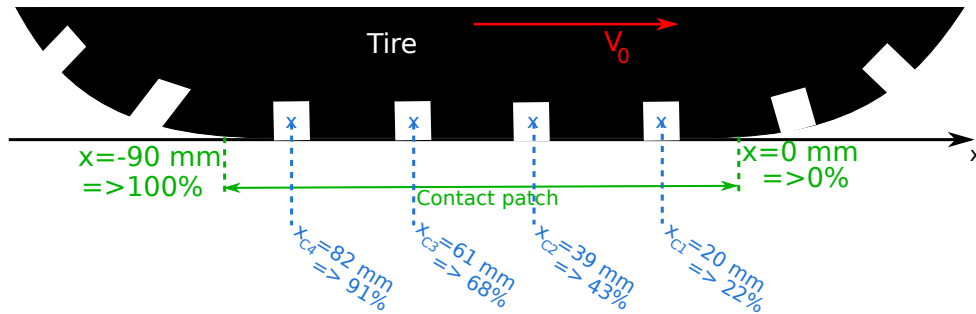


Figure 6.22: Sketch of an example illustrating the position of Type C grooves in the contact patch area in percentage.

The evolution of the spatially averaged velocity ($\overline{V_C^*}$) as a function of the groove location is presented for both tire models in Fig.6.23.

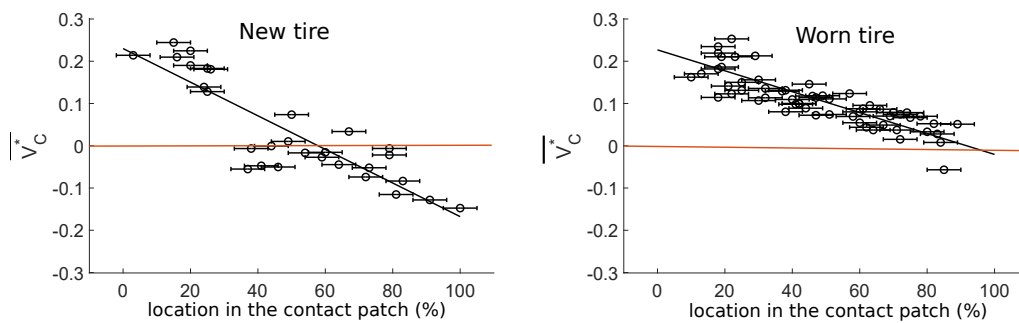


Figure 6.23: Velocity profiles in every the Type C grooves in both cases.

On this figure 6.23 are also plotted some linear regression corresponding to the points. This shows more clearly that the global velocity inside the type C grooves decreases with the location of the grooves compare to the contact patch area coordinates. In the case of the new tire, the velocity inside the type C grooves at the beginning of the contact patch area is positive and negative at the end that not shown for worn tire case. For new tire case behavior, an attempt of explanation could lye to the probable closure of some grooves, due to pressure exerted on ribs at the beginning of the rolling cycle, leading to water

expulsion by the side whereas water is sucked at the end of the rolling cycle when the stress on the RIB is relaxed.

This difference between new and worn tires will be discussed in Sec.7.2.

6.2 CCP Tire.

As explained previously, results on the CCP tire concern only the new tire configuration. As for the PCY4 tire, all the velocity profiles are presented for a vehicle speed $V_0 = 50$ km/h and with the same notations concerning averaging, non dimensionalisation, etc. Geometry design is more complex (see on figure 3.17). This could lead to more variability in masking and thus coincidence of the spatial domain from run to run.

6.2.1 Flow in front of the Tire.

For the CCP tire model the same process is repeated. The measurements in the front of the tire are made in the same zones than for the PCY4 tire.

The velocity component maps obtained for every independent measurement can be repositioned according to the coordinate system origin defined in Section3.4. Thus, the ensemble averaged velocity field over all the 8 independent measurements can be done and are presented in Fig.6.24.

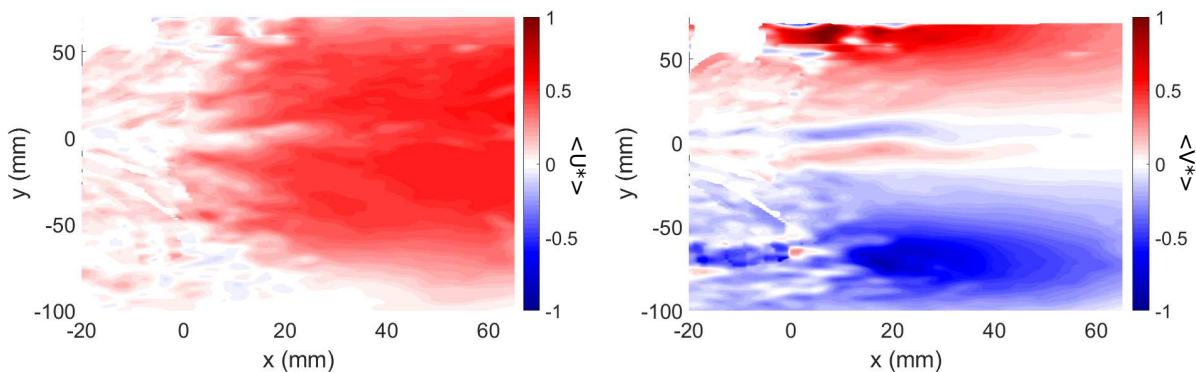


Figure 6.24: Ensemble averaged velocity component maps for CCP tire.

The general behaviour of the flow in front of the tire is similar than the one with the PCY4 tire. However, in front of the center of the contact patch area (in front of the central RIB for the PCY4 and in front of the zigzag groove for the CCP), the velocity U seems lower for the CCP. If we take a look at the velocity in front of the Type A groove for the PCY4 (Fig.6.2), the velocity U seems lower in the tire vicinity than for the CCP tire.

In order to illustrate the variability between each measurements the standard deviation are calculated for both U and V . These maps are presented Fig.6.25.

This figure shows the general low variability of the measurement in front of the tire. However, in the vicinity of the tire side, high standard deviation spots are visible between $x = 0$ mm to $x = 30$ mm (shoulder). This can be explained by the structure of the tire grooves.

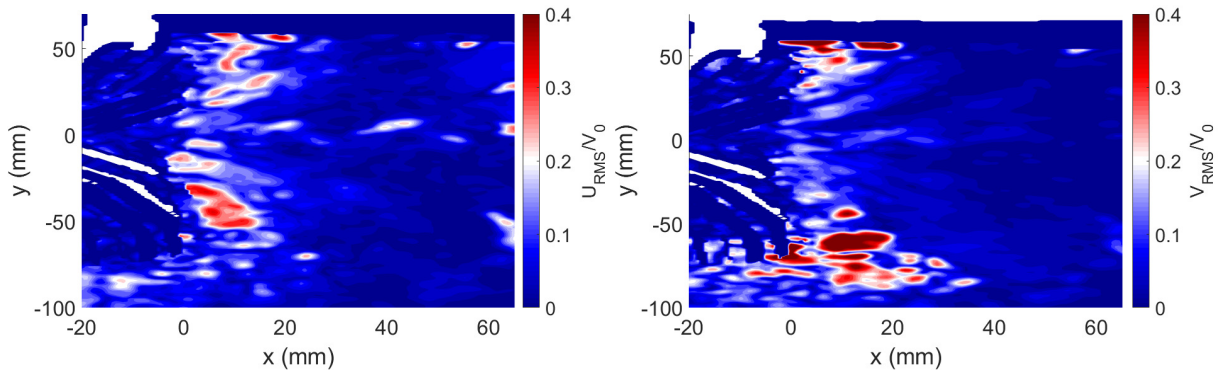
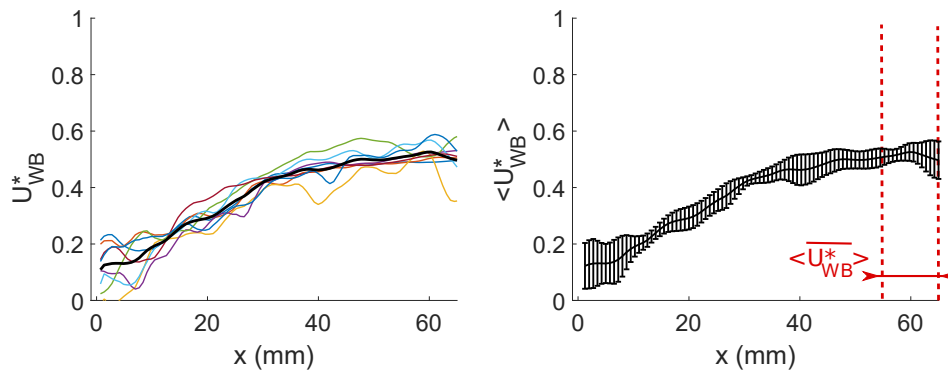


Figure 6.25: RMS velocity component maps for CCP tire.

6.2.1.1 Water-Bank

As for the PCY4 tire, we will firstly focus our analysis on the flow in front of the tire in the water-bank. The velocity component U is firstly spatially averaged over the central RIB zone of the PCY4 tire (from $y = -11$ to $y = 11$ mm) to calculate U_{WB} for every run. The evolution of the resulting velocity profiles $U_{WB}(x)$ and their ensemble averaged value are given in a nondimensionnal form in Fig.6.26.

Figure 6.26: Averaged longitudinal velocity profiles in the WB U_{WB}^* in front of the tire.

As for the PCY4 new tire, the configuration does not allow to analyse the forehead of the water-bank. The profiles show a specific behaviour for this tire model. The velocity in the tire vicinity is almost null and grows while x grows. The characteristic velocity in the water-bank is then calculated as the spatially averaged velocity in the maximum velocity zone as $\overline{U_{WB}} = \frac{1}{x_{max} - x_{min}} \int_{x_{min}}^{x_{max}} U_{WB}(x) dx$ (here $x_{min} = 55$ mm and $x_{max} = 65$ mm).

For this tire model, the ensemble averaged characteristic velocity, normalised by the vehicle speed, is $\langle \overline{U_{WB}^*} \rangle = 0.52$, with a standard deviation $RMS(\overline{U_{WB}^*}) = 0.02$. The velocity in the water-bank appears to be lower for the CCP tire than for the PCY4 tire. The standard deviation appears to be lowered too. However, this reduction of the standard deviation should be taken carefully knowing that all CCP measurements presented were made the same day and are less subject to weather condition variations.

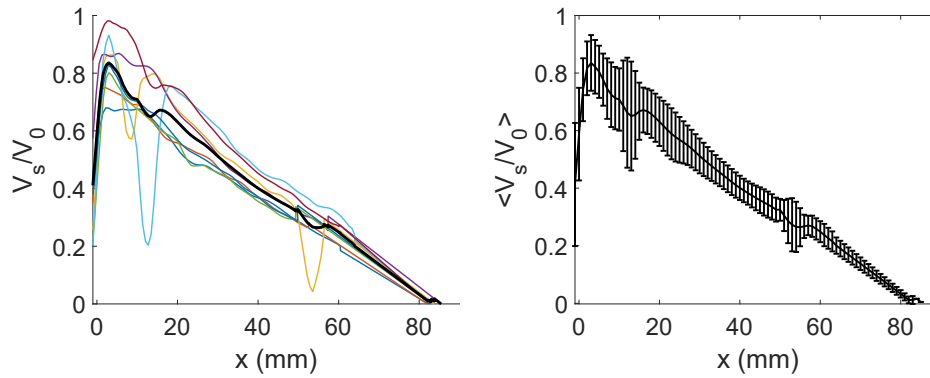


Figure 6.27: Averaged transverse velocity profiles at the shoulder V_s^* in front of the tire.

6.2.1.2 Shoulder

In this section, results are focused on the flow at the shoulder. In this region, the water is driven off the tire rolling path by the side. Therefore, the quantity of interest here is the transverse velocity component (V). To analyse this value, the velocity V_s^* is spatially averaged over a narrow band of 2 mm thickness centred at $y = 65$ mm. The evolution of this velocity in front of the tire is studied with the standard deviation in errorbar Fig.6.27.

For this tire model, the shape of the velocity profile is similar to the one obtained for the new PCY4 tire. However, some holes are visible in the blue and yellow curves. These holes correspond to a zone where the RIB between two transverse grooves appears on the images and generate a hole in the correlation. As for the PCY4 tire, these profiles can be well described by the analysis of the maximum velocity at the shoulder $max.V_s$ by considering a structure of the flow with a maximum velocity at the shoulder and then a linear decrease down to zero with x . As for the PCY4 tire, we also define a more global characteristic velocity \bar{V}_s , integrating the profiles from the tire until the last point of the shoulder zone : $\bar{V}_s = \frac{1}{L} \int_0^L V_s(x) dx$, with L the length of the shoulder line $L = 100$ mm (length needed for the velocity to reach $V_s(x) = 0$).

With the CCP tire, the ensemble averaged characteristic velocities at the shoulder are $\langle max.V_s^* \rangle = 0.86$ and $\langle \bar{V}_s^* \rangle = 0.43$, with standard deviations $RMS(max.V_s^*) = 0.1$ and $RMS(\bar{V}_s^*) = 0.04$ respectively. The averaged values are quite similar to the ones obtained for the PCY4 tire. Even if, in this case, few disturbances of the profiles were observed in Fig.6.27, the integration of the profile reduces the standard deviation as a characteristic velocity.

6.2.2 Flow inside the grooves.

6.2.2.1 Flow inside the "zigzag" zone.

The first part to analyse is the central zigzag groove zone in the center of the tire. The spanwise velocity component V is presented on Fig.6.28 for a snapshot in order to illustrate the change of direction of the flow in every change of direction of the zigzag groove part.

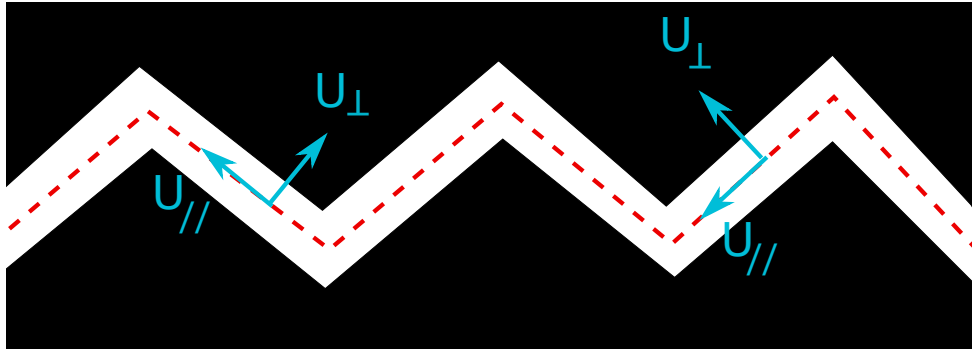


Figure 6.29: Sketch of the velocity components projected on the zigzag groove axis.

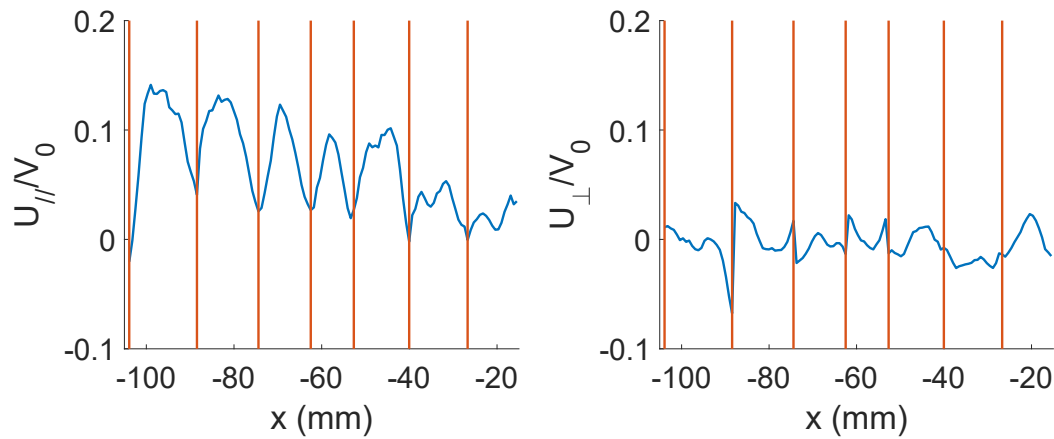


Figure 6.30: Velocity component $U_{//}$ and U_{\perp} profiles along the contact patch area. Orange lines represents the weld positions.

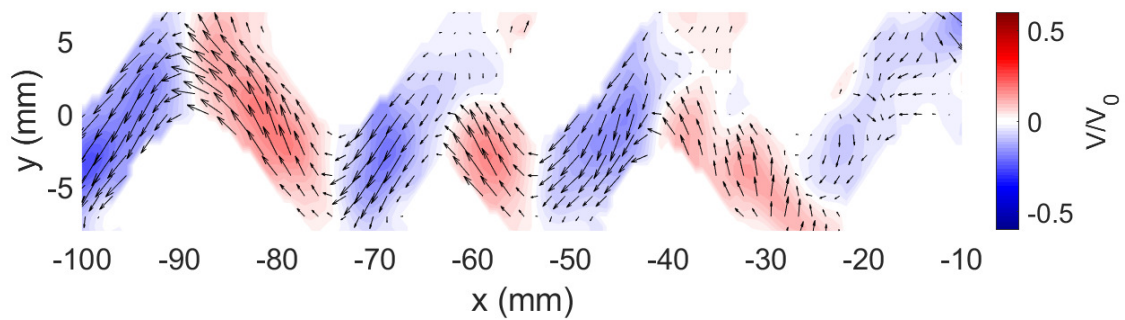


Figure 6.28: Velocity map $V^* = V/V_0$ in the Type zigzag groove.

This figure shows that the vectors are well aligned with the groove direction with a change of sign of the velocity V at each change of direction of the grooves.

To determine the velocity in the groove direction and in the transverse direction, $U_{//}$ and U_{\perp} are calculated with the projection of the velocity on the groove axis (\vec{x}_g, \vec{y}_g) as sketched on Fig.6.29.

Thus, the spatially averaged velocities $U_{//}$ and U_{\perp} over the width of the groove are calculated all along the contact patch area in order to determine the evolution of the flow (Fig.6.30)

This figure highlights that the velocity in the perpendicular direction (U_{\perp}) is low inside the zigzag groove except in the weld zone. Therefore, the velocity in the zigzag groove fits well the shape of the

groove. In the parallel direction, the velocity grows from the beginning of the contact patch area ($x = 0$ mm) to the end of the contact patch ($x = -100$ mm). Holes are visible for the parallel component profile which corresponds to the position of the weld and therefore to the change of direction of the groove.

6.2.2.2 Flow inside Type W grooves.

For this tire, each directional groove is composed of 3 segments with various inclinations (Fig.6.31). We can see with the velocity map in y direction V Fig.6.31, that the velocity change sign inside the mid-zone and the shoulder zone between the grooves W2 and W3. Therefore the sign seems to change sign with the position in the contact patch area.

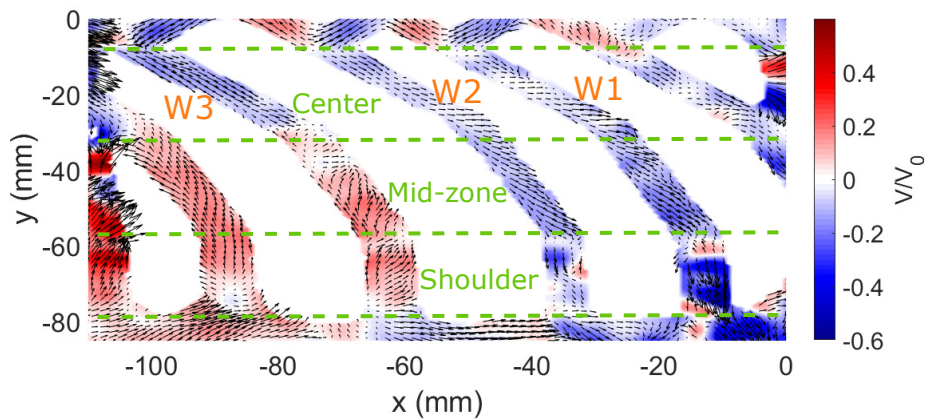


Figure 6.31: Velocity map $V^* = V/V_0$ in the Type W grooves.

To describe well the flow inside the type W grooves, the velocity inside the grooves is projected in the groove direction (that changes from center to side-zone) (Fig.6.32).

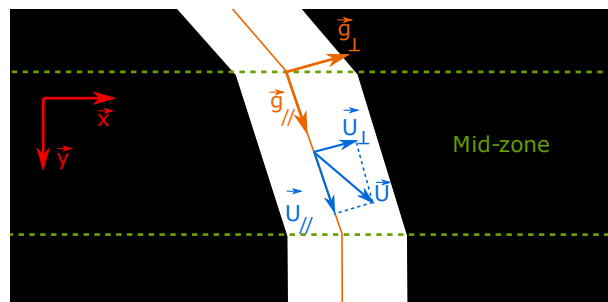


Figure 6.32: Scheme of the projection of velocity vectors on the axes of the grooves with $\vec{U}_{//}$, the velocity in the groove direction and \vec{U}_{\perp} transverse velocity in the groove.

To make this projection, every vector is projected on the referential of the part of the grooves where the vector has its origin following : $\vec{U}_{//} = \vec{U} \cdot \cos(\theta)$ and $\vec{U}_{\perp} = \vec{U} \cdot \sin(\theta)$. Then the spatially averaged velocities in x direction in and out (respectively $\vec{U}_{//}$ and \vec{U}_{\perp}) the grooves axis can be studied for the three complete grooves in the contact patch.

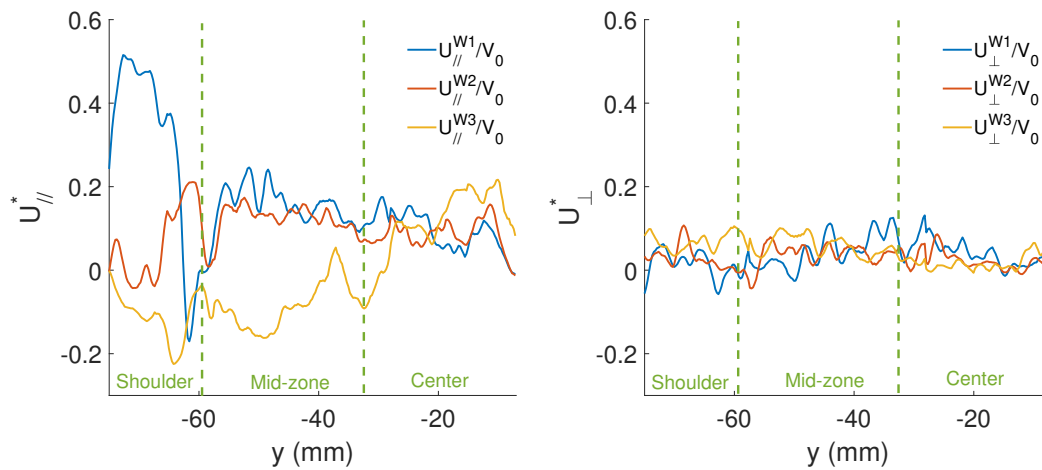


Figure 6.33: Mean velocity projected in the grooves a) in the groove axis and b) perpendicularly to the groove axis.

The velocity in the axes of the grooves $U_{//}$ (Fig.6.33 a)) highlights that the direction of the flow is well aligned with the results presented for the transverse grooves of the summer tire. Especially in the shoulder zone, the velocity obtained in the groove $W1$ is higher than the one in the $W2$ groove which is higher than the one in the $W3$ groove. To illustrate this behaviour in the different portions (center, mid-zone, shoulder). The position of the groove portion in the contact patch area is quantified with the location of the center of the groove portion (as sketched Fig.6.34).

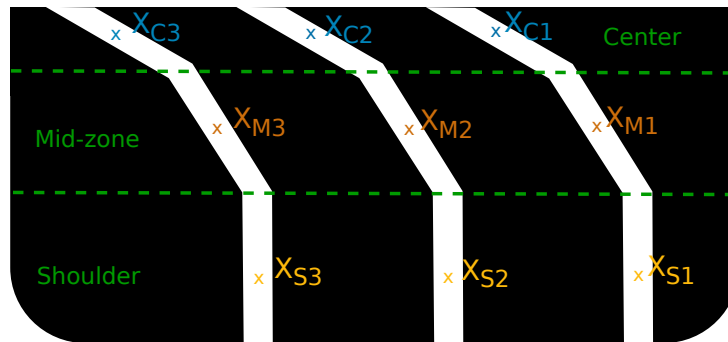


Figure 6.34: Sketch of the position determination of the groove parts position in the contact patch.

The location of the geometric barycentre of each groove portion is quantified in percentage of its position inside the contact patch area as for the PCY4 Type C groove (Fig.6.22). The spatially averaged velocity $U_{//}$ is calculated for every tire groove portion. Results of the spatially averaged velocity $\overline{U_{//}}$ in every portion of the grooves (respectively $\overline{U_{//}^C}$ for the center part, $\overline{U_{//}^M}$ in the mid-zone and $\overline{U_{//}^S}$ at the shoulder) are represented in function of the position in the contact patch area on Fig.6.35.

The spreading of the plotted data is very large. It has to be noticed that for such plot probably a greater number of runs is necessary to converge. Nevertheless a linear regression is plotted for each groove portion.

This plot shows the same behaviour for the shoulder zone than the one observed for the Type C groove of the PCY4 model : the velocity $\overline{U_{//}^S}$ is clearly a decreasing function of the location of the groove portion inside the contact patch area. A similar trend is obtained for $\overline{U_{//}^M}$. For the center zone, this can not clearly

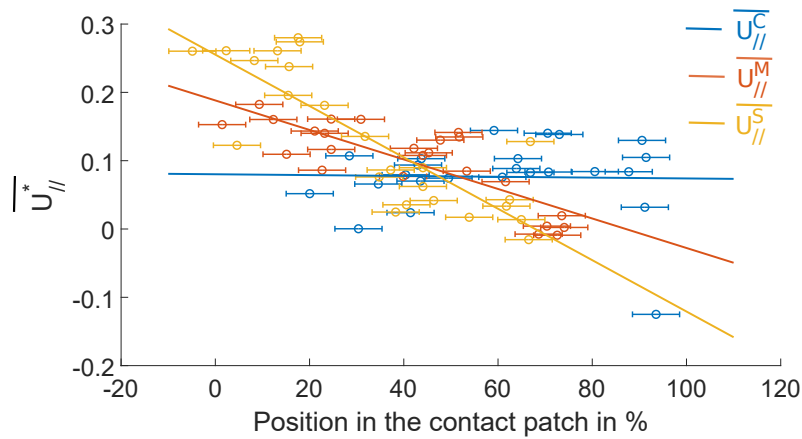


Figure 6.35: Averaged $U_{//}$ velocity component in a groove segment versus the location of its geometric barycentre of the groove inside the contact patch area.

be observed. This also shows that the slope of the linear regression is of a slightly higher magnitude for the shoulder zone than the mid-zone. This can be linked to the inclination of the groove part compared to the car rolling direction with an inclination in the shoulder zone of approximately $\theta_s = 90^\circ$ compared to approximately $\theta_m = 60^\circ$ for the mid-zone and approximately $\theta_c = 40^\circ$ for the center zone (as sketched in Fig.6.36). This inclination could possibly influence the deformation of the groove and with the contact and then modify the flow in it.

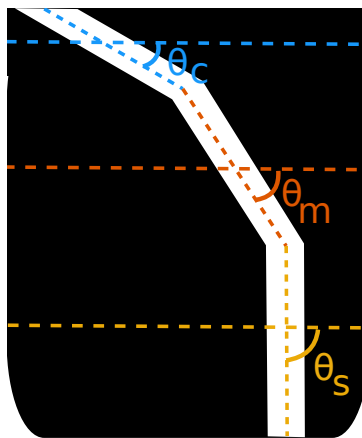


Figure 6.36: Inclination of the groove portions compared to the car rolling direction.

6.3 Conclusions.

In this chapter, we have seen that the measurement technique proposed in this work allows us to measure the velocity field in different tire configurations and in different flow zones. This also highlight that even with metrological differences between both tire configuration, the measurements appears to be repeatable. No major differences can be observed including inside the grooves where direct illumination is available for the PCY4 longitudinal groove as opposed to to the CCP tire grooves.

It also appears that the post processing proposed in this work is compatible for both tire configurations. The tire positioning procedure allows us to analyse specific behaviour in the contact patch area

from different snapshots. The averaging process in front of the tire gives satisfying results in front of both tire model.

Firstly, the measurements of the flow velocity field in front of the tire has been demonstrated quite repeatable with low standard deviations for both tire model and wear state. It also shows differences in the averaged velocities in the water-bank and at the shoulder between new and worn tires. It also highlighted difference between the velocity in the water-bank for the PCY4 and the CCP tire.

In the tire grooves, two main classes of grooves have been highlighted by their differences in the structure of the flow. Firstly in longitudinal grooves (Type A and Type B), a primary flow is going through the grooves and drives water through the contact patch area with an influence of the wear indicator on the velocity of this primary flow. Then a secondary flow is observed with a vortex like structure which varies depending of the aspect ratio of the tire groove. This vortex structure is measured for the first time in this work and confirms the hypothesis proposed by Yeager 1974.[81].

The second main class of grooves is the transverse grooves as (Type C and Type W). In these grooves, present at the shoulder of the PCY4 tire, or in the CCP tire, the flow is mainly in the groove direction with a low velocity perpendicular to the groove axis. This velocity in the groove direction is highly dependent on the groove position in the contact patch area and seems to also depends on the groove inclination.

Finally the "zig-zag" groove in the center of the CCP tire can be qualified as similar to a longitudinal groove in its primary flow with a growing velocity through the contact patch area which is driving the water through the contact patch area.

7 Analysis of the tire flow.

In this chapter, we propose to go deeper on the velocity field analysis for the three main types of flow (In front of the tire, Inside longitudinal grooves (Type A and B) and inside transverse grooves (Type C and W)). We will also present our hypothesis which can explain the different phenomenon highlighted.

In a first section, we will focus our analysis on the self-similarity of the flow in front of the PCY4. This analysis will be based on the study of the evolution of the characteristic velocities defined in Chapter.6 as a function of the vehicle speed for every tire model studied. Afterwards, the analysis of the length of the water-bank allows the determination of a characteristic length of the flow. This length of the water-bank is studied only for the PCY4 worn tire. This is because it is the only case where the forehead of the water-bank appears in the field of view. Thus, velocity field maps normalised in length and in velocity allow us to discuss the self-similarity of the flow with the increase of the vehicle speed.

In a second section, the flow in straight grooves (Type A and B) will be discussed. In this section, similarity of the velocity component profiles $\langle U_A^* \rangle$ inside Type A groove will be analysed for the new tire case. Then, the evolution of the vortex intensity with the vehicle speed is discussed highlighting a non-symmetrical aspect between A1 and A2 grooves. To finish this section, propositions are made in order to explain the vortex creation mechanism shown in the previous chapter.

Finally, the mechanisms involved in the evolution of the velocity in transverse grooves (Type C and W) is proposed with afterwards a discussion on the interactions between these transverse grooves with the longitudinal grooves for PCY4 tire (interactions Type C/Type B).

7.1 Flow in front of the tire.

This part will be segmented in three sections. Firstly, the evolution of the characteristic velocities in the water-bank and at the shoulder with the vehicle speed will be studied for both wear state and both tire model. This will highlight some specific characteristics of the flow according to what was observed for $V_0 = 50$ km/h in Chapter.6. In a second section, the evolution of the length of the water-bank will be studied highlighting the evolution of the shape of the water-bank with the vehicle speed for the worn PCY4 tire. Finally, the self-similarity of velocity component maps and profiles will be studied for the worn PCY4 tire, showing repeatable behaviours with the increase of the vehicle speed but also differences.

7.1.1 Evolution of the velocity with the vehicle speed.

In this section, the evolution with the car speed of the characteristic velocities defined in Chapter.6 for both water-bank ($\overline{U_{WB}}$) and shoulder ($max.V_s$ and $\overline{V_s}$) flows are studied. This analysis is performed for both tire model.

Firstly, for the PCY4 tire, the evolution of $\overline{U_{WB}}$ with the vehicle speed V_0 is presented on Fig.7.1, for both new and worn tires.

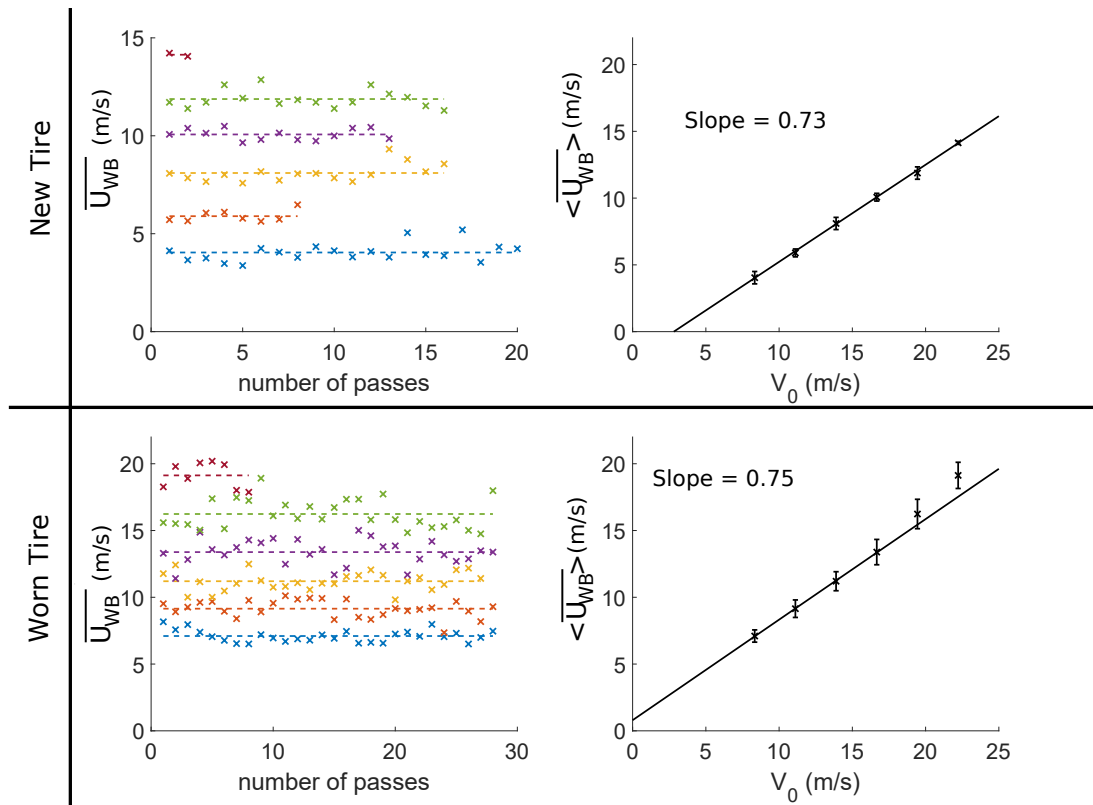


Figure 7.1: Spatially averaged velocity in the WB $\overline{U_{WB}}$ in front of the tire for different passes (left). Ensemble averaged $\langle \overline{U_{WB}} \rangle$ versus the vehicle speed (right).

Fig.7.1 highlights, for every vehicle speed, a low dispersion of the characteristic velocity in the WB especially for the new tire with standard deviations presented in Tab.7.1. These deviations in Tab.7.1 are slightly higher for the worn tire case which shows a stronger variability for low water height $h_{water} = 1.5$ mm. However, these deviations remain small (around 5% of V_0). This figure shows a linear evolution of the fluid velocity in the WB with the vehicle speed. The slope of the linear regression is approximately the same for both new and worn tire, around 0.75. The difference between both configurations is a shift of the regression. Therefore, in the worn tire configuration with $h_{water} = 1.5$ mm the velocity in the WB is greater than for a new tire with $h_{water} = 8$ mm. An other aspect that can be observed here is the deviation to the linearity for the worn configuration at high speeds ($V_0 = 70$ up to $V_0 = 80$ km/h).

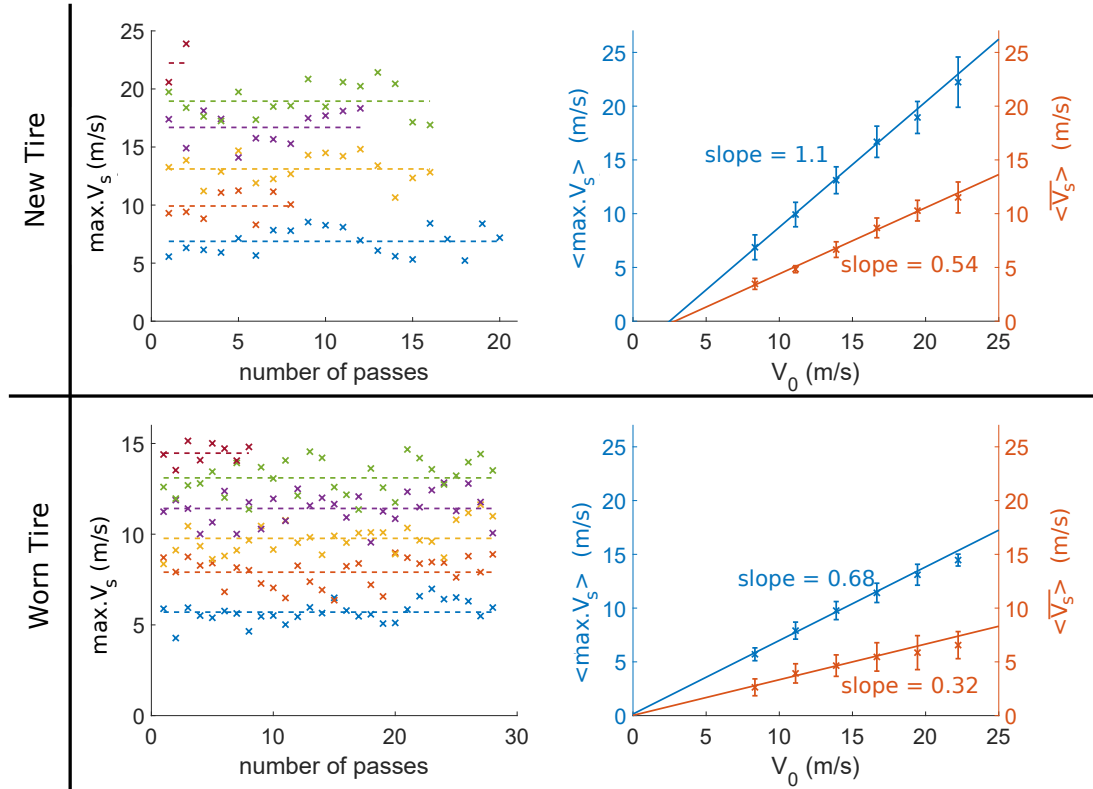


Figure 7.2: Maximum velocity in the shoulder $max.V_s$ in front of the tire for different passes (Left). Maximum velocity $max.V_s$ and averaged velocity \overline{V}_s function of the vehicle speed (Right).

Case	30 km/h	40 km/h	50 km/h	60 km/h	70 km/h	80 km/h
PCY4 New	5.6%	2.7%	4.1%	1.8%	2.4%	none
PCY4 worn	5.5%	5.9%	5.1%	5.7%	5.4%	4.4%

Table 7.1: Table of the standard deviation in $\langle \overline{U}_{WB} \rangle$ normalised by the vehicle speed.

The same analysis is proposed for the shoulder zone with both characteristic velocities represented for both tire wear states (Fig.7.2).

With this figure, the global velocity at the shoulder \overline{V}_s appears to be approximately $\overline{V}_s = \frac{max.V_s}{2}$. Therefore, our analysis can be based on both values. For the new tire, the standard deviation in $max.V_s$ is greater than the standard deviation in \overline{V}_s . Contrarily, the standard deviation is greater for \overline{V}_s than with $max.V_s$ for the worn tire as observed at $V_0 = 50$ km/h in Chapter.6. Those standard deviations are presented in Tab.7.2 and Tab.7.3.

Those standard deviations are higher than for the flow in the WB. Here the standard deviation is around 10% of the vehicle speed for $max.V_s$ for the new tire. For the worn tire, the standard deviation is lower for $max.V_s$, approximately 6% (except for $V_0 = 80$ km/h). This higher standard deviation than in the WB can be explained by the Type C groove locations at the vicinity of the contact patch area which has a large influence on the velocity field for the worn tire.

The velocity at the shoulder $max.V_s$, appears to be greater for the new tire with a coefficient for the linear regression of approximately 1.1 compared to the coefficient 0.68 for the worn tire.

For the worn tire, the velocities $max.V_s$ and \overline{V}_s appears to be slightly under the linear regression for

high vehicle speed ($V_0 = 70$ up to 80 km/h).

Case	30 km/h	40 km/h	50 km/h	60 km/h	70 km/h	80 km/h
PCY4 New	13.8%	10.3%	9.0%	8.5%	7.7%	none
PCY4 worn	7.2%	7.1%	6.1%	5.4%	5.0%	2.5%

Table 7.2: Table of the standard deviation in $max.V_s$ normalised by the vehicle speed.

Case	30 km/h	40 km/h	50 km/h	60 km/h	70 km/h	80 km/h
PCY4 New	4.9%	3.7%	5.2%	2.9%	6.1%	none
PCY4 worn	9.4%	8.1%	7.2%	7.9%	8.1%	5.6%

Table 7.3: Table of the standard deviation in \bar{V}_s normalised by vehicle speed.

The exact same analysis is now made with the CCP tire. The evolution of the characteristic velocity in the water-bank (\bar{U}_{WB}) is presented in Fig.7.3.

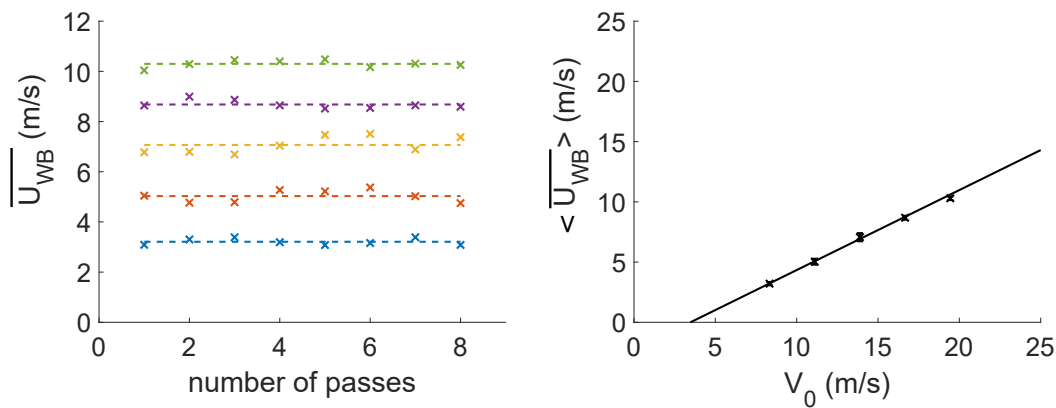


Figure 7.3: Spatially averaged velocity in the WB \bar{U}_{WB} in front of the tire for different passes (Left). Ensemble averaged $\langle \bar{U}_{WB} \rangle$ function of the vehicle speed (Right).

Fig.7.3 highlights a low dispersion of the velocity in the WB with standard deviations presented Tab.7.4. This disparity appears to be approximately 2% of the vehicle speed which is noticeably lower than for the PCY4 Tire. This figure shows a linear evolution of the fluid velocity in the WB with the increase of the vehicle speed. The slope of the linear regression is approximately 0.64. This coefficient is lower than for the PCY4 Tire. The velocity in front of the tire center is lower for the CCP tire than for the PCY4 tire for every vehicle speed as observed Chapter.6 for $V_0 = 50$ km/h.

Case	30 km/h	40 km/h	50 km/h	60 km/h	70 km/h
CCP	1.6%	2.2%	2.4%	1%	0.8%

Table 7.4: Table of the standard deviation in \bar{U}_{WB} as a percentage of the vehicle speed.

For the shoulder flow, the characteristic velocities are presented for the CCP tire in Fig.7.4.

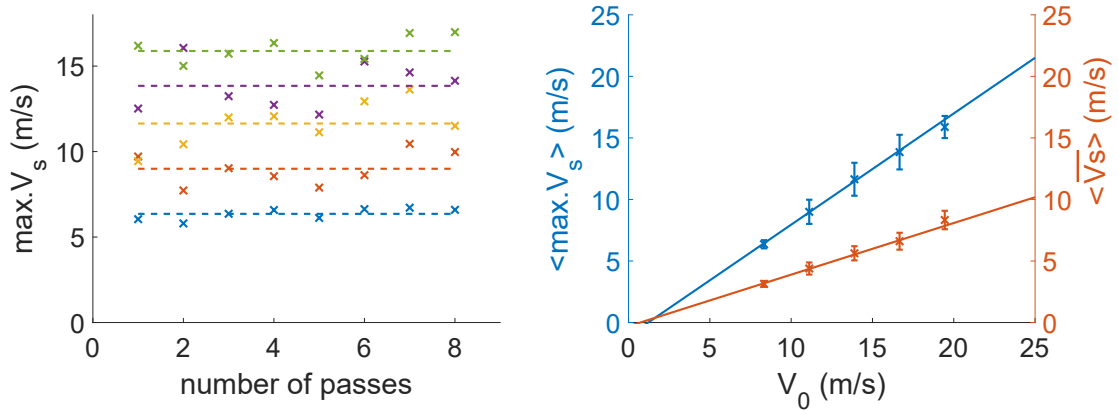


Figure 7.4: Maximum velocity in the shoulder $\max.V_s$ in front of the tire for different passes (Left). Maximum velocity $\max.V_s$ and averaged velocity \overline{V}_s function of the vehicle speed (Right).

In the case of the CCP tire, it appears that the standard deviation of the \overline{V}_s is lower than the standard deviation of $\max.V_s$. A table of standard deviation for both value is presented Tab.7.5. This behaviour of the standard deviations was the same for the PCY4 tire in new configuration.

Case	30 km/h	40 km/h	50 km/h	60 km/h	70 km/h
\overline{V}_s	2.9%	4.4%	4.2%	4.1%	3.9%
$\max.V_s$	4%	8.8%	9.6%	8.4%	4.6%

Table 7.5: Table of the standard deviation in \overline{V}_s and $\max.V_s$ in percentage of the vehicle speed.

In this configuration, the evolution of the maximum and averaged velocities are both linear with the tire rolling speed. In this case, with the CCP Tire, the coefficient of the linear evolution of the maximum velocity at the shoulder function of the vehicle speed is 0.9. Therefore, the coefficient of the velocity at the shoulder function of the vehicle speed is lower for the CCP tire than for the PCY4 tire (respectively 0.9 and 1.1).

In conclusion, the characteristic velocities in front of the tire are close to a linear evolution for both wear state and both tire model. The difference lays in the slope and the intercept of the regressions. Therefore, the velocities can be normalised by V_0 in order to study the self-similarity of the flow.

The length of the water-bank also varies with the vehicle speed. This parameter can not be quantified for new tire cases due to the large length of the water-bank which is greater than the field of view. However, the evolution of this parameter with the vehicle speed can be analysed for the worn tire and is proposed in the following section.

7.1.2 Evolution of the water-bank length with the vehicle speed.

The length of the water-bank (L_{WB}) vary with the vehicle speed. This length is defined for every vehicle speed as the length needed to reach a normalised velocity of 0.4 in the forehead as $U_{WB}^*(L_{WB}) = 0.4$. Due to the evolution of the maximum velocity in the water-bank as $0.75.V_0$ the threshold value $U_{WB}^*(L_{WB}) = 0.4$ is chosen arbitrarily to be approximately half the maximum velocity in the water-bank. To study this variation of the water-bank length, the worn tire case is studied here which is the only configuration where

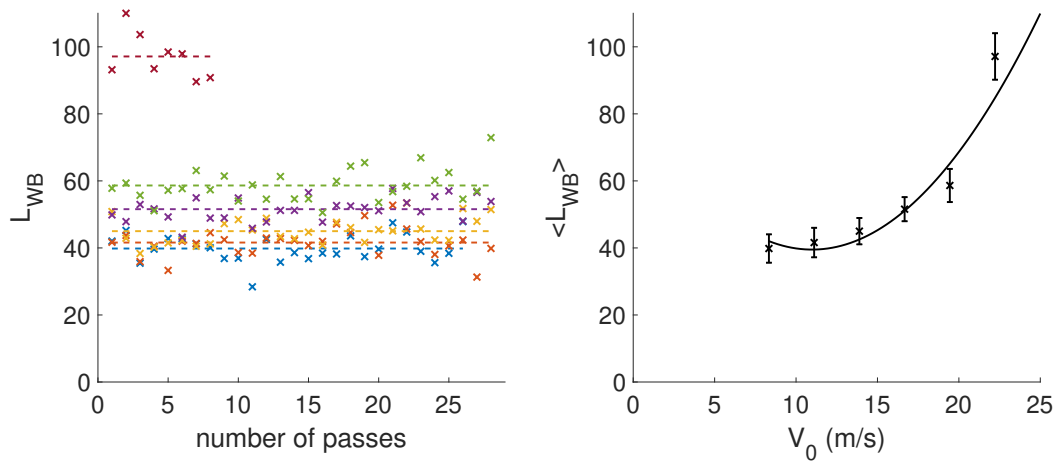


Figure 7.6: L_{WB} for every measurements and its evolution function of the vehicle speed.

the whole water-bank is visible. The analysis of this length is repeated for all the vehicle speed based on the water-bank velocity profiles $U_{WB}^*(x)$ (Fig.6.4) as illustrated for two snapshots at two different vehicle speeds $V_0 = 30$ and $V_0 = 50$ km/h (Fig.7.5).

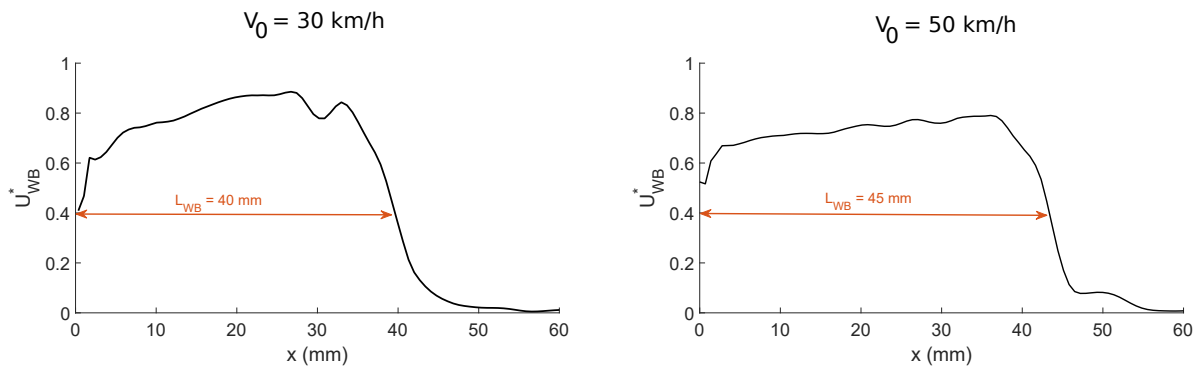


Figure 7.5: Measurement of the length of the water-bank for two single shot PIV measurements.

From these instantaneous cases, we can observe a growth of the water-bank length L_{WB} with the car speed from $V_0 = 30$ km/h to $V_0 = 50$ km/h. We show the whole values obtained from all cases on Fig.7.2 (left). The evolution of the associated ensemble averaged length of the water-bank as a function of the car speed is presented Fig.7.6 (right).

First, this figure shows a slight disparity in the length of the water-bank between each run at every vehicle speed. This could be caused by the uncertainties of the contact patch area location determination and on the water height regulation. Unsteady phenomenons can also induce variations of the length of the water-bank from run to run as the presence of wear indicator or the location transverse grooves. Nevertheless, this figure shows that the ensemble averaged length of the water-bank L_{WB} evolves non linearly with the vehicle speed V_0 . At higher vehicle speed, the water-bank length grows fast (between $V_0 = 70$ and $V_0 = 80$ km/h) and corresponds to the zone where the loss of contact between the tire and the road grows significantly according to the study of the evolution of the contact patch area with the vehicle speed made by Todoroff et al. 2018 [72].

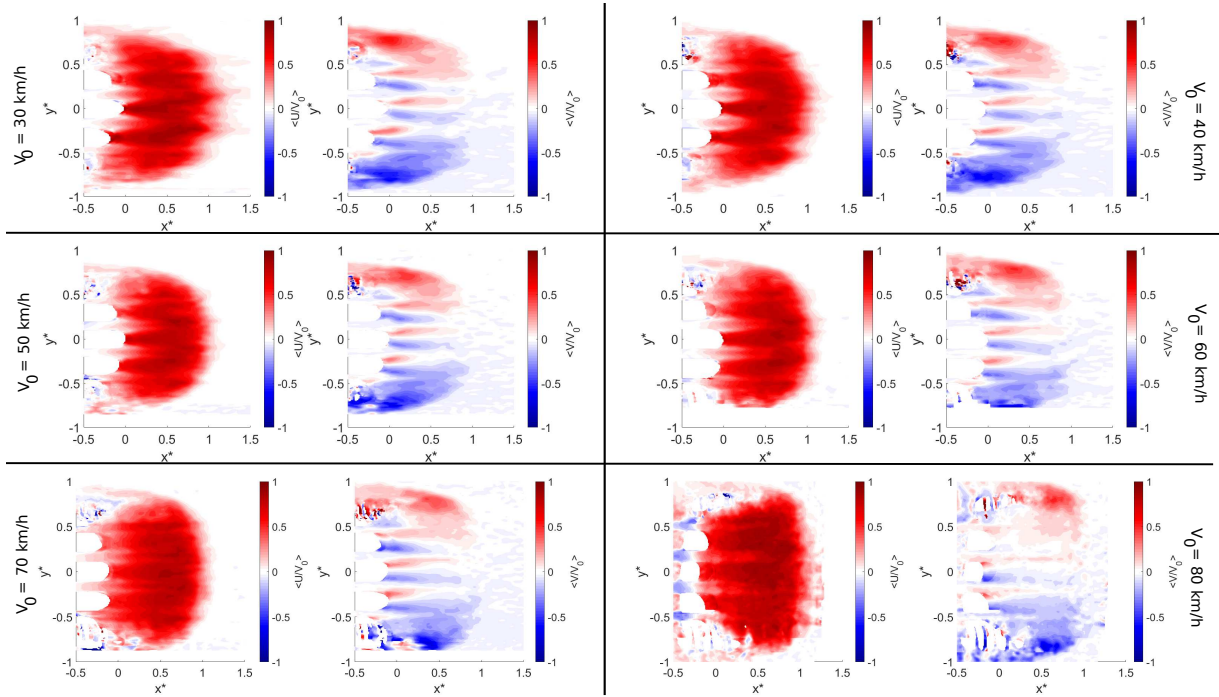


Figure 7.7: Normalized ensemble averaged velocity component maps for cases with $V_0 \in [30; 80]$ km/h.

7.1.3 Self-similarity of the flow.

Evolution of characteristic velocities at the shoulder and in the water-bank with the vehicle speed were studied. This highlighted the linear evolution of these velocities with V_0 . Thus, ensemble averaged velocity maps, as shown Fig.6.2, can be normalized by the vehicle speed V_0 for comparison. The evolution of the water-bank length with the vehicle speed was also quantified. Therefore, the x axis can be normalised by the length of the water-bank as $x^* = x / \langle L_{WB} \rangle$. In y direction no specific evolution with the vehicle speed is observed. Thus, the y axis is normalised by the half width of the tire ($y^* = y/w_t$, with $w_t = 112.5$ mm, half width of the tire). This allows us to confront the structure of the normalised velocity component maps at each vehicle speed (Fig.7.7).

The similarity between these maps highlights that the velocity in front of the tire mostly depends on the vehicle speed V_0 . However, a difference of the water-bank shape is visible at high vehicle speeds. The shape of a velocity lobe $\langle U \rangle$ in front of the tire seems to evolve. Isoslines at $\langle U \rangle = 0.4$ are shown for every vehicle speeds (Fig.7.8) that shows such lobe evolution.

To highlight this similarity in details, the ensemble averaged velocity component profiles in the water-bank ($\langle U_{WB}^* \rangle$) and at the shoulders ($\langle V_s^* \rangle$) with the normalised axis x^* are studied in Fig.7.9 for vehicle speed in the range $V_0 \in [30; 80]$ km/h. For the velocity component profiles at the shoulder the maximum are superposed to better visualise the similitude between profiles.

These velocity component profiles shows a similarity between the normalised profiles. A difference to notice between these profiles is the decrease of the velocity $\langle U_{WB}^* \rangle$ in the tire vicinity with the increase of the vehicle speed (an exception can be highlighted for $V_0 = 80$ km/h). This decrease can be due to the thin film in the tire vicinity that is generated by the lift of the tire envelope with the car speed increase. At the shoulder, when the axis x is normalised by the water-bank length, the velocity component profile seems to become shorter in x^* direction with the increase of the vehicle speed V_0 . The location x^*

for which the velocity at the shoulder is null ($\langle V_s^* \rangle = 0$) corresponds to $x^* \sim 1$ for $V_0 = 30$ km/h and $x^* \sim 0.5$ for $V_0 = 80$ km/h. This illustrates a different evolution of the length of the shoulder line with the vehicle speed compared to the length of the water-bank. This difference is mainly due to the evolution of the shape of the contact patch area with the increase of the vehicle speed (Fig.7.11). At high vehicle speed ($V_0 = 70 - 80$ km/h), the shape of the contact patch area is modified and the reduction of the contact length L_{cont} becomes different in the center of the tire than at the shoulder. Thus, characteristic length of the velocity component profiles in front of the tire are modified as well.

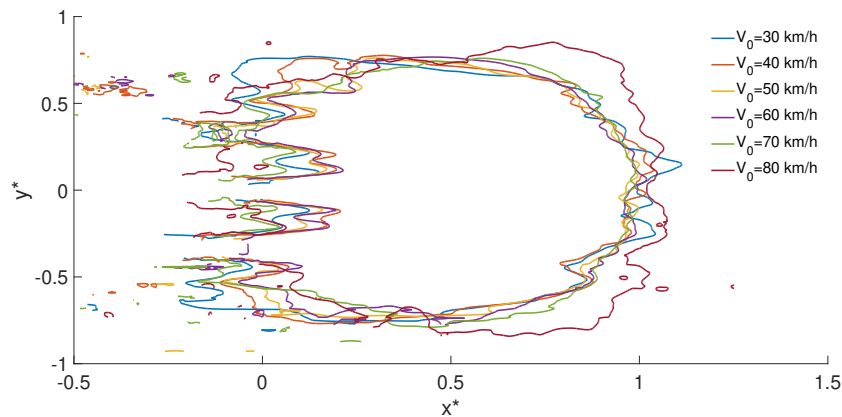


Figure 7.8: Isolines $\langle U^* \rangle = 0.4$ of the normalised velocity component maps (from Fig.7.7) at each vehicle speed.

As discussed, the general behaviour of the flow in front of the tire is generally linear with the vehicle speed. This is particularly visible for the new tire case (for the CCP or for the PCY4 tire) and also for worn tire in the range $V_0 \in [30;60]$ km/h as discussed previously. However, at high vehicle speed (especially $V_0 = 80$ km/h, the deviation from the linearity grows. This is slightly visible Fig.7.1 for the water-bank, more visible at the shoulder Fig.7.2 and way more visible for the length of the water bank Fig.7.6. At high speed it seems that non-linear phenomenon occurs. Based on the Todoroff et al. 2018 [72] visualisations, it appears that at high speed, the length of the contact patch area decreases rapidly and the shape of the contact patch area becomes more cupped shaped (Fig.7.10).

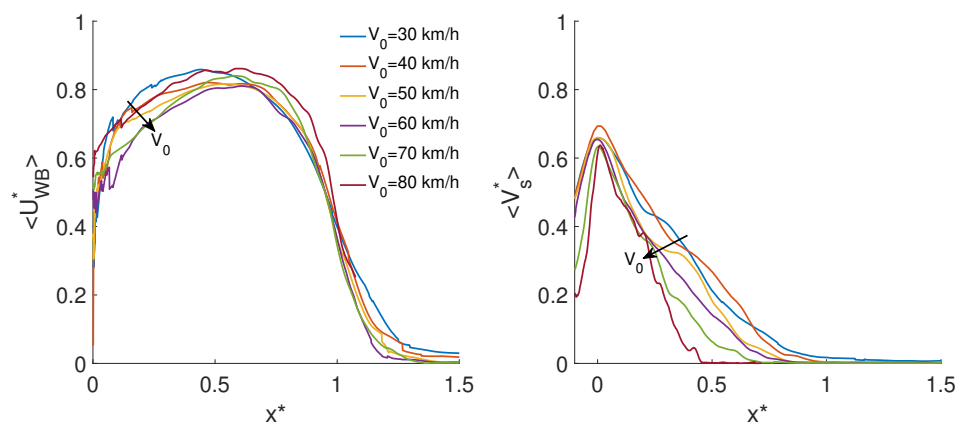


Figure 7.9: Normalised velocity component profiles in the water-bank and at the shoulder for $V_0 \in [30;80]$ km/h.

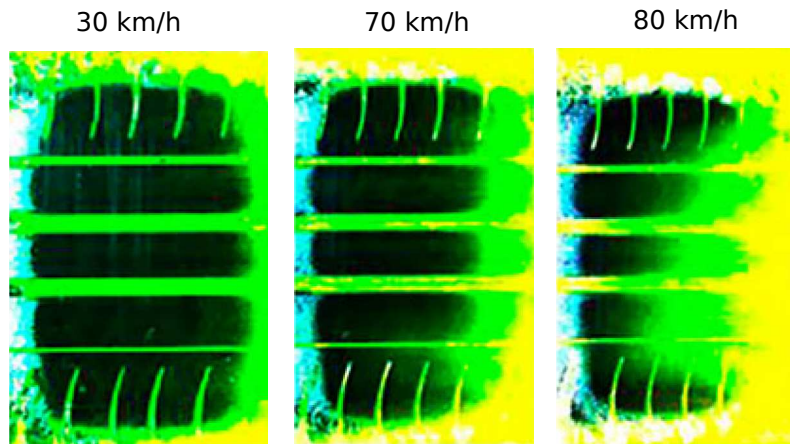


Figure 7.10: Shape of the contact patch area with an increasing speed according to Todoroff et al. 2018 [72].

In these visualisations, the green dye in the water is visible and the contact patch area corresponds to the black area. We can see here a similar contact patch shape between the vehicle speed $V_0 = 30$ and $V_0 = 70$ km/h with an ovoid shape. The decrease of the length of the contact patch area is visible between $V_0 = 30$ and $V_0 = 70$ km/h. However, the contact patch length drastically decreases between $V_0 = 70$ and $V_0 = 80$ km/h. At $V_0 = 80$ km/h, the contact patch shape changes and becomes more cupped shape. A direct link seems to exist between the contact patch shape and the behaviour of the flow in front of the tire.

We can emit an hypothesis to explain the behaviour of the flow. It is shown on the streamline schemes (as presented on Fig.7.11). Let's remind that the deviation to the linearity in terms of velocity is an over velocity in the water-bank and an under velocity at the shoulder for the worn tire at $V_0 = 80$ km/h. At $V_0 = 30$ and $V_0 = 70$ km/h, for the ovoid shape (Fig.7.11 left), the flow comes in front of the tire and is evacuated by the side. For the cupped shape (Fig.7.11 right), a part of the flow is trapped in the center of the tire and can not be evacuated by the side due to the sharpness of the contact patch area at the shoulder. If we associate a global (both zones) conservation of the flow rate to this change of evacuation ways, the transverse velocity decreases at the shoulder and the longitudinal velocity increases in the center. Such explanation is coarse due to large 3D effects but at the first order this could explain the local flow behaviour.

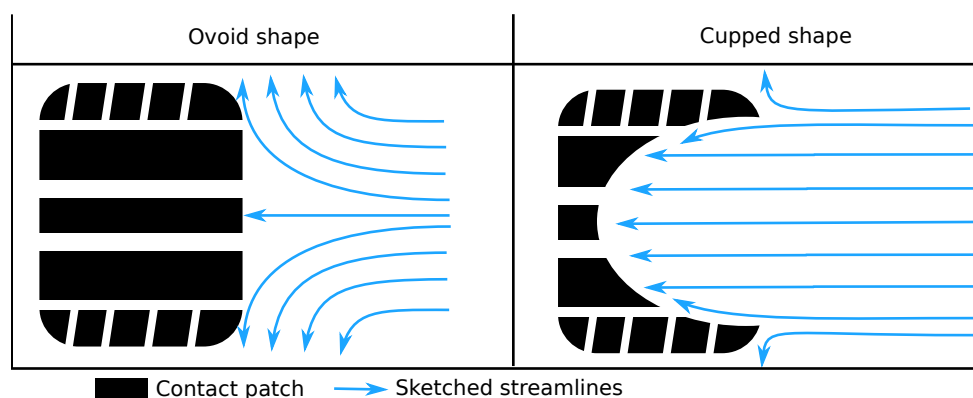


Figure 7.11: Scheme of the hypothesis proposed for the loss of linearity in the velocity at high speed.

However, the number of data for the highest speeds does not allow us to ascertain this non linear deviation. Measurements should be performed at higher speeds for both new and worn tire configurations.

7.2 Flow in straight grooves.

The second flow zone analysed in this chapter is the straight groove zone (Type A and Type B grooves of the PCY4 tire).

7.2.1 Flow in the streamwise direction.

This Section will be segmented into two parts. In the first one, the analysis of the velocity in the streamwise direction function of the vehicle speed is proposed for both PCY4 wear states. This will highlight the general evolution of this velocity with the vehicle speed and also enforce the influence of the presence of the wear indicator. In the second part, the similarities and differences are presented between the normalised velocity profiles for different vehicle speed.

7.2.1.1 Evolution of the velocity with the Vehicle speed.

To analyse the evolution of the velocity inside tire grooves with the vehicle speed. Characteristic velocity is defined as in Chapter.6. If we note x_{min} the location where is found the minimum velocity inside the tire groove (see Fig.6.10 and Fig.6.11), the characteristic velocity \overline{U}_A is calculated as the spatially averaged velocity between $[x_{min} - 5; x_{min} + 20]$. We will now focus our analysis on this plateau averaged velocity \overline{U}_A depending on the vehicle speed for both new and worn tire configurations.

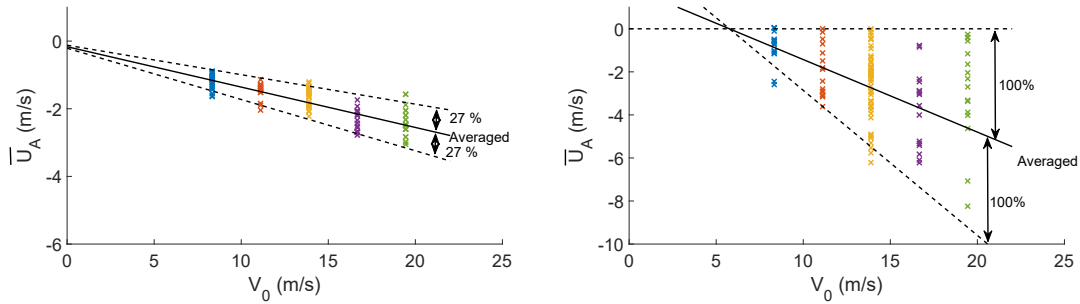


Figure 7.12: Velocity in the streamwise direction inside Type A grooves function of the vehicle speed.

This figure highlights a higher variability inside the tire grooves than in front of the tire in the streamwise direction. This variation is illustrated by a cone of averaged velocity inside the tire grooves in the streamwise direction. The cone spreading is higher for the worn tire grooves with a variation of $\pm 100\%$ between two measurements. For the new tire the spreading of this cone is lower (approximately $\pm 27\%$). Let's note that the ratio τ_{height} between the height of the wear indicator h_{WI} and the height of the groove h_g is $\tau_{height} = 100\%$ for the worn tire and $\tau_{height} = 26.7\%$ for the new tire. Which corresponds to the spreading of the cone presented in Fig.7.12.

In conclusion, the water averaged velocity in the streamwise direction in Type A grooves is almost linearly linked to the vehicle speed. However, a dispersion also linked to the vehicle speed and seems to be influenced by the portion of the groove taken by the wear indicator. In type B grooves, the same

conclusion is available for worn tire configuration where the Type B grooves are isolated and not directly linked to type C grooves (Fig.7.13). However, for new tires, where the Type B grooves are linked to the Type C grooves, the flow is highly variable with a general tendency to change the flow direction at the center of the groove (Fig.6.10).

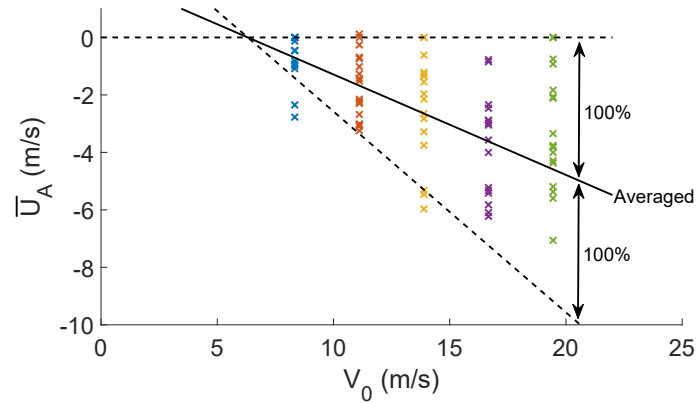


Figure 7.13: Velocity in the streamwise direction inside Type B grooves for the worn tire function of the vehicle speed.

For the worn tire, the averaged velocity in the streamwise direction in the Type B grooves is of the same order of magnitude than the velocity in the Type A grooves.

Therefore, a similarity analysis is not possible for the worn tire due to the high influence of the wear indicator which makes every run unique with a unique wear indicator location. However, even if the wear indicator might have an influence for new tire Type A grooves, the general linear evolution of the velocity with the vehicle speed makes possible a normalisation by the vehicle speed.

7.2.1.2 Similarity of the profiles.

In this Section an analysis is proposed in order to define similarity and differences for the velocity component U inside Type A grooves for the PCY4 new tire with the increase of the vehicle speed. The velocity component profiles in the streamwise direction were studied (Fig.6.10 up right). In Type A grooves, the profiles were described as decreasing at the beginning of the contact patch area down to a plateau. This description corresponds to the $V_0 = 50$ km/h profile. Let's now see the evolution of the velocity component profiles for new tire configuration in Type A grooves with an increasing vehicle speed V_0 Fig.7.14. Results at $V_0 = 80$ km/h are not presented here due to the lack of data for new tire at this speed.

Fig.7.14 shows the superimposition of these velocity profiles $\langle U_A^* \rangle$ for all presented vehicle speeds. The evolution at the beginning of the contact patch area is the same for every vehicle speed with a decrease of the velocity at the beginning of the contact patch area (before $x = 0$). Afterward, for $x < 0$ the gradient progressively reduces inside the tire groove to reach a plateau. At the end of the contact patch area, the profiles show a step which corresponds to the loss of contact. For the vehicle speeds in the range $V_0 \in [30; 50]$ km/h, the contact patch length is slightly reduced with the increase of the speed. Therefore, the length of the plateau is slightly reduced with the vehicle speed increase. For higher V_0 , the contact patch length start to drastically decrease and becomes shorter than the distance necessary for the flow to reach the plateau in the groove. Therefore, at higher vehicle speed, the corresponding profiles inside the

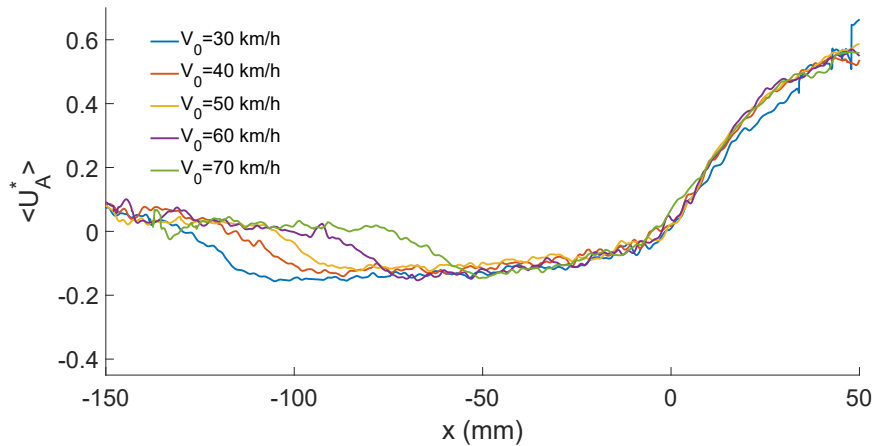


Figure 7.14: Ensemble averaged velocity profiles obtained at different vehicle speed.

tire grooves look like a linear evolution with a slope more than a plateau because of the reduction of the contact patch area.

In conclusion, to obtain a complete self similarity, it would be necessary to non dimensionalise the longitudinal coordinate by a characteristic length of the flow inside the groove. The length of the contact patch area could be a good candidate.

The length of the contact patch area is quantified for each vehicle speed as the length necessary to reach the half of the minimum velocity $\langle U_A^* \rangle = -0.075$ as $min. \langle U_A^* \rangle \sim -0.15$. Therefore, velocity profiles (Fig.7.14) are represented with a normalised longitudinal axis $x^* = x/L_{cont}$ in Fig.7.15.

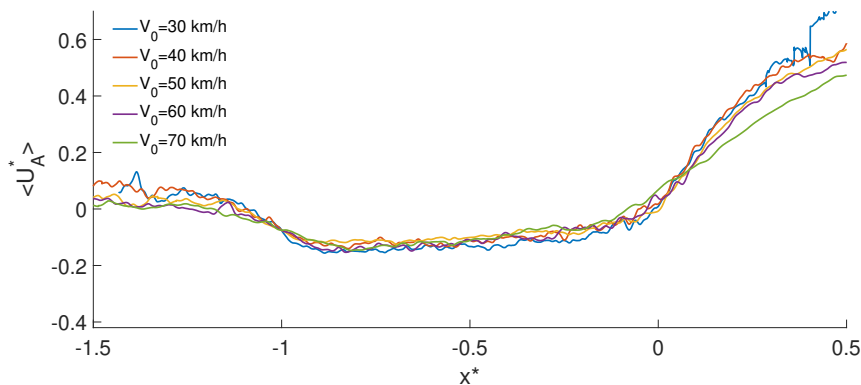


Figure 7.15: Ensemble averaged velocity profiles obtained at different vehicle speed.

The self-similarity of the profiles in the contact patch area is quite satisfying using V_0 and L_{cont} as characteristic velocity and length scales.

7.2.2 Vortex structure of the flow.

7.2.2.1 Vortices intensity.

In Type A grooves for the new tire case, velocity profiles presented in Fig.6.7 show a difference of velocity component V between two half parts of the groove (external and central as shown on the following figure)

with a higher velocity in the half part near the central RIB and a lower velocity in the half part near the external RIB. This separation between the central and external parts of the groove is illustrated Fig.7.16.

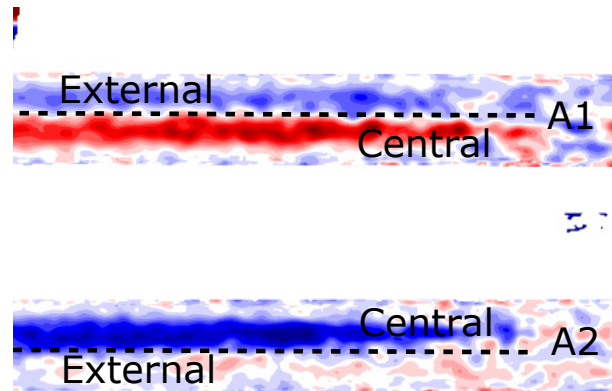


Figure 7.16: Velocity component map extracted from Fig.6.7 (up right) with the representation of the external and central part of both grooves.

We have clearly shown in the Chapter.6 the existence of vortices in the grooves. We can easily observe with these velocity component maps that the intensity of the vortex in the central part of each groove is higher than the one in the external part. This velocity map is as presented in the chapter.6, with a vehicle speed $V_0 = 50$ km/h. The same analysis is made for other vehicle speed and the ensemble averaged velocity profiles obtained for both A1 and A2 grooves are compared in Fig.7.17. The profiles are here spatially averaged in x direction in the contact patch area as for Fig.6.13. As for the velocity profile U , the case $V_0 = 80$ km/h is not presented due to the lack of data for new tire at this speed.

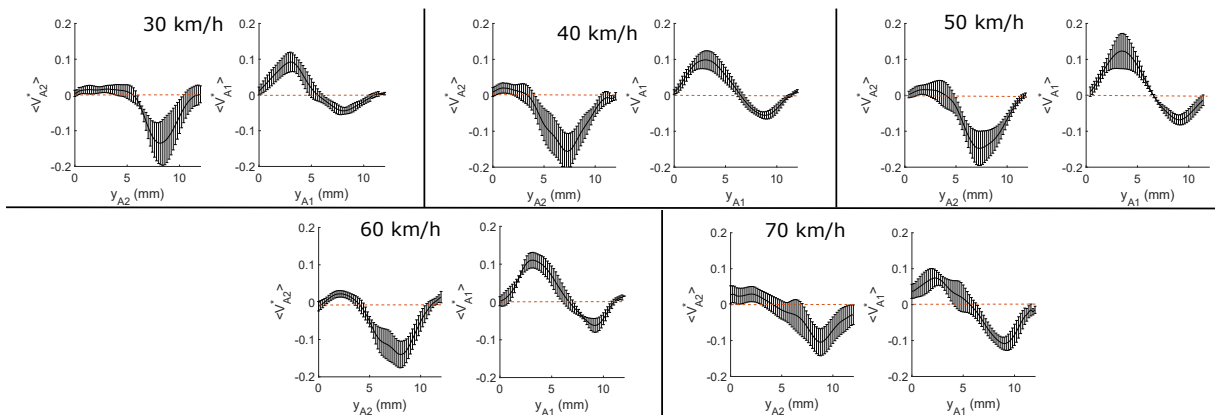


Figure 7.17: Ensemble averaged velocity profiles in spanwise direction.

For vehicle speeds from $V_0 = 30$ km/h up to $V_0 = 60$ km/h, velocity profiles are similar. For every vehicle speed, it appears that the external lobe (a lobe is a positive or negative extrema in the groove) in the A2 groove is lower than the one in A1 groove. The strength of both vortices inside a groove is characterised by both maximal positive and minimal negative values of each profiles. The evolution of this strength with the car speed is shown in Fig.7.18.

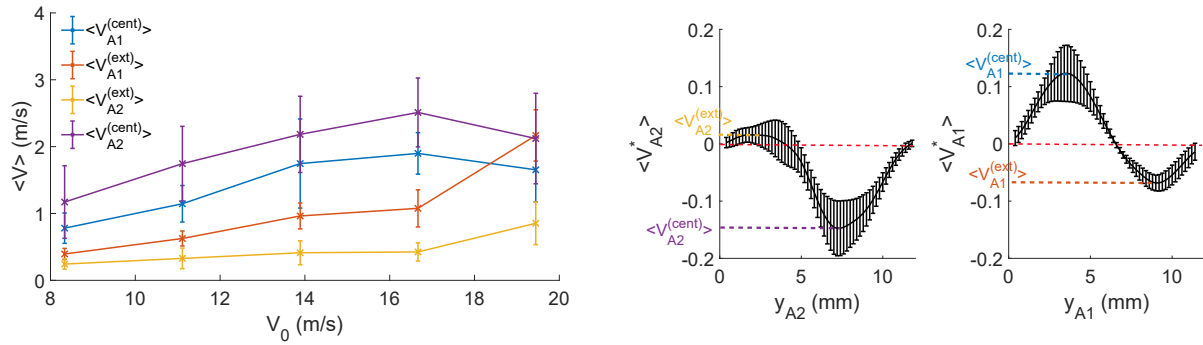


Figure 7.18: Lobes amplitudes as a function of the vehicle speed (left). Lobe amplitude definition with the case $V_0 = 50$ km/h (right)

It appears, that the strength of the central vortex in each groove is higher than the one of the external vortex. We can also observe a slight non symmetric features of the vortex strength between both Type A grooves. For the A1 groove, the velocity of the central vortex is lower than in the A2 and contrarily, the intensity of the external vortex is higher for the A1 than for the A2. These observations are available for all the range $V_0 \in [30; 60]$ km/h.

The explanation of this asymmetry proposed here is associated with the influence of the smallest Type D grooves linking longitudinal grooves. Based on visualisations of bubbles expulsion, these grooves are considering as rejecting bubbles from both extremities. The direction of expulsion of these Type D grooves are sketched in Fig.7.19 with vectors d . This direction of expulsion can enhance or reduce the intensity of the vortices and then explain the difference between both tire grooves depending on Type D grooves orientation as sketched Fig.7.19.

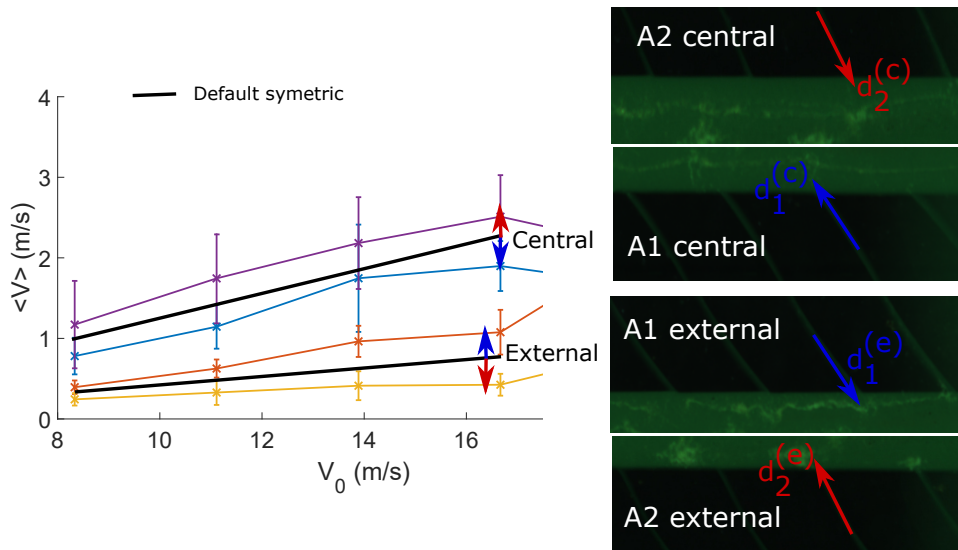


Figure 7.19: Sketch of the effect of Type D grooves linking longitudinal grooves with arrows highlighting their expulsion direction.

This figure illustrates the difference between grooves. The indices c stands for center and e stands for external. If we projected the vector $d_1^{(c)}$, $d_1^{(e)}$, $d_2^{(c)}$ and $d_2^{(e)}$ on the x axis as $x_1^{(c)}$, $x_1^{(e)}$, $x_2^{(c)}$ and $x_2^{(e)}$, we can observe that the vortices with enhanced strength are the ones with $x > 0$ as $x_1^{(e)}$ and $x_2^{(c)}$ and, contrarily, the ones with $x < 0$ as $x_1^{(c)}$ and $x_2^{(e)}$ are less intense. Thus, the angle of the Type D grooves seems to have

an influence on the intensity of the vortices inside tire grooves.

What also enforces the hypothesis of the effect of small transverse grooves in the intensity of the vortices is the absence of drastically different rotation velocities in worn tire case Fig.6.13. In the worn tire case, these small transverse grooves are no more present. Thus, the influence of these grooves is not visible.

7.2.2.2 Hypothesis on the vortices creation phenomena.

These vortices existence in the water flow have been supposed by Yeager 1974[81]. They are for first time, at our knowledge, shown and quantified through this work. Noticeably, similar vortices have been observed with aerodynamic numerical simulations by Croner 2014[21] and at the best of our knowledge no results exist on this with water puddle presence. It seems that these vortices are common to air and water flow inside tire grooves. Thus the question of the creation mechanism for these vortices will be studied in this section. It is here difficult to know the exact source of the vortices creation in this highly complex free-surface flow. However, based on the literature, 2 different vortices creation mechanisms can be proposed :

- The first one proposed is the creation of a horseshoe vortex in front of the tire ribs which infiltrates the grooves. For partially immersed obstacle in low water height, this kind of vortices can appear as studied by Launay 2017 [41] and Chou and Chao 2000 [19]. In these studies analysis on the conditions of creation of the horseshoe vortices is due to the separation of the boundary layer in the partially immersed obstacle vicinity. In the tire case, this hypothesis can be put in question. In the literature, the cases presented always involved isolated obstacle in free-surface flow. Here tire RIBs are not isolated and interaction between them can influence the creation of these vortices. Additionally, the reflection for this mechanism is made in the tire referential and not the ground referential. The creation of these vortices as presented in the literature is due to a separation of the boundary layer in the vicinity of the obstacle. If we consider the referential of the tire, the ground is moving at $-V_0$. Therefore, the separation of the boundary layer in the tire referential should be put in question. Sketch Fig.7.20 summarises this discussion.

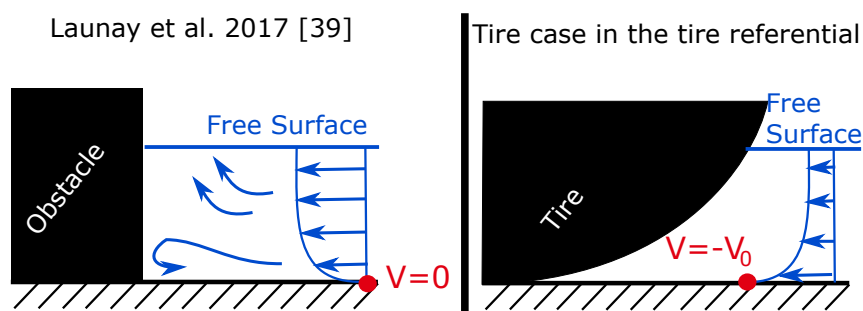


Figure 7.20: Sketch of the differences in the boundary layer structure between Launay et al. 2017 [41] case and the tire rolling puddle flow case.

- A more suitable vortex creation mechanism could be from the edges of the central RIB in the water. This kind of vortex creation is the same as could be observed for delta wings in aerodynamic. These instabilities have been extensively studied in the literature by Miao et al. 1995 [51] who studied the

vortex formation at the leading edge of a delta wing with an incidence angle of 10° . The formation of these vortices as discussed by Gad-el-Hak et al. 1985 [28] were based on flow visualisations. They observed the classical large vortices originated from smaller merged vortices created at the leading edge of the delta wing. In the tire case, hypothesis consists in the creation of the vortex at the RIB sharp angles at the beginning of the contact patch area. This hypothesis could be easily applied to the tire case and analysis of the flow visualisations could help us to prove the existence of this mechanism.

Let's assume that the presence of straight bubble columns is the signature of the presence of vortices. Based on Todoroff et al. 2018[72] visualisations a zoom can be made on the free surface zone to observe where the bubble columns appears for a vehicle speed $V_0 = 50$ km/h in the new tire case (Fig.7.21).

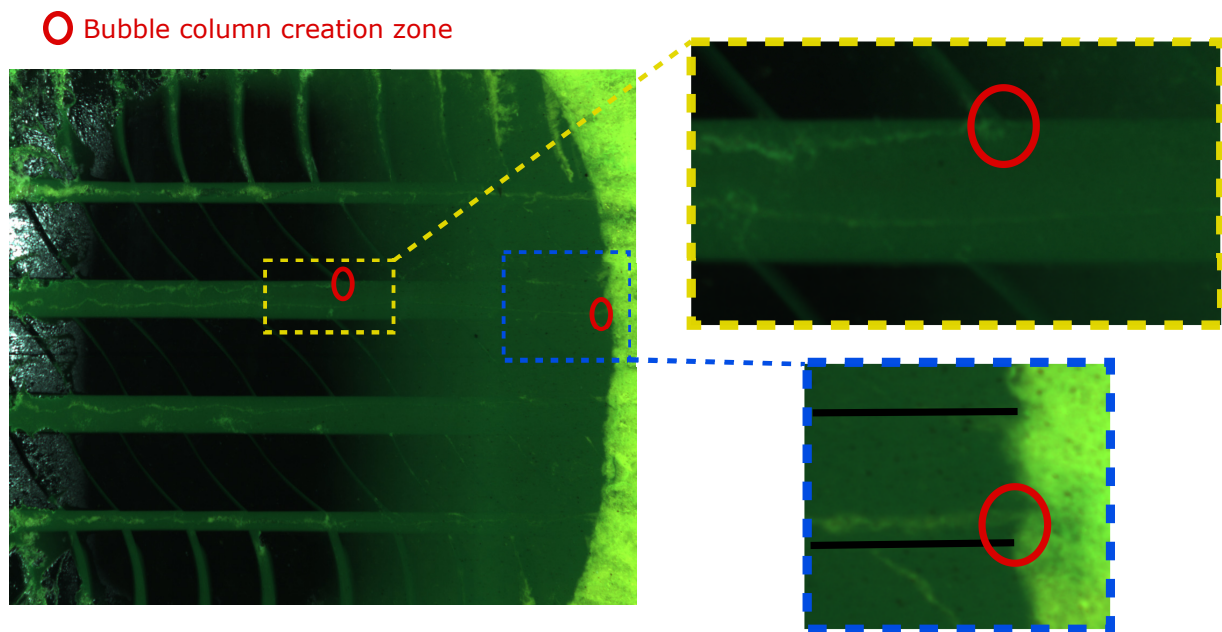


Figure 7.21: Visualisation of the bubble column creation zone in Type A grooves.

It appears that in Type A grooves, the bubble column at the central RIB side is created at the free surface at the RIB corner. The second bubble column in this grooves appears further in the contact patch area. Thus, based on these observations, we can propose the hypothesis of a single vortex creation at the free surface with a cornering effect similar to the one observed for delta wing could be questioned in the future. This vortex is driven though the contact patch with the water flow in x direction. Later on, a second vortex takes birth at the beginning of the contact patch area. The creation of this second vortex requests some possible explanations.

Again, two mechanism are proposed for the creation of the secondary vortex. Firstly, the creation of this second vortex could be driven by the viscous shear generated by the first one in the tire groove. A sketch in Fig.7.22 summarize the hypothesis on the vortex creation mechanism.

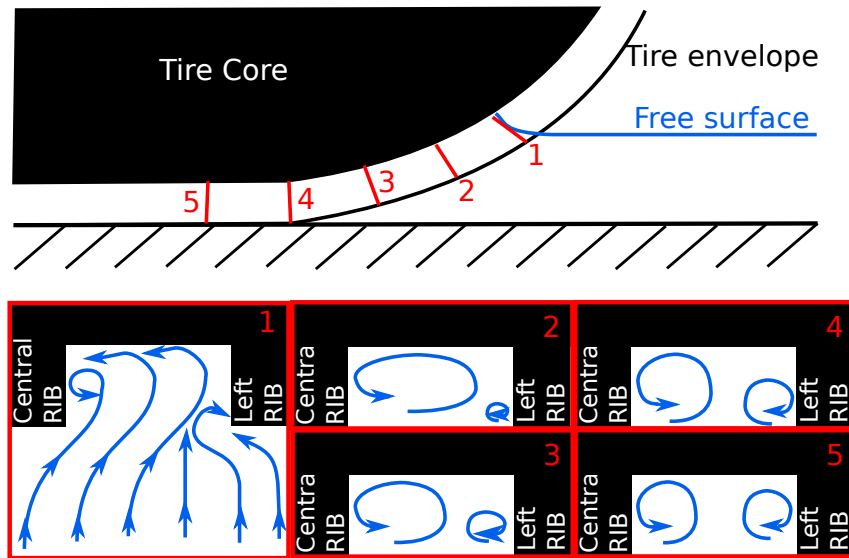


Figure 7.22: Sketch of the tire case with the vortex creation evolution between cross-section 1 and 5.

For the second vortex, a second proposition is the squishing effect of the RIB on the water in the contact patch area vicinity. Near the contact patch the load exerted by the tire on a thin layer of water will generate a squishing which can allow the creation of a second vortex as sketched Fig.7.23.

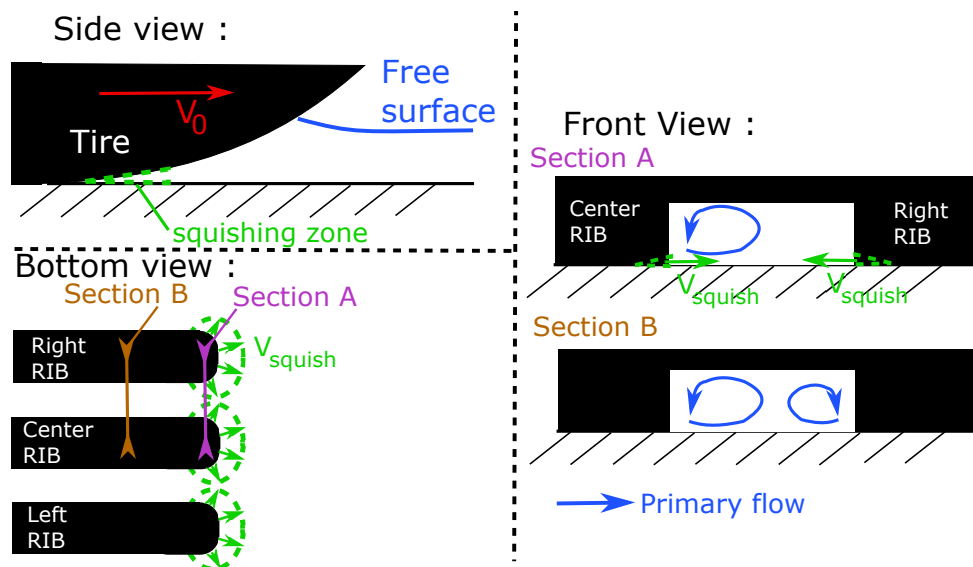


Figure 7.23: Sketch of the squishing effect to create a second vortex in Type A grooves.

In new tire Type B grooves, visualisations show that the creation of the vortex appears at the free surface. Thus, the creation mechanism of the primary vortex in type A groove is supposed to be the same than the one of the creation of the vortex in Type B groove. The difference is here the aspect ratio of the cross-section of the groove. In the Type B groove, the aspect ratio of 1 does not allow the development of a secondary vortex due to the lack of geometrical space.

For worn tire, the aspect ratio of the Type B groove is approximately 3. In this case, enough space is available for the development of a secondary vortex. In type A grooves for the worn tire, the aspect ratio is approximately 6. In this situation, more space is available and the number of vortices which developed

in these grooves is greater (4 vortices).

7.3 Flow in transverse grooves.

In transverse grooves, observations have been made on the water velocity projected in the groove axis, either for PCY4 Type C grooves (Section.6.1.2.3) or in CCP Type W grooves (Section.6.2.2.2). It appears that the velocity inside the tire groove is highly correlated with its position in the contact patch area. This phenomenon could be explained by the deformation of the rubber block between grooves when the tire load exert a compression on it. In the contact patch the pressure distribution is of a complex shape as shown by Tielking and Roberts 1987 [71] based on different experimental sources. However, at the shoulder, the pressure distribution in x direction can be approximated by a parabolic curve as used by Heinrich and Klüppel 2008 [29] for their analysis of the friction coefficient during braking as $p(x) = 4 \cdot p_m \cdot x / L_{cont} \cdot (1 - x / L_{cont})$, with p_m averaged pressure and L_{cont} the length of the contact patch area.

Thus, the total load exerted on a rubber block at the shoulder can be written as $F = w_b \cdot \int_{x_{min}}^{x_{max}} p(x) dx$, where w_b is the width of the rubber block and x_{min} and x_{max} are the limits of the block in x direction. With the exerted load the compression of the rubber block appears and the deformation with it. A sketch Fig.7.24 illustrate the deformation of the rubber block function of the load on the block. The normalised load is calculated as $F^* = F / \max(F)$ and represented considering a rubber block size $\Delta_b = x_{max} - x_{min} = 15$ mm which is approximately the size of the rubber block at the shoulder of the PCY4 tire.

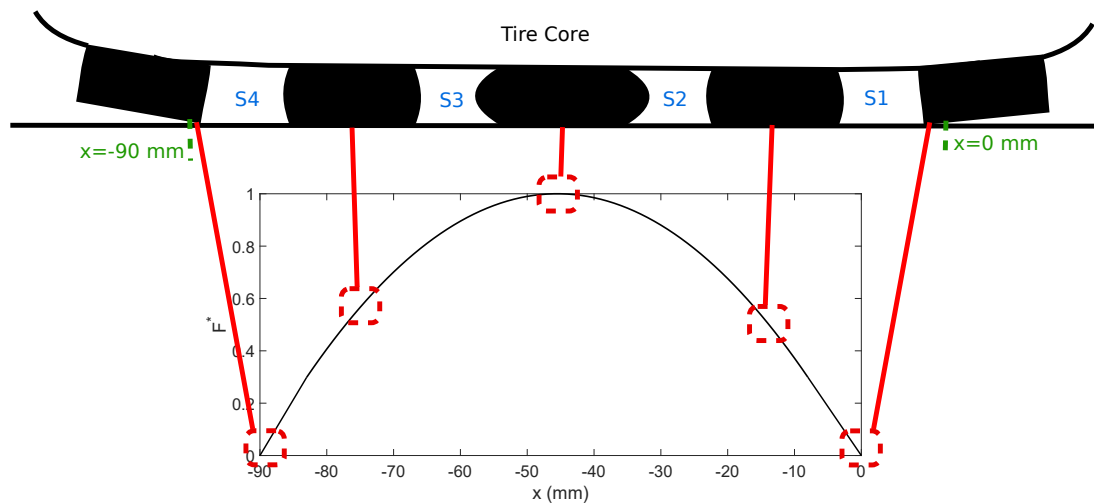


Figure 7.24: F^* with the corresponding deformation sketched in the contact patch area.

During the compression, the rubber block is subject to a Poisson's ratio expansion. This deformation of rubber block depends on its elasticity properties and are extensively studied in the literature as by Gent and Lindley 1959 [27] for which the influence of a corrected Young Modulus function of the shape ratio of the rubber block is discussed. This deformation of the rubber block can not be precisely calculated here as we don't know the exact composition and properties of the tire rubber. However, the shape of the deformation of a rubber block as sketched in Fig.7.24, allows us to deduce the reduction of the groove section between the beginning of the contact patch area and the center ($S1 > S2$) and then a growth of the groove section between the center of the contact patch and the end ($S3 < S4$). The cross section surface

of the groove is reduced at the beginning of the contact patch area which will push the water out of the groove. At the end of the contact patch area, the relaxation of the rubber block generates a reopening of the tire groove which will induce a suction in the new tire case.

Such evolution is also proposed for the CCP tire Fig.6.33. With this analysis, it appears that the evolution of the velocity in the Type W grooves depending on their location in the contact patch area matches the behaviour described previously. However, the slope of the linear regression is not the same for every groove part (Fig.6.35). The slope observed at the shoulder Fig.6.35 is of a higher magnitude than the one in the mid-zone which is higher than the one in the center zone. This can be explained by the angle of the groove with the tire axis. This hypothesis seems possible considering that when a tire groove is perpendicular to the rolling axis, the rubber block is homogeneously compressed and deformed as sketched Fig.7.24 and then the closing and opening effect on the groove will be homogeneous in all the groove. When the angle is high, the deformation of the rubber block at the side of the groove depends on the x position considered. Therefore the deformation of the groove is not uniformly distributed along the groove. Thus the spatially averaged velocity in the whole groove is less dependent on the deformation.

7.4 Interaction of connected grooves.

One last point that could be questioned is the interactions between Type B and Type C grooves in the PCY4 tire case. The flow in Type B grooves is highly influenced by the interaction with the Type C grooves. In the worn Tire case, when the Type C grooves are not linked to the Type B (Fig.7.25), the flow in Type B grooves is similar to the one in Type A grooves (Fig.6.11). Thus, without this link, the flow in longitudinal grooves in x direction is similar with a decreasing velocity at the beginning of the contact patch area down to a minimum velocity at the end of the contact patch area.

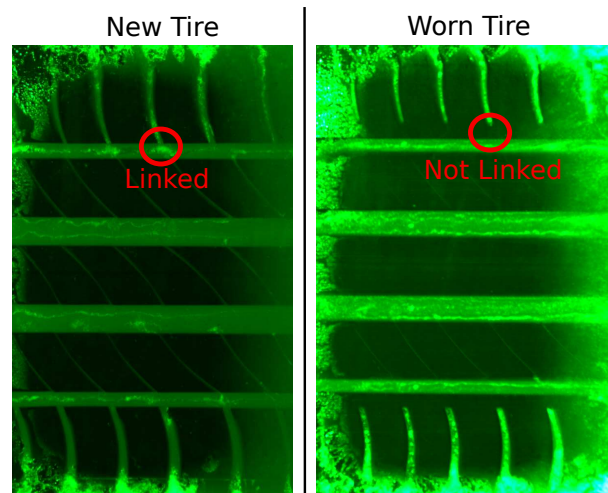


Figure 7.25: Visualisation of the link between Type B and Type C grooves.

As shown before, for the new tire case, the velocity component U in the Type B groove is totally different than the one in the Type A groove. A difference with the worn tire case is the geometrical link between Type B and Type C grooves. Thus, this link influences the flow in Type B grooves.

In the Type C grooves, the spatially averaged velocity $\langle V \rangle$ depending on the location in the contact patch area for the new tire, presented Fig.6.21 (left), shows a change of sign at approximately 57% of

the whole contact patch area. For the same new tire case, a change of sign occurs in the ensemble averaged profile $\langle U_B^* \rangle$, presented in Fig.6.10 (bottom) for the Type B groove, at $x = -53$ mm which is approximately 59% of the contact patch area. This correspondence illustrates the link between Type B groove flow and Type C groove flow.

This interaction is also highlighted by the comparison of the velocities V in Type C grooves between new and worn tire case. When the link between Type B and Type C grooves exists (new tire case) the change of sign between the beginning and the end of the contact patch area appears (Fig.6.21, left). When the link does not exist, the change of sign does not appear (Fig.6.21, right).

8 Conclusions and Perspectives

8.1 Major findings.

The purpose of this PhD work was to develop an experimental method to allow measurements of the velocity field in a water puddle when a car is rolling. A PIV technique based on the refraction of the laser sheet at the flow window interface called R-PIV has been proposed in order to perform these measurements. This technique allows PIV measurements in confined space where only one optical access is available.

Firstly, the R-PIV technique was studied in a channel laboratory experiment in order to understand the bias introduced by the specific optical properties of the method. The refraction has an effect on the structure of the light sheet emerging in the water. The influence of the specific structure of the light sheet was quantified by revisiting cross-correlation models from μ PIV or classic planar PIV. This model was validated with a channel flow experiment and allows us to take into account the optical set-up in the prediction of the R-PIV results.

This technique was adapted to the facility at the In-Situ Michelin pit to perform velocity measurements in case of car tires rolling in a puddle. This highlighted some source of bias induced by :

- Tire positioning with the contact patch area determination.
- Effect of multiphase flow inside the tire grooves.
- The integration effect intrinsic to the technique.

To overcome these issues, different analysis have been proposed to quantify these bias and try to reduce them :

- Identification of the beginning of the contact patch area based on a robust gray level analysis.
- Quantification of the optical effect of bubble presence in the tire rolling flow and improvement of the Cross-Correlation Model for such bubbly flows.
- Use of the Cross-Correlation Model to quantify the effect of different features of the flow as the boundary layer presence in front of the tire or the bubble presence in groove vortices.

Then R-PIV measurements have been performed for a tire rolling through a puddle. In front of the tire, the linear evolution of the defined global velocities in the water-bank and the shoulder have been

highlighted with a departure from linearity at car high speeds for worn tires. The satisfying repeatability of measurements in front of the tires shows the robustness of the measurement technique.

First ever done measurements have also been performed inside tire grooves. In these grooves, the velocity field in the groove direction have been quantified highlighting different features of the grooves :

- In transverse grooves, variations of the velocity field depend on the position of the groove in the contact patch area due to deformation of the tire.
- The wear indicator influences the water flow driven through the contact patch area in the longitudinal grooves.

These measurements combined to stereoscopic measurements also gave us access to informations on the secondary flow inside longitudinal groove. Therefore, the vortical structure of the flow inside longitudinal grooves has been identified and confirms the Yeager 1974 [81] hypothesis, which proposed the presence of counter rotating vortices inside tire grooves. Through the chapter 7, several possible formation mechanisms of these vortices have been identified.

Finally, normalisations by a characteristic velocity and a characteristic length scale show some self-similarities in the velocity field in different regions as in the water-bank or inside the tire grooves. This also highlight some structural differences in the flow linked to the deformation of the contact patch area which influences the structure of the flow in front of the tire.

8.2 Perspectives.

This work covered a large range of analysis about the applicability of the R-PIV measurement method and the results obtained. However, it raises some interesting questions for other works to come. The major perspective of this work will be to reproduce measurements for different tire models with a large amount of data to better understand the different effects of pattern tire shapes on the hydroplaning characteristics of the tire.

Firstly, variations between measurements in the water-bank in terms of velocity and length of the water-bank let us think that the structure of the water-bank varies over the time. Therefore, it could be interesting to perform high frequency R-PIV measurements to perform time resolved measurements during a single run. This could also allow to determine the evolution of the flow in transverse grooves while they travel through the contact patch area and the evolution of the flow in longitudinal grooves for worn tires depending on the position of the wear indicator inside the grooves.

In this study, the analysis of the flow is based on the positioning of the beginning of the contact patch area. A coordinate system origin was arbitrary chosen. However, different approaches can be used as the positioning of the tire with respect to the end of the contact patch area. In this work the analysis is made based on the gray levels of the images. This was chosen to allow a geometrical positioning of the coordinate system. However, the positioning of the coordinate system could be based on the velocity field analysis in order to align the forehead of the water-bank from each run.

In this PhD, the difficulty to well identify the contact patch area from PIV images has been discussed. Thus, the combination PIV/visualisations could be used with a system of two cameras with two wave-lengths of fluorescence. One dye in the water to determine the contact patch and one for the particles which will allow to determine the contact patch boundary with camera and the velocity field with the other. Also, other image processing or algorithms could be studied to determine the contact patch area from PIV images as deep-learning algorithm or correlation-based mask matching.

Different fundamental flow studies could be interesting. We observed in this work the presence of counter rotating vortices inside tire grooves. It seems that these vortices take birth at different zones inside the contact patch area. These vortices also appears to be persistent inside the tire grooves. In this work creation mechanisms have been proposed in order to explain their presence. Therefore, other studies could be proposed in order to understand the creation of the vortices inside the grooves. A study could also be focused on the stability in the contact patch area of these vortices and the conditions to destroy or enhance their strength. Afterwards, to go deeper on this stability analysis, the effect of bubbles on the vortices could be investigated. Under certain conditions, the vortices could be unstable and destroyed without bubbles while they could be persistent with bubbles due to interactions of the two phases.

Finally, forward-looking experimental methods could be investigated to apply to tire measurements as the 4D PTV. This technique is the particle tracking velocimetry in 3 spatial dimensions and resolved in time. With the use of 4 cameras, the 3D localisation of a particle could be calculated with triangulation method (quite similar to stereoscopic PIV calibration). Thus, the particle localisation is tracked over the time, giving us access to the 3D displacement of a particle. This could be really interesting to apply to the tire rolling flow in order to determine the 3D structure of the flow whereas in this work we were limited to 2D measurements. The application of this measurement technique to the particle tracking is challenging especially for the calibration with a thick window.

A Demonstration of the cross-correlation model calculation.

For a single particle

We here demonstrate the cross-correlation formula for the case of a single particle whose image is recorded at two instants separated by a time step dt . Let be the center of the particle image on image 1 (μ_{1X}, μ_{1Y}) and on image 2 (μ_{2X}, μ_{2Y}) , (U, V, W) being the particle velocity. Between the two recording instants the particle moves of a distance $(dx = U \cdot dt, dy = V \cdot dt, dz = W \cdot dt)$. On the camera sensor, the image of the particle moves of a distance $(DX = M \cdot dx, DY = M \cdot dy)$ if M is the magnification factor of the used recording camera lens, leading to : $(\mu_{2X} = \mu_{1X} + DX, \mu_{2Y} = \mu_{1Y} + DY)$.

Note for the following of the annexes that the depth z corresponds to the perpendicular direction of plane of view but for the channel flow it is the height.

Consider that the intensity function describing the 2D particle image (projection on the sensor plane) is a normal distribution of the intensity as expressed by Olsen and Adrian[60], the particle image on the first image is :

$$I_1(X, Y) = \frac{I_{p1} Da^2 \beta^2}{4\pi d_{e1}^2 (s_0 + z'_1)^2} \cdot e^{-\frac{4\beta^2}{d_{e1}^2} ((X - \mu_{1X})^2 + (Y - \mu_{1Y})^2)} \quad (\text{A.1})$$

where I_{p1} is the reemitted particle intensity recorded on image 1, Da is the aperture diameter of the lens, β^2 is a constant value set to 3.67 to best approximate the Airy diffraction (according to Olsen and Adrian[60]), s_0 is the distance between the camera and the object plane and z'_1 is the distance between the particle and the object plane in depth. d_{e1} is the particle image diameter on the image 1 and is given by Olsen and Adrian[60] as :

$$d_{e1} = \sqrt{M^2 d_p^2 + 5.95(M + 1)^2 \lambda^2 f^\#^2 + \frac{M^2 z_1'^2 D_a^2}{(s_0 + z_1')^2}} \quad (\text{A.2})$$

where d_p is the physical particle diameter, λ is the wavelength of the light reemitted by the particle and $f^\#$ is the aperture number of the camera lens.

With this consideration, the image of the particle on the second image is :

$$I_2(X, Y) = \frac{I_{p2} D a^2 \beta^2}{4\pi d_{e2}^2 (s_0 + z'_2)^2} \cdot e^{-\frac{4\beta^2}{d_{e2}^2} ((X - \mu_{2X})^2 + (Y - \mu_{2Y})^2)} \quad (\text{A.3})$$

Let us take :

$$\begin{cases} C_1 = \frac{I_{p1} D a^2 \beta}{4\sqrt{\pi} d_{e1} (s_0 + z'_1)^2} \\ C_2 = \frac{I_{p2} D a^2 \beta}{4\sqrt{\pi} d_{e2} (s_0 + z'_2)^2} \end{cases} \Rightarrow \begin{cases} \sigma_1 = \frac{d_{e1}}{\sqrt{8}\beta} \\ \sigma_2 = \frac{d_{e2}}{\sqrt{8}\beta} \end{cases} \quad (\text{A.4})$$

The intensities on image 1 and 2 can be rewritten as :

$$\begin{cases} I_1(X, Y) = \frac{C_1}{\sqrt{2\pi}\sigma_1} \cdot e^{-((X - \mu_{1X})^2 + (Y - \mu_{1Y})^2)/(2\sigma_1^2)} \\ I_2(X, Y) = \frac{C_2}{\sqrt{2\pi}\sigma_2} \cdot e^{-((X - \mu_{2X})^2 + (Y - \mu_{2Y})^2)/(2\sigma_2^2)} \end{cases} \quad (\text{A.5})$$

which are the equations of two normal intensity distributions of amplitudes (C_1 and C_2) with standard deviations of (σ_1 , σ_2).

The cross-correlation between an interrogation window (IW) on image 1 and an IW on image 2, that is globally shifted of (δx , δy) compared to the first IW, gives (Scarano and Riethmuller 2000[64]) :

$$R_{12}(\delta x, \delta y) = \int_{\Delta w_x} \int_{\Delta w_y} I_1(X, Y) I_2(X + \delta x, Y + \delta y) dX dY \quad (\text{A.6})$$

where Δw_x and Δw_y are the sizes of interrogation windows in X and Y direction.

With ($u = X + \delta x$, $v = Y + \delta y$), this cross correlation becomes :

$$R_{12}(\delta x, \delta y) = \int_{\Delta w_x} \int_{\Delta w_y} I_1(u - \delta x, v - \delta y) I_2(u, v) du dv \quad (\text{A.7})$$

Taking : $I_3(u, v) = I_1(-u, -v) = \frac{C_1}{\sqrt{2\pi}\sigma_1} \cdot e^{-((-u - \mu_{1X})^2 + (-v - \mu_{1Y})^2)/(2\sigma_1^2)}$, the cross correlation becomes :

$$R_{12}(\delta x, \delta y) = \int_{\Delta w_x} \int_{\Delta w_y} I_3(\delta x - u, \delta y - v) I_2(u, v) du dv = I_3 * I_2 \quad (\text{A.8})$$

The cross correlation between I_1 and I_2 is written as a convolution of I_3 and I_2 . This induces that the cross-correlation can be calculated with the Fourier transforms as:

$$R_{12}(\delta x, \delta y) = I_3 * I_2 = \mathcal{F}^{-1}(\mathcal{F}(I_3(\delta x, \delta y)) \cdot \mathcal{F}(I_2(\delta x, \delta y))) \quad (\text{A.9})$$

where \mathcal{F} is the Fourier transform symbol.

Let us consider $(E_{3X}(\delta x), E_{3Y}(\delta y))$ and $(E_{2X}(\delta x), E_{2Y}(\delta y))$ the exponential components of I_3 and I_2 respectively as :

$$\begin{cases} I_3(\delta x, \delta y) = A_1 \cdot e^{-(-\delta x - \mu_{1X})^2 / (2\sigma_1^2)} \cdot e^{-(-\delta y - \mu_{1Y})^2 / (2\sigma_1^2)} = A_1 \cdot E_{3X}(\delta x) \cdot E_{3Y}(\delta y) \\ I_2(\delta x, \delta y) = A_2 \cdot e^{-(\delta x - \mu_{2X})^2 / (2\sigma_2^2)} \cdot e^{-(\delta y - \mu_{2Y})^2 / (2\sigma_2^2)} = A_2 \cdot E_{2X}(\delta x) \cdot E_{2Y}(\delta y) \end{cases} \quad (\text{A.10})$$

where $A_1 = \frac{C_1}{\sqrt{2\pi}\sigma_1}$ and $A_2 = \frac{C_2}{\sqrt{2\pi}\sigma_2}$.

Here A_1 and A_2 are no dependent on δx and δy . E_{3X} and E_{2X} are dependent on δx , E_{3Y} and E_{2Y} on δy . The cross-correlation can be now rewritten as :

$$R_{12}(\delta x, \delta y) = A_1 A_2 \cdot \mathcal{F}_X^{-1} [\mathcal{F}_X(E_{3X}) \mathcal{F}_X(E_{2X})] \cdot \mathcal{F}_Y^{-1} [\mathcal{F}_Y(E_{3Y}) \mathcal{F}_Y(E_{2Y})] \quad (\text{A.11})$$

where $(\mathcal{F}_X, \mathcal{F}_Y)$ are the Fourier transforms in the X and Y directions and $(\mathcal{F}_X^{-1}, \mathcal{F}_Y^{-1})$ are the inverse Fourier transforms in the X and Y directions.

Let us calculate the Fourier transform of E_{3X} in the direction X :

$$\begin{aligned} \mathcal{F}_X(E_{3X}(\delta x)) &= \int_{-\infty}^{\infty} e^{-(-\delta x - \mu_{1X})^2 / (2\sigma_1^2)} \cdot e^{-2i\pi k_X \delta x} d\delta x \\ \text{Let } \delta x' &= -\delta x - \mu_{1X} \\ &= - \int_{-\infty}^{\infty} e^{-\delta x'^2 / (2\sigma_1^2)} e^{-2i\pi k_X (-\delta x' - \mu_{1X})} d\delta x' \\ &= -e^{2i\pi k_X (\mu_{1X})} \int_{-\infty}^{\infty} e^{-\delta x'^2 / (2\sigma_1^2)} e^{2i\pi k_X \delta x'} d\delta x' \\ \text{With } e^{-i\theta} &= \cos(\theta) - i\sin(\theta) \\ &= -e^{2i\pi k_X (\mu_{1X})} \int_{-\infty}^{\infty} e^{-\delta x'^2 / (2\sigma_1^2)} [\cos(-2\pi k_X \delta x') - i\sin(-2\pi k_X \delta x')] d\delta x' \\ \text{Where } \sin &\text{ odd function} \\ &= -e^{2i\pi k_X (\mu_{1X})} \int_{-\infty}^{\infty} e^{-\delta x'^2 / (2\sigma_1^2)} \cos(-2\pi k_X \delta x') d\delta x' \end{aligned}$$

As we know $\int_{-\infty}^{\infty} e^{-at^2} \cos(2xt) dt = \sqrt{\frac{\pi}{a}} e^{-x^2/a} (i)$. Here we have $a = \frac{1}{2\sigma_1^2}$ and $x = -\pi k_X$. Therefore :

$$\mathcal{F}_X(E_{3X}(\delta x)) = -e^{2i\pi k_X (\mu_{1X})} \sqrt{\pi(2\sigma_1^2)} e^{-2(-\pi k_X \sigma_1)^2}$$

In the same way we calculate the Fourier transform of E_{2X} in the X direction :

$$\begin{aligned}
\mathcal{F}_X(E_{2X}(\delta x)) &= \int_{-\infty}^{\infty} e^{-(\delta x - \mu_{2X})^2 / (2\sigma_2^2)} \cdot e^{-2i\pi k_X \delta x} d\delta x \\
&\text{if } \delta x' = \delta x - \mu_{2X} \\
&= \int_{-\infty}^{\infty} e^{-\delta x'^2 / (2\sigma_2^2)} e^{-2i\pi k_X (\delta x' + \mu_{2X})} d\delta x' \\
&= e^{-2i\pi k_X (\mu_{2X})} \int_{-\infty}^{\infty} e^{-\delta x'^2 / (2\sigma_2^2)} e^{-2i\pi k_X \delta x'} d\delta x' \\
&\text{if } e^{-i\theta} = \cos(\theta) - i\sin(\theta) \\
&= e^{-2i\pi k_X (\mu_{2X})} \int_{-\infty}^{\infty} e^{-\delta x'^2 / (2\sigma_2^2)} [\cos(2\pi k_X \delta x') - i\sin(2\pi k_X \delta x')] d\delta x' \\
&\text{as } \sin \text{ is an odd function} \\
&= e^{-2i\pi k_X (\mu_{2X})} \int_{-\infty}^{\infty} e^{-\delta x'^2 / (2\sigma_2^2)} \cos(2\pi k_X \delta x') d\delta x'
\end{aligned}$$

If $a = \frac{1}{2\sigma_2^2}$ and $x = \pi k_X$, we have :

$$\mathcal{F}_X(E_{2X}(\delta x)) = e^{-2i\pi k_X (\mu_{2X})} \sqrt{\pi(2\sigma_2^2)} e^{-2(\pi k_X \sigma_2)^2}$$

The product of both Fourier transform becomes :

$$\begin{aligned}
\mathcal{F}_X(E_{3X}(\delta x)) \cdot \mathcal{F}_X(E_{2X}(\delta x)) &= -e^{2i\pi k_X (\mu_{1X})} \sqrt{\pi(2\sigma_1^2)} e^{-2(-\pi k_X \sigma_1)^2} \cdot e^{-2i\pi k_X (\mu_{2X})} \sqrt{\pi(2\sigma_2^2)} e^{-2(\pi k_X \sigma_2)^2} \\
&= -2\pi \sigma_1 \sigma_2 \cdot e^{-2i\pi k_X (\mu_{2X} - \mu_{1X})} \cdot e^{-2\pi^2 k_X^2 (\sigma_1^2 + \sigma_2^2)}
\end{aligned}$$

The inverse Fourier transform of this product can be calculated :

$$\begin{aligned}
\mathcal{F}_X^{-1}(\mathcal{F}_X(E_{3X}(\delta x)) \cdot \mathcal{F}_X(E_{2X}(\delta x))) &= - \int_{-\infty}^{\infty} 2\pi \sigma_1 \sigma_2 \cdot e^{-2i\pi k_X (\mu_{2X} - \mu_{1X})} \cdot e^{-2\pi^2 k_X^2 (\sigma_1^2 + \sigma_2^2)} \cdot e^{2i\pi k_X \delta x} dk_X \\
&= -2\pi \sigma_1 \sigma_2 \int_{-\infty}^{\infty} e^{-2\pi^2 k_X^2 (\sigma_1^2 + \sigma_2^2)} \cdot e^{-2i\pi k_X (\mu_{2X} - \mu_{1X} - \delta x)} dk_X \\
&\text{if } e^{-i\theta} = \cos(\theta) - i\sin(\theta) \\
&= -2\pi \sigma_1 \sigma_2 \int_{-\infty}^{\infty} e^{-2\pi^2 k_X^2 (\sigma_1^2 + \sigma_2^2)} \cdot [\cos(2\pi k_X (\mu_{2X} - \mu_{1X} - \delta x)) \\
&\quad + i\sin(\pi k_X (\mu_{2X} - \mu_{1X} - \delta x))] dk_X \\
&= -2\pi \sigma_1 \sigma_2 \int_{-\infty}^{\infty} e^{-2\pi^2 k_X^2 (\sigma_1^2 + \sigma_2^2)} \cdot \cos(2\pi k_X (\mu_{2X} - \mu_{1X} - \delta x)) dk_X
\end{aligned}$$

If $a = 2\pi^2(\sigma_1^2 + \sigma_2^2)$ and $x = \pi(\mu_{2X} - \mu_{1X} - \delta x)$ this leads to :

$$\begin{aligned} \mathcal{F}_X^{-1}(\mathcal{F}_X(E_{3X}(\delta x)) \cdot \mathcal{F}_X(E_{2X}(\delta x))) &= -\sqrt{2\pi} \frac{\sigma_1 \sigma_2}{\sqrt{\sigma_1^2 + \sigma_2^2}} \cdot e^{-\frac{(\mu_{2X} - \mu_{1X} - \delta x)^2}{2(\sigma_1^2 + \sigma_2^2)}} \\ \text{With } \mu_{2X} &= \mu_{1X} + DX \\ &= -\sqrt{2\pi} \frac{\sigma_1 \sigma_2}{\sqrt{\sigma_1^2 + \sigma_2^2}} \cdot e^{-\frac{(DX - \delta x)^2}{2(\sigma_1^2 + \sigma_2^2)}} \end{aligned}$$

In the same way in the y direction for the last product term on the right of eq. A.11, we obtain :

$$\mathcal{F}_Y^{-1}(\mathcal{F}_Y(E_{3Y}(\delta y)) \cdot \mathcal{F}_Y(E_{2Y}(\delta y))) = -\sqrt{2\pi} \frac{\sigma_1 \sigma_2}{\sqrt{\sigma_1^2 + \sigma_2^2}} \cdot e^{-\frac{(DY - \delta y)^2}{2(\sigma_1^2 + \sigma_2^2)}}$$

The cross-correlation eq. A.11, in the sensor coordinate system, can now be written as :

$$\begin{aligned} R_{12}(\delta x, \delta y) &= A_1 A_2 \cdot \mathcal{F}_X^{-1}[\mathcal{F}_X(E_{3X}) \mathcal{F}_X(E_{2X})] \cdot \mathcal{F}_Y^{-1}[\mathcal{F}_Y(E_{3Y}) \mathcal{F}_Y(E_{2Y})] \\ &= A_1 A_2 \cdot \frac{2\pi \sigma_1^2 \sigma_2^2}{\sigma_1^2 + \sigma_2^2} \cdot e^{-((DX - \delta x)^2 + (DY - \delta y)^2)/(2(\sigma_1^2 + \sigma_2^2))} \\ &= C_1 C_2 \cdot \frac{\sigma_1 \sigma_2}{\sigma_1^2 + \sigma_2^2} \cdot e^{-((DX - \delta x)^2 + (DY - \delta y)^2)/(2(\sigma_1^2 + \sigma_2^2))} \end{aligned} \quad (\text{A.12})$$

Substituting C_1 , C_2 , σ_1 and σ_2 to Eq.A.12, we finally obtain :

$$R_{12}(\delta x, \delta y) = \frac{I_{p1} I_{p2} D a^4 \beta^2}{16\pi(d_{e1}^2 + d_{e2}^2)(s_0 + z'_1)^2 (s_0 + z'_2)^2} \cdot e^{-4\beta^2 \frac{(DX - \delta x)^2 + (DY - \delta y)^2}{d_{e1}^2 + d_{e2}^2}} \quad (\text{A.13})$$

For N particles

We now extend the previous demonstration to obtain the cross-correlation formula for the case of N particles whose images are recorded at two instants separated by a time step dt . We can consider the total image as the summation of each individual particle image i . For each we have a normal intensity distribution as seen previously with its center at (μ_{1Xi}, μ_{1Yi}) on the first image and at $(\mu_{2Xi} = \mu_{1Xi} + DX_i, \mu_{2Yi} = \mu_{1Yi} + DY_i)$ on the second image, with (DX_i, DY_i) the displacement of the particle i between both instants. The diameter of the i^{th} particle image is defined as d_{e1i} for the first image and d_{e2i} for the second image. Therefore as in Eq.A.4 :

$$\left\{ \begin{array}{l} C_{1i} = \frac{I_{p1i} D a^2 \beta}{4\sqrt{\pi} d_{e1i} (s_0 + z'_{1i})^2} \\ C_{2i} = \frac{I_{p2i} D a^2 \beta}{4\sqrt{\pi} d_{e2i} (s_0 + z'_{2i})^2} \end{array} \right\} \Rightarrow \left\{ \begin{array}{l} \sigma_{1i} = \frac{d_{e1i}}{\sqrt{8\beta}} \\ \sigma_{2i} = \frac{d_{e2i}}{\sqrt{8\beta}} \end{array} \right\} \Rightarrow \left\{ \begin{array}{l} A_{1i} = \frac{C_{1i}}{\sqrt{2\pi}\sigma_{1i}} \\ A_{2i} = \frac{C_{2i}}{\sqrt{2\pi}\sigma_{2i}} \end{array} \right. \quad (\text{A.14})$$

The intensities I_1 , I_2 and I_3 are equals to :

$$\begin{cases} I_1(X, Y) = \sum_{i=1}^N A_{1i} e^{-((X-\mu_{1X_i})^2 + (Y-\mu_{1Y_i})^2)/(2\sigma_{1i}^2)} \\ I_3(X, Y) = \sum_{i=1}^N A_{1i} e^{-((-X-\mu_{1X_i})^2 + (-Y-\mu_{1Y_i})^2)/(2\sigma_{1i}^2)} \\ I_2(X, Y) = \sum_{i=1}^N A_{2i} e^{-((X-\mu_{2X_i})^2 + (Y-\mu_{2Y_i})^2)/(2\sigma_{2i}^2)} \end{cases}$$

where i is the index of the i^{th} particle.

Following Eq.A.8, the Fourier transforms of I_3 and I_2 are :

$$\begin{aligned} \mathcal{F}(I_3(\delta x, \delta y)) &= \int_{-\infty}^{\infty} \int_{-\infty}^{\infty} \left(\sum_{i=1}^N A_{1i} e^{-((- \delta x - \mu_{1X_i})^2 + (- \delta y - \mu_{1Y_i})^2)/(2\sigma_{1i}^2)} \right) e^{-2i\pi(k_X \delta x + k_Y \delta y)} d\delta x d\delta y \\ &= \sum_{i=1}^N \left(\int_{-\infty}^{\infty} \int_{-\infty}^{\infty} A_{1i} e^{-((- \delta x - \mu_{1X_i})^2 + (- \delta y - \mu_{1Y_i})^2)/(2\sigma_{1i}^2)} e^{-2i\pi(k_X \delta x + k_Y \delta y)} d\delta x d\delta y \right) \\ &= \sum_{i=1}^N \mathcal{F}(I_{3i}) \end{aligned}$$

where I_{3i} is the intensity of the i^{th} particle image.

We can consider $\mathcal{F}(I_2) = \sum_{i=1}^N \mathcal{F}(I_{2i})$ as well. Therefore the product of the Fourier transform can be written as :

$$\begin{aligned} \mathcal{F}(I_3) \cdot \mathcal{F}(I_2) &= \sum_{i=1}^N \mathcal{F}(I_{3i}) \cdot \sum_{i=1}^N \mathcal{F}(I_{2i}) \\ &= \sum_{i=1}^N \sum_{j=1}^N \mathcal{F}(I_{3i}) \cdot \mathcal{F}(I_{2j}) \end{aligned}$$

The cross-correlation between both images can be written as :

$$\begin{aligned} R_{12}(\delta x, \delta y) &= \mathcal{F}^{-1} \left(\sum_{i=1}^N \sum_{j=1}^N \mathcal{F}(I_{3i}) \cdot \mathcal{F}(I_{2j}) \right) \\ &= \int_{-\infty}^{\infty} \int_{-\infty}^{\infty} \left(\sum_{i=1}^N \sum_{j=1}^N \mathcal{F}(I_{3i}) \cdot \mathcal{F}(I_{2j}) \right) \cdot e^{-2i\pi(k_X \delta x + k_Y \delta y)} dk_X dk_Y \\ &= \sum_{i=1}^N \sum_{j=1}^N [\mathcal{F}^{-1}(\mathcal{F}(I_{3i}) \cdot \mathcal{F}(I_{2j}))] \\ &= \sum_{i=1}^N \sum_{j=1}^N (R_{12})_{i,j} \\ &= \sum_{i=j} (R_{12})_{i,j} + \sum_{i \neq j} (R_{12})_{i,j} \\ &= R_{12D} + R_{12F} \end{aligned} \tag{A.15}$$

where R_{12D} and R_{12F} are respectively the displacement and fluctuation components of the cross-correlation according to Adrian decomposition (Adrian 1988[1]). In this case we will focus our analysis on the displacement component of the cross-correlation as $R_{12D}(\delta x, \delta y) = \sum_{i=1}^N (R_{12})_{i,i}$. According to Sec.A, the displacement cross-correlation component for the i^{th} particle is equal to :

$$(R_{12D})_{i,i} = \frac{I_{p1i} I_{p2i} D a^4 \beta^2}{16\pi (d_{e1i}^2 + d_{e2i}^2) (s_0 + z_{1i}')^2 (s_0 + z_{2i}')^2} \cdot e^{-4\beta^2((DX_i - \delta x)^2 + (DY_i - \delta y)^2)} / (d_{e1i}^2 + d_{e2i}^2)$$

Here we have fluorescent particles. The intensity of fluorescence reemitted by a particle is considered as proportional to the incident intensity and to the square of the physical particle diameter if we suppose a particle as spheric $I_{p1} = I_{01} \cdot d_p^2$ and $I_{p2} = I_{02} \cdot d_p^2$, where I_{01} and I_{02} are the laser pulse intensities for the two successive instants of particle image recordings.

Hypothesis 1 : If we consider a low inclination of the laser sheet, the intensity variation in an interrogation window is independent of the location (x, y) of the particle and is only dependent on z ($I_{01i} = I_{01}(z_{1i})$, $I_{02i} = I_{02}(z_{2i})$). The reception optic is considered as perfectly horizontal. Therefore, the object plane location is perfectly horizontal and the particle diameter depends only on the depth of the particles ($d_{e1i} = d_{e1}(z_{1i})$, $d_{e2i} = d_{e2}(z_{2i})$). At the scale of an interrogation window, the velocity is considered as independent of (x, y) and only dependent on the depth z ($DX_i = M \cdot U_i dt = M \cdot U(z_{1i}) dt = DX(z_{1i})$, $DY_i = M \cdot V_i dt = M \cdot V(z_{1i}) dt = DY(z_{1i})$).

Therefore, the cross-correlation becomes only dependent on the depths of the particle at the two instants z_{1i} and z_{2i} :

$$(R_{12})_{i,i} = \frac{I_{01}(z_{1i}) I_{02}(z_{2i}) d_p^4 D a^4 \beta^2}{16\pi (d_{e1}(z_{1i})^2 + d_{e2}(z_{2i})^2) (s_0 + z_{1i}')^2 (s_0 + z_{2i}')^2} \cdot e^{-4\beta^2((DX(z_{1i}) - \delta x)^2 + (DY(z_{1i}) - \delta y)^2)} / (d_{e1}(z_{1i})^2 + d_{e2}(z_{2i})^2)$$

Hypothesis 2 : We consider that the two laser pulses are of the same intensity and that the focus is equivalent when recording the two images.

If we consider the displacement of a particle in depth, for image 2 we have : $z_{2i} = z_{1i} + DZ_i$, with $DZ_i = w(z_{1i}) dt$, and $z_{2i}' = z_{1i}' + DZ_i$.

$$(R_{12})_{i,i} = \frac{I_0(z_{1i}) I_0(z_{1i} + DZ_i) d_p^4 D a^4 \beta^2}{16\pi (d_e(z_{1i})^2 + d_e(z_{1i} + DZ_i)^2) (s_0 + z_{1i}')^2 (s_0 + z_{2i}')^2} \cdot e^{\frac{-4\beta^2((DX(z_{1i}) - \delta x)^2 + (DY(z_{1i}) - \delta y)^2)}{d_e(z_{1i})^2 + d_e(z_{1i} + DZ_i)^2}} \quad (\text{A.16})$$

With the flow studied in a square channel, the velocity in depth is null ($W = 0$). Therefore, $DZ_i = 0$ which induces $z_{1i} = z_{2i} = z_i$.

$$(R_{12})_{i,i} = \frac{I_0(z_i)^2 d_p^4 Da^4 \beta^2}{32\pi d_e(z_i)^2 (s_0 + z_i)^4} \cdot e^{-2\beta^2 \frac{(DX(z_i) - \delta x)^2 + (DY(z_i) - \delta y)^2}{d_e(z_i)^2}} \quad (\text{A.17})$$

For N particles, the displacement component of the cross-correlation can be calculated as the summation over all particles with Eq.A.16 equivalent for the channel flow to the Eq.A.17 that is finally used for the summation.

If we consider a probability density law $p(z)$ of particle presence at a depth z , the mean displacement component of the cross-correlation converge to the integral of the contribution at every depth when the number of particle tends to the infinity.

$$\langle R_{12D}, z \rangle = \lim_{N \rightarrow \infty} \left(\frac{1}{N} R_{12D}(\delta x, \delta y) \right) = \int_{z_{min}}^{z_{max}} p(z) R_{12D}(z) dz \quad (\text{A.18})$$

In a channel flow with an homogeneous mixing of particles in the initial water tank, the probability density of particle presence at every height can be considered as uniform. Therefore, in the channel case, $p(z) = 1/h$.

For N particles with background noise.

If some background noise appears on images recorded by the camera, we note B_1 the background noise pattern on image 1 and B_2 the pattern on image 2. The grey-level function describing the total image is considered as a summation of the N particle image intensity functions and the background noise. The Intensity distributions on image 1 and 2 are :

$$\begin{cases} I_1(X, Y) = \sum_{i=1}^N I_{1i}(X, Y) + B_1 \\ I_2(X, Y) = \sum_{i=1}^N I_{2i}(X, Y) + B_2 \end{cases}$$

or

$$\begin{cases} I_3(X, Y) = \sum_{i=1}^N I_{3i}(X, Y) + B_1 \\ I_2(X, Y) = \sum_{i=1}^N I_{2i}(X, Y) + B_2 \end{cases}$$

where $I_{1i}(X, Y) = A_{1i} e^{-((X - \mu_{1Xi})^2 + (Y - \mu_{1Yi})^2) / (2\sigma_{1i}^2)}$, $I_{2i}(X, Y) = A_{2i} e^{-((X - \mu_{2Xi})^2 + (Y - \mu_{2Yi})^2) / (2\sigma_{2i}^2)}$ and $I_{3i}(X, Y) = A_{1i} e^{-((-X - \mu_{1Xi})^2 + (-Y - \mu_{1Yi})^2) / (2\sigma_{1i}^2)}$, with A_{1i} , A_{2i} , σ_{1i} and σ_{2i} calculated according to equation A.4.

Taking Eq.A.8, the Fourier transforms of I_3 and I_2 are :

$$\begin{aligned}
 \mathcal{F}(I_3(\delta x, \delta y)) &= \int_{-\infty}^{\infty} \int_{-\infty}^{\infty} \left(\sum_{i=1}^N \left[A_{1i} e^{-((-\delta x - \mu_{1x_i})^2 + (-\delta y - \mu_{1y_i})^2) / (2\sigma_{1i}^2)} \right] + B_1 \right) e^{-2i\pi(k_x \delta x + k_y \delta y)} d\delta x d\delta y \\
 &= \sum_{i=1}^N \left(\int_{-\infty}^{\infty} \int_{-\infty}^{\infty} A_{1i} e^{-((-\delta x - \mu_{1x_i})^2 + (-\delta y - \mu_{1y_i})^2) / (2\sigma_{1i}^2)} e^{-2i\pi(k_x \delta x + k_y \delta y)} d\delta x d\delta y \right) \\
 &\quad + \int_{-\infty}^{\infty} B_1 e^{-2i\pi(k_x \delta x + k_y \delta y)} d\delta x d\delta y \\
 &= \sum_{i=1}^N [\mathcal{F}(I_{3i})] + \mathcal{F}(B_1)
 \end{aligned}$$

in the same way, we have $\mathcal{F}(I_3(\delta x, \delta y)) = \sum_{i=1}^N [\mathcal{F}(I_{2i})] + \mathcal{F}(B_2)$. The product of the Fourier transforms is :

$$\begin{aligned}
 \mathcal{F}(I_3) \cdot \mathcal{F}(I_2) &= \left[\sum_{i=1}^N \mathcal{F}(I_{3i}) + \mathcal{F}(B_1) \right] \cdot \left[\sum_{i=1}^N \mathcal{F}(I_{2i}) + \mathcal{F}(B_2) \right] \\
 &= \sum_{i=1}^N \sum_{j=1}^N [\mathcal{F}(I_{3i}) \cdot \mathcal{F}(I_{2j})] + \sum_{i=1}^N [\mathcal{F}(I_{3i})] \cdot \mathcal{F}(B_2) + \sum_{j=1}^N [\mathcal{F}(I_{2j})] \cdot \mathcal{F}(B_1) + \mathcal{F}(B_2) \cdot \mathcal{F}(B_1)
 \end{aligned}$$

Thus, the cross-correlation between both images is obtained:

$$\begin{aligned}
 R_{12}(\delta x, \delta y) &= \mathcal{F}^{-1} \left(\sum_{i=1}^N \sum_{j=1}^N [\mathcal{F}(I_{3i}) \cdot \mathcal{F}(I_{2j})] + \sum_{i=1}^N [\mathcal{F}(I_{3i})] \cdot \mathcal{F}(B_2) + \sum_{j=1}^N [\mathcal{F}(I_{2j})] \cdot \mathcal{F}(B_1) + \mathcal{F}(B_2) \cdot \mathcal{F}(B_1) \right) \\
 &= \int_{-\infty}^{\infty} \int_{-\infty}^{\infty} \left\{ \sum_{i=1}^N \sum_{j=1}^N [\mathcal{F}(I_{3i}) \cdot \mathcal{F}(I_{2j})] + \sum_{i=1}^N [\mathcal{F}(I_{3i})] \cdot \mathcal{F}(B_2) + \sum_{j=1}^N [\mathcal{F}(I_{2j})] \cdot \mathcal{F}(B_1) \right. \\
 &\quad \left. + \mathcal{F}(B_2) \cdot \mathcal{F}(B_1) \right\} \cdot e^{-2i\pi(k_x \delta x + k_y \delta y)} dk_x dk_y \\
 &= \int_{-\infty}^{\infty} \int_{-\infty}^{\infty} \left(\sum_{i=1}^N \sum_{j=1}^N [\mathcal{F}(I_{3i}) \cdot \mathcal{F}(I_{2j})] \cdot e^{-2i\pi(k_x \delta x + k_y \delta y)} \right) dk_x dk_y \\
 &\quad + \int_{-\infty}^{\infty} \int_{-\infty}^{\infty} \left(\sum_{i=1}^N [\mathcal{F}(I_{3i})] \cdot \mathcal{F}(B_2) \cdot e^{-2i\pi(k_x \delta x + k_y \delta y)} \right) dk_x dk_y \\
 &\quad + \int_{-\infty}^{\infty} \int_{-\infty}^{\infty} \left(\sum_{j=1}^N [\mathcal{F}(I_{2j})] \cdot \mathcal{F}(B_1) \cdot e^{-2i\pi(k_x \delta x + k_y \delta y)} \right) dk_x dk_y \\
 &\quad + \int_{-\infty}^{\infty} \int_{-\infty}^{\infty} \left(\mathcal{F}(B_2) \cdot \mathcal{F}(B_1) \cdot e^{-2i\pi(k_x \delta x + k_y \delta y)} \right) dk_x dk_y \tag{A.19}
 \end{aligned}$$

According to equation A.15, for N particles without background noise, the first term of the last equation A.19 is the sum of the displacement and the fluctuating components of the correlation function as $R_{12D} + R_{12F}$. The three other components are all involving the background noise. Therefore, their sum constitutes together the background component R_{12C} of the cross correlation.

$$\left\{ \begin{array}{l} R_{12D} + R_{12F} = \int_{-\infty}^{\infty} \int_{-\infty}^{\infty} \left(\sum_{i=1}^N \sum_{j=1}^N [\mathcal{F}(I_{3i}) \cdot \mathcal{F}(I_{2j})] \cdot e^{-2i\pi(k_x \delta_x + k_y \delta_y)} \right) dk_x dk_y \\ = \sum_{i=j} (R_{12})_{i,j} + \sum_{i \neq j} (R_{12})_{i,j} \\ R_{12C} = \mathcal{F}^{-1} \left(\sum_{i=1}^N [\mathcal{F}(I_{3i})] \cdot \mathcal{F}(B_2) \right) + \mathcal{F}^{-1} \left(\sum_{j=1}^N [\mathcal{F}(I_{2j})] \cdot \mathcal{F}(B_1) \right) + \mathcal{F}^{-1} (\mathcal{F}(B_2) \cdot \mathcal{F}(B_1)) \\ R_{12} = R_{12D} + R_{12F} + R_{12C} \end{array} \right.$$

In this study we focus our analysis on the displacement component R_{12D} in which the background noise is not involved. Therefore, the calculation of the displacement component of interest R_{12D} is the same as the one presented in Section A.

B Image Treatment.

In this section, a discussion on the effect of a preprocessing of the images before the vector field calculation is intended. As discussed in Section 3.5, the uneven gray level of the images especially in tire grooves can be a problem for the calculation of the cross-correlation. Therefore, a preprocessing of the images with a subtraction of the sliding minimum (see Deen et al. 2010.[23]) can be used to enhance the signal noise ratio. The difference between raw images and preprocessed images of the particles in the Type A grooves of the PCY4 tire are presented in Fig.B.1.

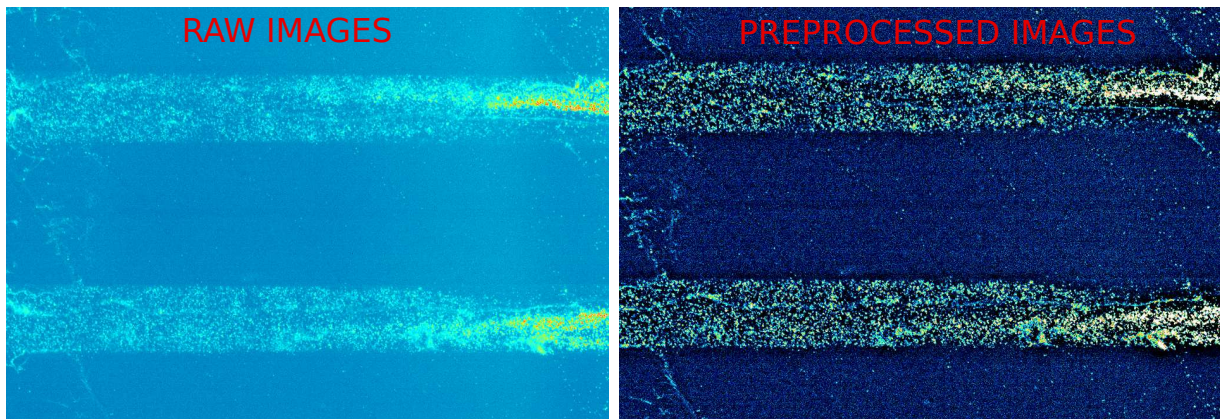


Figure B.1: Raw image and preprocessed image comparison in Type A grooves.

This shows the effect of the image treatment on the enhancement of the relative gray levels of particles compared to the background gray level. The comparison between two correlation maps is presented for a snapshot for an interrogation window centered at $x = -41.78$ mm and $y = 19.85$ mm in Fig.B.2.

The processing does not seem to have an influence on the cross-correlation for this interrogation window. Both correlation maps are mainly the same. Therefore, the question of the effect of a processing can be discussed. To visualise this effect on the overall grooves, ensemble averaged velocity maps of the components U and V are presented for both raw images and preprocessed images on Fig.B.3.

In order to visualise in detail the differences, ensemble averaged velocity profiles $\langle U_A^* \rangle$ averaged on the groove width is presented Fig.B.4. The ensemble averaged velocity profile $\langle V_{A1}^* \rangle$ is also presented for both raw images and treated images Fig.B.4.

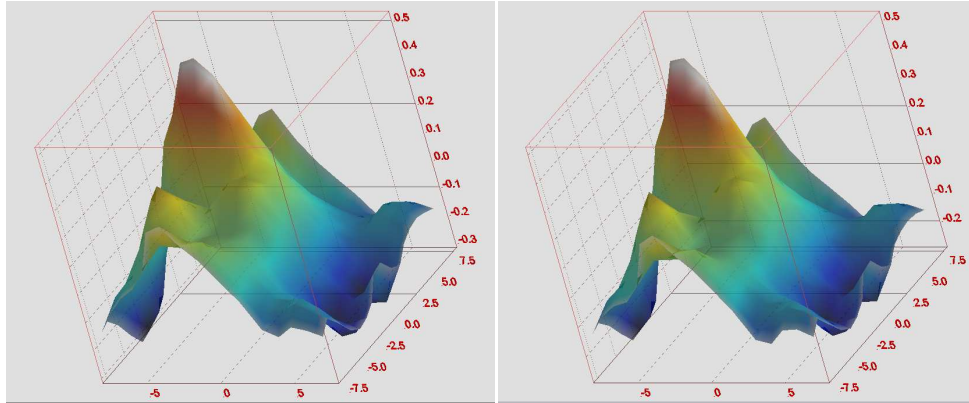


Figure B.2: Correlation map for a single interrogation window, right for raw images, left for treated images.

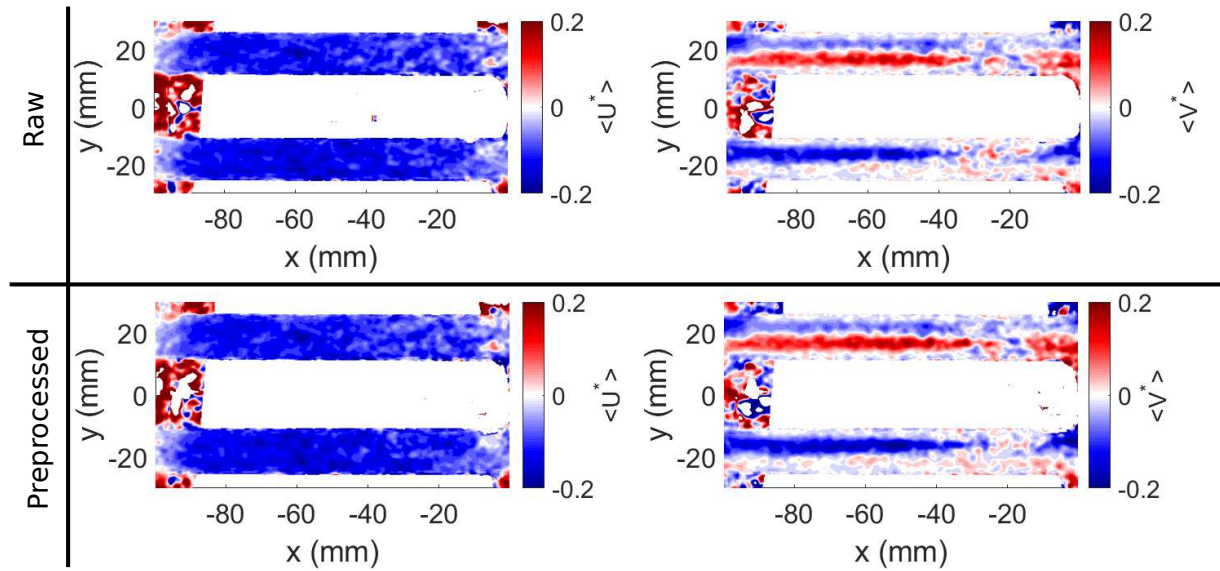


Figure B.3: Velocity maps for both raw images and preprocessed images.

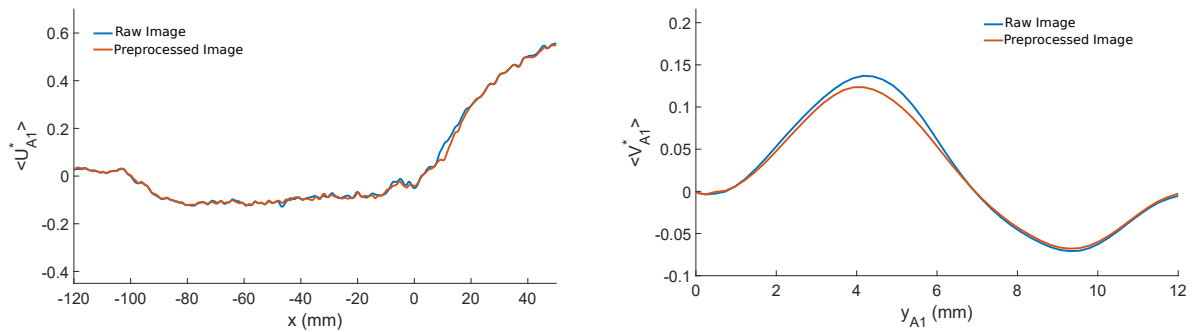


Figure B.4: Velocity profiles obtained for both raw images and preprocessed images.

The difference between velocity profiles $\langle U_{A1}^* \rangle$ obtained with or without image treatment is quite similar. The fluctuations for the processed images seems to be slightly reduced. However, the image processing does not seem to have a great influence and improvement on the cross-correlation. This is

also visible on the velocity profile $\langle V_{A1}^* \rangle$ with a slightly inferior velocity obtained in the positive lobe at $y_{A1} \sim 4$ mm for preprocessed images.

In conclusion, the preprocessing does not have a major effect on the cross-correlation for tire images. Therefore, it is chosen in this work to keep working with raw images.

C Decreasing interrogation windows size in tire grooves.

In this section, the effect of a decreasing interrogation window size inside the tire groove is discussed. The spatial resolution for measurements for analysis inside tire grooves is important to increase in order to catch the vortices with more precision. The interrogation window size should be minimised to increase resolution without deteriorating the correlation. To show the influence of the interrogation window size δw_x , velocity field maps inside tire grooves are presented for PCY4 tire with a decreasing size $\delta w_x = 32$ pixels (2.7 mm, which correspond to 1/4 of the Type A groove), $\delta w_x = 16$ pixels (1.3 mm, which correspond to 1/9 of the Type A groove) and $\delta w_x = 12$ pixels (1 mm, which correspond to 1/12 of the Type A groove) in Fig.C.1.

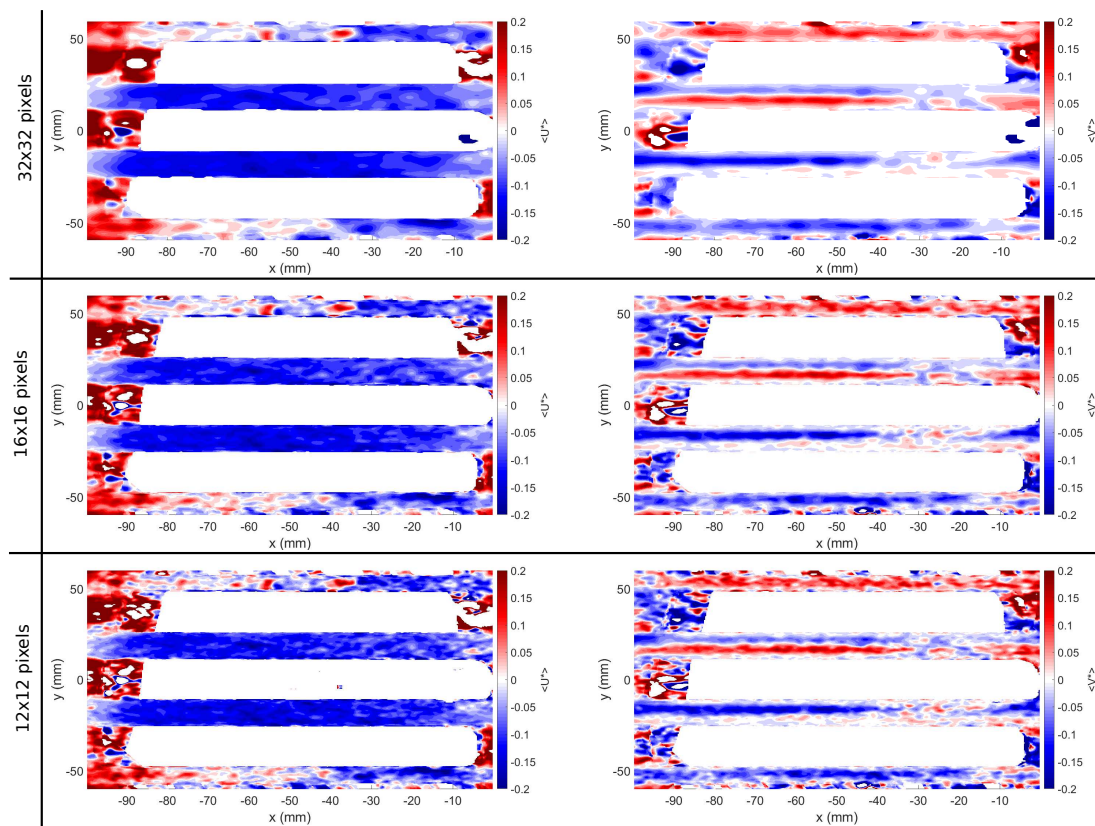


Figure C.1: Velocity maps for a decreasing interrogation window size.

The decreasing size of the interrogation window does not affect the general behaviour of the flow. For small interrogation windows, small scale fluctuations in the ensemble averaged maps are more present due to the resolution of the flow. In order to visualise these fluctuations with more precision, ensemble averaged velocity profile $\langle U_A^* \rangle$ averaged on the groove width is presented Fig.C.2. The ensemble averaged velocity profile $\langle V_{A1}^* \rangle$ is also presented for decreasing size of interrogation window Fig.C.2.

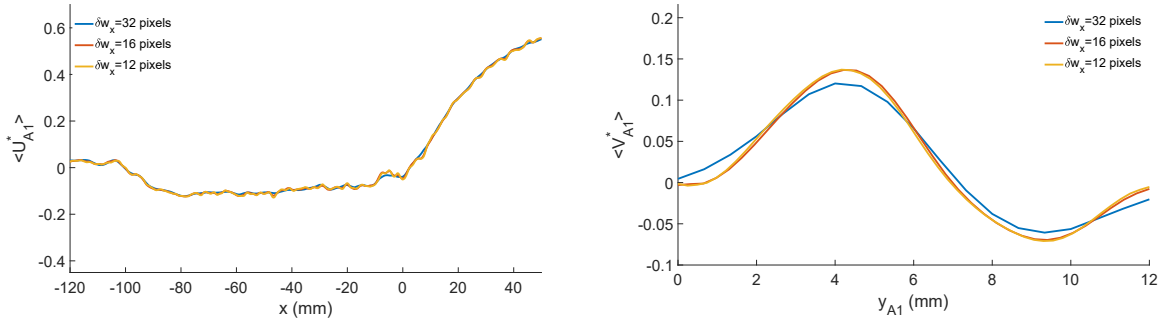


Figure C.2: Velocity profiles for a decreasing interrogation window size.

This confirms that a little more small scale fluctuations are visible for $\delta w_x = 12$ pixels due to the higher resolution. For the spanwise velocity in the groove V , the general tendency is the same for every interrogation window size. The precision on the velocity near the wall is higher for $\delta w_x = 16$ pixels and $\delta w_x = 12$ pixels. However, the difference between $\delta w_x = 12$ pixels and $\delta w_x = 16$ pixels is negligible. Thus, the decrease of the interrogation window size down to $\delta w_x = 12$ pixels does not affect the velocity field measurements and increases the spatial resolution for analysis of the flow in the groove.

The same procedure is now repeated for the CCP Tire. The velocity maps are presented Fig.C.3 without ensemble averaging due to the impossibility to perform an ensemble averaging on Type W grooves.

These velocity field maps highlight that the decrease of the interrogation window size does not affect the cross-correlation at first sight. The velocity field maps are quite similar.

In order to quantify with more accuracy the effect of a decreasing size of interrogation windows, the profiles of the two component projected along and perpendicularly the groove axis are presented Fig.C.4. These velocity projections are made according to Fig.6.32 in order to obtain the same profiles than those presented Fig.6.33.

These profiles show more local fluctuations for the profiles obtained with $\delta w_x = 16$ pixels or $\delta w_x = 12$ pixels compared to $\delta w_x = 32$ pixels. This is the consequence of the increased spatial resolution due to smaller interrogation windows. Small differences of amplitudes are visible between the case of the interrogation windows of size $\delta w_x = 16$ pixels and the one with $\delta w_x = 12$ pixels in the fluctuations. However, the two profiles are really close.

Based on this analysis, in both tire cases, the cross-correlation window size chosen for analysis inside tire grooves is $\delta w_x = 12$ pixels. This allows us to increase to a maximum the spatial resolution of the velocity field without deteriorating the accuracy of the measurements.

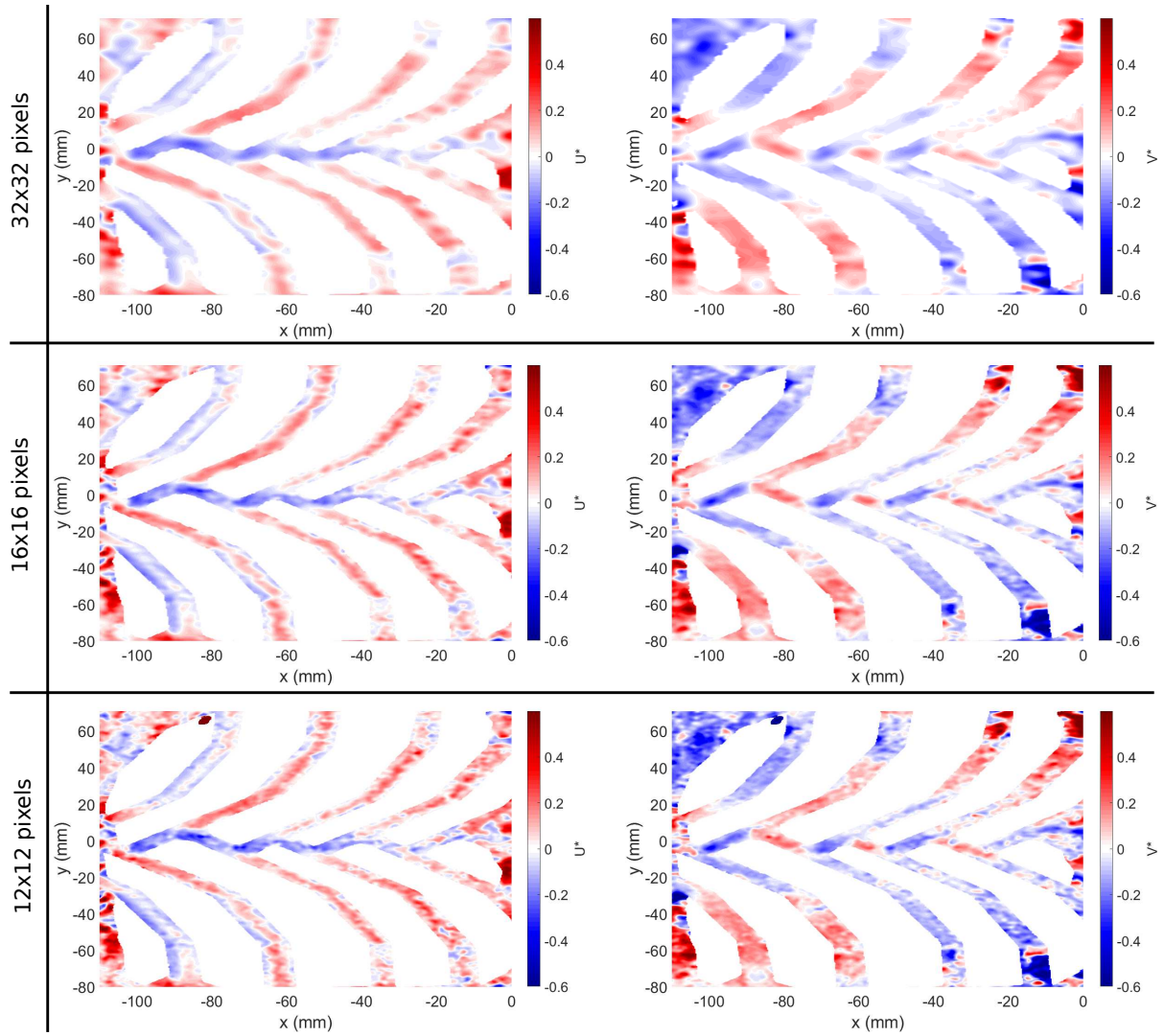


Figure C.3: Velocity maps for a decreasing interrogation window size.

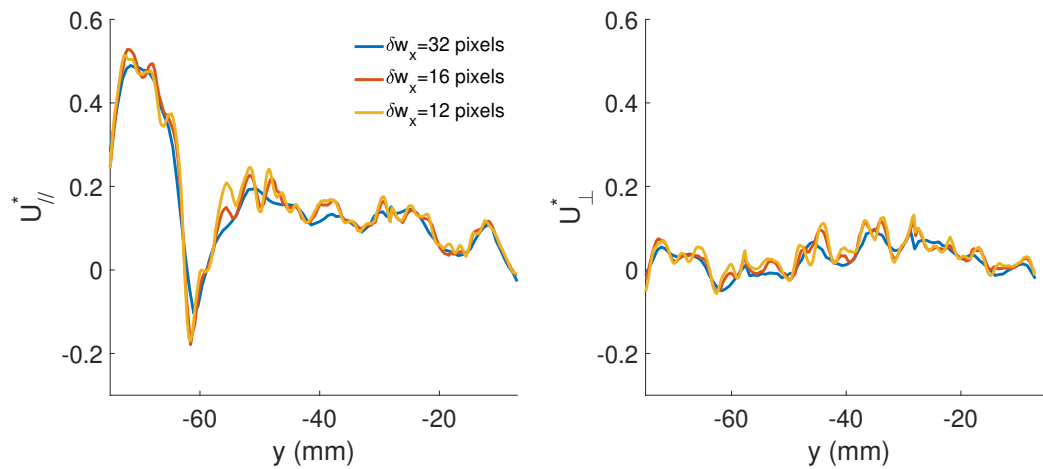


Figure C.4: two velocity component, $U_{//}$ and U_{\perp} profiles for a decreasing interrogation window size.

D The change of object plane position for the flow in the grooves.

In this Section, measurements results are presented and compared for PCY4 measurements inside tire grooves for $z_{OP}^* = 0$ and $z_{OP}^* = 1$ to visualise the effect of a change of object plane location. For the new tire configuration, 8 measurements have been performed during a session with a vehicle speed at $V_0 = 50$ km/h with an object plane location $z_{OP} = 8$ mm ($z_{OP}^* = 1$). These measurements are made to confirm the effect of the presence of bubbles inside tire grooves on R-PIV measurements as studied in Section.5.2.2. Ensemble averaged velocity component maps for the spanwise direction $\langle V^* \rangle$ are presented for both object plane positions in Fig.D.1

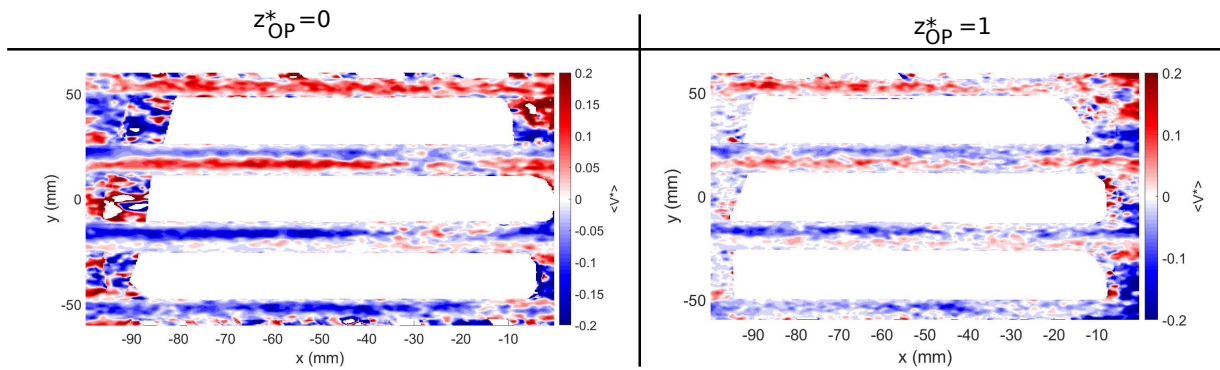


Figure D.1: Velocity component maps $\langle V^* \rangle$ for both object plane positions.

The measurements presented here show that with a change of object plane position, the velocity component V in the tire groove does not change its sign between $z_{OP}^* = 1$ than for $z_{OP}^* = 0$, as predicted by the BCCM. It also shows that the velocity component appears to be lowered with $z_{OP}^* = 1$ than for $z_{OP}^* = 0$ as predicted by the model. To confirm these conclusions, the profiles $\langle V_{A1}^* \rangle$ are presented in both configurations in Fig.D.2.

These profiles confirm the observations made and shown on the velocity component maps. It also shows that velocity component V measured with $z_{OP}^* = 1$ is reduced compared to $z_{OP}^* = 0$. Therefore, the BCCM model well predicted qualitatively the R-PIV measurement results in the case of a vortex like flow with bubble columns in their core.

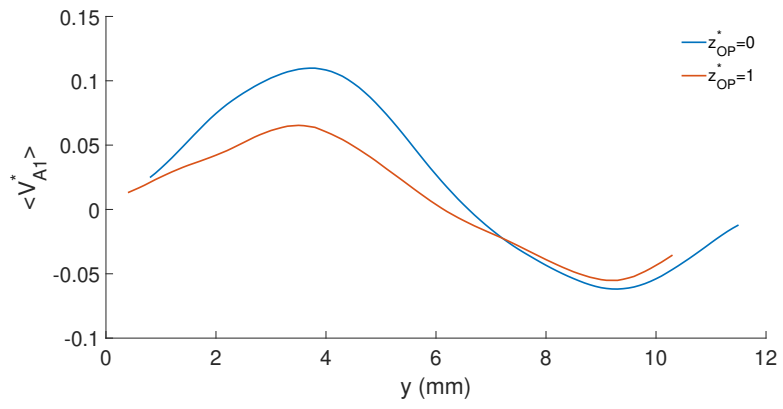


Figure D.2: Transverse velocity component profiles $\langle V_{A1}^* \rangle$ for both object plane locations.

E Boundary layer in tire groove.

Along the tire grooves wall domain, the dimension of the boundary layer thickness (δ_{BL}) remains unknown. In order to qualify this thickness, an analysis can be based on laboratory experiments. In the laboratory, in order to test the protocols for applying R-PIV and stereoscopic R-PIV to tire rolling over puddle flow studied, a test bench is mounted with a static tire over a prismatic bloc (Fig.E.1). The water flow inside grooves is forced thanks to an hydraulic loop with a pump generating a puddle flow on the tire. This situation is slightly different to the rolling case on the track with lower velocities. However, this could be used to test our methods and settlements in tire rolling over puddle flow conditions.

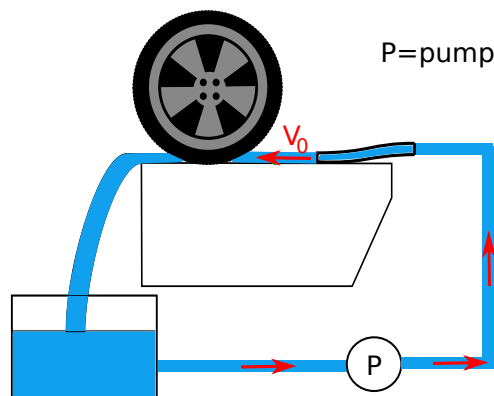


Figure E.1: Hydraulic loop in laboratory for tire preliminary tests.

In this configurations, measurements have been performed inside Type A tire grooves (of cross section 6x12 mm) for different fluid velocities. The vector field is determined with 1x1 mm interrogation windows. The spatially averaged velocity field inside the tire groove is quantified in each case to calculate an associated Reynolds number based on the tire groove hydraulic diameter. With this bench, two different Reynolds number have been tested $Re = 20$ and $Re = 1200$. The velocity profiles obtained are presented in Fig.E.2.

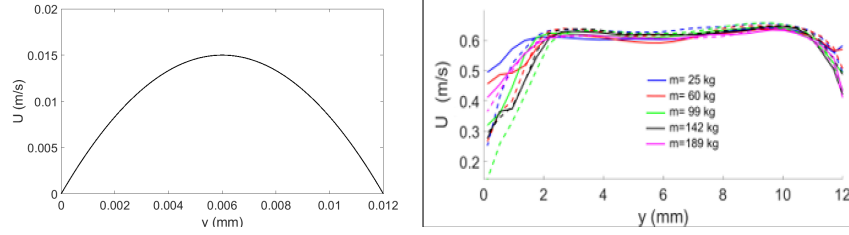


Figure E.2: Profiles obtained for different Reynolds number.

With these profiles, we can observe a parabolic profile at low Reynolds number ($Re = 20$) as expected in a fully developed laminar channel flow. On the other hand, for $Re = 1200$, the boundary layer thickness decreases down to $\delta_{BL} = 2$ mm which correspond to $1/6$ times the groove width. This case is slightly different from the rolling tire case. However, if we consider the non slippage condition on the floor, the tire envelope in the contact patch is at $V_e = 0$ m/s. Therefore, in the ground referential with a rolling tire, the walls of the grooves in the contact patch area are at $V = 0$ m/s. Therefore, the boundary conditions can be considered as similar to the laboratory situation.

For tire measurements, the averaged velocity in the type A grooves is approximately $\langle \overline{U}_A \rangle = 0.1.V_0$, with V_0 vehicle speed. Therefore, for a tire rolling at $V_0 = 50$ km/h, the Reynolds number is as described in Section 1.3.3 $Re \sim 3000$. Therefore, based on the results obtained for the lower Reynolds number in laboratory, the boundary layer thickness can be estimated at an order of magnitude about $\delta_{BL} = 0.1$ mm (1/120 of the groove width) or even less.

Acknowledgment :

The authors would like to thank BPI France (grant n° DOS0051329/00) and Région Auvergne-Rhône-Alpes (grant n° 16 015011 01) for funding the Hydrosafe Tire FUI project.

Bibliography

- [1] Ronald J Adrian. “Double exposure, multiple-field particle image velocimetry for turbulent probability density”. In: *Optics and lasers in engineering* 9.3-4 (1988), pp. 211–228.
- [2] Ronald J Adrian. “Particle-imaging techniques for experimental fluid mechanics”. In: *Annual review of fluid mechanics* 23.1 (1991), pp. 261–304.
- [3] Ronald J Adrian and Chung-Sheng Yao. “Pulsed laser technique application to liquid and gaseous flows and the scattering power of seed materials”. In: *Applied optics* 24.1 (1985), pp. 44–52.
- [4] BJ Allbert and JC Walker. “Tire to Wet Road Friction at High Speeds”. In: *rubber Chemistry and Technology* 41.4 (1968), pp. 753–779.
- [5] Vincenzo Armenio and Virgilio Fiorotto. “The importance of the forces acting on particles in turbulent flows”. In: *Physics of fluids* 13.8 (2001), pp. 2437–2440.
- [6] MP Arroyo and CA Greated. “Stereoscopic particle image velocimetry”. In: *Measurement science and technology* 2.12 (1991), p. 1181.
- [7] Alexey N Bashkatov and Elina A Genina. “Water refractive index in dependence on temperature and wavelength: a simple approximation”. In: *Saratov Fall Meeting 2002: Optical Technologies in Biophysics and Medicine IV*. Vol. 5068. International Society for Optics and Photonics. 2003, pp. 393–395.
- [8] Guy Beadie et al. “Refractive index measurements of poly (methyl methacrylate)(PMMA) from 0.4–1.6 μm ”. In: *Applied optics* 54.31 (2015), F139–F143.
- [9] Yannick Beautru et al. “Influence of Road Surface Microtexture on Thin Water Film Traction”. In: 2012.
- [10] H Blasius. “Boundary layers in fluids of small viscosity”. In: *Z Math Physik* 56.1 (1908), pp. 1–37.
- [11] Craig F Bohren and Donald R Huffman. *Absorption and scattering of light by small particles*. John Wiley & Sons, 2008.
- [12] ME Brachet. “Géométrie des structures a petite échelle dans le vortex de Taylor-Green”. In: *CRAS II* 311 (1990), p. 775.
- [13] C Brücker. “PIV in two-phase flows”. In: *Von Karman Institute for Fluid Dynamics, Chapter Lecture series* 1 (2000).
- [14] Yu A Buevich. “Motion resistance of a particle suspended in a turbulent medium”. In: *Fluid Dynamics* 1 (1970), pp. 119–119.
- [15] Giuseppe Carlo Alp Caridi, Andrea Sciacchitano, and Fulvio Scarano. “Helium-filled soap bubbles for vortex core velocimetry”. In: *Experiments in Fluids* 58.9 (2017), p. 130.

- [16] Georges L Chahine. “Bubble interactions with vortices”. In: *Fluid vortices*. Springer, 1995, pp. 783–828.
- [17] Nian-Sheng Cheng. “Comparison of formulas for drag coefficient and settling velocity of spherical particles”. In: *Powder Technology* 189.3 (2009), pp. 395–398.
- [18] JR Cho et al. “Numerical investigation of hydroplaning characteristics of three-dimensional patterned tire”. In: *European Journal of Mechanics-A/Solids* 25.6 (2006), pp. 914–926.
- [19] Jung-Hua Chou and SY Chao. “Branching of a horseshoe vortex around surface-mounted rectangular cylinders”. In: *Experiments in fluids* 28.5 (2000), pp. 394–402.
- [20] Roland Clift, John R Grace, and Martin E Weber. *Bubbles, drops, and particles*. Courier Corporation, 2005.
- [21] Emma Croner. “Etude de l’écoulement autour des ensembles roulants d’un véhicule en vue de l’optimisation aérodynamique du pneumatique”. PhD thesis. Toulouse, ISAE, 2014.
- [22] Emma Croner et al. “Aerodynamic characterization of the wake of an isolated rolling wheel”. In: *International journal of heat and fluid flow* 43 (2013), pp. 233–243.
- [23] Niels G Deen et al. “On image pre-processing for PIV of single-and two-phase flows over reflecting objects”. In: *Experiments in fluids* 49.2 (2010), pp. 525–530.
- [24] David Dussol et al. “Automatic dynamic mask extraction for PIV images containing an unsteady interface, bubbles, and a moving structure”. In: *Comptes Rendus Mécanique* 344.7 (2016), pp. 464–478.
- [25] Shelagh Fackrell. “Study of the added mass of cylinders and spheres”. In: (2011).
- [26] TF Fwa et al. “Effectiveness of tire-tread patterns in reducing the risk of hydroplaning”. In: *Transportation research record* 2094.1 (2009), pp. 91–102.
- [27] AN Gent and PB Lindley. “The compression of bonded rubber blocks”. In: *Proceedings of the Institution of Mechanical Engineers* 173.1 (1959), pp. 111–122.
- [28] Mohamed Gad-el Hak and Ron F Blackwelder. “The discrete vortices from a delta wing”. In: *AIAA journal* 23.6 (1985), pp. 961–962.
- [29] Gert Heinrich and Manfred Klüppel. “Rubber friction, tread deformation and tire traction”. In: *Wear* 265.7-8 (2008), pp. 1052–1060.
- [30] Corentin Hermange. “Numerical simulation of the fluid-structure interactions inside the aquaplaning problem”. PhD thesis. 2017.
- [31] Corentin Hermange. “Private communication between Michelin in-house simulations and LMFA”. In: (2019).
- [32] Walter B Horne and Robert C Dreher. “Phenomena of pneumatic tire hydroplaning”. In: *National Aeronautics and Space Administration* 2056 (1963).
- [33] Walter B Horne, Thomas J Yager, and Don L Ivey. “Recent studies to investigate effects of tire footprint aspect ratio on dynamic hydroplaning speed”. In: *The tire pavement interface*. ASTM International, 1986.

-
- [34] Richard D Keane and Ronald J Adrian. “Theory of cross-correlation analysis of PIV images”. In: *Applied scientific research* 49.3 (1992), pp. 191–215.
- [35] Inchul Kim, Said Elghobashi, and William A Sirignano. “On the equation for spherical-particle motion: effect of Reynolds and acceleration numbers”. In: *Journal of Fluid Mechanics* 367 (1998), pp. 221–253.
- [36] T-W Kim and H-Y Jeong. “Hydroplaning simulations for tires using FEM, FVM and an asymptotic method”. In: *International journal of automotive technology* 11.6 (2010), pp. 901–908.
- [37] A Kloosterman, C Poelma, and J Westerweel. “Flow rate estimation in large depth-of-field micro-PIV”. In: *Experiments in fluids* 50.6 (2011), pp. 1587–1599.
- [38] Masataka Koishi et al. “Hydroplaning simulation using fluid-structure interaction in LS-DYNA”. In: *The 3rd European LS-DYNA Users Conference*. 2001.
- [39] Robert F Kubin and Aaron N Fletcher. “Fluorescence quantum yields of some rhodamine dyes”. In: *Journal of Luminescence* 27.4 (1982), pp. 455–462.
- [40] Srirangam Santosh Kumar et al. “Study of hydroplaning risk on rolling and sliding passenger car”. In: *Procedia-Social and Behavioral Sciences* 53 (2012), pp. 1019–1027.
- [41] Gaby Launay et al. “An experimental investigation of the laminar horseshoe vortex around an emerging obstacle”. In: *Journal of Fluid Mechanics* 830 (2017), pp. 257–299.
- [42] P Lavoie et al. “Spatial resolution of PIV for the measurement of turbulence”. In: *Experiments in Fluids* 43.1 (2007), pp. 39–51.
- [43] Alessandro Masullo and Raf Theunissen. “Automated mask generation for PIV image analysis based on pixel intensity statistics”. In: *Experiments in Fluids* 58.6 (2017), p. 70.
- [44] Martin R Maxey and James J Riley. “Equation of motion for a small rigid sphere in a nonuniform flow”. In: *The Physics of Fluids* 26.4 (1983), pp. 883–889.
- [45] G Maycock. “Second Paper: Studies on the Skidding Resistance of Passenger-Car Tyres on Wet Surfaces”. In: *Proceedings of the Institution of Mechanical Engineers: Automobile Division* 180.1 (1965), pp. 122–157.
- [46] JK Meades. “Braking force coefficients obtained with a sample of currently available radial ply and crossed ply car tyres”. In: (1967).
- [47] R Mei. “Velocity fidelity of flow tracer particles”. In: *Experiments in fluids* 22.1 (1996), pp. 1–13.
- [48] Renwei Mei and Ronald J Adrian. “Flow past a sphere with an oscillation in the free-stream velocity and unsteady drag at finite Reynolds number”. In: *Journal of Fluid Mechanics* 237 (1992), pp. 323–341.
- [49] Renwei Mei, Christopher J Lawrence, and Ronald J Adrian. “Unsteady drag on a sphere at finite Reynolds number with small fluctuations in the free-stream velocity”. In: *Journal of Fluid Mechanics* 233 (1991), pp. 613–631.
- [50] Carl D Meinhart, Steve T Wereley, and MHB Gray. “Volume illumination for two-dimensional particle image velocimetry”. In: *Measurement Science and Technology* 11.6 (2000), p. 809.
-

- [51] Jiun-Jih Miao et al. “Flow developments above 50-deg sweep delta wings with different leading-edge profiles”. In: *Journal of Aircraft* 32.4 (1995), pp. 787–794.
- [52] Emmanuel Mignot and Nicolas Riviere. “Bow-wave-like hydraulic jump and horseshoe vortex around an obstacle in a supercritical open channel flow”. In: *Physics of Fluids* 22.11 (2010), p. 117105.
- [53] Yusuke Minami, Tomoaki Iwai, and Yutaka Shoukaku. “Observation of Water Behavior in the Contact Area between Porous Rubber and a Mating Surface during Sliding”. In: *Tire Science and Technology* 40.3 (2012), pp. 186–200.
- [54] Patricio A Moreno-Casas and Fabian A Bombardelli. “Computation of the Basset force: recent advances and environmental flow applications”. In: *Environmental Fluid Mechanics* 16.1 (2016), pp. 193–208.
- [55] Faith A Morrison. “Data correlation for drag coefficient for sphere”. In: *Department of Chemical Engineering, Michigan Technological University, Houghton, MI 49931* (2013).
- [56] Z Naumann and L Schiller. “A drag coefficient correlation”. In: *Z. Ver. Deutsch. Ing* 77.318 (1935), e323.
- [57] S Nogueira et al. “Simultaneous PIV and pulsed shadow technique in slug flow: a solution for optical problems”. In: *Experiments in Fluids* 35.6 (2003), pp. 598–609.
- [58] Fuat Odar and Wallis S Hamilton. “Forces on a sphere accelerating in a viscous fluid”. In: *Journal of fluid mechanics* 18.2 (1964), pp. 302–314.
- [59] C-W Oh et al. “Hydroplaning simulation for a straight-grooved tire by using FDM, FEM and an asymptotic method”. In: *Journal of Mechanical Science and Technology* 22.1 (2008), pp. 34–40.
- [60] MG Olsen and RJ Adrian. “Out-of-focus effects on particle image visibility and correlation in microscopic particle image velocimetry”. In: *Experiments in fluids* 29.1 (2000), S166–S174.
- [61] Marie Rastello, Jean-Louis Marié, and Michel Lance. “Drag and lift forces on clean spherical and ellipsoidal bubbles in a solid-body rotating flow”. In: *Journal of fluid mechanics* 682 (2011), pp. 434–459.
- [62] Marie Rastello et al. “Drag and lift forces on interface-contaminated bubbles spinning in a rotating flow”. In: (2009).
- [63] Nicolas Rivière et al. “Emerging obstacles in supercritical open-channel flows: Detached hydraulic jump versus wall-jet-like bow wave”. In: *Journal of Hydraulic Engineering* 143.7 (2017), p. 04017011.
- [64] Fulvio Scarano and Michel L Riethmuller. “Advances in iterative multigrid PIV image processing”. In: *Experiments in Fluids* 29.1 (2000), S051–S060.
- [65] Hermann Schlichting and Klaus Gersten. *Boundary-layer theory*. Springer, 2016.
- [66] Serge Simoens, Michel Ayrault, and James M Wallace. “The flow across a street canyon of variable width—Part 1: Kinematic description”. In: *Atmospheric Environment* 41.39 (2007), pp. 9002–9017.

- [67] Gabriel Stokes George. *On the effect of the inertial friction of fluids on the motion of pendulums*. Vol. 9.II. 1856, pp. 8–106.
- [68] Vincent Strubel et al. “Fluorescence Tracking and μ -PIV of Individual Particles and Lubricant Flow in and around Lubricated Point Contacts”. In: *Tribology Letters* 65.3 (2017), p. 75.
- [69] Tadashi Suzuki and Tatsuo Fujikawa. *Improvement of hydroplaning performance based on water flow around tires*. Tech. rep. SAE Technical Paper, 2001.
- [70] Tomohiko Tanaka and John K Eaton. “Sub-Kolmogorov resolution particle image velocimetry measurements of particle-laden forced turbulence”. In: *Journal of Fluid Mechanics* 643 (2010), pp. 177–206.
- [71] John T Tielking and Freddy L Roberts. “Tire contact pressure and its effect on pavement strain”. In: *Journal of Transportation Engineering* 113.1 (1987), pp. 56–71.
- [72] Violaine Todoroff et al. “The mechanisms involved during the wet braking of new and worn tires”. In: *Vehicle system dynamics* 57.11 (2019), pp. 1601–1620.
- [73] CWH Van Doorne and J Westerweel. “Measurement of laminar, transitional and turbulent pipe flow using stereoscopic-PIV”. In: *Experiments in Fluids* 42.2 (2007), pp. 259–279.
- [74] Maria-Rosaria Vetrano et al. “Applications de la micro-PIV dans des écoulements libre et confiné”. In: (2008).
- [75] Stéphane Vincent et al. “Augmented Lagrangian and penalty methods for the simulation of two-phase flows interacting with moving solids. Application to hydroplaning flows interacting with real tire tread patterns”. In: *Journal of Computational Physics* 230.4 (2011), pp. 956–983.
- [76] Yifei Wang et al. “Experimental study of wheel-vehicle aerodynamic interactions”. In: *Journal of Wind Engineering and Industrial Aerodynamics* 198 (2020), p. 104062.
- [77] Jerry Westerweel. “Digital particle image velocimetry”. In: *Theory and Application* (1993).
- [78] Frank M White and Isla Corfield. *Viscous fluid flow*. Vol. 3. McGraw-Hill New York, 2006.
- [79] Christian E Willert and Morteza Gharib. “Digital particle image velocimetry”. In: *Experiments in fluids* 10.4 (1991), pp. 181–193.
- [80] Brandon M Wilson and Barton L Smith. “Uncertainty on PIV mean and fluctuating velocity due to bias and random errors”. In: *Measurement Science and Technology* 24.3 (2013), p. 035302.
- [81] Robert W Yeager. “Tire hydroplaning: testing, analysis, and design”. In: *The Physics of Tire Traction*. Springer, 1974, pp. 25–63.